



University
of Glasgow

Wang, Lei (2016) Modelling dissection of the arterial wall. PhD thesis.

<http://theses.gla.ac.uk/7066/>

Copyright and moral rights for this thesis are retained by the author

A copy can be downloaded for personal non-commercial research or study, without prior permission or charge

This thesis cannot be reproduced or quoted extensively from without first obtaining permission in writing from the Author

The content must not be changed in any way or sold commercially in any format or medium without the formal permission of the Author

When referring to this work, full bibliographic details including the author, title, awarding institution and date of the thesis must be given

Modelling Dissection of the Arterial Wall

by

Lei Wang

A thesis submitted to the
College of Science and Engineering
at the University of Glasgow
for the degree of
Doctor of Philosophy

January 2016

Abstract Arteries are the highways through which oxygen-rich blood flows toward oxygen-hungry organs, such as the kidneys, heart, and brain. An *arterial dissection* is an axial tear within the arterial wall, which may create a false lumen by the action of blood flow through the tear. Propagation of the tear can quickly lead to death as a result of decreased blood supply to other organs, damage to the aortic valve, and sometimes rupture of the artery.

This thesis aims to develop computational models to simulate the inflation and propagation of a tear in the arterial wall and to investigate the mechanical issues in arterial dissection, with mainly focusing on the effects of the fibre orientation, geometry of the tear and residual stress on dissection propagation. The numerical methods used in our models include both the finite element method and the extended finite element method. We assume the mechanical response of the arterial wall is nonlinear, hyperelastic and anisotropic, and use the Holzapfel-Gasser-Ogden (HGO) strain energy function as the constitutive law.

A finite element computational framework, for the calculation of the energy release rate for a fibre-reinforced soft tissue subject to internal pressure, is developed. This model extends the Griffith failure theory such that we can consider pressure-driven tear propagation subject to a large nonlinear deformation of the arterial wall. Using this model to simulate the tear propagation in strips from the arterial wall, we found the increase in the length of a tear elevates the likelihood of propagation, and if the tissues surrounding the tear are stiff enough this leads to arrest.

Simulations of peeling- and pressure-driven tear propagation are performed through the extended finite element method. *Peeling-driven* propagation is caused by a displacement boundary condition, while *pressure-driven* propagation is due to pressure loading. We found the tear is likely to propagate along the material axis with the maximum stiffness, which is determined by the fibre orientation in the arterial wall. In models of pressure-driven tear propagation, we investigate the effect of the radial depth and circumferential length of a tear in the cross-section of a two-layer (media and adventitia) arterial wall model. The results show that a shallow and long tear leads to buckling of the inner wall (material section between tear and lumen), while a deep tear tends to propagate. Several shapes of deformed arterial wall with a tear predicted from our simulations are similar to CT images of arterial dissections. The critical pressure for propagation increases with the depth for a very short tear, but decreases for a long tear.

Two methods of introducing residual stress, quantified by an opening angle, into a finite

element model for the arterial wall are proposed. The computational programs, of using programming languages including Linux shell script, sed, AWK, Python and Matlab, to *automatically* build finite element models with both methods are developed. We have used them to investigate the effect of residual stress on the critical pressure for tear propagation in the cross-section of the two-layer arterial wall model. The first method is to import the analytical residual stress into a finite element model as an initial stress field, while the second method is to use a residual stress computed numerically. The first method is illustrated with the neo-Hookean material model, and the second method is used with the HGO material model. We find a similar trend of the critical pressure against the opening angles: the critical pressure increases with the opening angle. However, the increase of the critical pressure is less steep in the HGO model compared to the neo-Hookean model. This is presumably due to the interaction of the fibres. When more fibres are stretched, the loading bearing is shifted more towards the fibre structure, and the influence of the residual stress becomes less.

The implementation of an anisotropic hyperelastic material model with growth, for a living fibrous soft tissue, in a finite element program is presented. The problem of loss of anisotropy in the conventional approach when using the volumetric-isochoric decomposition of deformation gradient is analysed. A possible solution is suggested: avoiding use of this decomposition in the parts associated with anisotropy in the strain energy function. This suggestion is demonstrated through several examples using the Fung-type and HGO material models. The essential derivation of the HGO material model is presented for its finite element implementation with both the conventional approach and our suggestion. The corresponding user-subroutines used in a finite element program FEAP are included. In addition, the growth of tissue is also considered in this subroutine by introducing a growth tensor as a material parameter. The method on how to update this subroutine to consider a stress-, strain- or energy-driven growth law is discussed, which could be used to model the tear propagation in a living fibrous tissue.

In summary, this thesis presents computational techniques for modelling dissection of the arterial wall. These models characterise the mechanical factors in the arterial dissection, which could be adapted for other damage and failure of soft tissue. A prediction from these models opens a window to the mechanical issues of this disease and other injuries.

Acknowledgement There are many people that I would like to thank for their help and support during my PhD degree. This study would not have been possible without their willingness to share their experience with me.

I want to thank my supervisors, Dr Steven Roper, Prof. Xiaoyu Luo and Prof. Nicholas Hill for their consistent support and assistance. I have been greatly influenced by their guidance in my academic development. Their inspiration, patience and great efforts to explain things clearly and simply have been great help for me. Thanks to Dr Beibei Li who offered many important information about this topic at the beginning of my study.

The School of Mathematics and Statistics at the University of Glasgow provided a much welcoming and enjoyable environment to conduct my research. I have made many fantastic friends, each of which deserves thanks for either helping with some problem or simply providing some needed distraction. Everyone in my research group and office thanks to each of you, a great bunch of people.

My family have been a great source of help and inspiration over the years. I owe a special mention to my wife who has accompanied and supported me since my high school. The support of my parents, wife, daughter, brother and sister has been, as always, significant beyond what can be justly expressed in words.

Thanks for the China Scholarship Council, who has funded my research during my study. The financial support from School of Mathematics and Statistics of the University of Glasgow for conference travel and thesis writing-up is acknowledged.

My publications related to this thesis

1. L Wang, SM Roper, XY Luo and NA Hill, “Modelling of tear propagation and arrest in fibre-reinforced soft tissue subject to internal pressure” [\[PDF\]](#), *Journal of Engineering Mathematics*, 95(1):249–265, 2015. This paper is based on Chapter 3.
2. L Wang, SM Roper, XY Luo and NA Hill, “Numerical simulation of arterial dissection” [\[PDF\]](#), *Computational and Mathematical Biomedical Engineering Proceedings*, 216–219, Paris, 2015. This paper is based on the peeling-driven tear propagation in Chapter 4.
3. L Wang, SM Roper, XY Luo and NA Hill, “Modelling peeling- and pressure-driven propagation of arterial dissection” [\[PDF\]](#), to be submitted into *International Journal for Numerical Methods in Biomedical Engineering*. This paper is based on Chapter 4.
4. L Wang, SM Roper, NA Hill and XY Luo, “The effect of residual stress on the propagation of arterial dissection” [\[PDF\]](#), submitted into *Journal of the Mechanical Behavior of Biomedical Materials*. This paper is based on Chapters 5 and 6.

Contents

1	Introduction	13
1.1	Anatomy of arterial dissection	13
1.2	Geometry of the arterial wall with a tear	15
1.3	Residual stress and pre-stretch	17
1.4	Mechanical response of the arterial wall	19
1.5	Damage and failure models	24
1.6	Mathematical models of arterial dissection	29
1.7	Numerical methods	32
1.8	Research aims	34
1.9	Outline of thesis	34
2	Basic theory and formulations	36
2.1	Finite elasticity	36
2.1.1	Description of the deformation	36
2.1.2	Stress response	40
2.1.3	Stress-strain relationship	40
2.1.4	Balance equations	45
2.2	FEM	46
2.2.1	Discretisation	47
2.2.2	Linearisation	48
2.3	XFEM	51
2.4	Conclusion	53
3	Onset of propagation of a dissection in a 2D strip	54
3.1	Introduction	55
3.2	Methodology	56

3.2.1	The energy budget	56
3.2.2	Computational approach for ERR	56
3.2.3	Calculation of the strain energy U_e	58
3.2.4	Calculation of the work done by pressure	59
3.3	Results	60
3.3.1	Numerical experiments	60
3.3.2	Effects of the connective tissue — tear arrest	65
3.4	A simple beam model for ERR	69
3.5	Discussion	72
3.6	Conclusion	75
4	Models of peeling- and pressure-driven tear propagation	76
4.1	Introduction	77
4.2	The computational model	78
4.2.1	Mechanical response	78
4.2.2	Damage and failure	79
4.2.3	Extended finite element method	80
4.3	Peeling-driven propagation	81
4.3.1	Tear propagation in strips	81
4.3.2	Tear propagation in discs	83
4.4	Pressure-driven propagation	86
4.4.1	Geometry and boundary conditions	86
4.4.2	Simulations and Results	88
4.5	Conclusion	97
5	Effect of residual stress in an isotropic material	99
5.1	Introduction	100
5.2	Methods	101
5.2.1	Material	101
5.2.2	Geometry	101
5.2.3	Damage and failure	103
5.2.4	Boundary conditions	103
5.3	Residual stress calculation	103
5.3.1	Forward analysis	104

5.3.2	Inverse analysis	105
5.3.3	Calculation of the stress	105
5.4	Importing residual stress to the FE model: <code>sigini.f</code>	105
5.5	Verification	106
5.6	Results	109
5.7	Discussion	113
5.7.1	The material model	113
5.7.2	Boundary condition	113
5.8	Conclusion	117
6	Effect of residual stress in an anisotropic material	118
6.1	Introduction	118
6.2	Methods	120
6.2.1	Material	120
6.2.2	Geometry	121
6.2.3	Boundary conditions	121
6.2.4	Damage and failure	123
6.3	Results	123
6.3.1	The neo-Hookean material	124
6.3.2	HGO material	133
6.3.3	The effect of fibre orientation	142
6.4	Conclusion	145
7	FE material model for living fibrous soft tissues	146
7.1	Introduction	147
7.2	Problem of a $\widehat{\Psi}$	150
7.2.1	Isotropic SEF	150
7.2.2	Anisotropic SEF	152
7.2.3	The problem of $\widehat{\Psi}$ and a possible solution	153
7.3	Comparison of $\widehat{\Psi}$ and $\widetilde{\Psi}$ through analytical examples	154
7.3.1	Stress in uniform dilatation	155
7.3.2	Deformation subject to a hydrostatic compression or tension	157
7.3.3	Performance of approximation to incompressibility	159
7.4	A FE subroutine for the HGO SEF	161

7.4.1	Derivatives of Cauchy stress and spatial tangent moduli	161
7.4.2	Verification	165
7.5	Add growth property of tissue in the FE subroutine	167
7.6	Conclusion	173
8	Conclusions	174
8.1	Limitations and future directions	176

List of Symbols

Ω_0	The stress-free reference configuration
Ω_r	The zero-external-loading configuration with residual stress
Ω	Deformed configuration
\mathbf{X}	The coordinate of a material point in Ω_0
\mathbf{x}	The coordinate of \mathbf{X} in Ω
\mathbf{u}	Displacement vector
\mathbf{F}	Deformation gradient
\mathbf{R}	Rotation tensor
\mathbf{U}	Right stretch tensor
\mathbf{V}	Left stretch tensor
\mathbf{C}	Right Cauchy-Green strain tensor $\mathbf{C} = \mathbf{F}^T \mathbf{F}$
\mathbf{I}	Second-order identity tensor
\mathbf{E}	Green strain tensor $\mathbf{E} = \frac{1}{2}(\mathbf{C} - \mathbf{I})$
$\boldsymbol{\epsilon}$	The linear (infinitesimal) strain tensor
\mathbf{B}	Left Cauchy-Green strain tensor
λ	Principal stretch ratio
\mathbf{A}	Unit vector along fibre direction in reference configuration
\mathbf{a}	Vector $\mathbf{a} = \mathbf{F} \mathbf{A}$ along fibre direction in deformed configuration

\mathbf{t}_0	Traction with respect to the reference configuration
\mathbf{t}	Traction with respect to the deformed configuration
λ_f	The stretch ratio of fibres
J	The determinant of \mathbf{F}
$I_i, i = 1, 2, 3$	The invariants of \mathbf{C}
$I_i, i = 4, \dots, 6$	The anisotropic invariants associated with fibres
$\bar{I}_i, i = 1, \dots, 6$	The deviatoric part of I_i
Ψ	Strain energy function
\mathbf{S}	The second Piola–Kirchhoff stress tensor
\mathbf{P}	The first Piola–Kirchhoff stress tensor
$\boldsymbol{\sigma}$	Cauchy stress tensor
$\boldsymbol{\tau}$	Kirchhoff stress tensor
$\sigma_i, i = 1, 2, 3$	Principal Cauchy stress
\mathfrak{C}	Fourth-order material tangent moduli
\mathfrak{c}	Fourth-order spatial tangent moduli
\mathcal{P}	Lagrange multiplier associated with the constraint of incompressibility
p_c	Critical pressure for tear propagation
p'_c	Dimensionless critical pressure for tear propagation
a	Axial length of a tear in a strip
η	Central angle of a circumferential tear
d	Normalized radial depth of of a circumferential tear
G	Energy release rate
G_c	Critical energy release rate
Δu_c	Critical displacement jump in the cohesive law

T_c	Critical traction in the cohesive law
α	Opening angle
β	The angle of fibres respect to the circumferential direction of artery
R_i	Inner radius of stress-free artery
R_o	Outer radius of stress-free artery
D_m	Thickness of media in the stress-free artery
D_a	Thickness of adventitia in the stress-free artery
r_i	Inner radius of deformed artery
r_o	Outer radius of deformed artery

List of Abbreviations

AD	Arterial Dissection
BC	Boundary Condition
CT	Computed Tomography
ERR	Energy Release Rate
FDM	Finite Difference Method
FE	Finite Element
FEA	Finite Element Analysis
FEAP	Finite Element Analysis Program
FEM	Finite Element Method
FL	False Lumen
GOH	Gasser–Ogden–Holzapfel
HGO	Holzapfel–Gasser–Ogden
NHK	Neo-Hookean
PDE	Partial Differential Equations
SEF	Strain Energy (density) Function
SIF	Stress Intensity Factor
TL	True Lumen
XFEM	eXtended Finite Element Method

Chapter 1

Introduction

1.1 Anatomy of arterial dissection

A large artery is composed of three layers: intima, media and adventitia (Figure 1.1). The intima, the innermost layer, is thin and easily traumatized. This layer is in direct contact with the blood inside the vessel and mainly lined by endothelium [Holzapfel et al., 2000]. The media is responsible for imparting strength to the artery and consists of laminated but intertwining sheets of elastic tissue. The arrangement of these sheets in a spiral provides the artery with its maximum allowable tensile strength. The outermost layer is adventitia, which largely consists of collagen to prevent the artery from over inflation and stretch.

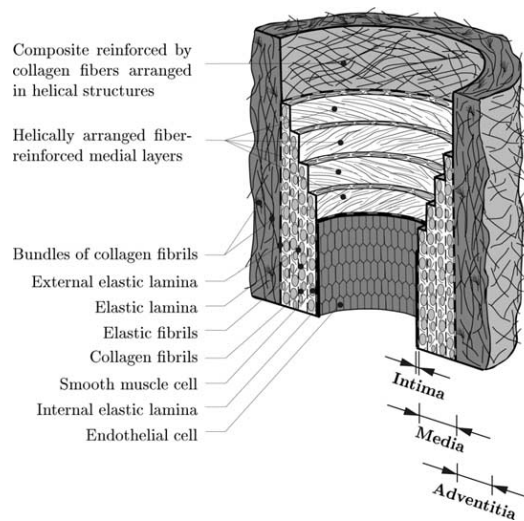


Figure 1.1: The idealized structure analysis of the arterial wall for a large blood vessel from [Holzapfel et al., 2000].

Arterial Dissection (AD) is defined as separation of the layers or a longitudinal tear within the arterial wall (Figure 1.2). This tear may be created by the blood flow, which leaks into the wall through a defect in the intima. Subject to high blood pressure in the artery, the tear may extend proximally (closer to the heart) or distally (away from the heart) or both, so creating a *false lumen* in the wall and narrowing the *true lumen*. A true lumen is the normal vessel, in which the blood flows through in a healthy artery.

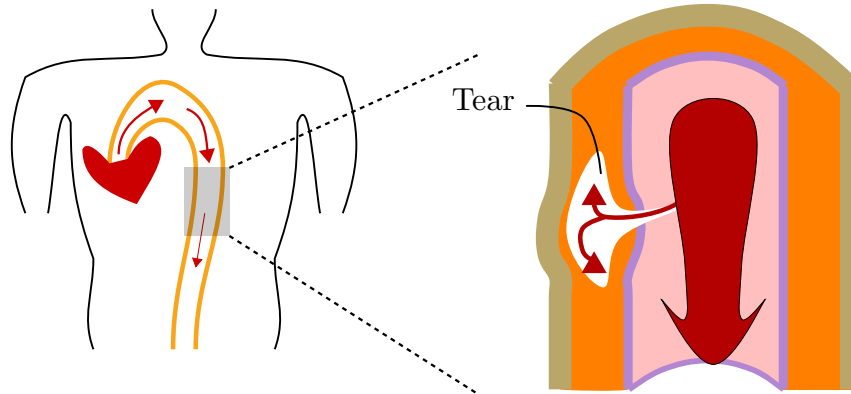


Figure 1.2: The idealized arterial dissection is a longitudinal tear subject to the blood pressure. It might propagate further if the critical condition is reached.

AD is most commonly found in the aorta, the main artery of the body, supplying oxygenated blood to the circulatory system [Hagan et al., 2000]. These AD, generally named aortic dissections, are classified into two groups based on where the tear is located, Stanford A and B. The Stanford A aortic dissection involving the ascending aorta and/or arch, which is directly connected to the heart, generally has a high mortality rate and requires emergency surgical interventions. Certain types of aortic dissection, if left untreated, kill 33% of patients within the first day, 50% within the first two days, and 75% within the first two weeks [Khan and Nair, 2002]. This pattern of mortality rate has remained essentially unchanged over the last sixty years [Foundation., 2013], so early diagnosis and treatment are critical for survival. On the other hand, the Stanford B aortic dissection involving the descending aorta is less life-threatening than the Stanford A and is generally treated medically.

AD is also presented in other arteries, among which the most life-threatening is the dissection of the arteries in the neck [Bogousslavsky et al., 1987; Showalter et al., 1997]. It includes carotid (large) and vertebral (small) AD. After the tear, blood enters the arterial

wall and forms a blood clot, thickening the arterial wall and often impeding blood flow. Vertebral AD is less common than carotid AD. The two types of dissections combined account for about 25% of strokes in young and middle-aged people [Campos-Herrera et al., 2008].

The advancement of diagnostic and therapeutic strategies depends crucially on improving our knowledge of the pathogenesis of AD. There are various hypotheses of the pathogenesis of AD, most of which involve three stages. Firstly, haemodynamic changes modify the loading on the arterial walls [Rajagopal et al., 2007]; secondly, remodelling of the tissue occurs in response to the changed loading condition [de Figueiredo Borges et al., 2008]; and thirdly, the mechanical environment changes due a presence of a small initial lesion. Of particular importance is the development of an understanding of the factors governing the propagation of the initial tear in the anisotropic soft tissue under blood pressure and large deformation. This is the focus of this thesis.

1.2 Geometry of the arterial wall with a tear

The geometric characteristics of arterial wall and dissection are commonly used in the current clinical guidelines that determine whether a surgical intervention or a medical treatment is suggested for a patient [e.g. Tsai et al., 2009]. The impacts of dissection size and number of dissections on the false lumen pressure were studied through experiments in [Tsai et al., 2008]. The percentage of false lumen diastolic pressure out of the true lumen diastolic pressure were computed: 100.4% in model A, 107.9% in model B and 104.6% in model C. Comparison from three models (Figure 1.3) shows that the false lumen pressure is elevated most in model B especially when the entry tear is small and the re-entry tear is occluded.

The correlation of propagation pressure, beyond which the dissection starts to propagate, on the radial depth of tear was reported in the experimental study by Tam et al. [1998]. This study includes pressure-driven tear propagation in 16 isolated porcine thoracic aortas. Each thoracic aorta was cut to approximately 17–19 cm in length. These aortas were turned inside out, and then about 4 ml of 0.9% saline solution was injected into the media of the aorta. This injection created an elliptical bleb, simulating the false lumen in AD, between 2.5 and 3.0 cm in length with its long axis parallel to the long axis of the aorta. A circumferential-radial slit was made in each bleb to simulate an intimal

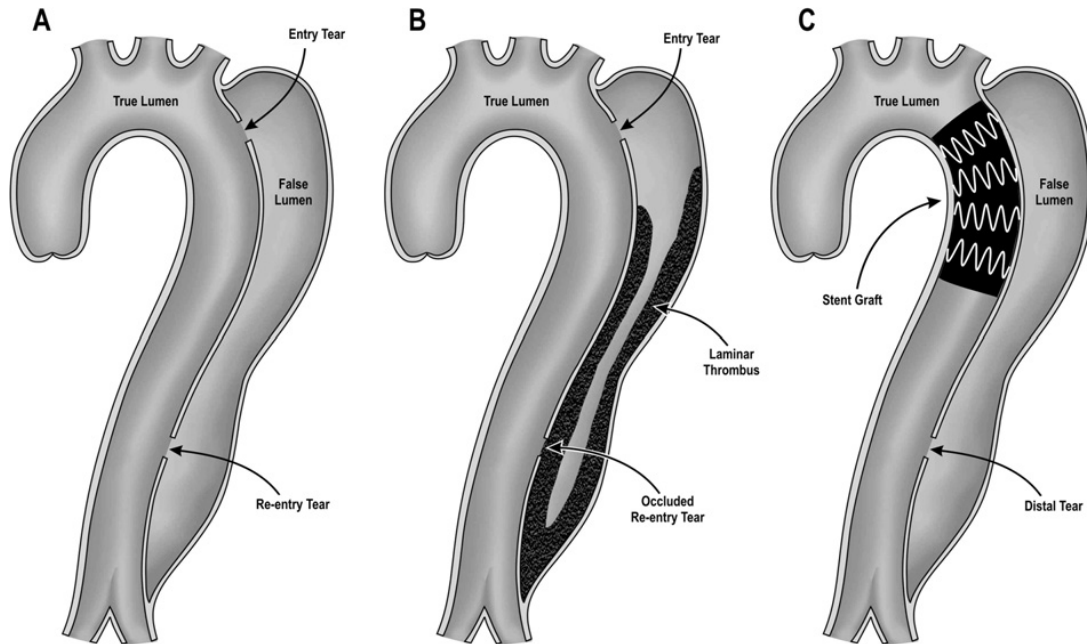


Figure 1.3: Three representative consequences of type B aortic dissection in follow-up period [Tsai et al., 2008]. Model A has both entry and re-entry tears, Model B has a smaller entry tear and the distal tear is occluded by a thrombus, and Model C the proximal tear is treated by a stent graft. The false lumen diastolic pressure is found to be about 100.4% in model A, 107.9% in model B and 104.6% in model C, out of the true lumen diastolic pressure.

tear. Both bleb and slit spanned approximately one-half the circumference of the aorta. The aortas were then flipped right side out, cannulated, submerged in 0.9% saline and pressurized under static conditions. Since the bleb connected the true lumen through the slit, the pressures within the bleb and true lumen were identical. The pressure was increased until each dissection propagated; the pressure at which this occurred is taken to be the ‘propagation pressure’ of the bleb at the particular radial depth. The result (Figure 1.4) shows that the propagation pressure decreases almost linearly as the depth increases.

An aneurysms (the part of arterial wall is inflated like a balloon) is highly correlated with arterial dissection. The size of thoracic aneurysms has a profound impact on dissection or rupture of an arterial wall [Davies et al., 2002]. The patient with an aneurysm exceeding 6 cm in diameter can expect a yearly rate of dissection at least 6.9% and a death rate of 11.8% statistically. However, Pape et al. [2007] postulated that the aortic diameter

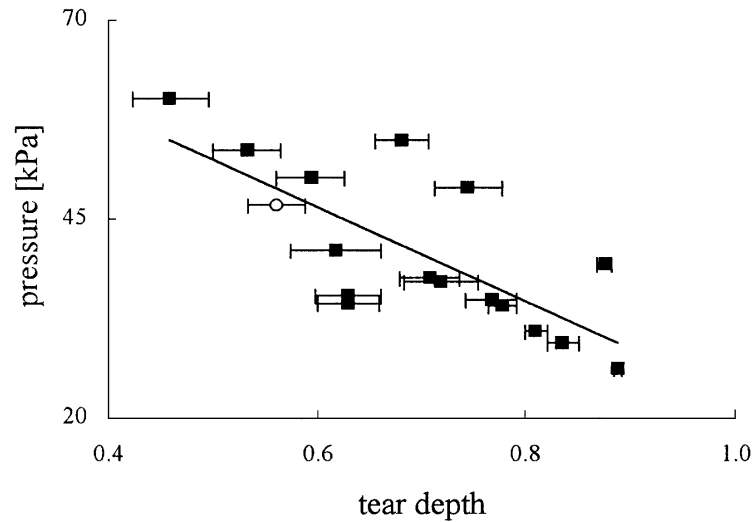


Figure 1.4: The relationship between tear depth and propagation pressure, presented from the experimental study performed by Tam et al. [1998]. The open symbol indicates the bleb that ruptured. The bars represents uncertainties calculated from standard deviations.

≥ 5.5 cm is not a good predictor of type A aortic dissection. This statistical study is based on the data of 591 type A dissection patients enrolled in the International Registry of Acute Aortic Dissection.

1.3 Residual stress and pre-stretch

The stress that exists in an unloaded solid body is called residual stress. The existence and importance of residual stress in the arterial mechanics is recognized in many experiments [e.g. Chuong and Fung, 1986; Fung, 1991]. One representative experiment (Figure 1.5) shows that one cut along a radius of a segment of artery from a rat, which results in an open-sector sample, can release most of the residual stress. The opening angle in the open-sector sample is a common quantification of the residual strain. The residual stress is calculated from the residual strain via a constitutive law.

A notable study on using the opening angle in stress analysis of arterial wall is performed by Holzapfel et al. [2000]. In [Holzapfel et al., 2000], the importance of residual stress, which can decrease the stress concentration in the inner layer of arterial wall and smooth the stress distribution through the wall, is clearly shown (Figure 1.6). In addition, the mathematical model [Holzapfel et al., 2000] also includes the axial pre-stretch, λ_z . A

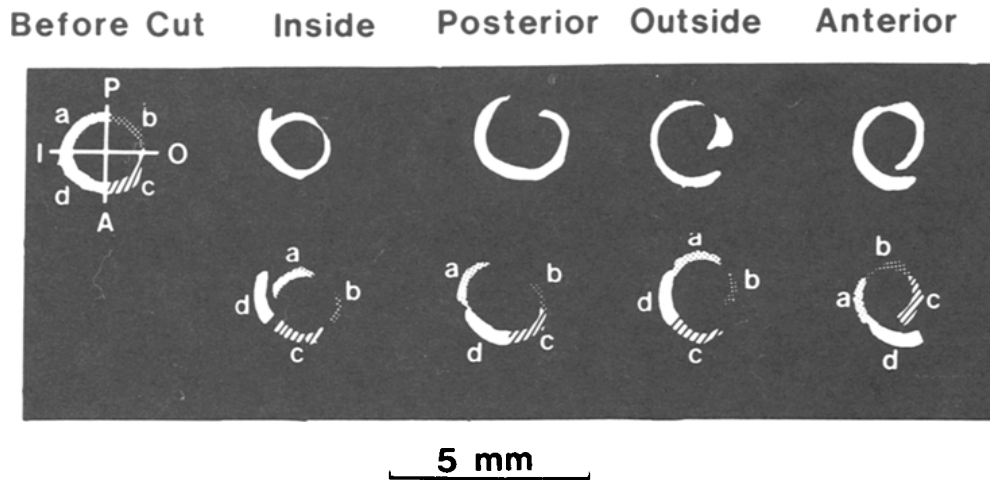


Figure 1.5: The figures in the upper row show an artery segment of a rat before cut and after cutting at four positions. The lower row shows the same vessel cut into four pieces and reassembled in four ways. Since the geometry of each segment in the upper row is similar to the corresponding one in the lower row, it appears that one cut is sufficient to reduce an unloaded arterial segment to the zero-stress state. The opening angle in the segment after one cut is a common measure of the residual strain. This figure is from [Fung, 1991].

value of greater than 1 for λ_z is commonly used, since many studies have observed that the artery will shorten axially just after being cut off [e.g. Dobrin et al., 1990].

Residual stress and axial pre-stretch are due to the different growth rates of different components. Cardamone et al. [2009] employed the constrained mixture theory to study the origin of axial pre-stretch and residual stress in an artery. The arterial wall is modelled as a mixture of the elastin, fibrillar collagens and smooth muscle. Each component is assumed to have a different compression or stretch ratio when relaxed and exist in each point of arterial wall. This assumption is the kernel of the constrained mixture theory, which was originally developed by Humphrey and Rajagopal [2002]. Associating, a rule-of-mixtures constitutive relation used in [Cardamone et al., 2009] is

$$\Psi = \phi_e \Psi_e(\mathbf{F}_e) + \sum_{f=1}^4 \phi_f \Psi_f(\lambda_f) + \phi_m \Psi_m(\lambda_m), \quad (1.1)$$

where ϕ_i are mass fractions for each constituent and Ψ_i are individual strain energy functions, using subscripts e for amorphous elastin, $f = 1, 2, 3, 4$ for four oriented families of collagen fibres, and m for circumferentially-oriented passive smooth muscle.

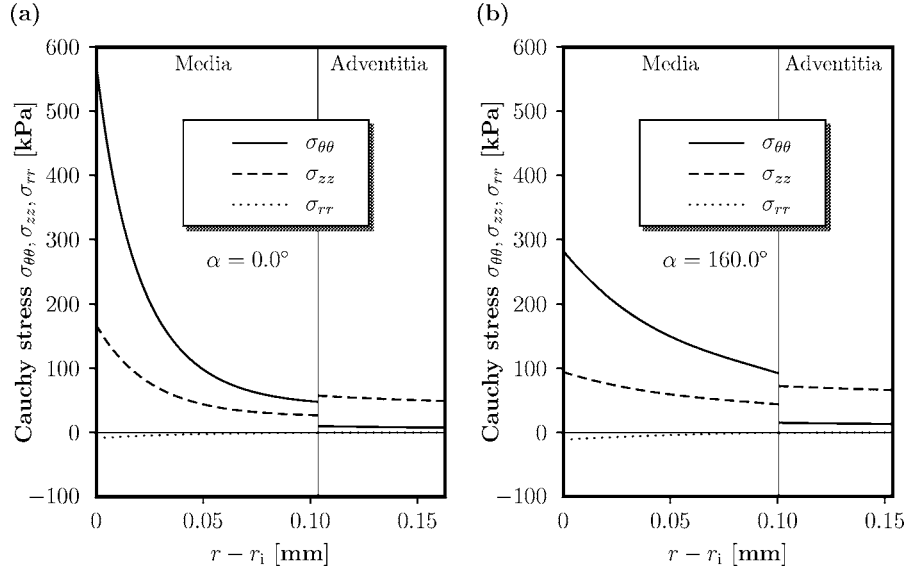


Figure 1.6: The stress distribution through the two-layer arterial wall of a rabbit carotid artery subject to physiological loading ($p_i=100$ mmHg and $\lambda_z=1.7$): (a) without and (b) with residual stress. $r - r_i$ is the distance of a point in arterial wall from the inner radial surface at r_i , and α is the opening angle with respect to the center of artery. The stress at the inner radial surface ($r - r_i = 0$) with residual stress is significantly lower than that without residual stress. The stress distribution with residual stress is smoother than that without residual stress. This figure is from the Figure 18 in [Holzapfel et al., 2000].

To compare a phenomenological constitutive equation, (1.1) is used to investigate the separate contribution of each constituent on the physiological function of the artery. In [Cardamone et al., 2009], it is shown that the prestretched elastin contributes significantly to both the retraction of arteries that is observed upon transection and the opening angle that follows the introduction of a radial cut in an unloaded segment. Axial prestresses and residual stresses in arteries contribute to the homeostatic state of stress in vivo as well as adaptations to perturbed loads, disease, or injury.

1.4 Mechanical response of the arterial wall

The axial stretch ratio, the ratio of axial length in the physiological condition to that after unloading, is 1.7 for the carotid artery [Holzapfel et al., 2000]. That shows the deformation is large, so the infinitesimal strain theory, which assumes the displacement of material particles to be much smaller than any relevant dimension of the body, is invalid

for characterizing the dynamics of the arterial wall. Instead, the finite strain theory has to be employed. Let the *deformation gradient* be denoted by \mathbf{F} , which transforms a material point at \mathbf{X} to \mathbf{x} during deformation,

$$\mathbf{x} = \mathbf{F}\mathbf{X}. \quad (1.2)$$

The Green strain tensor is

$$\mathbf{E} = \frac{1}{2} (\mathbf{F}^T \mathbf{F} - \mathbf{I}), \quad (1.3)$$

where \mathbf{I} is the second-order identity tensor.

The constitutive law is defined through a *Strain-Energy Function* (SEF), from which the stress-strain relationship is derived. A direct extension of the linear isotropic elastic material model is the St.Venant–Kirchhoff SEF

$$\Psi = \frac{\lambda}{2} [\text{tr}(\mathbf{E})]^2 + \mu \text{tr}(\mathbf{E}^2), \quad (1.4)$$

where λ and μ are the material parameters or Lamé constants. The associated second Piola–Kirchhoff stress is

$$\mathbf{S} = \frac{\partial \Psi}{\partial \mathbf{E}} = \lambda \text{tr}(\mathbf{E})\mathbf{I} + 2\mu\mathbf{E}. \quad (1.5)$$

Equation (1.5) shows that the stress-strain relationship is linear, so the St.Venant–Kirchhoff SEF characterises a deformation with geometric nonlinearity and material linearity.

Many studies have shown the mechanical response of arterial wall is nonlinear both geometrically and materially. Holzapfel et al. [2000] made a systematic comparison study of a range of constitutive laws for the passive mechanical response of the arterial wall and proposed a new SEF now known as the *Holzapfel–Gasser–Ogden* (HGO) material model. In [Holzapfel et al., 2000], several different SEFs are used to calculate for the equilibrium and stress distribution of a thick-walled circular cylindrical tube, which simulates the arterial wall. The tube is subject to a combined extension, inflation and torsion and with residual stress incorporated. The kinematic, equilibrium equations and constitutive equations are also included in [Holzapfel et al., 2000]. The comparison shows that some models [e.g. Delfino et al., 1997] oversimplify through use of isotropy, but the anisotropy of arterial tissue is evident [e.g. Roach and Burton, 1957; Shah et al., 2014]. A phenomenological Fung-type SEF in [Humphrey, 1994], can represent the anisotropy of arterial tissues through its material parameters. However, material parameters in this Fung-type SEF are without any physical meanings. The values for these parameters are generally obtained through a nonlinear curve fitting, but they can be still difficult to get, and non-uniqueness

results in a problem. Figure 6 of [Holzapfel et al., 2000] shows that the convexity, which is necessary to guaranty the robustness and efficiency of the computation [Holzapfel, 2006], of this Fung-type SEF is lost for some material parameter values. In contrast, the HGO model is based on the histology of the arterial wall (Figure 1.1). A two-layer arterial wall model (media and adventitia), shown in Figure 1.7, is developed in [Holzapfel et al., 2000]. Each layer of the arterial wall is assumed to consist of fibre-reinforced soft tissue, so the HGO SEF includes two terms associated with the mechanical response of matrix and collagen fibres. The response of the matrix is described by a neo-Hookean material model, and the response of fibre is an exponential function. The fibres are stiffer than the matrix with a high stretch ratio. The fibres can only take on the load in tension, and then result in material anisotropy.

For an incompressible fibre-reinforced material with one orientated-family of fibres, the direction of which is quantified by a unit vector say \mathbf{A} in the stress-free configuration, the HGO SEF is

$$\begin{aligned}\Psi(I_1, I_4) &= \Psi_m(I_1) + \Psi_f(I_4) \\ &= \frac{c}{2}(I_1 - 3) + H(I_4)\psi_f(I_4),\end{aligned}\tag{1.6}$$

where $H(\cdot)$ is the switch condition, for indicating that fibres can only take stretch load, defined as

$$H(x) = \begin{cases} 0 & x \leq 1 \\ 1 & x > 1 \end{cases}$$

and $\psi_f(\cdot)$ is the exponential stretch stiffening stored energy function for fibres

$$\psi_f(x) = \frac{k_1}{k_2} \{ \exp [k_2(x - 1)^2] - 1 \}.$$

In (1.6), the deformation of material is quantified through invariants I_i , $i = 1, 4$.

$$I_1 = \text{tr } \mathbf{C},\tag{1.7}$$

where

$$\mathbf{C} = \mathbf{F}^T \mathbf{F}\tag{1.8}$$

is the right Cauchy–Green strain tensor. The eigenvalues of \mathbf{C} are the square of the principal stretch ratios. A principal stretch ratio is the ratio of the length of material along the associated principal axis after deformation to before deformation.

$$I_4 = \frac{\mathbf{a} \cdot \mathbf{a}}{\mathbf{A} \cdot \mathbf{A}} = \mathbf{a} \cdot \mathbf{a} = \mathbf{C} : \mathbf{M},\tag{1.9}$$

where $\mathbf{a} = \mathbf{F}\mathbf{A}$ is the vector to quantify fibres orientation in the deformed configuration, and

$$\mathbf{M} = \mathbf{A} \otimes \mathbf{A} \quad (1.10)$$

is a second-order structure tensor. \otimes denotes the tensor product, such that \mathbf{M} is a second-order tensor with the components $M_{ij} = A_i A_j$, $i, j = 1, 2, 3$. I_4 has obvious physical meaning, it is the square of fibre stretch.

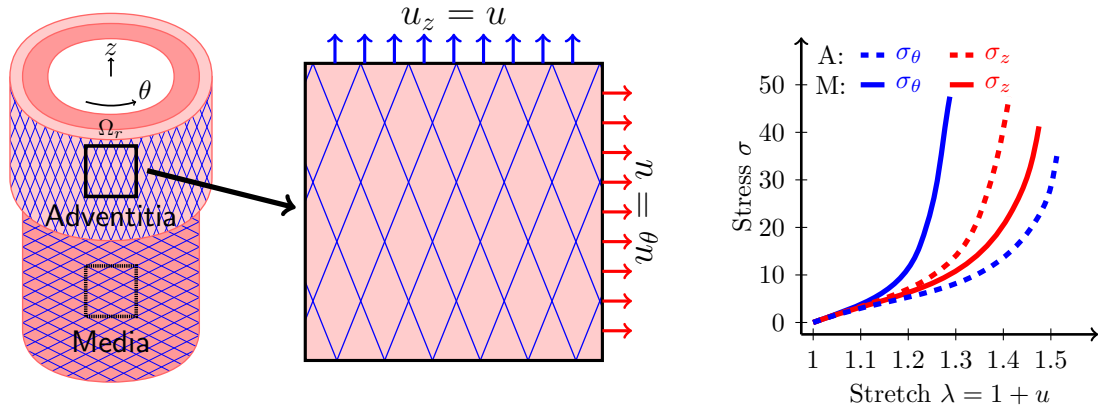


Figure 1.7: Demonstration of the two-layer arterial wall model and the mechanical response of arterial wall in uniaxial stretch of a unit-square sample. u is the displacement used in the uni-axial test, dashed curves show the stress-stretch response of the adventitia, and solid curves show the stress-stretch response of the media. For each layer, the stress response along circumferential direction (blue curves) is different compared with that along the axial direction (red curves). The stress-stain for each layer is nonlinear and directional. The directional preference or anisotropy is determined by the orientation of collagen fibres (blue lines). The two-layer assumption is because the adventitia and media have different mechanical response.

Gasser et al. [2006] generalized the HGO model by additionally considering the dispersion of collagen fibres, now known as the *Gasser–Ogden–Holzapfel* (GOH) model. The polarized light microscopy of arterial tissue shows the dispersion of collagen fibres is significant in both the intima and adventitia [CANHAM et al., 1989]. The degree of dispersion is characterised by a scalar κ , which can be determined as follows. Let the density function $\rho(\mathbf{N})$ characterise the distribution of fibres with respect to the referential orientation \mathbf{N} , which may be expressed in terms of two angles $\theta \in [0, \pi]$ and $\phi \in [0, 2\pi]$, which are the

spherical coordinates of \mathbf{N} , by

$$\mathbf{N}(\theta, \phi) = \sin \theta \cos \phi \mathbf{e}_1 + \sin \theta \sin \phi \mathbf{e}_2 + \cos \theta \mathbf{e}_3, \quad (1.11)$$

where \mathbf{e}_1 , \mathbf{e}_2 and \mathbf{e}_3 denote the orthogonal unit vectors in a rectangular Cartesian coordinate system. The density function $\rho(\mathbf{N})$ is normalised such that

$$\frac{1}{4\pi} \int_{\omega} \rho(\mathbf{N}(\theta, \phi)) d\omega = 1, \quad (1.12)$$

where ω is the unit sphere and $d\omega = \sin \theta d\theta d\phi$. Then a structure tensor for quantifying fibres orientation with dispersion is defined by

$$\widehat{\mathbf{M}} = \frac{1}{4\pi} \int_{\omega} \rho(\mathbf{N}(\theta, \phi)) \mathbf{N}(\theta, \phi) \otimes \mathbf{N}(\theta, \phi) d\omega. \quad (1.13)$$

If we assume that the collagen fibres are distributed with rotational symmetry respect to a mean referential direction \mathbf{A} , and let \mathbf{A} be coincided with the Cartesian basis vector \mathbf{e}_3 , then the density function $\rho(\mathbf{N})$ only depends on θ (the angle between \mathbf{N} and \mathbf{A}), and then (1.13) may be simplified by

$$\widehat{\mathbf{M}} = \kappa \mathbf{I} + (1 - 3\kappa) \mathbf{A} \otimes \mathbf{A}, \quad (1.14)$$

where

$$\kappa = \frac{1}{4\pi} \int_0^\pi \int_0^{2\pi} \rho(\theta) \sin^3 \theta \cos^2 \phi d\theta d\phi = \frac{1}{4} \int_0^\pi \rho(\theta) \sin^3 \theta d\theta. \quad (1.15)$$

As a result, the stretch of fibres is quantified by an invariant of averaging-sense

$$\hat{I}_4 = \mathbf{C} : \widehat{\mathbf{M}}. \quad (1.16)$$

The GOH model becomes an isotropic exponential function when $\kappa = 1/3$, i.e., $\widehat{\mathbf{M}} = 1/3\mathbf{I}$, which is independent of fibre orientations. In contrast, the GOH model is anisotropic and does not involve fibre dispersion when $\kappa = 0$, same is true for the HGO model. In all the fibre reinforced models, the switch for determining that fibres only takes on load if stretched is needed. Unlike I_4 in (1.9), \hat{I}_4 lost the significance of physical meaning, and is not enough to determine if a individual fibre is stretched. $\hat{I}_4 > 1$ does not necessarily require $I_4 > 1$, which indicates fibres at direction \mathbf{A} are stretched. Holzapfel and Ogden [2015] analysed drawbacks of using \hat{I}_4 and provided a possible solution by introducing a modified fibre distribution model. In this modified fibre distribution model, a deformation-dependent range of value for θ during which fibres are stretched, is computed. The integral is done only in this range when computing κ in (1.15).

Babu et al. [2015] studied the biomechanical properties of human ascending thoracic aortic tissues excised from patients with type A aortic dissection through mechanical biaxial stretch testing. These tissue samples were obtained from 16 patients at 7–71 years old, selected in the regions without the presence of visible calcifications or existing dissected layers, and cut to the shape of square with edges along the longitudinal and circumferential directions of aorta. The stress-strain curves of these tissue samples showed that the stiffness of the aortic tissues with Type A dissection is significantly greater than the control aorta without arterial disease, and that the stiffness of these tissue samples does not correlate with the aortic diameter measured prior to surgery nor is there any age dependent difference in the tissue property.

1.5 Damage and failure models

This material complexity of arterial tissue requires the development of new macroscopic and microscopic failure criteria.

The macroscopic failure criteria use the quantities in continuum mechanics, e.g. stress and energy. The three most common failure criteria in fracture mechanics are defined through the failure parameters: crack-tip *Stress (field) Intensity Factor* (SIF) K , *Energy Release Rate* (ERR) G , and cohesive traction on separation.

The SIF represents the strength of the stress fields surrounding the crack-tip. By comparing with fracture toughness K_c , the highest value of SIF that the material can withstand without fracture, an engineer can predict a crack will propagate if $K > K_c$. K is determined by the boundaries of the body and the loads imposed, consequently formulas for its evaluation come from a complete stress analysis of a given configuration, loading and asymptotic crack tip stress field expression. For example, asymptotic analysis [Tada et al., 2000] for linear elastic fracture plain strain problem gives the stress distribution in the vicinity of crack tip

$$\sigma_{ij}(r, \theta) = Kr^{-1/2}f_{ij}(\theta) + o(r^{-1/2}), \quad i, j = 1, 2 \quad (1.17)$$

where (r, θ) is the coordinate of a point near tip in the polar coordinate system with origin

at the crack tip (Figure 1.8), and

$$\begin{aligned} f_{11}(\theta) &= \frac{1}{\sqrt{2\pi}} \cos \frac{\theta}{2} \left(1 - \sin \frac{\theta}{2} \sin \frac{3\theta}{2} \right), \\ f_{12}(\theta) &= \frac{1}{\sqrt{2\pi}} \cos \frac{\theta}{2} \left(1 + \sin \frac{\theta}{2} \sin \frac{3\theta}{2} \right), \\ f_{22}(\theta) &= \frac{1}{\sqrt{2\pi}} \cos \frac{\theta}{2} \sin \frac{\theta}{2} \sin \frac{3\theta}{2}. \end{aligned}$$

One method to calculate the value of K of the opening mode (Figure 1.8) is via [see Tada et al., 2000]

$$K = \lim_{r \rightarrow 0} \sqrt{r} \sigma_{22}(r, 0). \quad (1.18)$$

The tip stress field is calculated generally by the *Finite Element* (FE) based method, including the extended FE method [Dolbow and Belytschko, 1999], adaptive h-p FE method [Peano et al., 1978] or some special element with reflecting singularity [Henshell and Shaw, 1975].

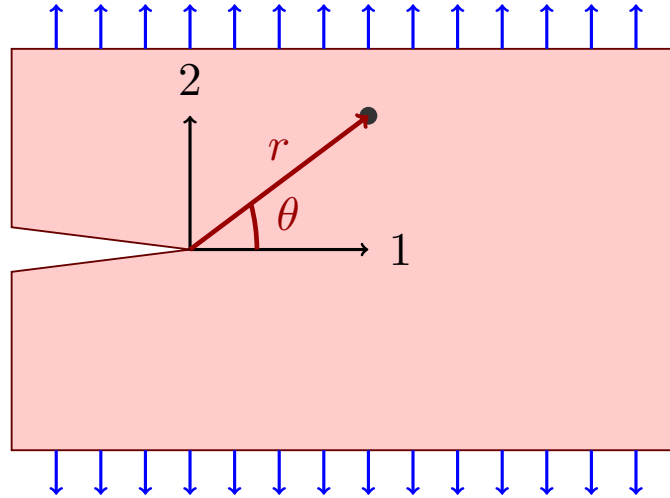


Figure 1.8: Polar coordinate system at the tear tip in a sample loaded by tension (blue arrows), which results in an opening-mode failure.

The calculation of K depends on two key techniques, i.e. obtaining an asymptotic crack-tip stress field in terms of K , and computing an accurate stress field. However, the asymptotic crack-tip stress field is generally not available for non-linear materials [Allegrini and Scarpa, 2014]. One particular example is the asymptotic crack-tip stress field for finite plane stress deformation of a neo-Hookean sample [Stephenson, 1982]. The tip Cauchy

stress as $r \rightarrow 0$ is different to that in a linear elastic solid [Tada et al., 2000],

Neo-Hookean (nonlinear)	Linear isotropic	
$\sigma_{11} = \mu C_1^2$	$\sigma_{11} = \frac{K}{\sqrt{2\pi r}} \cos \frac{\theta}{2} \left(1 - \sin \frac{\theta}{2} \sin \frac{3\theta}{2}\right)$	(1.19)
$\sigma_{12} = -\mu \frac{C_1 C_2}{\sqrt{2r}} \sin \frac{\theta}{2}$	$\sigma_{12} = \frac{K}{\sqrt{2\pi r}} \cos \frac{\theta}{2} \left(1 + \sin \frac{\theta}{2} \sin \frac{3\theta}{2}\right)$	
$\sigma_{22} = \mu \frac{C_2^2}{4r}$	$\sigma_{22} = \frac{K}{\sqrt{2\pi r}} \cos \frac{\theta}{2} \sin \frac{\theta}{2} \sin \frac{3\theta}{2},$	

where C_1 and C_2 , analogous to K , are constants, and μ is the shear modulus in the incompressible neo-Hookean SEF. Similar to (1.18), the values for C_1 and C_2 can be determined, provided the crack-tip stress field is available, via

$$C_1 = \lim_{r \rightarrow 0} \sqrt{\sigma_{11}/\mu}, \quad C_2 = \lim_{r \rightarrow 0} \sqrt{4\sigma_{22}r/\mu}. \quad (1.20)$$

The stress singularity, $\sigma_{ij} \rightarrow \infty$, $i, j = 1, 2$, as $r \rightarrow 0$, exists in each component for a linear isotropic material, with the same degree of singularity $-1/2$ to the power of r . While the stress singularity in σ_{11} disappears for the opening mode of neo-Hookean specimen subject to finite deformation, and the degree of singularity in σ_{22} is -1 , which is different with that in σ_{12} is $-1/2$. Krishnan et al. [2008] employed the FE method to compute the Cauchy stress in the vicinity of crack tip, and used these stresses to determine the value of C_1 and C_2 by using (1.20). However, we do not know the asymptotic tip stress field for HGO material model.

A cohesive zone approach was originally proposed for failure in concrete, to model the process zone where the damage of the material takes place. A cohesive law gives equations relating separation (normal and tangential displacement jumps across the cohesive surfaces) at the front of a tip to the cohesive tractions bonding the two cohesive surfaces. It can be used to analyse tear propagation, nucleation and arrest [Volokh, 2004]. A cohesive law requires at least two of three parameters, the maximum traction just before activation of damage, the maximum displacement jump and the fracture energy, i.e. the area under the curve of cohesive traction against the relative displacement of the faces of the tear. Cohesive models have been used for the analysis of fracture in biological tissues for modelling a peeling test of an arterial strip under external loading [Gasser and Holzapfel, 2006]. Elices et al. [2002] illustrated that the shape of the cohesive curve also has a significant effect on the simulation of failure, thus detailed experiments are required to determine the cohesive law for soft tissue [Bhattacharjee et al., 2013]. Recently, Pandolfi and colleagues

developed the anisotropic cohesive elements based on standard finite element method for a strongly oriented fibre reinforced material model [Ferrara and Pandolfi, 2010; Ortiz and Pandolfi, 1999], and used a direction-dependent resistance ellipsoid surface to reflect the anisotropic response of the material in the tearing process.

The energy approach to failure is based on calculating the ERR, G , which is the change in total potential energy per unit extension of the tear. It is developed by, *inter alios*, Griffith [1921] and extended by Irwin and Wells [1965]. Using the ERR to analyse the effects of defects historically preceded use of the SIF and is equivalent to the cohesive zone model in some circumstances [Willis, 1967]. The concept of ERR stems from the energy balance principle during an infinitesimal quasi-static tear extension; it is the energy per unit area released from the system by extending the tear surface by an infinitesimal area dA . In plane strain, the deformation is two-dimensional and G is calculated per unit length instead of per unit area. Given the material parameter G_c , the critical energy required to break all bonds across dA , we can evaluate the potential for propagation of the tear: if $G > G_c$, the tear may propagate (i.e. it is energetically feasible), otherwise it is stationary. Thus $G - G_c$ is the potential for tear propagation. In particular, ignoring any plastic effects, G can be calculated from just the work done by loads and changes in strain energy accompanying the increase in tear area. There are many numerical methods for calculating G [see Zehnder, 2007], and most of them do not rely on evaluating the singular stress field at the tip, rather on the global energy and work, so an accurate value for G can be obtained with modest mesh refinement.

A microscopic failure model for fibre-reinforced material considers the damage and failure at the microscopic scale, which is of a length scale of fibres. A failure criterion for characterising the damage of individual components has been used, Ionescu et al. [2006] assumes that the matrix fails due to over-shear while the fibres are broken when they are over stretched (Figure 1.9). The shear strain of matrix and the stretch ratio of fibres are the parameters for determining the status of damage. For example, when the stretch ratio of fibres is greater than the maximum stretch ratio, the stress terms associated with the fibres vanish in their computation.

Shah et al. [2014] introduced a multi-scale failure model. As shown in the Figure 1.10, four length-scales are used in this computational model. The damage occurs when a fibre at nanometer scale is broken, if the stretch ratio of this fibre is greater than a critical value λ_{crit} . This breaking results in the modulus of elasticity for fibres being reset to a

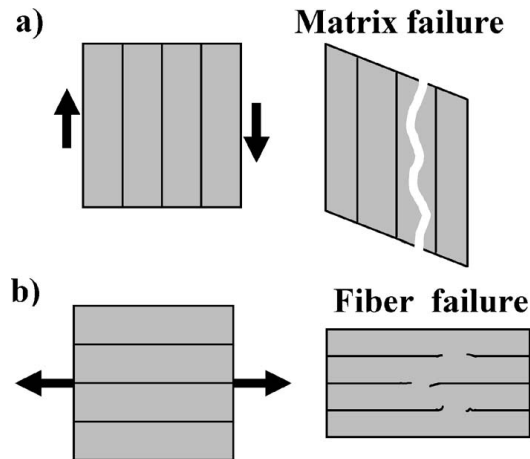


Figure 1.9: Two types of failure mode are assumed for fibre-reinforced soft tissue: matrix fails to take on load when over-sheared and fibres fails when over-stretched [Ionescu et al., 2006].

near-zero value. Through a multi-scale force relationship, the failure at nanometre scale will be spread into the finite element calculation for equilibrium. The failure of the matrix is not specified, but depends on the failure of the fibre network. Therefore, the breaking of a single fibre is the only source of failure in this model.

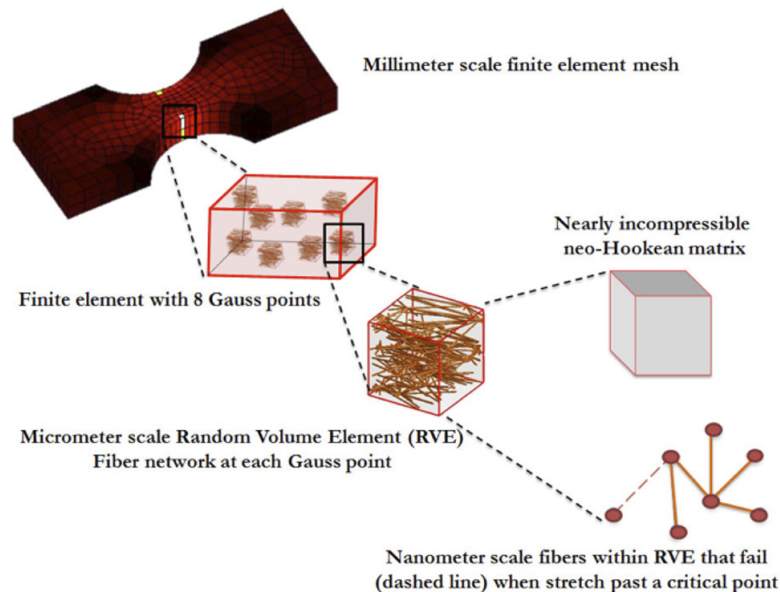


Figure 1.10: Four-length-scale model for characterising the failure of fibre-reinforced soft tissue [Shah et al., 2014]. The breaking of a fibre when overstretched is only source of failure. The failure of matrix is dedicated to the failure of fibre network.

1.6 Mathematical models of arterial dissection

Rajagopal et al. [2007] presented a fundamental mathematical model towards understanding mechanical factors for the initiation and propagation of a tear. It was postulated that the clinical haemodynamic disturbances that render the aorta susceptible to the initiation of dissection are principally elevated maximum systolic aortic blood pressure, whereas the haemodynamic disturbances that facilitate propagation of dissection are principally elevated pulse pressure and heart rate. The systolic pressure is the highest blood pressure, measured when the heart beats and pushes the blood around body. The diastolic pressure is the lowest pressure, measured when the heart relaxes between beats. The pulse pressure is the difference between the systolic and diastolic pressure.

In this model [Rajagopal et al., 2007], the aortic wall is assumed to be a composition of N viscoelastic layers. The Cauchy stress of the i -th layer at time t is

$$\boldsymbol{\sigma}^i = \mathbf{F}^i(t) \left[\mathbf{R}^i(\mathbf{C}^i(t), 0) + \int_0^t \frac{\partial}{\partial(t-\tau)} \mathbf{R}^i(\mathbf{C}^i(\tau), t-\tau) d\tau \right] (\mathbf{F}^i(t))^T - \mathcal{P}^i \mathbf{I}, \quad (1.21)$$

where $-\mathcal{P}^i \mathbf{I}$ denotes the response stress due to the incompressibility, and \mathbf{R}^i represents a tensorial relaxation function for the i -th layer. The term $\mathbf{R}^i(\mathbf{C}^i(t), 0)$ denotes the instantaneous elastic response of the i -th layer at time $t = 0$.

Based on this multi-layer assumption for the aortic wall, the dissection is assumed to be delamination between layers in [Rajagopal et al., 2007]. There are several criteria for the initiation of this delamination. The first criterion is based on the statement that the magnitude of normal traction at a point on the interface is greater than a critical value, i.e.

$$t_1(\mathbf{x}_i, t) \begin{cases} \leq t_c^{(1)} & \text{the interface between layers is intact,} \\ > t_c^{(1)} & \text{delamination is initiated,} \end{cases} \quad (1.22)$$

where

$$t_1(\mathbf{x}_i, t) = \sigma_{r\theta}^2(\mathbf{x}_i, t) + \sigma_{rz}^2(\mathbf{x}_i, t) + \sigma_{rr}^2(\mathbf{x}_i, t), \quad (1.23)$$

\mathbf{x}_i is a point at the interface and $t_c^{(1)}$ is the critical value for the first criterion. The second criterion assumes that sufficiently high traction acting for a sufficient length of time leads to delamination. Thus, the second delamination condition is

$$t_2(\mathbf{x}_i, t) \begin{cases} \leq t_c^{(2)} & \text{the interface between layers is intact,} \\ > t_c^{(2)} & \text{delamination is initiated,} \end{cases} \quad (1.24)$$

where

$$t_2(\mathbf{x}_i, t) = \int_{t-\hat{t}}^t t_1(\mathbf{x}_i, \tau) d\tau \quad (1.25)$$

and $t_c^{(2)}$ is the critical value for the second criterion.

Li [2013] proposed a mathematical model for arterial dissection. In that model, the inflation of a tear is simulated as an incremental deformation in the loaded configuration. The corresponding incremental nominal stress and incremental moduli were derived from the HGO strain energy function, and used for characterising the tissue samples with a tear subject to the pressure [Li, 2013]. The discontinuity at the tear is modelled as a jump condition. A semi-analytical method, which transforms these PDEs to ordinary partial differential equations, is also developed in [Li, 2013]. Using this model, Li solved the deformation of an arterial wall, with both linear and nonlinear materials, including an existing axisymmetric tear. Both lumen and tear are loaded by a static pressure. The deformation agree with the numerical results from solving the PDEs by *Finite Element Analysis* (FEA) we performed (Figure 1.11–1.13). Notably, the FE computation starts from the stress-free configuration while Li [2013] starts from a geometry loaded by pressure in the lumen.

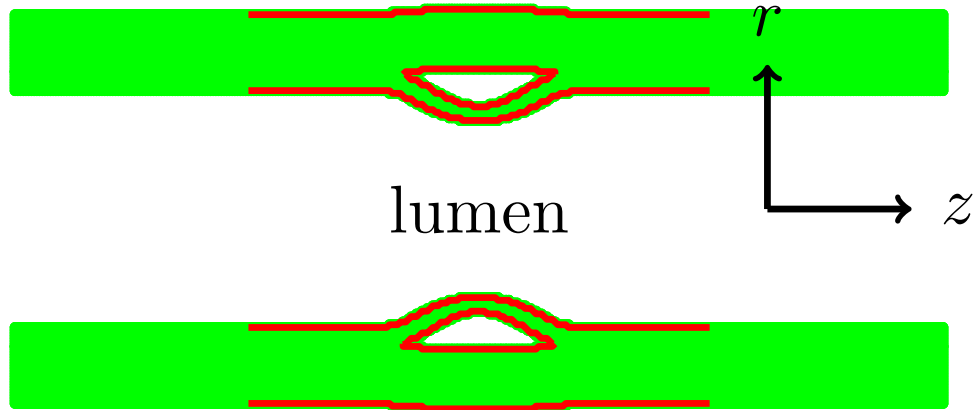


Figure 1.11: The deformed configuration of the arterial wall with an axisymmetric tear subject to a pressure in both lumen and on the tear. The red curves shows the boundaries of deformed arterial wall with a tear from the semi-analytical method in [Li, 2013], and the green-fill region shows the deformed arterial wall with a tear from our FE computation using the computational model in Chapter 3.

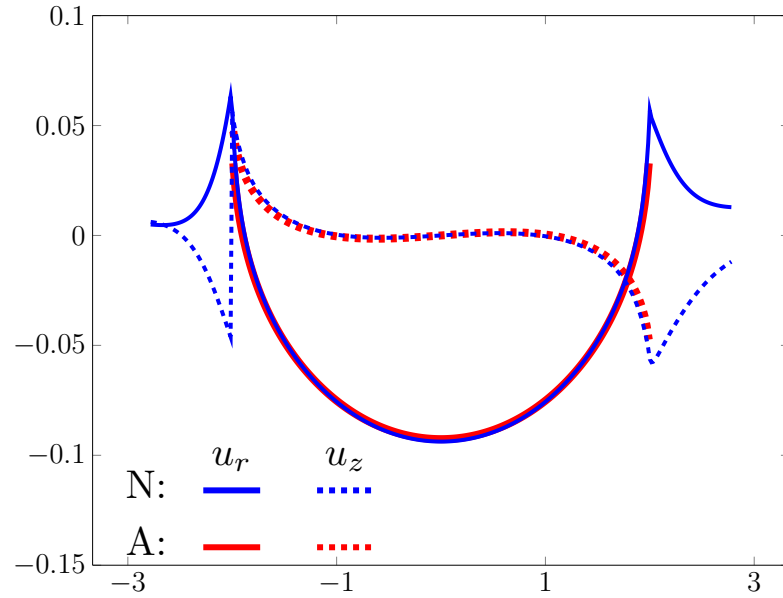


Figure 1.12: Comparison of displacements u_i , $i = r, z$, computed by the semi-analytical method (A) [Li, 2013] and our numerical FE computation (N) using the computational model in Chapter 3, of the inner tear surface.

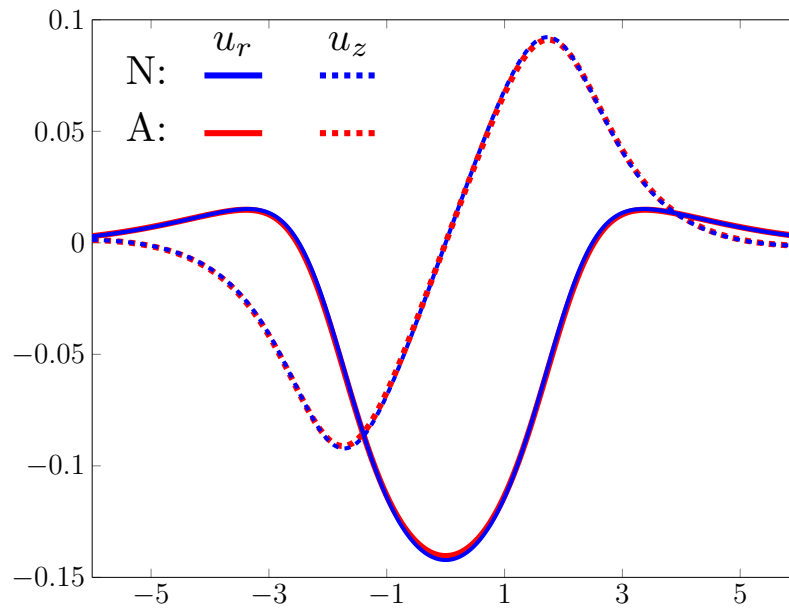


Figure 1.13: Comparison of displacements u_i , $i = r, z$, computed by the semi-analytical method (A) [Li, 2013] and our numerical FE computation (N) using the computational model in Chapter 3, of the lumen surface.

1.7 Numerical methods

The *Finite Element Method* (FEM) is the most commonly used numerical method for solving a system of PDEs in computational solid mechanics [Bathe, 1996; Zienkiewicz and Taylor, 2005]. Analogous to the idea that connecting many tiny straight lines can approximate a larger circle, FEM encompasses methods for connecting many simple element equations over many small subdomains, named finite elements, to approximate a more complex equation over a larger domain. The solution of a system of PDEs is approximated by the sequence of discrete values. For example, the displacement field $u(x)$, where x is the coordinate of a material point in a one-dimensional deformable body, is calculated by solving the balance equations of elasticity. Instead of the analytical expression $u(x)$, FEM uses the approximation

$$u(x) \approx u^h(x) = \sum_i N_i(x)u_i, \quad (1.26)$$

where u_i is the displacement at node x_i of elements and $N_i(x)$ is the shape function for computing the value for $u^h(x)$ inside of elements via interpolation. The nodal displacement u_i instead of displacement field $u(x)$ becomes the unknown variables in the FEM. The shape functions satisfy

$$N_i(x) = \begin{cases} 1, & x = x_i \\ 0, & x = x_j, j \neq i \end{cases} \quad (1.27)$$

and

$$\sum_i N_i(x) = 1 \quad (1.28)$$

such that

$$u^h(x_i) = u_i. \quad (1.29)$$

Using the FEM to analyse crack or tear propagation requires additional development because of the singularity of the stress field in the vicinity of tear tips and discontinuity at tear surfaces. The failure parameters (SIF, ERR, cohesive traction or material force) can be obtained after solving for the equilibrium, strain energy and stress as a post-process. Therefore obtaining high accuracy of the strain energy and stress terms from the finite element analysis is very important. There are many techniques to improve the accuracy and cope with the challenges due to the presence of the singularity in the tip stress field.

A direct method to cope with the stress singularity is using a locally finer mesh and/or higher order shape functions in the vicinity of tips. Because the analytical tip stress field

is derived in a polar coordinate system, the vicinity of a tip is considered to be a special region or a subdomain in the FE model [Knees and Mielke, 2008]. Using a subdomain is also good strategy to overcome the difficulty caused by high gradients in mesh size with a single domain. The posterior error is often used as the criterion to determine where to refine mesh Alshoaibi et al. [2007]; Babuvška and Rheinboldt [1978]. The strategy for refining the mesh locally is also important to maintain the robustness and efficiency of the numerical calculation Phongthanapanich and Dechaumphai [2004]. For analysing the tear propagation to get the path of propagation, the posterior-error based adaptive strategy is important, since the region which needs finer mesh is updated as the tear tips move during propagation. In these methods, the tear surfaces are considered to be common boundaries. Therefore, remeshing is required when the tear propagates.

An alternative to the time-consuming remeshing is to employ cohesive elements or a cohesive surface [e.g. Abaqus, 2014; Rahulkumar et al., 2000]. In a FE model, the cohesive elements are governed by a cohesive law that characterises the cohesive traction on the ‘virtual separation’ quantified by the strain of the cohesive elements. When the thickness of the cohesive elements shrinks to zero, it becomes a cohesive surface. The cohesive elements have to specified in the pre-process of a FE model, so they are useful for investigating the tear propagation along a pre-defined path.

Using a continuum damage model has a similar idea [e.g. Alastrué et al., 2007; Balzani et al., 2012; Waffenschmidt et al., 2015; Wulandana and Robertson, 2005], in which the concept of internal variables which provides a very general description of materials involving irreversible effects. In this approach, every element has the potential for damage through the degrading of stiffness or directly by setting the stress to a near-zero value when the damage, quantified by the strain, is beyond a critical value. Consequently, the virtual tear propagation, expressed by the degrading of stiffness, can happens anywhere when the critical condition is satisfied.

Another approach is the *eXtended Finite Element Method* (XFEM) [Belytschko et al., 2009]. The XFEM models a tear as an enriched feature by adding degrees of freedom in elements with special displacement functions. Therefore, the XFEM does not require the mesh to match the geometry of the discontinuity due to a tear. It can be used to simulate initiation and propagation of a tear along an arbitrary, solution-dependent path without the requirement of remeshing.

1.8 Research aims

Our research aims are to develop computational models to predict the onset of AD propagation and investigate the mechanical issues during dissection of the arterial wall.

The computational method we used includes both the FEM and the XFEM. Our aims on developing computational techniques include

- to find a suitable failure criterion governing the tear propagation in the arterial wall, assumed to be a fibre-reinforced soft tissue in Chapter 3,
- to develop methods for introducing the residual stress into a finite element model in Chapters 5 and 6,
- to implement a modified HGO material model including a growth tensor within a finite element program FEAP in Chapter 7.

The effects of structure and mechanical characters of the arterial wall on the dissection are also our concern. In particular, we aim to find

- the critical pressure, beyond which the tear would propagate, in Chapter 3,
- the effect of surrounding tissues on tear propagation in Chapter 3,
- the effect of collagen fibres and their orientation on tear propagation in Chapters 3 and 4,
- the most likely direction of tear propagation and what factor determines this preference in Chapter 4,
- the effect of length and radial depth of a tear on the critical pressure for tear propagation in Chapter 4,
- the effect of residual stress on tear propagation in Chapters 5 and 6.

1.9 Outline of thesis

The basic theory and formulations of finite elasticity, the FEM and the XFEM are summarized in Chapter 2. Chapter 3 focuses on proposing a fundamental failure criterion for pressure-driven tear propagation in fibre-reinforced soft tissues. Chapter 4 predicts the direction of tear propagation and investigates the effect of circumferential length and radial

depth of a tear on the critical pressure p_c , beyond which the tear propagates, and direction of propagation. Chapter 5 and 6 investigate the effect of residual stress, quantified by an opening angle α , on p_c for tear propagation. Two methods of introducing residual stress into a FE model within Abaqus are developed: importing the analytical residual stress in Chapter 5 and computing numerically the residual stress in Chapter 6, for a zero-loading artery with a tear. Chapter 7 presents suggestion on how to develop a material model in a FE program for the living fibrous soft tissues. The implementation of a modified HGO material model with a growth tensor in FEAP is shown in Chapter 7. Finally, conclusions and discussion are given in Chapter 8.

Chapter 2

Basic theory and formulations

In this chapter, the essential basic mathematical theory and formulations are summarized, including the finite elasticity, FEM and XFEM.

2.1 Finite elasticity

The basic equations of solid mechanics may be found in the textbooks on nonlinear mechanics [e.g. Gurtin, 1982; Holzapfel, 2000; Ogden, 1997]. Here only a summary of the basic equations is presented.

2.1.1 Description of the deformation

Let Ω_0 be a reference configuration of the continuous body \mathcal{B} that is stress-free (Figure 2.1). The configuration Ω_0 is defined as a set of material points whose positions are given by the vector \mathbf{X} in a three-dimensional space. In Cartesian coordinates, the position vector may be described in terms of its components as

$$\mathbf{X} = X_I \mathbf{e}_I \equiv \sum_{I=1}^3 X_I \mathbf{e}_I \quad (2.1)$$

where \mathbf{e}_I , $I = 1, 2, 3$ are unit base vectors. Notably, the *Einstein summation convention* is used. After the \mathcal{B} is loaded each material point $\mathbf{X} \in \Omega_0$ is transformed to a new position $\mathbf{x} = \boldsymbol{\chi}(\mathbf{X}) \in \Omega$ in the deformed configuration. The position vector in the deformed configuration may be given in terms of its components as

$$\mathbf{x} = x_i \mathbf{e}_i, \quad i = 1, 2, 3. \quad (2.2)$$

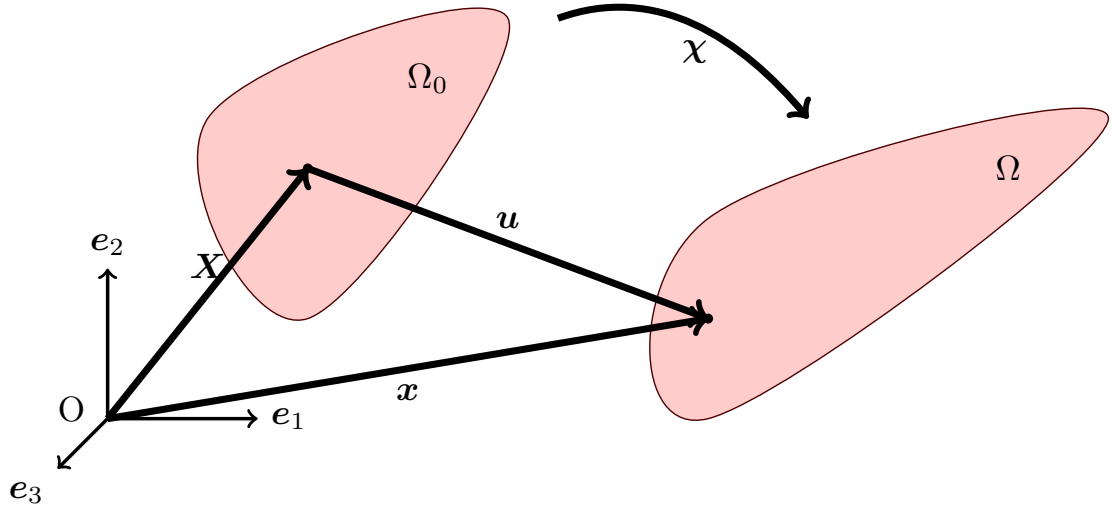


Figure 2.1: The deformation from the stress-free configuration Ω_0 to the deformed configuration Ω is defined by the one-to-one mapping $\mathbf{x} = \chi(\mathbf{X})$ from each material point $\mathbf{X} \in \Omega_0$ to a new position $\mathbf{x} \in \Omega$ in the deformed configuration.

Since the common origin and directions for the reference and current configurations are used, a displacement vector, \mathbf{u} , may be introduced as the change between the two configurations. Accordingly,

$$\mathbf{u} = \mathbf{x} - \mathbf{X} = u_i \mathbf{e}_i, \quad i = 1, 2, 3 \quad (2.3)$$

in used. A fundamental measure of deformation is described by the *deformation gradient*

$$\mathbf{F} = \frac{\partial \chi}{\partial \mathbf{X}} = \frac{\partial \mathbf{x}}{\partial \mathbf{X}} = \mathbf{I} + \frac{\partial \mathbf{u}}{\partial \mathbf{X}}, \quad (2.4)$$

where \mathbf{I} is the second-order identity tensor. In component form we then have

$$F_{iJ} = \frac{\partial x_i}{\partial X_J} = \delta_{iJ} + \frac{\partial u_i}{\partial X_J}, \quad i, J = 1, 2, 3, \quad (2.5)$$

where

$$\delta_{iJ} = \begin{cases} 1, & \text{if } i = J. \\ 0, & \text{if } i \neq J. \end{cases} \quad (2.6)$$

is the Kronecker delta. The deformation of a line element $d\mathbf{X}$ is defined as the the linear transformation by \mathbf{F} ,

$$d\mathbf{x} = \mathbf{F}d\mathbf{X}, \quad (2.7)$$

where $d\mathbf{x}$ is the deformed line element.

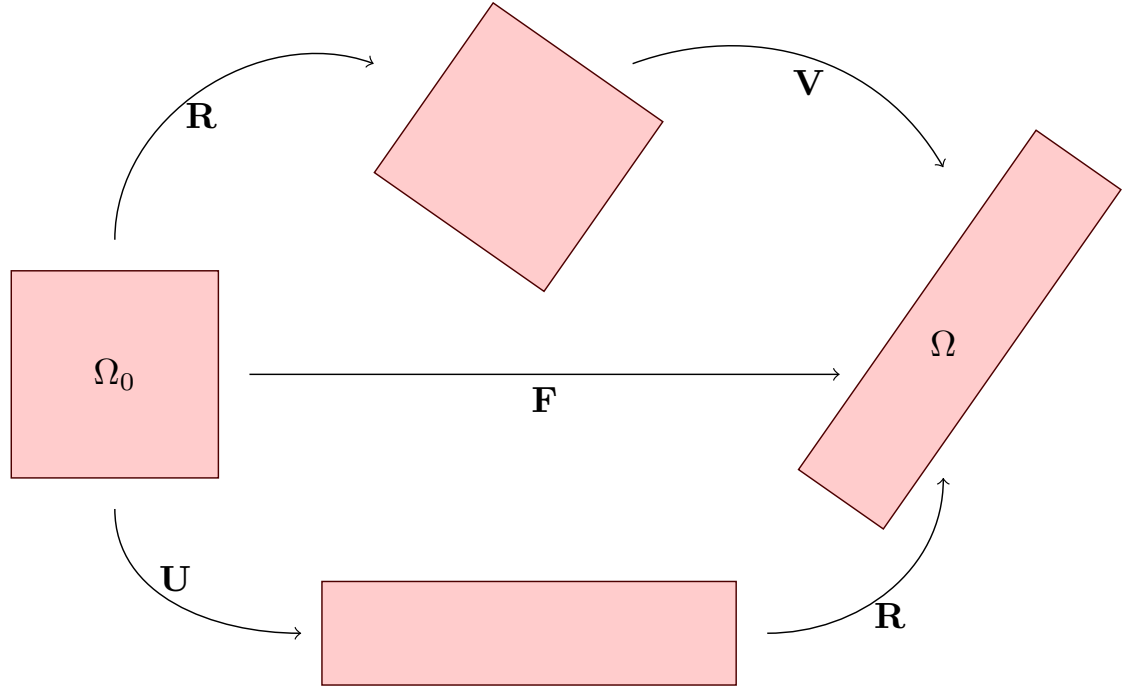


Figure 2.2: Representation of the polar decomposition of a deformation gradient.

The deformation gradient \mathbf{F} includes both rotation and stretch. The pure rotation of material does not result in any strain energy or stress, so it is better to use some rotation-independent deformation measures for formulating a constitutive equation. The isolation of rotation is done through the polar decomposition of the deformation gradient,

$$\mathbf{F} = \mathbf{R}\mathbf{U} = \mathbf{V}\mathbf{R}, \quad (2.8)$$

where \mathbf{U} and \mathbf{V} are the right and left stretch tensor, and \mathbf{R} is a proper orthogonal tensor, that is $\mathbf{R}^{-1} = \mathbf{R}^T$ and $\det \mathbf{R} = +1$. Both \mathbf{U} and \mathbf{V} are positive definite, i.e. $\mathbf{X} \cdot \mathbf{U} \cdot \mathbf{X} \geq 0$ and $\mathbf{x} \cdot \mathbf{V} \cdot \mathbf{x} \geq 0$, and symmetric, i.e. $\mathbf{U} = \mathbf{U}^T$ and $\mathbf{V} = \mathbf{V}^T$.

As shown in the Figure 2.2, both \mathbf{U} and \mathbf{V} are rotation-independent deformation measures: \mathbf{U} defines the stretch referring to the reference configuration while \mathbf{V} is the stretch to the deformed configuration. \mathbf{U} is called the *material stretch tensor* while the \mathbf{V} is called the *spatial stretch tensor*. Furthermore, the eigenvalues of \mathbf{U} and \mathbf{V} are the *principal stretch*, λ_i ($i = 1, 2, 3$). The principal stretches can be calculated by finding the roots of the characteristic equations

$$\det(\lambda \mathbf{I} - \mathbf{U}) = 0 \quad \text{or} \quad \det(\lambda \mathbf{I} - \mathbf{V}) = 0. \quad (2.9)$$

The \mathbf{U} and \mathbf{V} have the same eigenvalues but different eigenvectors. Let λ_i be the eigen-

values of \mathbf{U} corresponding to the eigenvectors \mathbf{N}_i , such that

$$\mathbf{U}\mathbf{N}_i = \lambda_i\mathbf{N}_i, \quad i = 1, 2, 3. \quad (2.10)$$

Use of (2.8) leads to

$$\mathbf{V}\mathbf{R}\mathbf{N}_i = \mathbf{R}\mathbf{U}\mathbf{N}_i = \lambda_i\mathbf{R}\mathbf{N}_i, \quad (2.11)$$

therefore, λ_i are also the eigenvalues of \mathbf{V} , corresponding to the eigenvectors $\mathbf{R}\mathbf{N}_i$.

Several other rotation-independent deformation measures are commonly used. The *right Cauchy–Green tensor*, \mathbf{C} , is

$$\mathbf{C} = \mathbf{F}^T\mathbf{F} = \mathbf{U}^2 \quad \text{or} \quad C_{IJ} = F_{kI}F_{kJ}. \quad (2.12)$$

Also the Green strain tensor, \mathbf{E} , is introduced as

$$\mathbf{E} = \frac{1}{2}(\mathbf{C} - \mathbf{I}) \quad \text{or} \quad E_{IJ} = \frac{1}{2}(F_{kI}F_{kJ} - \delta_{IJ}). \quad (2.13)$$

Substituting (2.4) and (2.5) into \mathbf{E} , we have the expression in terms of displacements as

$$\mathbf{E} = \frac{1}{2} \left[\frac{\partial \mathbf{u}}{\partial \mathbf{X}} + \left(\frac{\partial \mathbf{u}}{\partial \mathbf{X}} \right)^T + \left(\frac{\partial \mathbf{u}}{\partial \mathbf{X}} \right)^T \frac{\partial \mathbf{u}}{\partial \mathbf{X}} \right] \quad (2.14)$$

and

$$E_{IJ} = \frac{1}{2} \left(\frac{\partial u_I}{\partial X_J} + \frac{\partial u_J}{\partial X_I} + \frac{\partial u_K}{\partial X_I} \frac{\partial u_K}{\partial X_J} \right). \quad (2.15)$$

The last term on the RHS of (2.15) shows the geometric nonlinearity due to the large deformation. When the deformation is small, i.e. $\|\frac{\partial \mathbf{u}}{\partial \mathbf{X}}\| \ll 1$, the nonlinear term can be ignored, so the Green strain reduces to the linear strain

$$\epsilon_{IJ} = \frac{1}{2} \left(\frac{\partial u_I}{\partial X_J} + \frac{\partial u_J}{\partial X_I} \right). \quad (2.16)$$

With respect to the deformed configuration, a common deformation measure is the left Cauchy–Green strain tensor, \mathbf{B} , defined as

$$\mathbf{B} = \mathbf{F}\mathbf{F}^T = \mathbf{V}^2 \quad \text{or} \quad B_{ij} = F_{iK}F_{jK}. \quad (2.17)$$

For a fibre-reinforced material, the direction of a fibre at a point $\mathbf{X} \in \Omega_0$ is defined by a unit vector field $\mathbf{A}(\mathbf{X})$, $|\mathbf{A}| = 1$. It is commonly assumed that the fibres move with the material points of the continuum body during deformation. Therefore, the unit vector deforms according to (2.7)

$$\mathbf{a} = \mathbf{F}\mathbf{A}. \quad (2.18)$$

The ratio between the length of \mathbf{a} and \mathbf{A} defines the stretch of fibres,

$$\lambda_f = \frac{|\mathbf{a}|}{|\mathbf{A}|} = \sqrt{\mathbf{a} \cdot \mathbf{a}} = \sqrt{(\mathbf{F}\mathbf{A})^T(\mathbf{F}\mathbf{A})} = \sqrt{\mathbf{A}^T\mathbf{C}\mathbf{A}}. \quad (2.19)$$

2.1.2 Stress response

The elastic stress, generated when the body is elastically deformed, is a physical quantity that expresses the internal forces that neighbouring particles of a continuous material exert on each other. Analogous to the reaction force of a spring, the stress tends to restore the material to its original undeformed state. The stress measures the amount of force per unit area. In finite deformation problems, care must be taken to describe the configuration in which the stress is measured. The *second Piola–Kirchhoff stress*, \mathbf{S} , is defined with respect to the reference configuration, while the *Cauchy stress*, $\boldsymbol{\sigma}$, and the *Kirchhoff stress*, $\boldsymbol{\tau}$, are defined with respect to the deformed configuration. They are related by

$$\boldsymbol{\tau} = J\boldsymbol{\sigma} = \mathbf{F}\mathbf{S}\mathbf{F}^T, \quad (2.20)$$

where $J = \det \mathbf{F}$. $\boldsymbol{\tau}$, $\boldsymbol{\sigma}$ and \mathbf{S} are all symmetric second-order tensors.

The Cauchy stress $\boldsymbol{\sigma}$ describes the stress distribution in the deformed configuration. The traction at a point of a surface with outward normal \mathbf{n} is defined as

$$\mathbf{t} = \boldsymbol{\sigma}\mathbf{n}. \quad (2.21)$$

Similarly, the traction, \mathbf{t}_0 , is defined as the force per area in the reference configuration, such that

$$\mathbf{t}_0 dS = \mathbf{t} ds = \mathbf{T}, \quad (2.22)$$

where dS and ds are surface elements in the reference and deformed configurations, respectively, and \mathbf{T} is the force measured in the deformed configuration. The *first Piola–Kirchhoff stress* \mathbf{P} is associated with the internal force in the deformed configuration but with respect to area in the reference configuration, such that

$$\mathbf{t}_0 = \mathbf{P}\mathbf{N}, \quad (2.23)$$

where \mathbf{N} is an unit outward normal of the reference surface. The first Piola–Kirchhoff stress is related to the other stress tensors through

$$\mathbf{P} = \mathbf{F}\mathbf{S} = \boldsymbol{\tau}\mathbf{F}^{-T} = J\boldsymbol{\sigma}\mathbf{F}^{-T}. \quad (2.24)$$

2.1.3 Stress-strain relationship

For a hyperelastic material, the relationship between an isothermal reversible deformation and the stress response, the stress-strain relationship, is defined through a SEF, Ψ , which

is a scalar function of the deformation measure. Given Ψ , stresses are computed by taking a derivatives, for example,

$$\begin{aligned} \text{second Piola–Kirchhoff stress is} \quad \mathbf{S} &= \frac{\partial \Psi}{\partial \mathbf{E}} = 2 \frac{\partial \Psi}{\partial \mathbf{C}} \\ \text{and first Piola–Kirchhoff stress} \quad \mathbf{P} &= \frac{\partial \Psi}{\partial \mathbf{F}}. \end{aligned} \quad (2.25)$$

The other stress tensors, $\boldsymbol{\sigma}$ and $\boldsymbol{\tau}$, are obtained via the transformations in (2.20) or (2.24).

A number of SEFs have been proposed for the arterial wall. It is common to write the SEF in terms of strain tensors, strain invariants, or principal stretches. Some of most commonly used SEFs and the associated stress are shown below. All of these are defined for incompressible material, i.e. $J = \det \mathbf{F} = 1$.

Ψ in terms of a strain tensor

A general three dimensional Fung's type SEF proposed by Humphrey [1994] is

$$\Psi(\mathbf{E}) = \frac{a}{2} [\exp(Q) - 1], \quad (2.26)$$

where

$$\begin{aligned} Q &= b_1 E_{11}^2 + b_2 E_{22}^2 + b_3 E_{33}^2 + 2b_4 E_{11} E_{22} + 2b_5 E_{22} E_{33} + 2b_6 E_{33} E_{11} \\ &\quad + b_7 E_{12}^2 + b_8 E_{23}^2 + b_9 E_{31}^2. \end{aligned} \quad (2.27)$$

From (2.25) and (2.26), the second Piola–Kirchhoff stress is

$$\begin{aligned} \mathbf{S} &= \frac{\partial \Psi}{\partial \mathbf{E}} - \mathcal{P} \mathbf{C}^{-1} \\ &= \frac{a}{2} \exp(Q) \frac{\partial Q}{\partial \mathbf{E}} - \mathcal{P} \mathbf{C}^{-1}, \end{aligned} \quad (2.28)$$

where $\frac{\partial Q}{\partial \mathbf{E}}$ is a second-order symmetric tensor, the components of which are $\frac{\partial Q}{\partial E_{IJ}}$, $I, J = 1, 2, 3$, and \mathcal{P} is the Lagrangian multiplier associated with the incompressibility constraint. The value for \mathcal{P} is determined by the equilibrium equations and boundary conditions. From (2.27), we have

$$\frac{\partial Q}{\partial \mathbf{E}} = 2 \begin{bmatrix} b_1 E_{11} + b_4 E_{22} + b_6 E_{33} & b_7 E_{12} & b_9 E_{13} \\ b_7 E_{21} & b_2 E_{22} + b_4 E_{11} + b_5 E_{33} & b_8 E_{23} \\ b_9 E_{31} & b_8 E_{32} & b_3 E_{33} + b_5 E_{22} + b_6 E_{11} \end{bmatrix}$$

Then the Cauchy stress is obtained via (2.20) giving

$$\boldsymbol{\sigma} = \frac{a}{2} \exp(Q) \mathbf{F} \frac{\partial Q}{\partial \mathbf{E}} \mathbf{F}^T - \mathcal{P} \mathbf{I}. \quad (2.29)$$

Ψ in terms of strain invariants

The strain invariants, a scalar function of strain tensor, are independent of the coordinate transformation. For example, the most widely used invariants of right Cauchy-Green strain tensor \mathbf{C} in a SEF are I_i , $i = 1, 2, 3$:

$$\begin{aligned} I_1 &= \text{tr } \mathbf{C} \\ I_2 &= \frac{1}{2} [(\text{tr } \mathbf{C})^2 - \text{tr } \mathbf{C}^2] \\ I_3 &= \det \mathbf{C} = \frac{1}{6} [(\text{tr } \mathbf{C})^3 - 3(\text{tr } \mathbf{C})(\text{tr } \mathbf{C}^2) + 2 \text{tr } \mathbf{C}^3], \end{aligned}$$

where $\text{tr } \mathbf{C}$, $\text{tr } \mathbf{C}^2$ and $\text{tr } \mathbf{C}^3$ are independent of the choice of basis [Ogden, 1997]. For example, we consider two right-handed orthonormal bases, \mathbf{e}'_i and \mathbf{e}_p , such that

$$\mathbf{e}'_i = Q_{ip} \mathbf{e}_p, \quad i = 1, 2, 3, \quad (2.30)$$

where \mathbf{Q} is an orthogonal matrix, i.e. $Q_{ip}Q_{iq} = \delta_{pq}$. In \mathbf{e}'_i , we have the components of \mathbf{C} as

$$C'_{ij} = Q_{ip}Q_{jq}C_{pq}, \quad i, j = 1, 2, 3. \quad (2.31)$$

Then

$$\text{tr } \mathbf{C}' = C'_{ii} = Q_{ip}Q_{iq}C_{pq} = \delta_{pq}C_{pq} = C_{pp} = \text{tr } \mathbf{C}. \quad (2.32)$$

In other words, $I_1 = \text{tr } \mathbf{C}$ is invariant under change of orthogonal basis. Similarly, we have

$$\text{tr } \mathbf{C}'^2 = C'_{ii}{}^2 = C'_{ik}C'_{ki} = Q_{ip}Q_{kq}C_{pq}Q_{kr}Q_{is}C_{rs} = \delta_{ps}C_{pq}\delta_{qr}C_{rs} = C_{sq}C_{qs} = \text{tr } \mathbf{C}^2, \quad (2.33)$$

and

$$\begin{aligned} \text{tr } \mathbf{C}'^3 &= C'_{ii}{}^3 = C'_{ij}C'_{jk}C'_{ki} = Q_{ip}Q_{jq}C_{pq}Q_{jm}Q_{kn}C_{mn}Q_{kr}Q_{is}C_{rs} \\ &= \delta_{ps}C_{pq}\delta_{qm}C_{mn}\delta_{nr}C_{rs} = C_{sq}C_{qn}C_{ns} = \text{tr } \mathbf{C}^3, \end{aligned} \quad (2.34)$$

thus I_2 and I_3 are also invariant under change of orthogonal basis.

The three principal invariants are the coefficients of the characteristic polynomial of \mathbf{C} , i.e.

$$\det(\lambda^2 \mathbf{I} - \mathbf{C}) = (\lambda^2)^3 - I_1(\lambda^2)^2 + I_2(\lambda^2) - I_3 = 0, \quad (2.35)$$

where the λ^2 is a eigenvalue of \mathbf{C} , λ is the principal stretch, and we can write

$$\begin{aligned} I_1 &= \lambda_1^2 + \lambda_2^2 + \lambda_3^2, \\ I_2 &= \lambda_1^2\lambda_2^2 + \lambda_2^2\lambda_3^2 + \lambda_3^2\lambda_1^2, \\ I_3 &= \lambda_1^2\lambda_2^2\lambda_3^2. \end{aligned}$$

In other words, the three invariants can be expressed in terms of principal stretches λ_i .

Many commonly used isotropic SEFs are in terms of these invariants. For an incompressible material,

$$I_3 = J^2 = 1, \quad (2.36)$$

therefore only I_1 and I_2 are independent variants. For example,

- the neo-Hookean model is

$$\Psi = c(I_1 - 3), \quad (2.37)$$

- and the Mooney-Rivlin model is

$$\Psi = c_1(I_1 - 3) + c_2(I_2 - 3), \quad (2.38)$$

where c , c_1 and c_2 are constant material parameters.

As demonstrated in Figure 1.7, the stress-strain response is different along different directions. This directional mechanical response is due to the presence of collagen fibres. To model this fibre induced anisotropy, a SEF must introduce new invariants, associated with the direction of fibres. The simplest anisotropic model is a transversely isotropic model, which characterizes a material with one family of fibres. Assume the family of fibres has the direction defined by the unit vector \mathbf{A} in the reference configuration. In this case [Spencer, 1984], two additional anisotropic invariants are introduced

$$I_4 = \mathbf{A}^T \mathbf{C} \mathbf{A}, \quad I_5 = \mathbf{A}^T \mathbf{C}^2 \mathbf{A}, \quad (2.39)$$

or

$$I_4 = \mathbf{a} \cdot \mathbf{a}, \quad I_5 = \mathbf{a}^T \mathbf{C} \mathbf{a}. \quad (2.40)$$

The invariant I_4 has physical meaning, it is the *square of the fibre stretch* λ_f . However, it is difficult to relate I_5 to any physical quantity. For this reason and the lack of sufficient experimental data, it is common to neglect the effect of I_5 in the definition of a SEF [e.g. Holzapfel et al., 2000; Weiss et al., 1996]. Here we use the HGO SEF [Holzapfel et al., 2000] to demonstrate the derivative of stress-strain relationship for a SEF in terms of invariants.

For a transversely isotropic material, the incompressible HGO SEF is

$$\begin{aligned} \Psi(I_1, I_4) &= \Psi_m(I_1) + \Psi_f(I_4) \\ &= \frac{c}{2}(I_1 - 3) + H(I_4)\psi_f(I_4), \end{aligned} \quad (2.41)$$

where $H(\cdot)$ is used as the switch condition, to indicate that fibres can only take stretch loading, defined as

$$H(x) = \begin{cases} 0 & x \leq 1 \\ 1 & x > 1 \end{cases}$$

and $\psi_f(\cdot)$ is the exponential stretch stiffening stored energy function for fibres

$$\psi_f(x) = \frac{k_1}{k_2} \{ \exp [k_2(x-1)^2] - 1 \}.$$

Then the second Piola–Kirchhoff stress is

$$\mathbf{S} = 2 \left(\frac{d\Psi_m}{dI_1} \frac{\partial I_1}{\partial \mathbf{C}} + \frac{d\Psi_f}{dI_4} \frac{\partial I_4}{\partial \mathbf{C}} \right) - \mathcal{P} \mathbf{C}^{-1}. \quad (2.42)$$

Using

$$\left[\frac{\partial I_1}{\partial \mathbf{C}} \right]_{ij} = \frac{\partial I_1}{\partial C_{ij}} = \frac{\partial C_{kk}}{\partial C_{ij}} = \delta_{ki} \delta_{kj} = \delta_{ij} = [\mathbf{I}]_{ij}$$

$$\begin{aligned} \left[\frac{\partial I_4}{\partial \mathbf{C}} \right]_{ij} &= \frac{\partial I_4}{\partial C_{ij}} = \frac{\partial (A_k C_{kl} A_l)}{\partial C_{ij}} \\ &= A_k \frac{\partial C_{kl}}{\partial C_{ij}} A_l = A_k \delta_{ki} \delta_{lj} A_l = A_i A_j = [\mathbf{A} \otimes \mathbf{A}]_{ij} \end{aligned}$$

in (2.42) yields

$$\mathbf{S} = c \mathbf{I} + H(I_4) 4k_1 (I_4 - 1) \exp [k_2 (I_4 - 1)^2] \mathbf{A} \otimes \mathbf{A} - \mathcal{P} \mathbf{C}^{-1}, \quad (2.43)$$

where $\mathbf{A} \otimes \mathbf{A} = \mathbf{M}$ is a second-order tensor, called a *structure tensor* in [Holzapfel et al., 2000]. In components,

$$M_{ij} = A_i A_j. \quad (2.44)$$

The following the derivation of invariants are used for obtaining the explicit expression in (2.43):

Push forward (2.43) through (2.20) to obtain the Cauchy stress

$$\boldsymbol{\sigma} = \frac{1}{J} \mathbf{F} \mathbf{S} \mathbf{F}^T = c \mathbf{B} + H(I_4) 4k_1 (I_4 - 1) \exp [k_2 (I_4 - 1)^2] \mathbf{a} \otimes \mathbf{a} - \mathcal{P} \mathbf{I}, \quad (2.45)$$

where $\mathbf{a} \otimes \mathbf{a}$ is the structure tensor in the current configuration.

Ψ in terms of principal stretches

The Ogden material model [Ogden, 1972] is the most notable SEF in terms of the principal stretches, λ_i , $i = 1, 2, 3$ as:

$$\Psi = \sum_{p=1}^N \frac{\mu_p}{\alpha_p} (\lambda_1^{\alpha_p} + \lambda_2^{\alpha_p} + \lambda_3^{\alpha_p} - 3), \quad (2.46)$$

where N , μ_p and α_p are material parameters.

The principal stress is directly obtained from the derivative of (2.46) respect to the principal stretches. The components of the principal stress are

$$\sigma_i = \lambda_i \frac{\partial \Psi}{\partial \lambda_i} - \mathcal{P} = \sum_{p=1}^N \mu_p \lambda_i^{\alpha_p - 1} - \mathcal{P}. \quad (2.47)$$

2.1.4 Balance equations

The governing equations for describing the elastic deformation of a body are derived from the conservation laws of mass, angular momentum and linear momentum [Ogden, 1997].

Denote the mass density by $\rho_0(\mathbf{X})$ in the reference configuration Ω_0 and by $\rho(\mathbf{x})$ in the deformed configuration Ω , then from the principle of conservation of mass, we have

$$\int_{\Omega} \rho(\mathbf{x}) dv = \int_{\Omega_0} \rho_0(\mathbf{X}) dV, \quad (2.48)$$

where volume elements $dv = JdV$ and $J = \det \mathbf{F}$.

The balance of the angular momentum leads to the symmetry properties of the Cauchy stress tensor,

$$\boldsymbol{\sigma}^T = \boldsymbol{\sigma}. \quad (2.49)$$

In the absence of body forces the equilibrium equation is

$$\operatorname{div} \boldsymbol{\sigma} = \mathbf{0} \quad \text{or} \quad \frac{\partial \sigma_{ij}}{\partial x_j} = 0, \quad i, j = 1, 2, 3, \quad (2.50)$$

at steady state, where $\operatorname{div}(\cdot)$ represents the divergence with respect to the deformed configuration. This relation is true for any material point if the equilibrium is satisfied locally. The equivalent weak global equilibrium equation is

$$\int_{\Omega} \operatorname{div} \boldsymbol{\sigma} dv = \mathbf{0}, \quad (2.51)$$

where dv is a volume element of the deformed configuration Ω .

The strong and weak equilibrium equations may also be written with respect to the reference configuration as:

$$\text{Div } \mathbf{P} = \mathbf{0} \quad \text{or} \quad \frac{\partial P_{iJ}}{\partial X_J} = 0, \quad i, J = 1, 2, 3, \quad \text{and} \quad \int_{\Omega_0} \text{Div } \mathbf{P} \, dV = \mathbf{0}. \quad (2.52)$$

Alternatively, a boundary value problem of partial differential equations can be formulated as a problem of the calculus of variations [Courant, 1943]. Consider a deformable body, which is loaded by a surface traction \mathbf{t}_0 . The linear momentum of the body is in balance and it is then subject to an instantaneous, infinitesimal virtual displacement field $\delta \mathbf{u}$, which is consistent with all boundary conditions. The *principle of virtual work* states that the internal work done by the internal stress along the virtual strain consistent with the virtual displacements is equal to the net external work done by the external force along the virtual displacements.

With respect to the reference configuration, we have

$$\int_{\Omega_0} \text{tr} (\delta \mathbf{F}^T \mathbf{P}) \, dV = \int_{\partial \Omega_{0t}} \delta \mathbf{u}^T \mathbf{t}_0 \, dS, \quad (2.53)$$

where $\partial \Omega_{0t}$ is the boundary of Ω_0 where the traction \mathbf{t}_0 applies, dV and dS are the material volume and surface elements. The $\text{tr}(\cdot)$ is the trace operation such that in (2.53)

$$\text{tr}(\delta \mathbf{F}^T \mathbf{P}) = \delta F_{iJ} P_{iJ}. \quad (2.54)$$

Using (2.22), (2.24) and

$$\delta \mathbf{F} = \nabla(\delta \mathbf{u}) \mathbf{F}, \quad (2.55)$$

equation (2.53) is transformed to the deformed configuration as

$$\int_{\Omega} \text{tr} (\nabla(\delta \mathbf{u})^T \boldsymbol{\sigma}) \, dv = \int_{\partial \Omega_t} \delta \mathbf{u}^T \mathbf{t} \, ds, \quad (2.56)$$

where $\partial \Omega_t$ is the boundary of Ω where the traction \mathbf{t} applies, dv and ds are the spatial volume and surface elements, and

$$[\nabla(\delta \mathbf{u})]_{ij} = \frac{\partial \delta u_i}{\partial x_j}. \quad (2.57)$$

2.2 FEM

The finite element method is the most commonly used method to solve the equation (2.56) [Zienkiewicz and Taylor, 2005].

2.2.1 Discretisation

The finite element discretization may be constructed by dividing the continuous body into finite elements. Accordingly, we have

$$\Omega \approx \Omega_h = \sum_e \Omega_e, \quad (2.58)$$

where Ω_e is the domain of an individual element, e , and Ω_h is the domain covered by all elements. Generally, Ω_h is an approximation of the domain of the real body since the elements only have mapped polygonal shapes. With this approximation, the integrals in the variational equations is approximated as

$$\int_{\Omega} (\cdot) dv \approx \int_{\Omega_h} (\cdot) dv = \sum_e \int_{\Omega_e} (\cdot) dv. \quad (2.59)$$

Using this approximation in (2.56) yields

$$\sum_e \int_{\Omega_e} \text{tr}(\nabla(\delta\mathbf{u})^T \boldsymbol{\sigma}) dv = \sum_e \int_{\partial\Omega_{et}} \delta\mathbf{u}^T \mathbf{t} ds. \quad (2.60)$$

Furthermore, these continuous variables ($\delta\mathbf{u}$ and $\boldsymbol{\sigma}$) are approximated through the interpolation onto the nodal values.

Adopting an isoparametric formulation we may write for a typical element

$$\mathbf{X} = N_I(\boldsymbol{\xi})\mathbf{X}_I, \quad I = 1, 2, \dots, n, \quad (2.61)$$

where n is the number of nodes defining an element, $N_I(\boldsymbol{\xi})$ are shape functions for node I which maintain suitable continuity between elements and \mathbf{X}_I are the coordinates for the node I . Similarly, we may write approximations for the deformed configuration as

$$\mathbf{x} = N_I(\boldsymbol{\xi})\mathbf{x}_I \quad (2.62)$$

the displacement as

$$\mathbf{u} = N_I(\boldsymbol{\xi})\mathbf{u}_I \quad (2.63)$$

and the virtual displacements as

$$\delta\mathbf{u} = N_I(\boldsymbol{\xi})\delta\mathbf{u}_I. \quad (2.64)$$

Substitute (2.64) into the (2.60), we have

$$\sum_e \delta\mathbf{u}_I^T \left(\int_{\Omega_e} \text{tr}((\nabla N_I)^T \boldsymbol{\sigma}) dv \right) = \sum_e \delta\mathbf{u}_I^T \left(\int_{\partial\Omega_{et}} N_I \mathbf{t} ds \right). \quad (2.65)$$

Since $\delta \mathbf{u}_I$ is arbitrary, the finite element formulation of the linear momentum balance is obtained as

$$\sum_e \left(\int_{\Omega_e} \text{tr}((\nabla N_I)^T \boldsymbol{\sigma}) \, dv - \int_{\partial\Omega_{et}} N_I \mathbf{t} \, ds \right) = \mathbf{0}. \quad (2.66)$$

which may be written in the compact matrix form

$$\mathbf{f}^{int}(\boldsymbol{\sigma}) - \mathbf{f}^{ext} = \mathbf{0}, \quad (2.67)$$

where the nodal force vector

$$\mathbf{f}^{ext} = \sum_e \int_{\partial\Omega_{et}} N_I \mathbf{t} \, ds \quad (2.68)$$

is due to external loading and

$$\mathbf{f}^{int}(\boldsymbol{\sigma}) = \sum_e \int_{\Omega_e} \text{tr}((\nabla N_I)^T \boldsymbol{\sigma}) \, dv \quad (2.69)$$

denotes the internal force vector, calculated from the Cauchy stress $\boldsymbol{\sigma}$. $\boldsymbol{\sigma}$ depends on a displacement field \mathbf{u} through a material constitution and a strain measure introduced in Section 2.1. Through the interpolation of displacement field (2.63), the only unknown variables of equation (2.67) are the nodal displacement \mathbf{u}_I .

(2.67) together with the displacement boundary conditions forms a boundary value problem. A common solution procedure is to use a Newton–Raphson method and solve a sequence of linearised problems. As described in Section 2.2.2, a linearisation of this set of equations gives

$$\mathbf{K}_{i-1} \Delta \mathbf{u}_i = \mathbf{f}_{i-1}^{ext} - \mathbf{f}_{i-1}^{int}, \quad (2.70)$$

where $i, i-1$ denote the iteration steps associated with a global Newton iteration, $\Delta \mathbf{u}_i$ is an incremental displacement to solve, and calculation of the tangential stiffness matrix \mathbf{K}_{i-1} is given in (2.99).

2.2.2 Linearisation

The linearisation is considered in a referential formulation with respect to the fixed reference configuration Ω_0 . Accordingly, the term on the LHS of (2.53) is expressed in terms of the second Piola–Kirchhoff stress tensor by using (2.24), i.e.

$$\int_{\Omega_0} \text{tr}(\delta \mathbf{F}^T \mathbf{P}) \, dV = \int_{\Omega_0} \text{tr}(\delta \mathbf{F}^T \mathbf{F} \mathbf{S}) \, dV = \int_{\Omega_0} \text{tr}(\delta \mathbf{F} \mathbf{S} \mathbf{F}^T) \, dV. \quad (2.71)$$

A linearisation of the term on the RHS of (2.71) may be written as

$$\Delta \left(\int_{\Omega_0} \text{tr}(\delta \mathbf{F} \mathbf{S} \mathbf{F}^T) \, dV \right) = \int_{\Omega_0} \text{tr}(\delta \mathbf{F} \mathbf{S} \Delta \mathbf{F}^T) \, dV + \int_{\Omega_0} \text{tr}(\delta \mathbf{F} \Delta \mathbf{S} \mathbf{F}^T) \, dV, \quad (2.72)$$

where $\Delta(\cdot)$ denotes an increment of (\cdot) . Using (2.55) and

$$\Delta \mathbf{F} = \nabla(\Delta \mathbf{u}) \mathbf{F}, \quad (2.73)$$

(2.72) is transformed to the deformed configuration and expressed in terms of Cauchy stress,

$$\begin{aligned} \Delta \left(\int_{\Omega_0} \text{tr}(\delta \mathbf{F} \mathbf{S} \mathbf{F}^T) dV \right) &= \int_{\Omega} \text{tr}(\nabla(\delta \mathbf{u}) \mathbf{F} \mathbf{S} \mathbf{F}^T \nabla(\Delta \mathbf{u})^T) \frac{1}{J} dv + \int_{\Omega} \text{tr}(\nabla(\delta \mathbf{u}) \mathbf{F} \Delta \mathbf{S} \mathbf{F}^T) \frac{1}{J} dv \\ &= \int_{\Omega} \text{tr}(\nabla(\delta \mathbf{u}) \boldsymbol{\sigma} \nabla(\Delta \mathbf{u})^T) dv + \int_{\Omega} \text{tr}(\nabla(\delta \mathbf{u}) \Delta \boldsymbol{\sigma}) dv, \end{aligned} \quad (2.74)$$

where

$$J = \det \mathbf{F} = \frac{dv}{dV} \quad (2.75)$$

is the ratio of a volume element after to before deformation,

$$\nabla(\Delta \mathbf{u})^T = \left(\frac{\partial \Delta \mathbf{u}}{\partial \mathbf{x}} \right)^T \quad (2.76)$$

and

$$\Delta \boldsymbol{\sigma} = \frac{1}{J} \mathbf{F} \Delta \mathbf{S} \mathbf{F}^T. \quad (2.77)$$

The first term on the RHS of (2.74) leads to the *geometric* part of the stiffness in a finite element formulation, whereas, the second term depends on the material constitution and leads to the *material* part of the stiffness.

$\Delta \mathbf{S}$ is computed via

$$\Delta \mathbf{S} = \mathfrak{C} \Delta \mathbf{E}, \quad (2.78)$$

where \mathfrak{C} is a fourth-order *material tangential moduli* with respect to the reference configuration, and

$$\Delta \mathbf{E} = \frac{1}{2} \Delta(\mathbf{F}^T \mathbf{F} - \mathbf{I}) = \frac{1}{2} (\Delta \mathbf{F}^T \mathbf{F} + \mathbf{F}^T \Delta \mathbf{F}). \quad (2.79)$$

\mathfrak{C} is derived from a particular SEF Ψ via

$$\mathfrak{C} = \frac{\partial^2 \Psi}{\partial \mathbf{E} \partial \mathbf{E}} = 4 \frac{\partial^2 \Psi}{\partial \mathbf{C} \partial \mathbf{C}}. \quad (2.80)$$

Substituting (2.78) with (2.79), (2.73) into (2.77) gives

$$\Delta \boldsymbol{\sigma} = \mathfrak{c} \Delta \boldsymbol{\epsilon}, \quad (2.81)$$

where \mathfrak{c} is the *spatial tangential moduli* with respect to the deformed configuration, and $\Delta \boldsymbol{\epsilon}$ is the symmetric part of the gradient of the incremental displacement,

$$\Delta \boldsymbol{\epsilon} = \frac{1}{2} \left[\frac{\partial \Delta \mathbf{u}}{\partial \mathbf{x}} + \left(\frac{\partial \Delta \mathbf{u}}{\partial \mathbf{x}} \right)^T \right]. \quad (2.82)$$

Substitution of the above into the second term on the RHS of (2.74) yields

$$\int_{\Omega} \text{tr}(\nabla(\delta\mathbf{u})\Delta\boldsymbol{\sigma}) = \int_{\Omega} \text{tr}(\delta\boldsymbol{\epsilon}\mathbf{c}\Delta\boldsymbol{\epsilon}) \, dv. \quad (2.83)$$

Substituting to the RHS of (2.74) with (2.83) to (2.56) gives the *linearised form* for the variational equations

$$\int_{\Omega} \text{tr}(\nabla(\delta\mathbf{u})\boldsymbol{\sigma}\nabla(\Delta\mathbf{u})^T) \, dv + \int_{\Omega} \text{tr}(\delta\boldsymbol{\epsilon}\mathbf{c}\Delta\boldsymbol{\epsilon}) \, dv = \int_{\partial\Omega_t} \delta\mathbf{u}^T \mathbf{t} \, ds. \quad (2.84)$$

Using the approximation (2.59) in (2.84) yields

$$\sum_e \left(\int_{\Omega_e} \text{tr}(\nabla(\delta\mathbf{u})\boldsymbol{\sigma}\nabla(\Delta\mathbf{u})^T) \, dv + \int_{\Omega_e} \text{tr}(\delta\boldsymbol{\epsilon}\mathbf{c}\Delta\boldsymbol{\epsilon}) \, dv \right) = \sum_e \left(\int_{\partial\Omega_{et}} \delta\mathbf{u}^T \mathbf{t} \, ds \right). \quad (2.85)$$

The quantities in this equation are future specified in terms of nodal displacement through interpolations in (2.63) and (2.64).

Substitution of the interpolations described above into the first term on the LHS of (2.85) for each element yields

$$\int_{\Omega_e} \text{tr}(\nabla(\delta\mathbf{u})\boldsymbol{\sigma}\nabla(\Delta\mathbf{u})^T) \, dv = (\delta\mathbf{u}_I)^T \mathbf{K}_{IJ}^g \Delta\mathbf{u}_J, \quad (2.86)$$

where the geometric part of the stiffness matrix

$$\mathbf{K}_{IJ}^g = \int_{\Omega_e} \text{tr}(\nabla N_I^T \boldsymbol{\sigma} \nabla N_J) \, dv. \quad (2.87)$$

Using Voigt's notation for $\boldsymbol{\sigma}$, $\delta\boldsymbol{\epsilon}$ as

$$\boldsymbol{\sigma} = [\sigma_{11} \quad \sigma_{22} \quad \sigma_{33} \quad \sigma_{12} \quad \sigma_{23} \quad \sigma_{31}]^T \quad (2.88)$$

and

$$\delta\boldsymbol{\epsilon} = [\delta\epsilon_{11} \quad \delta\epsilon_{22} \quad \delta\epsilon_{33} \quad 2\delta\epsilon_{12} \quad 2\delta\epsilon_{23} \quad 2\delta\epsilon_{31}]^T. \quad (2.89)$$

Expressing the $\delta\boldsymbol{\epsilon}$ in terms of the virtual displacement gives

$$\delta\boldsymbol{\epsilon} = \left[\frac{\partial u_1}{\partial x_1} \quad \frac{\partial u_2}{\partial x_2} \quad \frac{\partial u_3}{\partial x_3} \quad \frac{\partial u_1}{\partial x_2} + \frac{\partial u_2}{\partial x_1} \quad \frac{\partial u_2}{\partial x_3} + \frac{\partial u_3}{\partial x_2} \quad \frac{\partial u_3}{\partial x_1} + \frac{\partial u_1}{\partial x_3} \right]^T. \quad (2.90)$$

Substitution of (2.64) to (2.90) yields

$$\delta\boldsymbol{\epsilon} = \begin{bmatrix} N_{I,1} & 0 & 0 \\ 0 & N_{I,2} & 0 \\ 0 & 0 & N_{I,3} \\ N_{I,2} & N_{I,1} & 0 \\ 0 & N_{I,3} & N_{I,2} \\ N_{I,3} & 0 & N_{I,1} \end{bmatrix} \begin{bmatrix} \delta u_{I1} \\ \delta u_{I2} \\ \delta u_{I3} \end{bmatrix} = \mathbf{B}_I \delta\mathbf{u}_I, \quad (2.91)$$

where

$$N_{I,i} = \frac{\partial N_I}{\partial x_i}, \quad i = 1, 2, 3. \quad (2.92)$$

With Voigt's notation, the second term on the LHS of (2.85) is

$$\int_{\Omega_e} \text{tr}(\delta \boldsymbol{\epsilon} \mathbf{c} \Delta \boldsymbol{\epsilon}) \, dv = \int_{\Omega_e} \delta \boldsymbol{\epsilon}^T \mathbf{D} \Delta \boldsymbol{\epsilon} \, dv, \quad (2.93)$$

where the 6×6 matrix \mathbf{D} denotes the matrix form of the fourth-order tensor \mathbf{c} . Use the interpolations in the incremental strain term

$$\Delta \boldsymbol{\epsilon} = \mathbf{B}_J \Delta \mathbf{u}_J, \quad (2.94)$$

and substitute to the RHS of (2.93), we have

$$\int_{\Omega_e} \delta \boldsymbol{\epsilon}^T \mathbf{D} \Delta \boldsymbol{\epsilon} \, dv = (\delta \mathbf{u}_I)^T \mathbf{K}_{IJ}^m \Delta \mathbf{u}_J, \quad (2.95)$$

where the material part of the element stiffness matrix

$$\mathbf{K}_{IJ}^m = \int_{\Omega_e} \mathbf{B}_I^T \mathbf{D} \mathbf{B}_J \, dv. \quad (2.96)$$

Using the interpolations on the RHS of (2.85) yields

$$\int_{\Omega_e} \delta \mathbf{u}^T \mathbf{t} \, ds = (\delta \mathbf{u}_I)^T \int_{\partial \Omega_{et}} N_I \mathbf{t} \, ds = (\delta \mathbf{u}_I)^T \mathbf{f}_I. \quad (2.97)$$

Accumulating the terms on the RHS of (2.86), (2.95) and (2.97), the variational equation (2.85) may be written as

$$\sum_e (\delta \mathbf{u}_I)^T [(\mathbf{K}_{IJ}^g + \mathbf{K}_{IJ}^m) \Delta \mathbf{u}_J - \mathbf{f}_I] = 0, \quad (2.98)$$

since $\delta \mathbf{u}_I$ is arbitrary, (2.98) leads to the basic finite element equations and we have components of the tangential stiffness matrix

$$\mathbf{K}_{IJ} = \sum_e (\mathbf{K}_{IJ}^g + \mathbf{K}_{IJ}^m). \quad (2.99)$$

2.3 XFEM

The basic concept of XFEM is to enrich the finite element approximation space so that it is capable of reproducing certain features of the problem of interest [Belytschko and Black, 1999; Mohammadi, 2008], in particular discontinuities such as a tear.

Consider \mathbf{X} , a point in a FE model. Assume there is a discontinuity in the arbitrary domain discretized into some n node finite elements. In the XFEM, the following approximation is utilised to calculate the displacement for the point \mathbf{X} within the domain.

$$\mathbf{u}^h(\mathbf{X}) = \mathbf{u}^{FE} + \mathbf{u}^{Enr} = \sum_{I=1}^n N_I(\mathbf{X})\mathbf{u}_I + \sum_{J=1}^m N_J(\mathbf{X})H(\mathbf{X})\mathbf{a}_J, \quad (2.100)$$

where \mathbf{u}_I is the vector of regular degree of nodal freedom in the FEM, \mathbf{a}_J is the added set of degrees of freedom to the standard FE model and $H(\mathbf{X})$ is the discontinuous enrichment function defined for the set of nodes that the discontinuity has in its influence domain. For example, to account for displacement jump across a tear Γ , $H(\mathbf{X})$ may be defined as

$$H(\mathbf{X}) = \begin{cases} 1, & \text{if } (\mathbf{X} - \mathbf{X}_\Gamma) \cdot \mathbf{n} \geq 0 \\ -1, & \text{otherwise} \end{cases} \quad (2.101)$$

where $\mathbf{X}_\Gamma \in \Gamma$ is the closest point to \mathbf{X} on the tear and \mathbf{n} is a outward-pointing normal vector of Γ at \mathbf{X}_Γ (Figure 2.3).

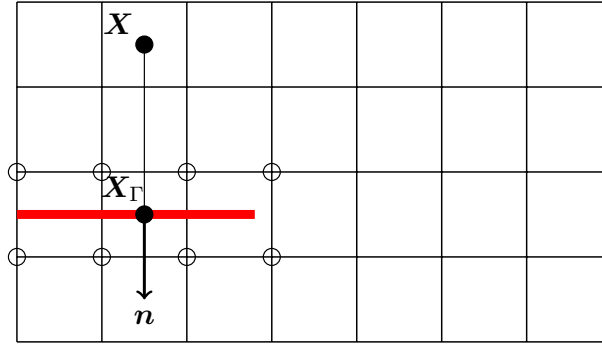
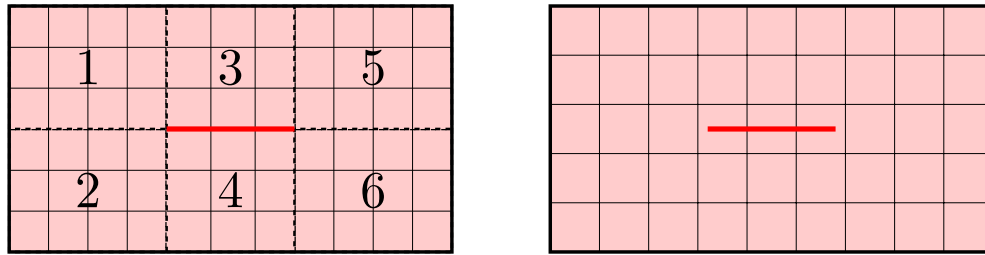


Figure 2.3: A mesh is used for the domain including a tear (red line). \mathbf{X} is an arbitrary point in the domain, \mathbf{X}_Γ is the closest point to \mathbf{X} on the tear, and \mathbf{n} is an outward-pointing normal vector of Γ at \mathbf{X}_Γ . The displacement at nodes circled are enriched.

The first term on the RHS of (2.100) is the conventional finite element approximation, including all nodes, while the second term is the enrichment approximation which takes into account the existence of any discontinuities, including only nodes of elements bisected by the tear.

The main advantage of XFEM is that the tear is not needed to be explicitly expressed in the finite element mesh, therefore the mesh generation in XFEM is independent of the tear. As an illustration, Figure 2.4 shows a typical mesh when using FEM and XFEM for a strip with a tear. Before applying loading, the upper and lower tear surfaces have the same position. It is not easy to generate directly a mesh for the domain including such a tear. As shown in Figure 2.4(a), a method is to separate the domain into six subdomains, mesh each individually with constraint that common edges (dashed lines) have the same mesh.

Finally the mesh of subdomains except 3 and 4 will be tied together, so the repeated nodes on the dashed lines are removed and have the mesh for both upper and lower tear surface.



(a) FEM mesh

(b) XFEM mesh

Figure 2.4: A typical FEM and XFEM mesh for a strip with a tear (red line). Dashed lines in (a) shows the boundaries of subdomains and numbers are the labels of these subdomains.

2.4 Conclusion

In this chapter, we summarise the essential basic mathematical theory and formulations of finite elasticity, FEM and XFEM. A comparison between FEM and XFEM shows that the mesh generation in XFEM is easier than in FEM. Therefore, we use the FEM in problems with a simple geometry (Chapter 3) and the XFEM in problems with complex geometry (Chapter 4–6). The ‘simple’ here means that such a decomposition shown in Figure 2.4(a) is easy. A complete derivative on using FEM to solve a nonlinear boundary value problem is presented. This derivative shows where the Cauchy stress and tangential moduli associated with a SEF is used in the computation of FEM. Understanding this derivative is essential to my developing of a material model in a finite element program in Chapter 7.

Chapter 3

Onset of propagation of a dissection in a 2D strip

Prediction of soft tissue failure may yield a better understanding of the pathogenesis of AD and help to advance diagnostic and therapeutic strategies for treatment of this and other diseases and injuries involving the tearing of soft tissue, such as an aortic dissection. In this chapter, we present computational models of tear propagation in fibre-reinforced soft tissue that undergoes finite deformation, modelled by a hyperelastic anisotropic constitutive law. We adopt the appropriate energy argument for anisotropic finite strain materials to determine if a tear can propagate when subject to internal pressure loading. The energy release rate is evaluated with an efficient numerical scheme that makes use of adaptive tear lengths. As an illustration, we present the calculation of the energy release rate for a two-dimensional strip of tissue with a pre-existing tear of length a under the internal pressure p and show the effect of fibre orientation. This calculation allows us to locate the potential bifurcation to tear propagation in the (a, p) plane. The numerical predictions are verified by analytical solutions for simpler cases. We have identified a scenario of tear arrest, which is observed clinically, when the surrounding connective tissues are accounted for. Finally, the limitations of the models and further directions for applications are discussed. This chapter has been published in the *Journal of Engineering Mathematics*, 95(1):249–265, 2015.

3.1 Introduction

To model a tear in arteries, one may follow the approaches used to describe material failure in damage and fracture mechanics. Two of the commonly used mathematical theories are based on the Stress Intensity Factor (SIF) and energy arguments.

The SIF criterion requires calculation of the stress field in the vicinity of the tip [Tada et al., 2000]. For a linear elastic isotropic material, the stress-field near the tip is characterised by a SIF K which exhibits an $r^{-1/2}$ singularity (Equation (1.17)), where r is the distance from the tip (Figure 1.8). A criterion for propagation is that, for a given mode of failure, K is greater than a specified material toughness K_c ($K > K_c$). However, the asymptotic stress field near the tip is not generally known for finite deformation non-linear elasticity, with the exception of simplified cases for isotropic power-law materials [Stephenson, 1982].

The energy approach to failure is based on calculating the *Energy Release Rate* (ERR), G , which is the change in total potential energy with per unit extension of the tear. It was developed by *inter alios* Griffith [1921] and extended by Irwin and Wells [1965]. The concept of ERR stems from the energy balance principle during an infinitesimal quasi-static tear extension; it is the energy per unit area released from the system by extending the tear surface by an infinitesimal area dA . In a plane strain problem, the deformation is two-dimensional and G is calculated per unit length instead of per unit area. Given the material parameter G_c , the critical energy required to break all the bonds across dA , we can evaluate the potential for propagation of the tear: if $G > G_c$, the tear may propagate (i.e. it is energetically feasible), otherwise it is stationary. Thus $G - G_c$ is the potential for tear propagation. In particular, ignoring any plastic effects, G can be calculated from the work done by loads and changes in the strain energy accompanying the increase in the tear area. There are many numerical methods for calculating G [e.g. Zehnder, 2007], and most do not rely on evaluating the singular stress field at the tip, rather on the global energy and work, so an accurate value for G can be obtained with modest mesh refinement. Hence for the arterial dissection problem, we choose to use the energy approach in this chapter.

We use an invariant homogeneous fibre-reinforced material model, i.e. the widely cited HGO strain energy function [Holzapfel et al., 2000], as a description for mechanics of the arterial wall, and focus on seeking the conditions that govern the onset of tear propagation. For simplicity, we assume that pressurised blood fills the tear hence the false lumen is subject to the same arterial pressure as the true lumen. Tsai et al. [2008] showed

that the false lumen diastolic pressure is slightly higher, i.e. it is 100.4%–107.9% of the true lumen diastolic pressure as shown in Figure 1.3. We also neglect flows in small radial tears that connect the main dissection to the lumen. A finite element model is developed to study the finite elastic deformation of the arterial wall containing an initial tear and analyse the potential for tear propagation. We derive a failure criterion in terms of the ERR, and describe a computational framework to calculate this. We illustrate the ideas by studying the behaviour of a tear in a two-dimensional strip of arterial material containing a single parallel tear. Using this computational framework, we obtain the condition for tear propagation in strips of material with different fibre distributions. In addition, we simulate constraint due to surrounding connective tissues and show that this can lead to tear arrest.

3.2 Methodology

3.2.1 The energy budget

A sample of tissue with a tear can deform and split apart when loaded, as illustrated in Figure 3.1. From the energy balance theory in fracture mechanics [see Zehnder, 2007], the total potential energy for the system is

$$\mathcal{E} = \Pi + G_c a, \quad (3.1)$$

where the mechanical energy $\Pi = U_e - W$, U_e is the strain energy of the tissue sample at equilibrium, G_c is the energy required for breaking bonds linking the new torn surfaces (per unit area a in 3D, or per unit length a in 2D), and W is work done by the load.

The minimal potential energy principle requires that

$$\frac{d\mathcal{E}}{da} < 0 \quad \text{or} \quad G > G_c, \quad (3.2)$$

where $G = -d\Pi/da$ is the *energy release rate* (ERR). In order to determine if a tear may propagate, it is essential to first evaluate the ERR for the system.

3.2.2 Computational approach for ERR

A simplified geometry for the arterial tissue is employed. A key clinical observation is that patients present with a dissection of fixed length at risk of further tearing. We seek to determine the conditions under which a tear of finite length will propagate in a large

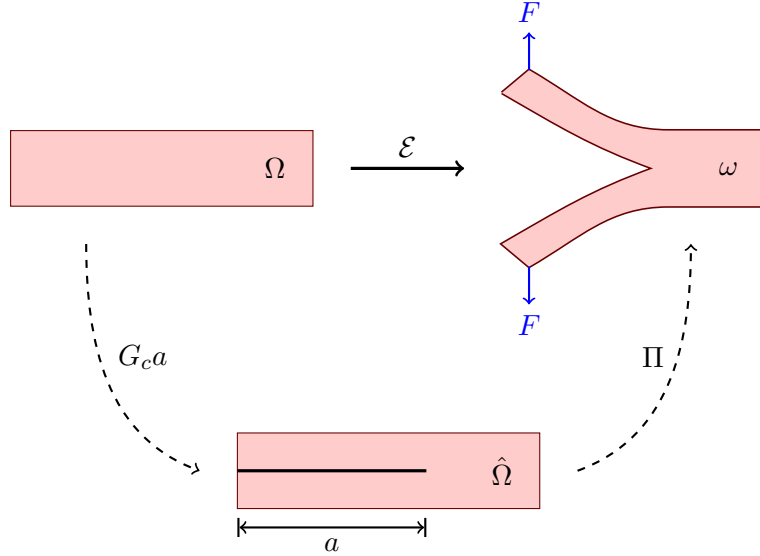


Figure 3.1: The change in the sample under force F , $\Omega \rightarrow \omega$, can be approached by two steps: creating a tear of area a , $\Omega \rightarrow \hat{\Omega}$, followed by elastic deformation, $\hat{\Omega} \rightarrow \omega$. Correspondingly, the total potential energy for the system, \mathcal{E} , is decomposed to the surface energy, $G_c a$, and mechanical energy, Π .

artery via the criterion given in (3.2). The geometry is simplified by modelling the artery as a cylinder with an axisymmetric tear subject to constant pressure p , approximating the blood pressure by its mean value, neglecting the small communicating tear between lumen and main dissection, considering a cross section through the wall and simplifying further to a two-dimensional strip, ω_a , as shown in Figure 3.2.

For the hyperelastic anisotropic soft tissues undergoing finite deformation, the criterion (3.2) needs to be evaluated numerically. There are two methods for calculating the ERR using the FEM. One is based on the variation of local energy at the vicinity of tip, the other is based on variation of the global energy [Knees and Mielke, 2008]. We use the latter approach as it avoids any difficulty when extended to finite deformation nonlinear elasticity, even when body forces and residual stress are included. The formula for calculating a numerical approximation to G is

$$G = -\frac{\delta\Pi}{\delta a} = -\frac{\Pi_{a+\delta a} - \Pi_a}{\delta a}. \quad (3.3)$$

To obtain the equilibrium value of Π_a , we solve a specified boundary value problem using the FEM package FEAP [Taylor, 2011b]. With the pressure loading, the solution can be obtained by a ‘proportional load process’, in which the loading parameter is increased

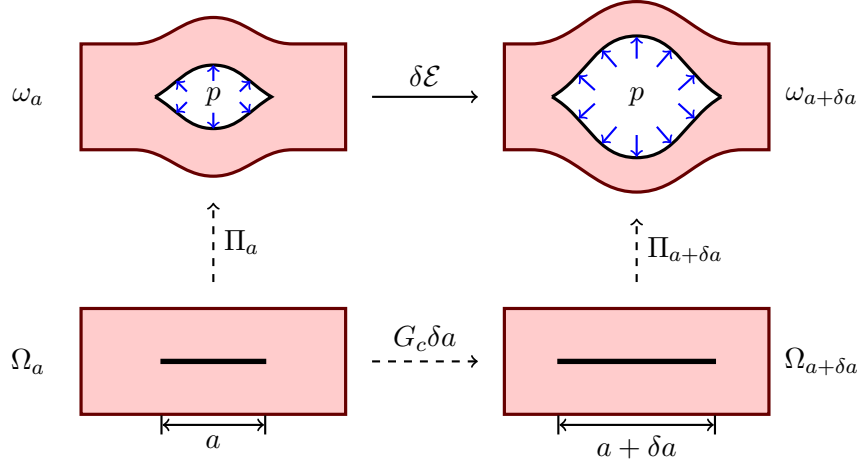


Figure 3.2: The variation of total potential energy due to a tear propagation from ω_a to $\omega_{a+\delta a}$ is $\delta\mathcal{E} = \delta\Pi + G_c\delta a = (\Pi_{a+\delta a} - \Pi_a) + G_c\delta a$. To get Π for calculating ERR in (3.3), we calculate the equilibria of Ω_a and $\Omega_{a+\delta a}$ subject to a constant uniform pressure, p , on the tear surfaces via the FEM.

(parametrised by an artificial ‘time’ t) incrementally towards its final value and the solution is updated at each increment. Depending on the material parameters and the particular method used to solve the discretised equations, this calculation can be time consuming.

In order to improve the computational efficiency, we incorporate interpolation techniques for Π_a . We evaluate Π_a for a collection of lengths and use cubic spline interpolation between these values. This gives a smooth approximation to $\Pi(a)$ that can be used to estimate $G = -\partial\Pi/\partial a$.

The numerical procedure described above relies on the numerical calculations of the strain energy U_e and the work done by external load W , which we now describe.

3.2.3 Calculation of the strain energy U_e

For the arterial tissue, we use the HGO constitutive law [Holzapfel et al., 2000], that is based on the histology of the artery. The strain energy function in the incompressible HGO model is split into contributions from the matrix Ψ_m and the fibres Ψ_f , viz.

$$\bar{\Psi}(\mathbf{C}) = \Psi_m(I_1) + \Psi_f(I_4, I_6) = \frac{c}{2}(I_1 - 3) + \sum_{n=4,6} \psi(I_n), \quad (3.4)$$

where c is the shear modulus of matrix, I_1 is the first invariant of the right Cauchy–Green strain tensor to quantify the deformation of matrix and I_n , $n = 4, 6$ are invariants to

describe the fibres stretch and $\psi(\cdot)$ is the strain energy density function of fibres. Assume the deformation gradient is denoted by \mathbf{F} and the orientations of two-family fibres are denoted by the referential unit vector directions \mathbf{A}_1 and \mathbf{A}_2 , then

$$I_1 = \text{tr } \mathbf{C}, \quad I_n = \mathbf{C} : \mathbf{M}_n \quad (n = 4, 6), \quad (3.5)$$

where $\mathbf{C} = \mathbf{F}^T \mathbf{F}$, $\mathbf{M}_4 = \mathbf{A}_1 \otimes \mathbf{A}_1$ and $\mathbf{M}_6 = \mathbf{A}_2 \otimes \mathbf{A}_2$, such that in component $M_{ij} = A_i A_j$. It is also assumed that fibres only take on load when stretched, thus

$$\psi(I_n) = \begin{cases} \frac{k_1}{2k_2} (\exp [k_2(I_n - 1)^2] - 1) & \text{when } I_n > 1, \\ 0 & \text{when } I_n \leq 1, \end{cases} \quad n = 4, 6, \quad (3.6)$$

where k_1 and k_2 are material parameters to definite the stiffness of fibres.

To approximate the incompressible behaviour in the finite element calculation, we employ the multiplicative decomposition of the deformation gradient [Flory, 1961] to form a quasi-incompressible material model

$$\Psi(\mathbf{C}) = \Psi_v(J) + \bar{\Psi}(\bar{\mathbf{C}}) = \frac{K}{2}(J - 1)^2 + \bar{\Psi}(\bar{\mathbf{C}}), \quad (3.7)$$

where $J = \det \mathbf{F}$ and $\bar{\mathbf{C}} = J^{-2/3} \mathbf{C}$. The incompressibility condition is satisfied to a good approximation when the penalty constant K is large enough. Then the Cauchy stress is

$$\boldsymbol{\sigma} = -\frac{d\Psi_v}{dJ} \mathbf{I} + c \text{dev}(\mathbf{b}) + \sum_{n=4,6} 2 \frac{d\psi}{dI_n} \text{dev}(\mathbf{m}_n), \quad (3.8)$$

where $\mathbf{b} = \mathbf{F} \mathbf{F}^T$, $\mathbf{m}_n = \mathbf{F} \mathbf{M}_n \mathbf{F}^T$ and $\text{dev}(\cdot) = (\cdot) - \frac{1}{3} \text{tr}(\cdot) \mathbf{I}$. The detailed derivation of the quasi-incompressible HGO model (3.7) for a user subroutine in FEAP [Taylor, 2011a] is shown in Chapter 7.

3.2.4 Calculation of the work done by pressure

Consider the tear surface specified by a position vector $\mathbf{x} = \mathbf{x}(s, t)$, $0 \leq s \leq a$, $0 \leq t \leq T$, as shown in Figure 3.3. At time $t = 0$, $\mathbf{x}(s, 0)$ specifies the initial tear surface. The force on a small portion of the tear of length dl is

$$d\mathbf{f} = -p dl \mathbf{n} = -p \left| \frac{\partial \mathbf{x}}{\partial s} ds \right| \mathbf{n},$$

and the work done in a small time dt is

$$dw = d\mathbf{f} \cdot \mathbf{v} dt = d\mathbf{f} \cdot \frac{\partial \mathbf{x}}{\partial t} dt.$$

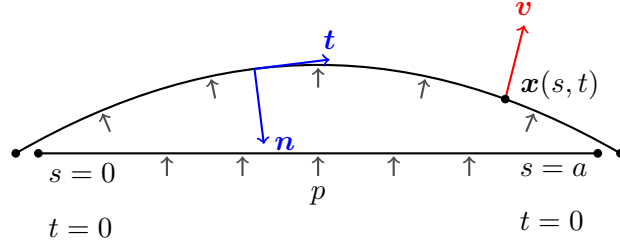


Figure 3.3: Sketch of the deformation of one tear surface under constant pressure: \mathbf{t} and \mathbf{n} are the tangent and normal unit vectors of the deformed tear surface, respectively, and \mathbf{v} is the velocity of the particle at time t that originated at $\mathbf{x} = \mathbf{x}(s, 0)$.

The work done by the distributed force (pressure) is then

$$W = \int dw = -p \int_0^T \int_0^a \mathbf{n} \cdot \frac{\partial \mathbf{x}}{\partial t} \left| \frac{\partial \mathbf{x}}{\partial s} \right| ds dt. \quad (3.9)$$

Let \mathbf{k} be the unit vector along the third direction into the diagram, then $\mathbf{n} = \mathbf{k} \times \mathbf{t}$, and $\mathbf{t} = \frac{\partial \mathbf{x}}{\partial s} \left| \frac{\partial \mathbf{x}}{\partial s} \right|^{-1}$. Substituting these expression into (3.9), gives

$$W = -p \int_0^T \int_0^a \left(\mathbf{k} \times \frac{\partial \mathbf{x}}{\partial s} \right) \cdot \frac{\partial \mathbf{x}}{\partial t} ds dt. \quad (3.10)$$

The triple scalar product is the signed volume of the parallelepiped defined by the three vectors and $|\mathbf{k}| = 1$, therefore the integral in (3.10) represents the area swept by the tear surface.

3.3 Results

3.3.1 Numerical experiments

Consider a strip with two ends fixed in the y -axis direction as shown in Figure 3.4. To avoid rigid body motions, the x -coordinate of the centreline of the strip is fixed. For a tear under the pressure loading, we consider the ERR due to the tear extension for four different materials, one without fibres and the others with different fibre orientations (see Table 3.1). In all cases, we set the values of the material parameters in the constitutive law (3.4) to be $c = 3.0$ kPa, $k_1 = 2.3632$ kPa and $k_2 = 0.8393$, which are typical values for the media of rabbit's carotid artery [Holzapfel et al., 2000].

Isotropic material

We seek a condition for the onset of tear propagation as a function of tear length and pressure, thus we calculate $G(a, p)$. In particular, we consider the possibility of propagation

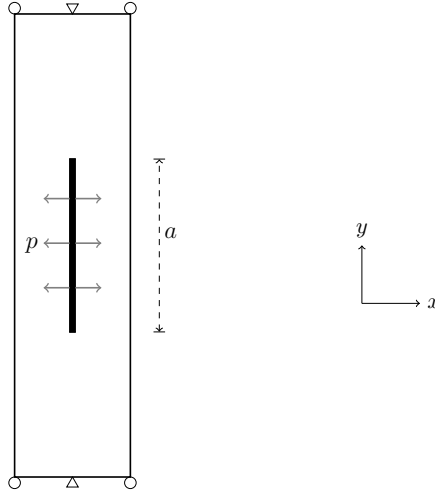


Figure 3.4: Sketch of the strip with a single parallel tear of length a under internal pressure p . The boundary conditions are that the two ends are fixed in the y -direction, and the centres of the two ends are also fixed in the x -direction. The tear is exactly at the middle of the strip. With this symmetry, we know the direction of tear extension a priori, which is along the strip, i.e. the direction of the pre-existing tear. Recall that this model computes the energy release rate for a given propagation path.

for a tear of length $a \in [0.4, 10.0]$ mm subject to pressure $p \in [0, 0.6]$ kPa. Note in this hypothetical test case, the pressure value used is not in the physiological range of realistic arteries. We focused on the trend of G on p and a for propagation of a *pre-existing* tear. For the sake of computational efficiency, we specified the range of pressure p and tear length a in our simulations. The value of pressure p is selected as big as possible for these two-dimensional strips, a deeper discussion on this selection is included in Section 3.5. For a pre-existing tear, the length $a > 0$, we selected $a = 0.4$ mm as the lower value such that a very short tear is considered. The upper value of $a = 10.0$ mm is selected such that the tear opening has already been very wide and the trend of $G(a)$ is clear to be shown.

In numerical experiment 1, the strip has no fibres and is isotropic. The ERR $G(a, p)$ is a monotonically increasing function of a for each value of p , as shown in Figure 3.5. A longer tear leads to an increased ERR and thus an increase in the likelihood of tear propagation. This observation agrees with the results of a beam model described in Section 3.4 (see equation (3.16)). A comparison of the curves for different pressures shows that $G(a, p)$ is also a monotonically increasing function of p for fixed values of a , in agreement with high pressure favouring tear propagation.

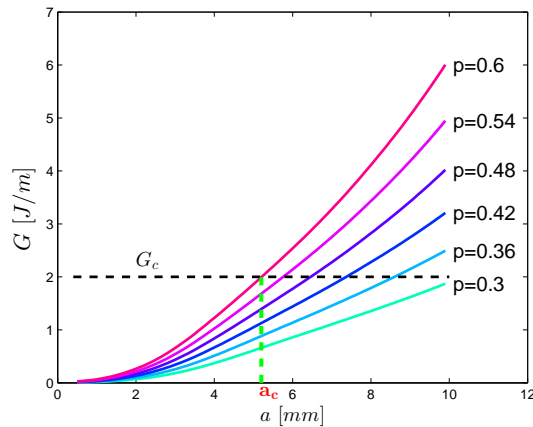


Figure 3.5: The energy release rate G for an isotropic strip, plotted against tear length a subject to various values of the pressure p . G_c is a material-dependent critical parameter and, e.g., when $G_c = 2 \text{ J/m}$ and $p = 0.6 \text{ kPa}$, it is energetically favourable for a tear of length greater than a_c to propagate.

Fibre-reinforced materials

To investigate the effect of collagen fibres on the ERR, we perform three more numerical experiments by reinforcing the strip with fibres of different orientations. In Exp. 2 the fibres are parallel to the tear, in Exp. 3 the fibres are aligned at $\pi/4$ to the tear, and in Exp. 4 the fibres are normal to the tear, as specified by the alignment vectors \mathbf{A}_1 and \mathbf{A}_2 in Table 3.1.

The curves of $G(a)$ when $p = 0.6 \text{ kPa}$ are shown in Figure 3.6. The curve for Exp. 2 is very close to that for Exp. 1. The fibres can only support loads in tension, and the regions with subject to stretch only occur in small regions just ahead of the tips of the tear (Figure 3.7). Consequently, the tear opening and stored energy, and thus the mechanical energy, are similar to those for Exp. 1, as is shown in Figure 3.8.

As the fibres become more parallel to the tear going from Exp. 2 to Exp. 4, the ERR decreases, because the fibres take a greater load to resist the opening of the tear, as shown in Figure 3.8. Specifically, the region with stretch along the fibre direction in Exp. 4 (Figure 3.9) is greater than that in Exp. 2 (Figure 3.7).

$G(a, p)$ is also shown as a contour plot in Figure 3.10. The region at highest risk of tear propagation is at the top right-hand corner. These contours are similar in all the numerical experiments.

Table 3.1: Characterisation of the materials used in four numerical experiments on the effect of fibres

Experiments	Material type	\mathbf{A}_1	\mathbf{A}_2
Exp. 1	isotropic	N/A	N/A
Exp. 2	transversely isotropic	(1, 0, 0)	N/A
Exp. 3	orthotropic	$(\cos(\pi/4), \sin(\pi/4), 0)$	$(\cos(\pi/4), -\sin(\pi/4), 0)$
Exp. 4	transversely isotropic	(0, 1, 0)	N/A

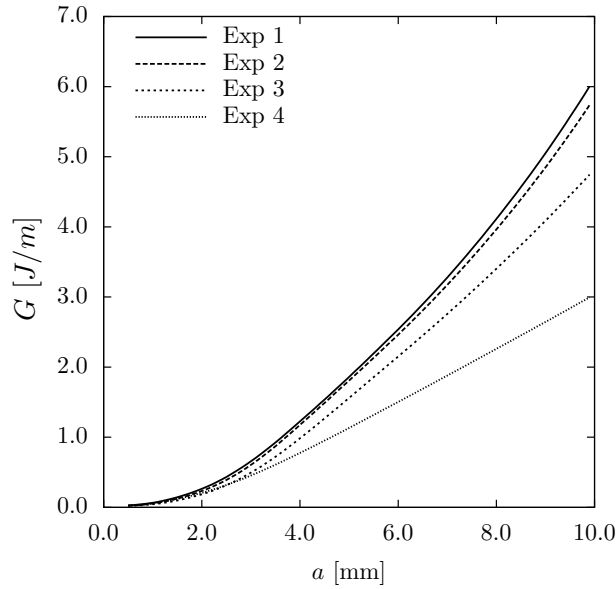


Figure 3.6: Graphs of the ERR $G(a)$ when $p = 0.6$ kPa for the four numerical experiments listed in Table 3.1. G is the greatest in the Exp.1 for the isotropic strip, and G decreases as the fibre direction \mathbf{A}_1 moves towards the direction of the tear from Exp.2 to Exp.4. In other words, fibres parallel to the tear will increase the resistance of the tear propagation.

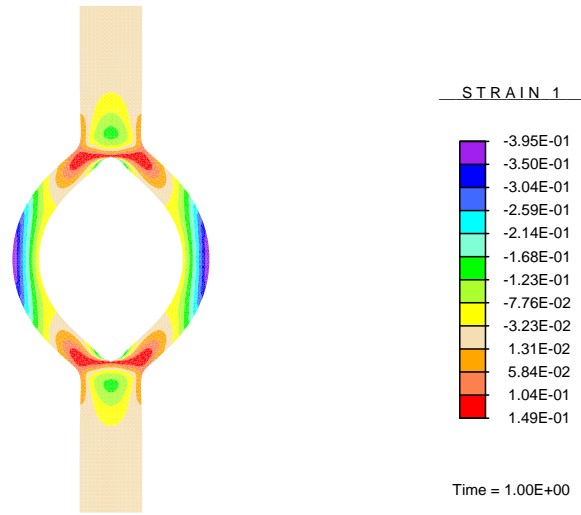


Figure 3.7: The first component of Almansi strain tensor $e_{11} = \frac{1}{2} (1 - I_4^{-1})$ for Exp. 2. The regions with positive values, close to the tear tips, indicate fibre stretching.

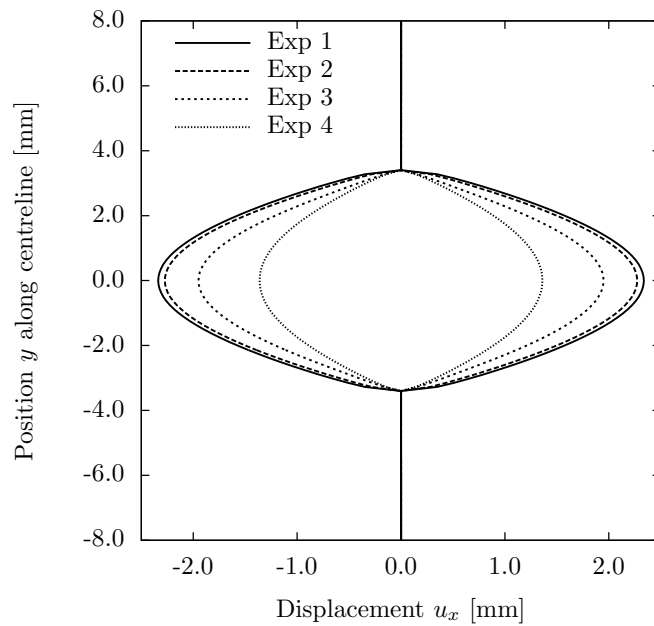


Figure 3.8: The width of tear with pressure $p = 0.6$ kPa for the four numerical experiments in Table 3.1. As the fibres become more parallel to tear, the width of tear decreases.

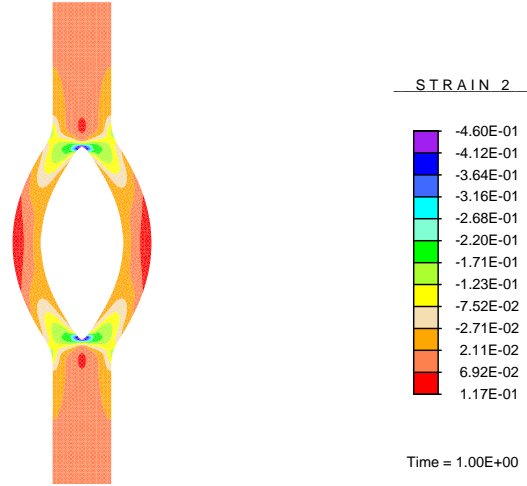
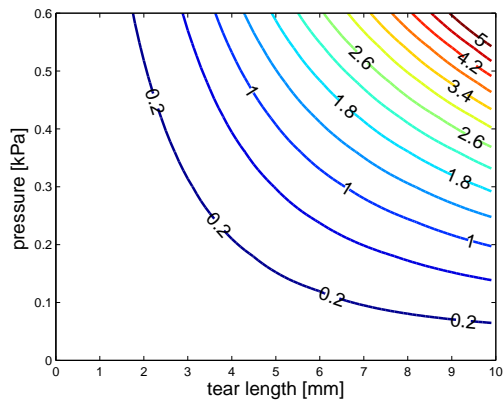


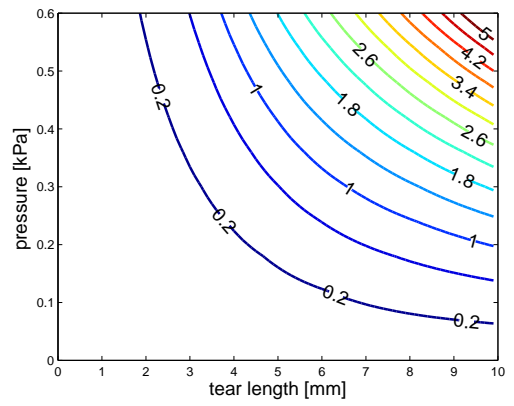
Figure 3.9: The second component of Almansi strain tensor $e_{22} = \frac{1}{2}(1 - I_4^{-1})$ for Exp. 4. The positive values indicate fibre stretching.

3.3.2 Effects of the connective tissue — tear arrest

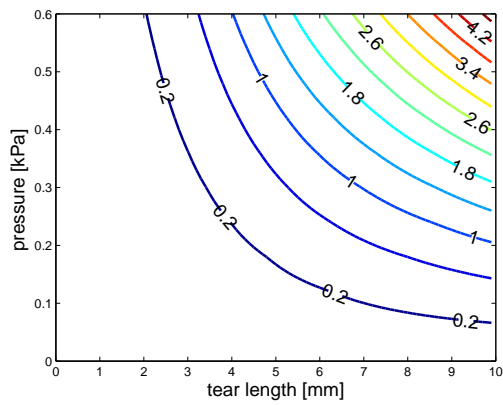
To consider the effect on tear propagation of the connective tissue around the strip, we add two linearly elastic blocks to the sides of the strip in the computational model. To assume both sides the tissue behaves the same is because we need to keep the symmetry, such that we know the direction of tear extension a priori. Recall that this model computes the energy release rate for a given propagation path. The reference configuration and boundary conditions are shown in Figure 3.11. The central strip is the fibre-free material used in Exp. 1. The plots of the ERR in Figure 3.12 show that arrest of the tear propagation can occur, due to the surrounding connective tissue resisting the deformation of the strip. Arrest of the propagation of the tear is also found in simple beam model described in Section 3.4 (see Figure 3.15). However, for softer connective tissue (with a Young's modulus $E = 0.01$ kPa instead of $E = 10$ kPa), the phenomenon of arrest disappears, as shown in Figure 3.13, and so the stiffness of surrounding connective tissue is an essential factor influencing the likelihood of tear propagation.



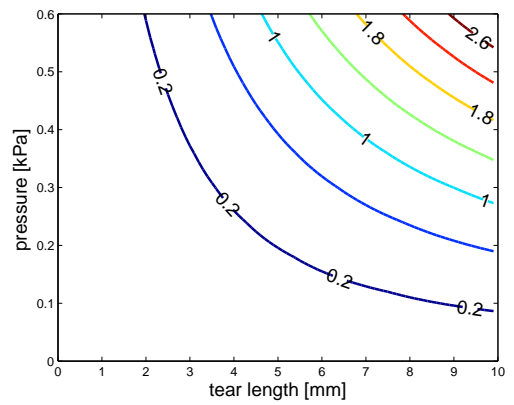
(a) Exp. 1



(b) Exp. 2



(c) Exp. 3



(d) Exp. 4

Figure 3.10: Contours of $G(a, p)$ for the four numerical experiments in Table 3.1. The numbers on the isolines are the value of $G(a, p)$ for particular values for a and p . The region at highest risk of tear propagation lies at the top right-hand corner in all the experiments. The energy release rate $G(a, p)$ is the smallest in Exp. 4.

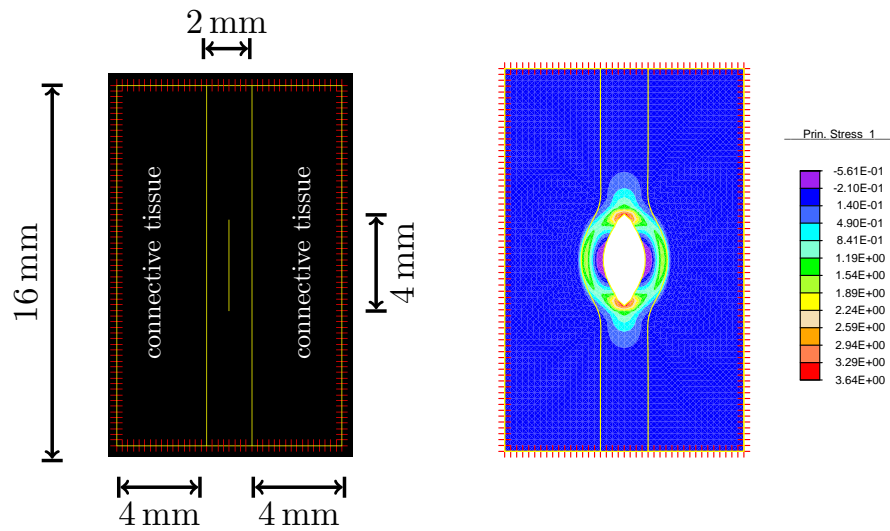


Figure 3.11: The reference (left) and current configurations with maximum principal stress (right) of a strip when constrained by the two blocks, which simulate the connective tissues. Using tissues at both sides of the strip maintains the symmetry of geometry, and so guarantees the tear to extend along the strip. The tear surface is subject to the pressure $p = 0.6$ kPa. The red lines show the boundary conditions: the left and right are constrained such that they cannot move horizontally, and the top and bottom are constrained such that they cannot move vertically.

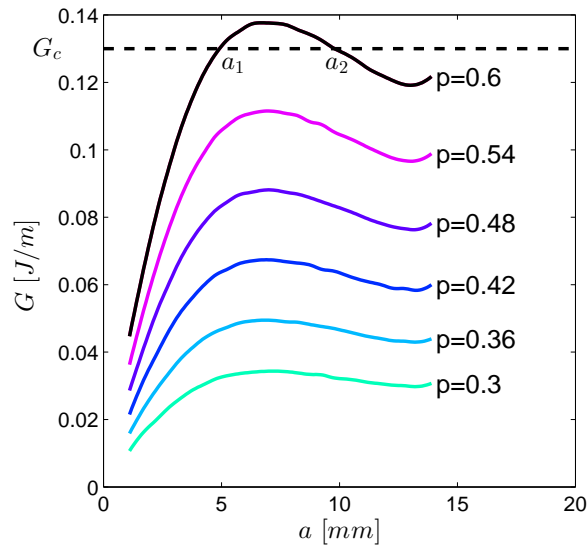


Figure 3.12: Graphs of the ERR G for a strip constrained by two linearly elastic blocks as shown in Figure 3.11. For example, when $G_c = 0.13 \text{ J/m}$ and $p = 0.6 \text{ kPa}$, it is only energetically favourable for a tear to propagate when its length $a \in (a_1, a_2)$ for which $G > G_c$. Recall that we compute the energy release rate for propagation of a *pre-existing* tear. In this example, the value of $a = 0.4 \text{ mm}$ rather than $a = 0$ for a very short tear is considered.

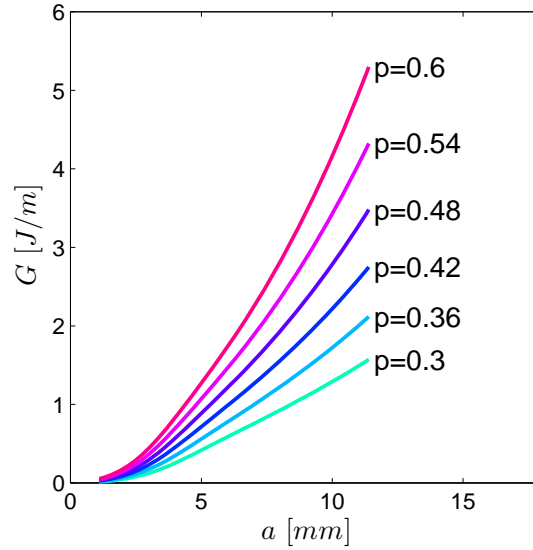


Figure 3.13: In contrast to the Figure 3.12, where the Young’s modulus of the surrounding tissue is $E = 10$ kPa, the ERR $G(a)$ for the case with much softer surrounding tissue ($E = 0.01$ kPa), is always a monotonically increasing function of the tear length, a , and tear arrest cannot occur.

3.4 A simple beam model for ERR

The inequality (3.2) is known as the Griffith criterion when applied to linear elastic problems. The exact mathematical expression of energy release rate is available for a simplified geometries and loading scenario. Here we derive the energy release rate for a semi-infinite linear isotropic beam subject to pressure and external constraint, and use these theoretical results to verify qualitatively the trend in energy release rate on tear length and pressure obtained from our computational model for arterial wall strips.

Consider a semi-infinite beam of constant Young’s modulus E and second moment of area J . The beam is bonded to a surface except for a region $0 \leq x \leq a$ where x measures the length along the beam from one end. The deflection of the beam is $w(x)$ and the boundary conditions are

$$w(x) = 0 \text{ for } x \geq a, \quad w''(0) = 0, \quad w'''(0) = 0, \quad (3.11)$$

where $w''(0) = 0$ means that there is no bending moment at the free end of the beam, and $w'''(0) = 0$ indicates that there is no shearing force acting at the free end of the beam. The equation satisfied by $w(x)$ depends on the loading experienced by the beam, we take

a general function $F(x, w)$ so that

$$EJw''''(x) = F(x, w). \quad (3.12)$$

Different choices of $F(x, w)$ give different external loading conditions, e.g. below we simulate the effect of the constraint of the surrounding connective tissue. In particular, we are interested in the calculation of the mechanical energy

$$\Pi(a) = \frac{1}{2} \int_{x=0}^{\infty} EJ (w''(x))^2 dx + \int_{x=0}^{\infty} f(x, w) dx, \quad (3.13)$$

where $F(x, w) = -\partial f/\partial w$ and in $G = -\partial\Pi/\partial a$. For a given value of G_c , (3.13) enables us to use (3.2) to determine if a tear of length a can propagate.

We now use this simple beam model to explore the type of phenomena we obtained from the numerical experiments. To simulate the boundary condition, we set $F(x, w) = p$, a constant. Solving the ordinary differential beam equation (3.12) gives

$$w(x) = \begin{cases} \frac{p}{24EJ} (x^4 - 4a^3x + 3a^4), & x < a \\ 0, & x > a \end{cases} \quad (3.14)$$

and, therefore, by substituting into (3.13), we find that

$$\Pi(a) = -p^2 a^5 / 40EJ. \quad (3.15)$$

The energy release rate is

$$G = -\frac{d\Pi}{da} = \frac{p^2 a^4}{8EJ}. \quad (3.16)$$

G is a monotonically increasing function of a and p , therefore either an increase in the length of the unbonded region (the tear), or the pressure, results in propagation of the tear being energetically favourable.

To consider the effect of surrounding connective tissues, we set $F(x, w) = p - kw$, where the constant k is the stiffness per unit length of the springs, as shown in Figure 3.14. Consequently, $f = -pw + kw^2/2$, and the solution for $w(x)$ is

$$w(x) = \frac{p}{k} + W(x), \quad (3.17)$$

where $W(x)$ satisfies

$$W'''' + 4\lambda^4 W(x) = 0, \quad \lambda^4 = k/4EJ. \quad (3.18)$$

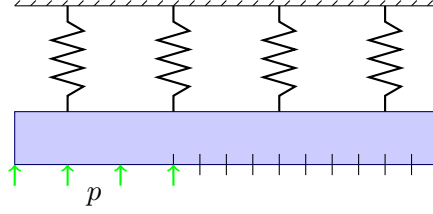


Figure 3.14: The effect of connective tissue using the beam model. The *semi-infinite* beam, of constant Young's modulus E and second moment of area J , is bonded to a surface except for a region $0 < x < a$ that represents the tear. The spring bed represents the surrounding connective tissues.

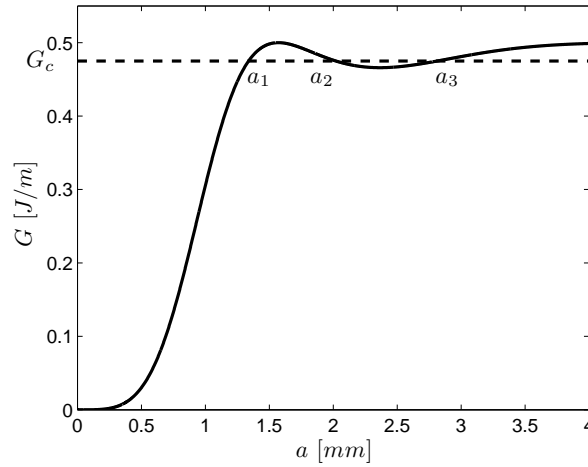


Figure 3.15: Tear arrest is also demonstrated by the beam model when the connective tissue is present. The ERR G is no longer a monotonic function of a , and for a given critical value G_c , a tear of length a where $a_1 < a < a_2$ or $a > a_3$ will propagate. However, the tear arrests when $a_2 < a < a_3$. Notice that the range of a is selected to show that the tear arrest is possible. The values of a_1 , a_2 , and a_3 will change depending on the value of G_c , as well as the stiffness of the connective tissue blocks.

This is solved to give

$$\begin{aligned}
 W(x) = & e^{-\lambda x} [A \cos(\lambda x) + B \sin(\lambda x)] \\
 & + e^{\lambda x} [C \cos(\lambda x) + D \sin(\lambda x)], \tag{3.19}
 \end{aligned}$$

with A , B , C and D chosen to satisfy the boundary conditions. Non-dimensionalising the deflection with p/k and x with $1/\lambda$, i.e. $y = w/(p/k)$ and $s = x\lambda$, leads to the canonical

problem

$$\frac{d^4 y}{ds^4} = 4 - 4y, \quad (3.20)$$

with boundary conditions $y''(0) = y'''(0) = 0$ and $y(\gamma) = y'(\gamma) = 0$ where $\gamma = a/l$. The solution to this problem is

$$\begin{aligned} y(s) = & 1 + [(\sin s \cosh s + \cos s \sinh s) (\cos \gamma \sinh \gamma - \sin \gamma \cosh \gamma) \\ & - 2 \cos s \cosh s \cos \gamma \cosh \gamma] / [\cos^2 \gamma + \cosh^2 \gamma]. \end{aligned} \quad (3.21)$$

The mechanical energy is

$$\Pi = \left(\frac{p}{k}\right)^2 EJ \frac{l}{l^4} \int_0^\gamma \frac{1}{2} (y''(s))^2 ds + \frac{1}{2} k \left(\frac{p}{k}\right)^2 l \int_0^\gamma y(s)^2 ds - \frac{p^2}{k} l \int_0^\gamma y(s) ds. \quad (3.22)$$

This expression simplifies to

$$\Pi = \frac{p^2 l}{k} \left[\int_0^\gamma \frac{1}{8} (y''(s)^2 + 4y(s)^2) - y(s) ds \right], \quad (3.23)$$

and then we get the ERR

$$G = -\frac{\partial \Pi}{\partial a} = -\frac{p^2}{k} \left\{ \frac{1}{8} [y''(\gamma)^2 + 4y(\gamma)^2] - y(\gamma) \right\}. \quad (3.24)$$

We display the curve of $G(a)$ for a set of typical parameters in Figure 3.15. When subject to a constant pressure, $G(a)$ is not a monotonically increasing function of a , and propagation arrest occurs. Comparison this result with (3.16), we observed that the arrest of tear propagation occurs in the beam model when we consider the constraint of connective tissues. That is qualitatively similar to what is shown in Figure 3.12 for a strip of fibre-reinforced tissues subject to finite strain. We remark that since the two models, the simple beam model and the 2D strip model, are very different in terms of the material and boundary conditions, one used the linear elastic material, and the other used the HGO model, it is not worthwhile to compare the results of the two models quantitatively, since either model is tuned to give physiological values. The purpose of the beam model is to demonstrate that a tear arrest is possible when the connective tissue is considered, which supports the observation of the 2D strip model.

3.5 Discussion

In this chapter, we have developed models to evaluate the likelihood of tear propagation in soft tissue with the failure criterion expressed in terms of the ERR. Models which build on

energy balance apply equally well both to linearly elastic isotropic problems and to finite strain and anisotropic problems, thus providing useful physical insight in the absence of detailed experimental data. By assuming the tear propagation to be an isothermal process, we have explored if a pre-existing dissection can propagate in artery wall under a penetrating pressure, which means the pressure is immediately applied on the new created tear surface during tear propagation. The pressure penetration is the simplest approach to model this fluid-driven tear propagation in the arterial dissection. Such an approach can be used to evaluate the risk of propagation of aortic dissection and other injuries of soft tissue.

A key element of the energy approach is to evaluate the change in the energy budget with the tear size, which is non-trivial for finite strain and fibre-reinforced soft tissue problems. Using a nearly incompressible HGO orthotropic constitutive law, in conjunction with a penalty method, we have developed a computational framework, that allows us to calculate the ERR for incompressible soft tissues. In particular, the ERR due to the tear extension is estimated by incorporating an interpolation technique on $\Pi(a)$ for the sake of computing efficiency.

Qualitative verification of the computational models has been carried out. This includes testing the models for simple scenarios (material and loading parameters) in which analytical solutions are available. In addition, we find that the ERR from the computational models has qualitatively the same trend as the ERR predictions from a beam model (Section 3.4) for the isotropic material.

Although the exact failure threshold depends on the tissue properties, the energy behaviour of such materials due to a pre-existing tear is clearly demonstrated through the contours of the ERR in the tear-length and pressure space, (a, p) . For both isotropic and fibre-reinforced materials with different fibre orientations, we use numerical experiments to show that the risk of tear propagation increases with both a and p . Interestingly, the particular fibre structure changes the gradient of the ERR curve, with non-fibrous (isotropic) material producing the steepest increase (Exp. 1), followed by the cases when the fibres are aligned normal (Exp. 2) and oblique (Exp. 3) to the tear. The case when the fibres are aligned parallel to the tear is the least steep (Exp. 4). This shows that the presence of fibres reduces the risk of tear propagation, and that the orientation of the fibres plays an important role, too. This effect may be more pronounced in physiological scenarios since the fibre-matrix interaction is represented simply in our models.

Our study shows that for a given pressure, the ERR increases monotonically with the tear length. In other words, once the tear is initiated, it will always grow. However, when the effect of connective tissues are considered, both computational and beam models predict tear arrest. Namely, at some critical values of a , the ERR decreases with the increase of a . Tear arrest is observed clinically, since patients that with aortic dissection that have arrested are then at the risk of further propagation of the dissection. This is the first time that tear arrest in soft tissues has been demonstrated in the computational models. We also find that the tear arrest only occurs when the Young's modulus of the surrounding connective tissue is sufficiently great, suggesting that disease-induced softening of the connective tissues may lead to further tear propagation. Although our study is only qualitative and is not based on physiological geometries, this finding nevertheless enhances our understanding of the relationship between pathological conditions of the connective tissues and arterial dissection.

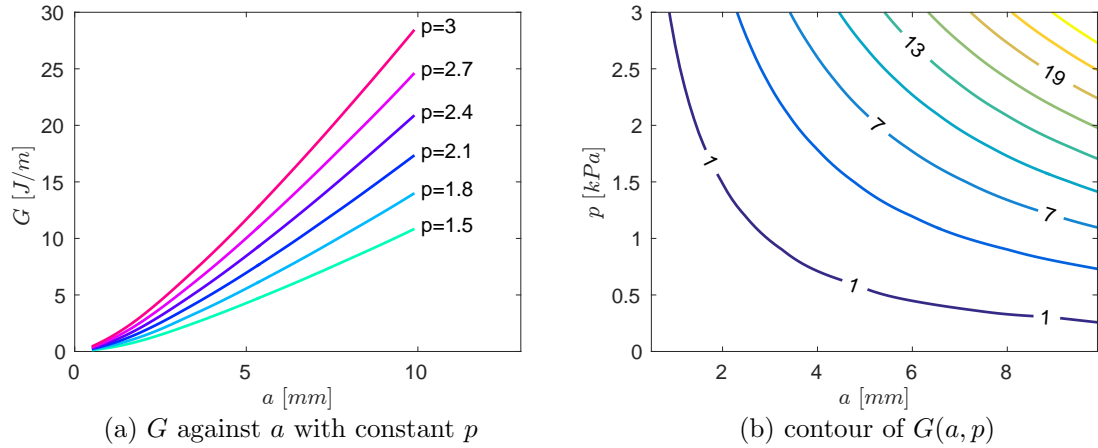


Figure 3.16: The energy release rate G against tear length a with a greater $p = 3$ kPa for strips in Exp. 4. G is an increasing function of a or p . The trend of G is the same as for smaller values of pressure used in Figures 3.5 and 3.10.

Finally, we would like to mention the limitations of this study. Using these two-dimensional strips we can not use the physiological pressure loading, $p = 13.33$ kPa for this carotid artery. As shown in Figure 3.8, subject to $p = 0.6$ kPa the width of tear opening has been significantly big in the Exp. 1 for this isotropic strip, more than twice of width of strip. Using a larger value of pressure, the computation might fail due to the extreme distortion of elements around the tear tips. Although the fibre-reinforced strips in Exp. 4 can take on more pressure loading than strips in other experiments, we used

$p = 0.6$ kPa in all experiments for the sake of comparison. In addition, we used a higher pressure $p = 3$ kPa in Exp. 4, and found that the trend of G on a and p as shown in Figure 3.16, which is our focus, is the same with what we obtained with smaller pressure $p = 0.6$ kPa. This good agreement shows that the trend of $G(a, p)$ is reliable even if the value of pressure is small in our examples. To use the physiological pressure, one has to first develop a realistic three dimensional artery model with fibre reinforced materials and consider other loading conditions, e.g. the residual stress and the axial pre-stretch. However, these three dimensional models are computational expensive, and hence we have used an alternative approach, that is to explore the important factors driving the tear propagation using simpler models.

To establish basic concepts without going into complex numerical modelling, we consider two-dimensional homogeneous tissue strips in which the tear can only propagate along its original direction since the geometry, material and load are symmetric. However, the direction of propagation is not known a priori in a problem with general geometry and material. In theory, the tear will propagate along the direction, along which the energy release rate is the greatest. To consider that by using the current computational model, we have to introduce the extension of tear in all of directions, solve for the equilibrium and compute the energy release rate for the extension along each direction. The implementation of such model is time-consuming, since the mesh has to be matched with the tear, e.g. see Figure 2.4(a). In contrast, the mesh generation is independent of tear within the XFEM, e.g. see Figure 2.4(b). Therefore, the XFEM is employed in the next chapter.

3.6 Conclusion

We have developed computational models for predicting the onset of tear propagation in two-dimensional artery models. These models extend the Griffith energy balance principle in linear elasticity to fibre-reinforced materials with finite deformation, and are verified using analytical solutions for simpler cases. The results show that the presence of fibres will in general slow down the ERR for driving tear propagation due to an existing tear, and that the fibres aligned parallel to the tear decrease the ERR most. However, the existence of the fibres alone cannot stop the growth of tears in our models. Tear arrest occurs only when the surrounding connective tissues with sufficient stiffness, are included.

Chapter 4

Models of peeling- and pressure-driven tear propagation

This chapter describes a computational model to predict tear propagation in an arterial wall by using the XFEM with a cohesive traction-separation law. Anisotropic hyperelasticity of the arterial wall is assumed and we use the HGO material model. The damage evolution is governed by a linear cohesive traction-separation law. We have studied tear propagation in peeling- and pressure-driven experiments using our computational models. We consider two types of experiment. In the first, which we call *peeling-driven* propagation, we use displacement boundary conditions to control the propagation of the tear. Both two-dimensional strips (Figure 4.2) and three-dimensional circular disc (Figure 4.4) with an initial tear are considered. From these models, we found that the collagen fibres play an important role in the direction of propagation. In the second, which we call *pressure-driven* propagation, we use pressure loading. The cross-section of an idealized two-layer model for a rabbit carotid artery is considered. An initial tear in the shape of a circular arc is introduced in the media (Figure 4.6). The circumferential length and radial depth of the initial tear are parametrised, we analyse the effect of length and depth on the critical pressure for tear propagation and the shape of the deformed arterial wall. The effect of depth on the critical pressure agrees with observations in an experimental study [Tam et al., 1998], the critical pressure decreases linearly as the depth increases (Figure 1.4). The shapes of the deformed arterial wall that we observe have also been observed in CT scans of patients. Results show that a long shallow tear tends to result in buckling of the inner wall, e.g. see Figure 4.13(a), and collapse of the lumen, e.g. see Figure 4.15(d),

while a deep tear tends to propagate.

4.1 Introduction

The peeling-driven propagation is a standard test in papers on the computational modelling of tear propagation. Gasser and Holzapfel [2006] developed an extended finite element model and Ferrara and Pandolfi [2010] used the conventional finite element method. Both of them use the HGO material model for the anisotropic hyperelasticity of the arterial wall and the cohesive traction-separation law for governing the evolution of tear propagation. The cohesive traction is an exponential isotropic function of separation in [Gasser and Holzapfel, 2006] but is a linear function with directional preference in [Ferrara and Pandolfi, 2010]. The directional preference of the cohesive law in [Ferrara and Pandolfi, 2010] is because of the presence of collagen fibres. Both of the computational models are used to simulate the peeling experiment of human aortic media, performed by Sommer et al. [2008]. See also [Wang et al., 2014] for peeling experiments of human coronary arteries.

Study of the pressure-driven tear propagation is considered in fewer papers. One experimental study is performed by Tam et al. [1998] on the pressure-driven tear propagation in the porcine aortic wall. In this study, it was predicted that the propagation pressure, beyond which the tear propagates, decreases linearly with the depth of the tear, where the depth is the radial distance of the initial tear from the inner radius of aorta (Figure 1.4). The AD during balloon angioplasty of atherosclerotic is modelled through Abaqus in [Badel et al., 2014] subject to an internal expansion, by applying the displacement boundary conditions, which simulates the balloon.

In this chapter, we simulate tear propagation subject to either peeling or pressure. We assume the arterial wall to be a fibre-reinforced hyperelastic incompressible material, and employ the HGO strain energy function. The tear initiation and propagation is governed by a linear traction-separation law. The computational method is the XFEM [Dolbow and Belytschko, 1999] implemented in Abaqus [Abaqus, 2014].

The simulations, of peeling-driven tear propagation in strips and discs of arterial wall sample, are used to study the direction of tear propagation. Both plane-strain and three-dimensional models are developed. The conclusions from these models agree each other: the tear prefers to propagate along the material axis with the maximum stiffness, deter-

mined by the fibre orientation. The simulations, of pressure-driven tear propagation in the cross-section of an idealized two-layer arterial wall, are employed to investigate the effects of tear circumferential length and radial depth on the critical pressure for tear propagation and shape of the deformed arterial wall. The results show that a shallow long tear tends to result in the buckling of inner wall, while a deep tear tends to propagate. Several shapes of deformed arterial wall from our simulations agree with the medical images of AD in patients.

This chapter is organized as follows. In Section 4.2, the common theoretical basis for the two studies are shown. Section 4.3 includes the models and results of studies on the peeling-driven tear propagation, while Section 4.4 presents the details of studies on the pressure-driven tear propagation. Finally, we summarize our findings in Section 4.5.

4.2 The computational model

4.2.1 Mechanical response

We assume the arterial wall to be a hyperelastic incompressible material, and employ the HGO constitutive law [Holzapfel et al., 2000]. However, in Abaqus the GOH material model [Gasser et al., 2006] is available. As we discussed in Section 1.4, the GOH model with $\kappa = 0$ is equivalent to the HGO model.

The implementation of the GOH material model in Abaqus is

$$\begin{aligned} \Psi &= \Psi_v(J) + \Psi_m(\bar{I}_1) + \Psi_f(\bar{E}_4, \bar{E}_6) \\ &= \frac{1}{Q} \left(\frac{J^2 - 1}{2} - \log J \right) + c(\bar{I}_1 - 3) + \frac{k_1}{2k_2} \sum_{n=4,6} \{ \exp[k_2 \langle \bar{E}_n \rangle^2] - 1 \}, \end{aligned} \quad (4.1)$$

where

$$\bar{E}_n = \kappa(\bar{I}_1 - 3) + (1 - 3\kappa)(\bar{I}_n - 1), \quad (4.2)$$

and Q is a parameter that is adjusted in order to satisfy, approximately, the incompressibility constraint. The parameters c and k_1 have units of shear modulus and k_2 is a dimensionless parameter that controls the exponential stiffening of the fibres, $\bar{I}_1 = \text{tr} \bar{\mathbf{C}}$ is the first invariant of the deviatoric part of the right Cauchy-Green tensor $\bar{\mathbf{C}} = J^{-2/3} \mathbf{C}$, and $\bar{I}_n = J^{-2/3} I_n$ are invariants related to $\bar{\mathbf{C}}$ and \mathbf{A}_i . We assume there are two fibre families aligned along the two referential directions represented by unit vectors \mathbf{A}_1 and \mathbf{A}_2 , respectively. The invariants

$$I_n = \mathbf{C} : \mathbf{M}_n, \quad n = 4, 6, \quad (4.3)$$

where the fibres-structure tensors $\mathbf{M}_4 = \mathbf{A}_1 \otimes \mathbf{A}_1$ and $\mathbf{M}_6 = \mathbf{A}_2 \otimes \mathbf{A}_2$, are the square of the stretches in the directions of \mathbf{A}_1 and \mathbf{A}_2 , respectively. Therefore, I_4 and I_6 quantify the deformation of fibres.

The first two terms in the strain energy function (4.1) represent the volumetric and deviatoric contributions of the isotropic matrix and the third term represents the contributions from the different families of collagen fibres. A basic assumption of the model is that collagen fibres can only support tension. This condition is enforced by the term $\langle \bar{E}_n \rangle$, where the operator $\langle \cdot \rangle$ stands for the Macauley bracket and is defined as $\langle x \rangle = \frac{1}{2}(|x| + x)$. Notably, with $\kappa = 0$, (4.2) reduces to

$$\bar{E}_n = \bar{I}_n - 1, \quad (4.4)$$

thus $\langle \bar{E}_n \rangle > 0$ is equivalent to $\bar{I}_n > 1$. Furthermore, note that $\bar{I}_n = I_n$ when the deformation is isochoric. As the parameter $Q \rightarrow 0$ theory predicts that the minimum energy configuration is one in which the $J = 1$ and so the limit represents the incompressibility. Therefore, the strain energy function (4.1) with $\kappa = 0$ and $Q \rightarrow 0$ approximates the HGO incompressible material model. As shown in Section 3.1.7 of Abaqus 6.13 Benchmarks Guide and Section 4.6.3 of Theory Guide [Abaqus, 2014], to use the HGO material model for an incompressible material, we specify $\kappa = 0$ and $Q = 0$ with using hybrid element in all of our simulations.

4.2.2 Damage and failure

We use a linear cohesive traction-separation law to govern the tear propagation. There are three parameters in the cohesive law: the maximum traction T_c the material can bear without any damage, the maximum separation or displacement jump Δu_c of cohesive surfaces with maintaining bonds and the fracture energy G_c . Two of them are independent as shown in the Figure 4.1(a).

The damage will be activated at any point where the maximum principal stress is greater than T_c , that is

$$1.0 \leq f \leq 1.0 + f_{tol}, \quad (4.5)$$

where

$$f = \frac{\langle \sigma_1 \rangle}{T_c}, \quad (4.6)$$

and f_{tol} is a tolerance. σ_1 is the maximum principal stress, which is the first eigenvalue of

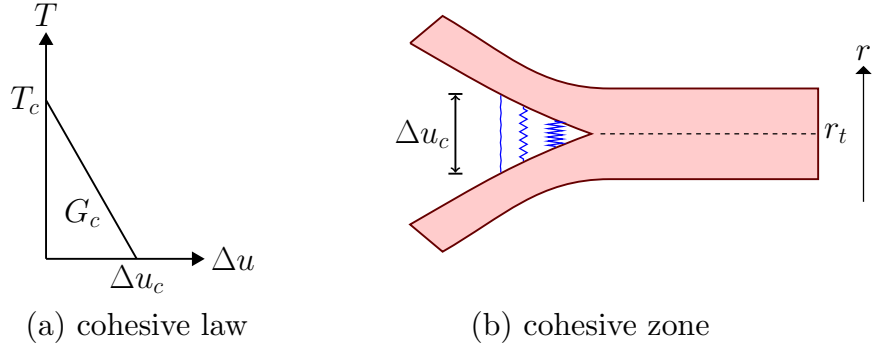


Figure 4.1: T is the traction between cohesive surfaces, Δu is the separation of cohesive surfaces. T_c , Δu_c and G_c are material-dependent parameters; (b) demonstrates that a cohesive zone, where separation $\leq \Delta u_c$; r denotes the radial direction consistent with Figure 4.2, and r_t indicate the tear surface in the reference configuration.

the Cauchy stress tensor $\boldsymbol{\sigma}$. Notably,

$$\langle \sigma_1 \rangle = \begin{cases} 0, & \text{if } \sigma_1 < 0 \\ \sigma_1, & \text{if } \sigma_1 \geq 0. \end{cases} \quad (4.7)$$

The Macaulay bracket is used to signify that a purely compressive stress state does not initiate damage.

Once the damage is activated at a material point when the initial criterion (4.5) is satisfied. The cohesive traction-separation law in Figure 4.1(a), instead of HGO material model, will be used on that point. Analogous to the stress-strain relation for elasticity, the cohesive law relates the traction T and separation Δu such that

$$T = \begin{cases} T_c \left(1 - \frac{\Delta u}{\Delta u_c}\right), & 0 \leq \Delta u \leq \Delta u_c \\ 0, & \Delta u > \Delta u_c, \end{cases} \quad (4.8)$$

where T_c and Δu_c are material parameters. Generally, the fracture energy G_c instead of critical separation Δu_c is specified in a computational model. In the linear traction-separation law

$$G_c = \frac{1}{2} T_c \Delta u_c. \quad (4.9)$$

4.2.3 Extended finite element method

The initiation and propagation of a tear is implemented under the theory of XFEM [Dolbow and Belytschko, 1999]. Comparing the conventional FEM, the displacement in XFEM

can include the discontinuities, such as tears, in the displacement through enriching the displacement field

$$u = u_{\text{fem}} + u_{\text{enrich}}, \quad (4.10)$$

where $u_{\text{enrich}} = H(r)\Delta u/2$. The function $H(r) = \pm 1$ when $r \gtrless r_t$, where r_t is the location of the tear surface in the configuration before the initialization of damage, for the example in Figure 4.1. The advantage of XFEM is that the tear surface does not need to coincide with the interfaces between elements. So the path of tear propagation can be automatically calculated based on the criterion (4.5) and the cohesive traction-separation law (4.8). With this maximum principal stress failure criterion, the direction of propagation is determined as normal to the principal axis of σ_1 .

4.3 Peeling-driven propagation

4.3.1 Tear propagation in strips

Geometry and boundary conditions

The peeling test performed in [Sommer et al., 2008] is a representative experimental study to characterise the failure properties of a material (in this case an arterial wall). In this experiment, a strip is cut out from the arterial wall and then the media layer is isolated by removing the adventitia and intima. An initial tear is introduced at one end of the middle radial plane. Subject to the displacement boundary condition (Figure 4.2), we solve this as a two-dimensional plane strain problem.

The two families of fibres are distributed in the θ - z plane and with 5° to the z -axis direction [Ferrara and Pandolfi, 2010]. The values for other parameters in the SEF (4.1) and cohesive law (4.8) are shown in Table 4.1. The geometry of the strip is same with that in [Ferrara and Pandolfi, 2010; Gasser and Holzapfel, 2006; Sommer et al., 2008]: its width is 4 mm and its height is 1.2 mm. The height is actually the radial *thickness* of arterial wall. The length of the initial tear (red dash in Figure 4.2) is 0.4 mm.

The Strip 1 is totally torn when the displacement is $u = 3.28$ mm and the other two strips can still take on loads until $u = 4$ mm. Thus we conclude that the tear is likely to propagate along the z -axis direction. The length of undamaged part of Strip 3 is the longest in the three simulations. Thus the circumferential strip (Strip 3) has the most resistance to the tear propagation.

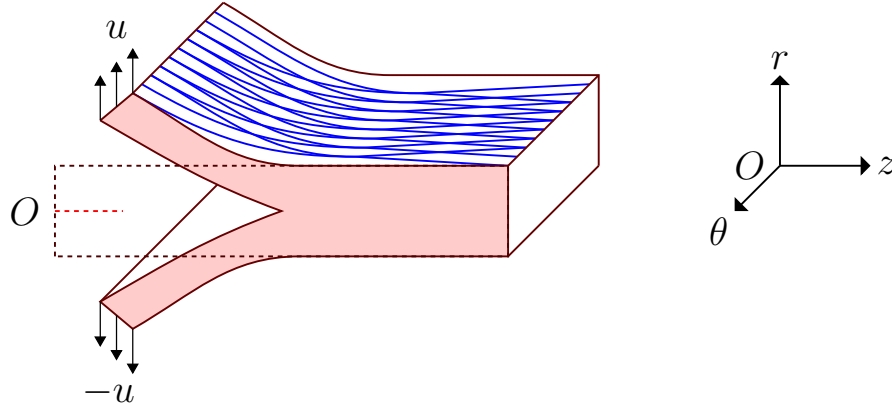


Figure 4.2: The sketch of the strip used in the peeling test [Sommer et al., 2008], the cross-section (pink-shading area) of which is the geometry we are using. Blue lines show the fibre distribution. Displacement boundary conditions with same magnitude u but opposite directions are applied on the two arms.

What results in this preference in direction of propagation? The orientation of collagen-fibre is 5° to the z -axis direction (Figure 4.3), therefore the stiffness along the z -axis is maximum. The results (Figure 4.3) show that the likely direction of propagation is also the z -axis, since Strip 1 is totally torn. Therefore, from these simulations it might be concluded that the tear prefers to propagate along the material axis with the maximum stiffness.

Table 4.1: The material parameters of the HGO SEF and cohesive traction-separation law for the samples used in simulations of the peeling test.

c [kPa]	k_1 [kPa]	k_2	T_c [kPa]	G_c [N/m]
1	1	10	5	0.001

Results

In order to find where the tear prefers to propagate, three strips with different orientations are simulated and their deformed configurations after tear propagation are shown in Figure 4.3.

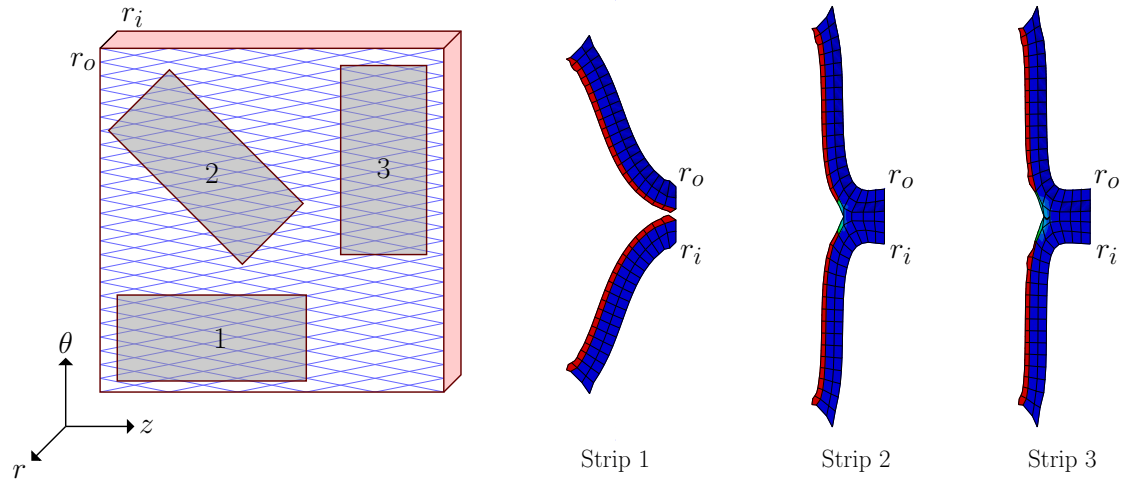


Figure 4.3: The failure status of three strips: red indicates the elements are torn, blue for elements without any damage and other colours for cohesive zone. In the deformed configuration, each strip has length 4 mm, width 1.2 mm and an initial tear of length 0.4 mm. The Strip 1 is totally torn when the displacement is $u = 3.28$ mm and the other two strips can still take on loads until $u = 4$ mm. The length of undamaged strip in Strip 3 is greater than that in Strip 2.

4.3.2 Tear propagation in discs

Geometry and boundary conditions

To further confirm our findings on the directional preference of tear propagation, we performed another simulation of the peeling of a circular disc. The disc is cut off from the same sample of arterial wall (Figure 4.4), which is used for the selection of strips in Figure 4.3.

The geometry of this disc is consistent with that of the strips. The radius is 4 mm and thickness is 1.2 mm. An initial tear with depth 0.4 mm along the radial direction is introduced. Therefore, all three of two-dimensional strips are included in this model, the cross-section at the black lines of Figure 4.4. This three-dimensional model includes strips with all of possible orientations.

The boundary conditions are also consistent with those in the simulation of peeling strips. The center of top and bottom circles are fixed to avoid the rigid body motion. The displacement ± 4 mm is gradually applied on the surrounding surfaces (pink areas in Figure 4.4).

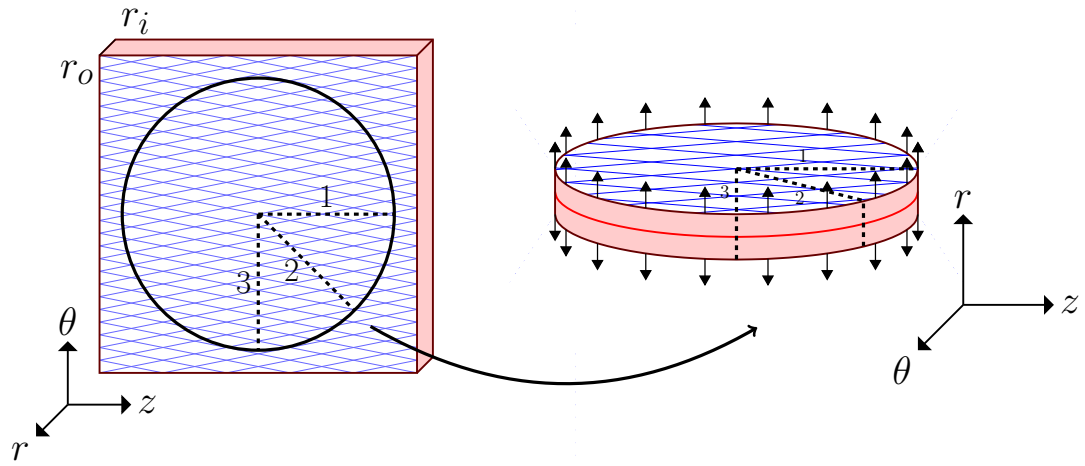


Figure 4.4: A circular disc is cut off from the same sample used for the selection of strips in the previous section. The radius of this disc is 4 mm, which is the same with the length of strips, and its thickness is 1.2 mm, which is the same with the width of strips in Figure 4.3. A circular tear (red lines) is initialized at the circumference of disc and the depth of the tear is 0.4 mm towards the center, which is the same with that in the simulations for strips. Apply displacement boundary condition (black arrows) on the upper and lower surrounding surfaces (pink areas). In the control simulation, the disc does not include fibres.

Results

The peeling of a disc with and without fibres are simulated. Subject to the displacement boundary conditions applied on the surrounding surfaces (pink areas in Figure 4.4), the undamaged fibrous disc becomes elliptical (Figure 4.5(b)). The short axis of the ellipse is the z -axis direction. That means the tear prefers to propagate along the z -axis direction. This phenomenon agrees with what we find from the simulations of peeling strips. On the other hand, the undamaged fibre-free disc is still a circular (Figure 4.5(a)). This comparison confirms that the directional preference of tear propagation is due to the orientation of collagen fibres.

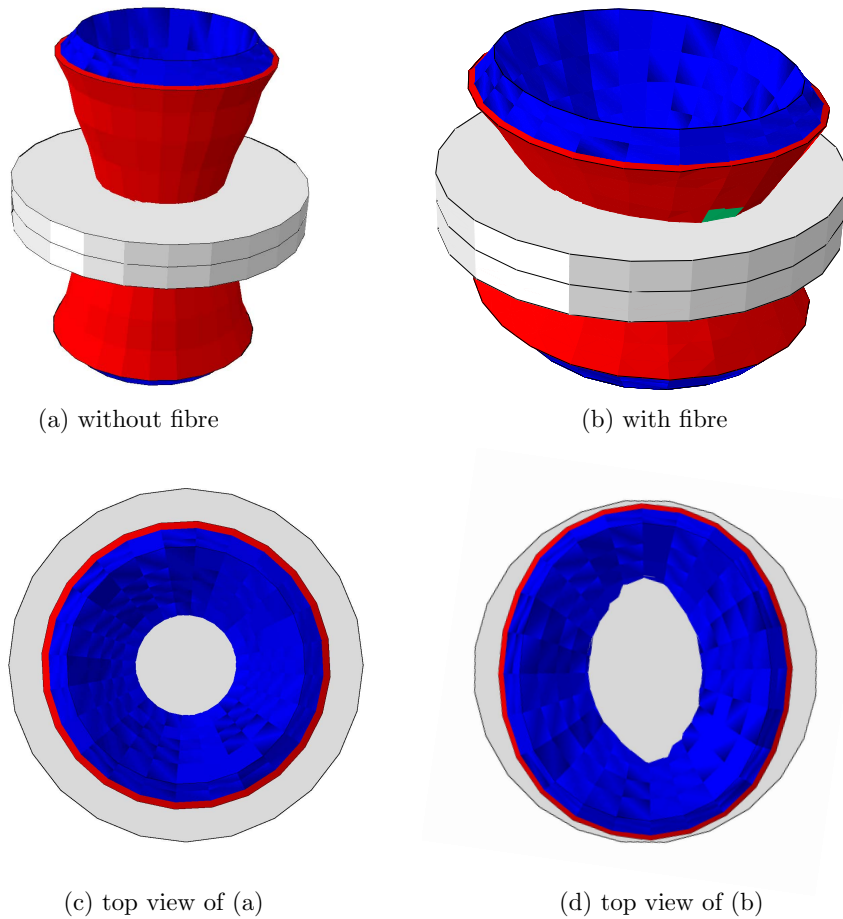


Figure 4.5: The grey regions are the undeformed configurations while the coloured ones show the deformed configurations after tear propagation. From the top view, it is clear that the undamaged fibrous disc becomes elliptical, while the undamaged fibre-free disc is still circular. The short axis of the ellipse is the z -axis.

4.4 Pressure-driven propagation

4.4.1 Geometry and boundary conditions

The length and depth of a tear are very important factors when diagnosing arterial dissections. In this section we investigate the effects of length and depth of a tear on its propagation.

In clinical cases, the length and depth of a tear are generally extracted from the images, for example a CT scan, about the cross-section of the arterial wall. Similar to the CT images of an arterial wall, we consider the propagation of an arterial dissection in a cross-section of the arterial wall (Figure 4.6) as a plane-strain problem. An idealized tear, the shape of an arc, is introduced in the media. The circumferential length of the initial tear is quantified by the central angle η . Assume the initial tear is only located in the media and its radial depth from the inner surface is normalized by the thickness of media as $d = D/D_m$, where D and D_m are denoted in Figure 4.6. If $d = 0$, this means the initial tear is on the inner surface and if $d = 1$, this means the tear is on the interface between media and adventitia. The different values for $0^\circ < \eta < 360^\circ$ and $0 < d < 1$ are employed in individual simulation of pressure-driven tear propagation. We compare the results to observe the effects of length and depth of a tear. The results include the critical pressure, beyond which the tear propagates, and the shape of deformed arterial wall with a tear subject to the critical pressure.

Some boundary conditions are applied to avoid rigid body motion. The radii 1 and 3 (Figure 4.6) are fixed at the y -axis direction such that both of them can only have the horizontal movement. The radii 2 and 4 are fixed at the x -axis direction such that both of them can only have the vertical movement.

We assume the pressure p is the same both in the lumen and on two faces of the tear and solve a quasi-static problem. In our simulations the pressure is ramped from zero, this means that initially the boundary value problem is solved with $p = 0$, the value of p is then increased by some increment, Δp , and the problem solved again. The value of Δp is determined by the program automatically, such that Δp is large enough and a convergent solution is obtained. The pressure is increased in this way until the tear begins to propagate, after which $\Delta p \rightarrow 0$.

At the onset of propagation the pressure is recorded and is called the *critical pressure* p_c . The value of p_c for a particular arterial dissection depends on the material parameters,

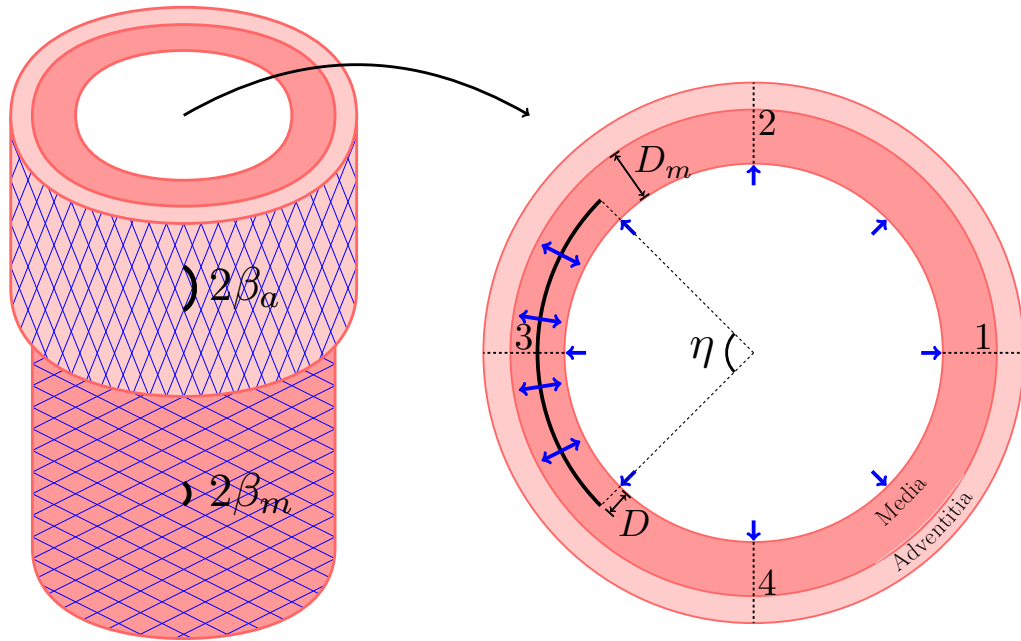


Figure 4.6: The cross-section of the two-layer model for a rabbit carotid arterial wall is considered with the plane-strain condition. This model has inner radius $R_i=0.74$ mm, thickness of media $D_m=0.26$ mm and thickness of adventitia $D_a=0.12$ mm. The inflation of lumen and the initial tear (black arc) in the media subject to pressure (blue arrows) is simulated. The circumferential length of the tear is characterised by the central angle η . The radial depth of tear D is normalized by the thickness of the media D_m to get the dimensionless depth $d = D/D_m$.

the geometry of the artery and the geometry of the tear. In particular, the maximum cohesive traction T_c plays an important role. The value of T_c is not easy to be estimated for a given tissue, Ferrara and Pandolfi [2010] used $T_c \approx 8.6 c$, where c is the shear modulus of matrix in (4.1), when modelling the peeling apart of strips using the standard FEM with cohesive surfaces. We found that simulations in Abaqus did not converge unless $T_c \leq 2c_m$, where c_m is the shear modulus of the matrix in the media, see Table 4.2. This ratio of T_c/c_m is lower than that achieved in the literature [Ferrara and Pandolfi, 2010], but the aim of the present study is to identify the trend in the variation of the critical pressure with d and η , and so we simply use the value of $T_c/c_m = 2$. For the purposes of reporting results, the critical pressure p_c we find from the simulation is also scaled by the shear modulus c_m to form a *dimensionless critical pressure*

$$p'_c = p_c/c_m. \quad (4.11)$$

As discussed in Section 1.1, the carotid artery is a common site of occurrence of arterial dissection. In this study, for the sake of illustration we use the two-layer arterial wall model, which originally is used for a rabbit carotid artery to propose the HGO SEF [Holzapfel et al., 2000]. Each layer is modelled by the SEF (4.1) and the material parameters are shown in Table 4.2. The geometric parameters are inner radius $R_i=0.74$ mm, thickness of the media $D_m=0.26$ mm and adventitia $D_a=0.12$ mm.

Table 4.2: The material parameters in the two-layer model for a rabbit carotid artery: the values for the parameters in HGO SEF (c , k_1 , k_2 and β) are from the Figure 14 in [Holzapfel et al., 2000].

	c [kPa]	k_1 [kPa]	k_2	β [°]	T_c [kPa]	G_c [N/m]
media	1.5	2.3632	0.8393	29	3.0	0.001
adventitia	0.15	0.5620	0.7112	62	0.3	0.0001

4.4.2 Simulations and Results

Verification

As a verification, we compare the deformation and the Cauchy stress computed in Abaqus with the analytical solutions for the two-layer arterial wall (without a tear) subject to

Table 4.3: Meshes used for the grid-independence test

Mesh	Nodes	Elements				Relative error in stress computed via (4.15)
		media	adventitia	circumference	total	
coarse	864	5	2	108	756	15.43%
intermediate	3740	11	5	220	3520	4.83%
fine	15260	23	11	436	14824	4.03%

internal pressure $p_i = 13.33$ kPa (corresponding to 100 mmHg). The analytical solutions are obtained using the HGO SEF with incompressibility:

$$\Psi = \Psi_m(I_1) + \Psi_f(I_4, I_6) = c(I_1 - 3) + \sum_{n=4,6} \psi(I_n), \quad (4.12)$$

where

$$\psi(I_n) = \begin{cases} \frac{k_1}{2k_2} \{ \exp [k_2(I_n - 1)^2] - 1 \} & \text{when } I_n > 1 \\ 0 & \text{when } I_n \leq 1. \end{cases} \quad (4.13)$$

The associated Cauchy stress is

$$\boldsymbol{\sigma} = -\mathcal{P}\mathbf{I} + 2c\mathbf{B} + \sum_{n=4,6} 2\psi'(I_n)\mathbf{m}_n, \quad (4.14)$$

where $\mathbf{B} = \mathbf{F}\mathbf{F}^T$, $\mathbf{m}_n = \mathbf{F}\mathbf{M}_n\mathbf{F}^T$, and \mathcal{P} is the Lagrange multiplier for the incompressibility constraint. The value of \mathcal{P} is determined through the equilibrium equation and the boundary conditions in any particular problem. The details of the method and formulae for the analytical solutions are included in Section 5.3. Solve this boundary value problem for inflation of the artery to obtain the value of inner radius r_i in the deformed configuration, and then the radius of each point across the wall is obtained from the incompressibility as

$$r = \sqrt{R^2 - R_i^2 + r_i^2},$$

where R is the radius of a point inside and R_i is the inner radius of the undeformed arterial wall. The deformation gradient of each point across the arterial wall is then computed as $\mathbf{F} = \text{diag}[\lambda_r, \lambda_\theta, 1]$, where

$$\lambda_r = \frac{R}{r} \text{ and } \lambda_\theta = \frac{r}{R}.$$

Finally, we compute the analytical stress through (4.14).

In the numerical calculations we use a number of different mesh sizes, the details of which are shown in Table 4.3. The coarse mesh is illustrated in Figure 4.7. When using the intermediate mesh, we obtain the inner radius $r_i^n = 1.332$ mm, which is similar to the value $r_i^a = 1.326$ mm from the analytical solution with a relative error of about 0.45%. In addition, a comparison between analytical and numerical values of components of the Cauchy stress shows convergence and agreement of the numerical solutions to analytical solutions within the maximum relative error of 4.83%, as shown in Figure 4.8. This *maximum relative error* is computed by

$$\max \left\{ \frac{\|\sigma_{rr} - \sigma_{rr}^a\|}{\|\sigma_{rr}^a\|}, \frac{\|\sigma_{\theta\theta} - \sigma_{\theta\theta}^a\|}{\|\sigma_{\theta\theta}^a\|} \right\}, \quad (4.15)$$

where σ_{rr}^a and $\sigma_{\theta\theta}^a$ are the vectors of all the nodal values of the exact analytical expression for the two components of the residual stress across the wall, and $\|\cdot\|$ denotes standard L^2 -norm, i.e. $\|\mathbf{x}\| = \left(\sum_i x_i^2\right)^{1/2}$ for any vector \mathbf{x} . The intermediate mesh was then chosen in all the simulations.

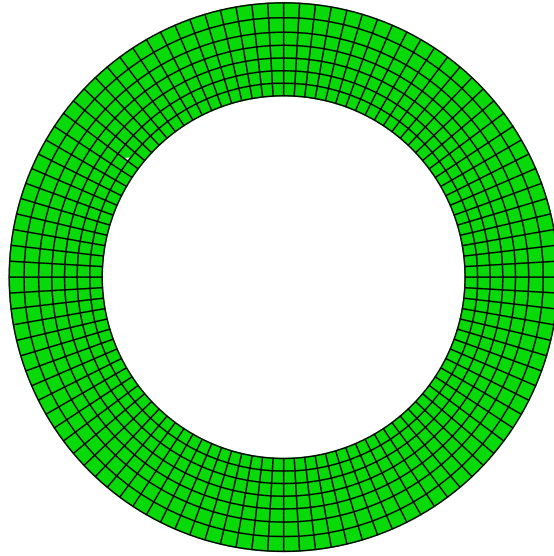


Figure 4.7: The coarse mesh we use in the numerical computations includes 7 elements along the radial direction (5 in media and 2 in adventitia) and 27 elements along the circumferential direction in a quarter of the arterial wall.

Selection of values for d and η

Recall that the tear length is measured by the angle the tear subtends, η , and the tear depth is measured by the normalised depth d , as shown in Figure 4.6. Then, as the tear

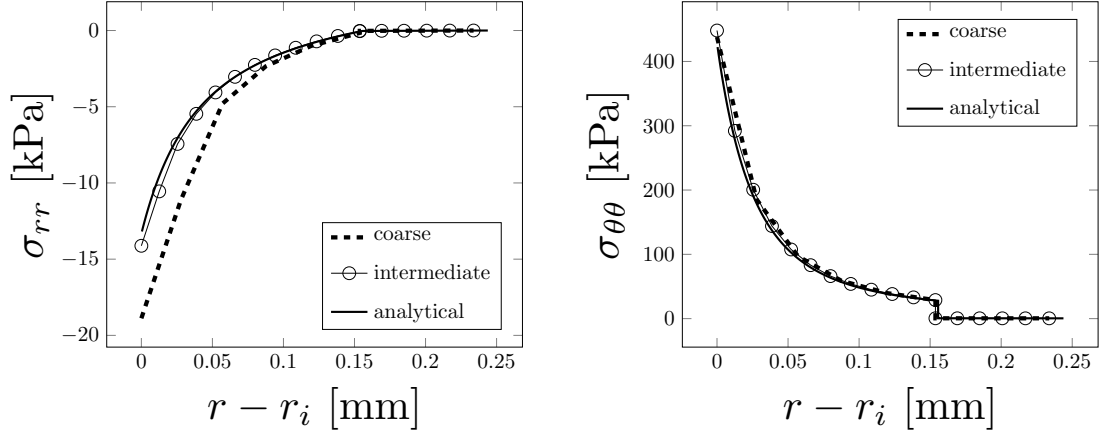


Figure 4.8: The Cauchy stress components of the arterial wall subject to $p_i = 13.33$ kPa are plotted against the radial distance $r - r_i$ from the inner surface in the deformed configuration. Numerical results with different mesh sizes and analytical results are plotted, and the relative error of numerical results with the intermediate mesh is less than 4.83%.

depth measures the depth within the medial layer and we only consider tears within the medial layer we have $0 < d < 1$ and the angular extent of the tear is $0^\circ < \eta < 360^\circ$.

The values of d and η chosen for simulations are such that the initial tear always bisects an element. In the XFEM, the tear is expressed in terms of its relative distances to the nodes of finite elements [e.g. Mohammadi, 2008]. The computation of a relative distance involves subtraction between coordinates of a node and its projection on the tear. Recall that all these coordinates are floating-point numbers, they have finite accurate (significant) digits, so the numerical subtraction of two close number may lead to that the number of significant digits in the result is reduced unacceptably. In order to avoid this numerical error, the initial tear should not coincide with the interface between elements. In practice, the best place to specify an initial tear is the bisector of an element. The mesh used in these simulations includes 11 elements along the radial direction in the media. Therefore, we use 11 values for d , that is $d_k = (k + 0.5)\Delta d$, where $\Delta d = 1.0/11$ and $k = 0, \dots, 10$, such that the initial tear is located at the bisector of an element. For a fixed value of η , we have 11 simulations for these values of d . From these simulations we obtain the critical pressure p_c , and plot the trend of the dimensionless critical pressure p'_c on d .

For η , we use the increment $\Delta\eta = 20^\circ$ from 20° to 340° to investigate the effect of circumferential length or angle η . Additionally, a smaller increment $\Delta\eta = 5^\circ$ is used because we identify the trend of p'_c against d changes quickly when $\eta < 40^\circ$.

Effects of d and η on the dimensionless critical pressure p'_c

The trends of dimensionless critical pressure p'_c against the radial depth d for different values of $20^\circ \leq \eta < 180^\circ$ and $180^\circ < \eta \leq 340^\circ$ are plotted in Figures 4.9 and 4.10, respectively. The Figure 4.9 shows that p'_c firstly increases and then decreases as d increases when $\eta = 20^\circ$. As the angle η increases to 60° and greater, the trend of $p'_c(d)$ becomes monotonically decreasing.

In order to understand the change in trend of $p'_c(d)$, we perform more simulations in the region between $20^\circ < \eta < 40^\circ$ with a smaller increment between values of η . In these simulations, we use $\Delta\eta = 5^\circ$ from 5° to 40° . The trends $p'_c(d)$ obtained from these simulations are plotted in Figure 4.11. It shows that p'_c increases monotonically with d when $\eta = 5^\circ$, while p'_c almost decreases as d increases when $\eta = 40^\circ$. To compare the trends $p'_c(d)$ for other values of η in Figure 4.11, it is evident that the trend $p'_c(d)$ changes gradually from an increasing function to a decreasing function.

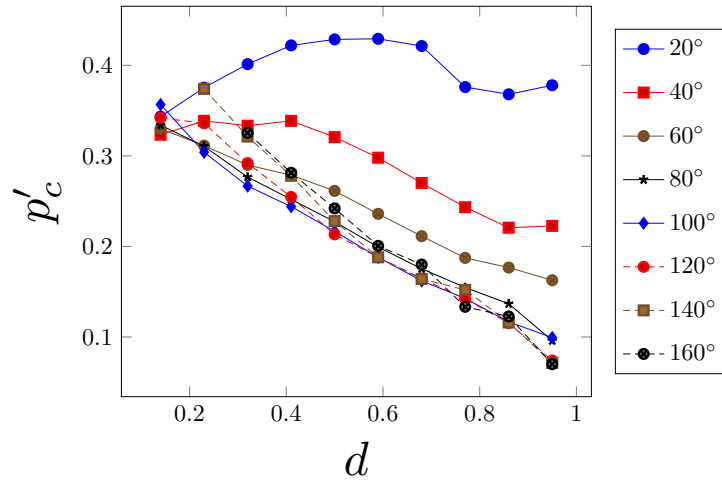


Figure 4.9: The dimensionless critical pressure p'_c is plotted against the radial depth d for different values of $20^\circ \leq \eta \leq 160^\circ$. When $\eta = 20^\circ$, p'_c increases and then decreases as d increases. The trend p'_c of d gradually becomes decreasing as η increases. For $\eta \geq 60^\circ$, p'_c decreases as d increases, and the trends $p'_c(d)$ are similar when $\eta \geq 80^\circ$.

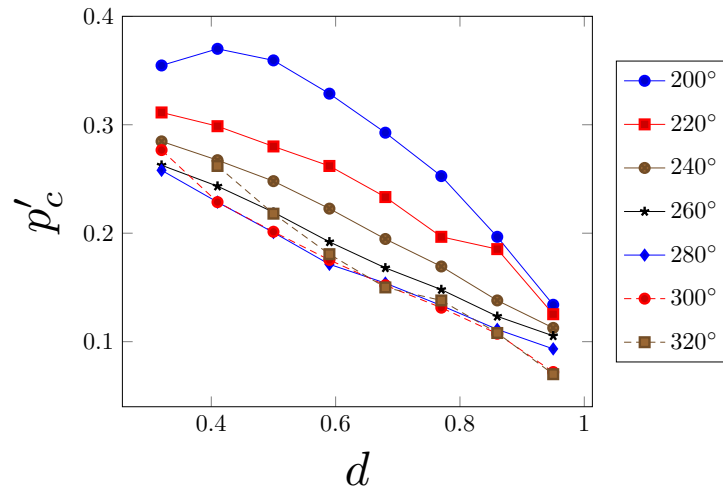


Figure 4.10: The dimensionless critical pressure p'_c is plotted against the radial depth d for different values of $200^\circ \leq \eta \leq 320^\circ$. p'_c decreases as d increases. p'_c is the maximum when $\eta = 200^\circ$. With a smaller depth $d \leq 0.32$ we do not have value for p'_c , because the buckling of inner wall occurred and the tear does not propagate, e.g. see Figure 4.15.

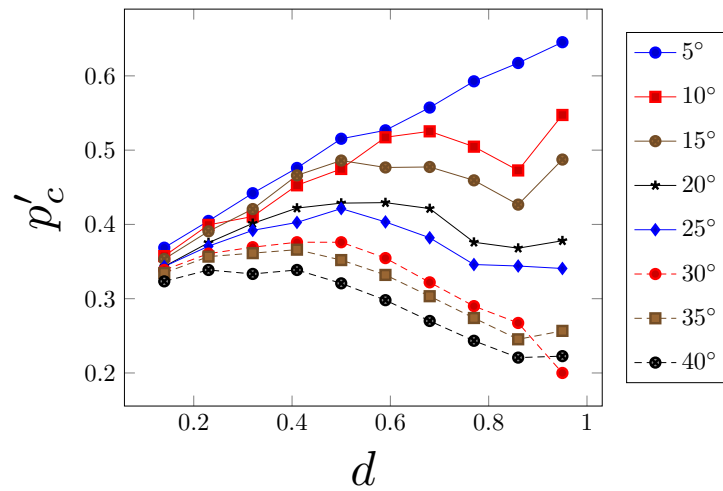


Figure 4.11: The dimensionless critical pressure p'_c is plotted against the radial depth d for different values of $5^\circ \leq \eta \leq 40^\circ$. When the tear is very short $\eta = 5^\circ$, the critical pressure increases with d . As η increases, p'_c increases and then decreases as d increases, for example when $\eta = 20^\circ$. These results show that the trend p'_c of d changes gradually from an increasing function to a decreasing function as η increases.

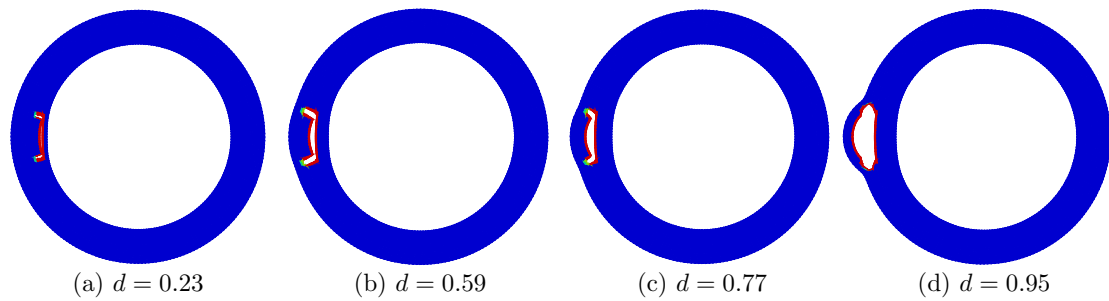


Figure 4.12: The representative shapes of deformed arterial wall with a short tear of $\eta = 20^\circ$ for different radial depth d , subject to the critical pressure. The direction of initial propagation changes gradually from the radial (a) to the circumferential (d) as d increases.

The dimensionless critical pressure p'_c for a fixed η increases firstly and then decreases as d increases when $10^\circ \leq \eta < 40^\circ$. This change may be related to the change in direction of tear propagation. For example, in Figure 4.12 we show the failure patterns of deformed arterial wall with a tear $\eta = 20^\circ$ subject to the critical pressure for different values of d . When $d = 0.23$ in Figure 4.12(a), it is evident that the tear propagates radially, but when $d = 0.95$ in Figure 4.12(d) it propagates circumferentially. When $d = 0.59$ and 0.77 , the direction of propagation is between the radial and the circumferential directions. The direction of propagation changes gradually from the radial to the circumferential with the increase in d for $\eta = 20^\circ$. In other simulations where the trends $p'(d)$ are also nonlinear, e.g. for $\eta = 10^\circ, 15^\circ$ and 25° , we have also observed this phenomenon in the failure patterns. Therefore, this nonlinear trend of $p'_c(d)$ for $10^\circ \leq \eta < 40^\circ$ may be due to this change in the direction of tear propagation.

Our results for $\eta > 60^\circ$ show that p'_c decreases almost linearly as the depth d increases. This conclusion agrees with the observation in the experimental study [Tam et al., 1998], although the geometry and material are different. The experiment [Tam et al., 1998] introduced an initial tear inside of the porcine aortic wall while varying the radial depth of the tear and then inflated this aorta with a gradually increasing pressure. At the instantaneous time of tear propagation, the pressure was regarded as the critical pressure. In [Tam et al., 1998], this critical pressure is called “propagation pressure”. The relationship showing that the critical pressure is a linearly decreasing function of the depth as shown in Figure 1.4, was reported in [Tam et al., 1998]. A detailed summary of this experimental study is also included in Section 1.2.

Effects of d and η on the deformed shapes

With angle $\eta = 160^\circ$, the buckling of the *inner wall*—the layer between the true and false lumen—occurs when d is small as shown in Figure 4.13(a)–(c). This buckling of the inner wall is also observed in CT scans of acute aortic dissections. For example, the buckling mode of the inner wall obtained from our simulation in Figure 4.13(a) is similar to that observed in the CT scan in Figure 4.14 (a) [Sun et al., 2014], and the buckling mode in Figure 4.13(b) is similar to that observed in the CT scan of a dissection in the ascending aorta in Figure 4.14 (b) [Braverman, 2010]. Of course, the geometry, loading and material of our computational models are different to those of the patients represented in the CT scans, and so these results are simply an acknowledgement that similar patterns

are observed in the clinical environment. Performing a detailed study is difficult in part due to the measurement of d from CT scans, since the inner wall is generally very thin.

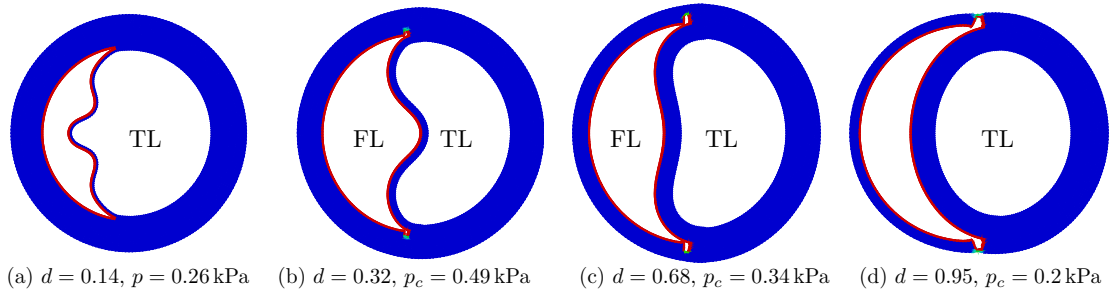


Figure 4.13: The representative shapes of deformed arterial wall with an initial tear $\eta = 160^\circ$ for different radial depth d . TL stands for true lumen and FL stands for false lumen. The buckling of the inner wall, the material between TL and FL, occurs, as shown in (a) and (b), which are similar to the CT scans of aortic dissection in patients in Figures 4.14 (a) and (b), respectively.

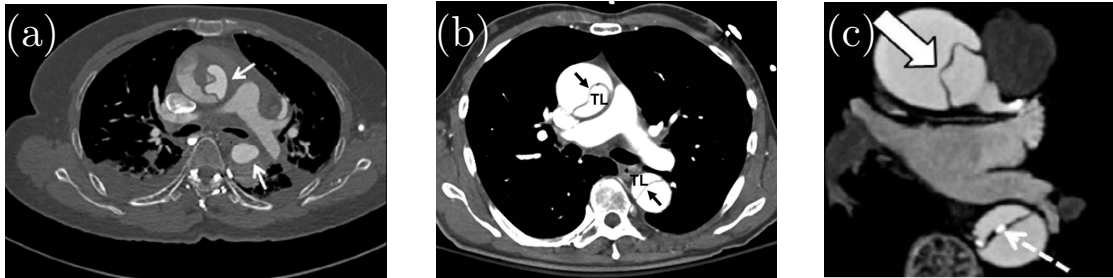


Figure 4.14: CT scans with buckling of the inner wall in type A aortic dissection: (a) Figure 9 in [Sun et al., 2014], (b) Figure 2 in [Braverman, 2010], and (c) Figure 2 in [Makarawate and Chaosuwannakit, 2013].

The comparison in deformed shapes of the arterial wall with a tear for different values of d suggests the radial depth of a tear plays an important role in the deformation. Comparison of the results in Figures 4.13 (a)–(d) shows that the buckling mode is the highest in (a), and this tear does not propagate. The buckling mode decreases as d increases from (a) to (c), and the buckling of the inner wall does not occur with a deeper tear in (d).

In addition, we plot the deformed shapes of the arterial wall with a longer tear $\eta = 340^\circ$ for different values of d in Figure 4.15. In these results, we also observed that the buckling mode of the inner wall with $d = 0.23$ in Figure 4.15(c) is similar to that in the CT scan of the aortic dissection in Figure 4.14 (c) [Makarawate and Chaosuwannakit, 2013]. Again,

this comparison is not one-to-one comparison, but just to show the buckling observed in our simulations exists in the aortic dissection. With $d = 0.32$ and 0.50 in Figures 4.15(d) and (e), we observed the *collapse of the true lumen* occurs as a result of buckling of the inner wall.

From the deformed shapes of the arterial wall in Figures 4.12, 4.13, 4.15 and others with different values of η and d , we conclude that a long shallow tear is more likely to result in buckling of the inner wall, in contrast a deep tear tends to propagate.

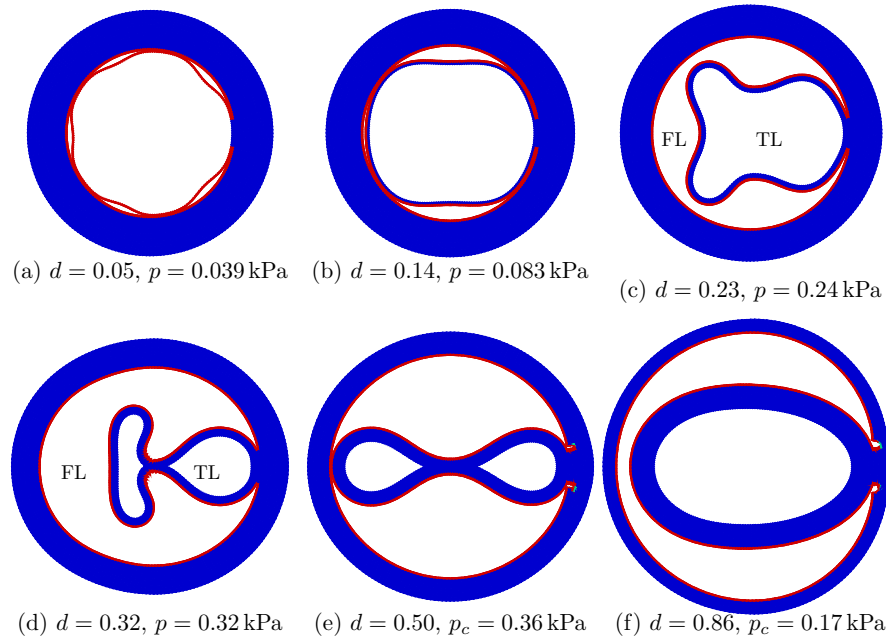


Figure 4.15: The representative deformed shapes of arterial wall with a long tear $\eta = 340^\circ$ for different radial depth d . When the depth is small (a–d), the propagation does not occur. Instead, buckling of the inner wall occurs and the true lumen is collapsed in (d) and (e). The shape of the buckled inner wall in (c) is similar to that in the CT scan of the aortic dissection for a patient in Figure 4.14 (c).

4.5 Conclusion

In this chapter, the peeling- and pressure-driven tear propagation are simulated. The simulations for the peeling of strips and discs show a tear is likely to propagate along the material axis with the maximum stiffness, which is determined by the fibre orientation. We investigate the effect of radial depth and circumferential length on the critical pressure for

tear propagation and shape of deformed arterial wall with a tear, through the simulations of pressure-driven tear propagation in the cross-section of an idealized two-layer arterial wall. We found the tear with the least length and largest depth is the most difficult to extend, while the tears with the largest depth and $\eta = 120^\circ$ to 160° and 300° to 340° are the most likely to propagate. A shallow long tear leads to buckling of the inner wall and collapse of true lumen, while a deep tear tends to propagate.

Chapter 5

Effect of residual stress in an isotropic material

In the absence of external loading, many biological soft tissues are not stress-free, but subject to residual stress. In artery, residual stress reduces variation in the stress stress distribution across the arterial wall and decreases the peak stress in the inner layer of the arterial wall. We study the effect of residual stress on the critical pressure for propagation of arterial dissection. Fung [1991] was the first to show that a radial cut along artery can release most of the residual stress. Hence using an opening angle is a theoretical approach to recover the stress-free configuration, and the value of the opening angle is often used to quantify the residual stress. For example, Holzapfel et al. [2000] employed this approach to obtain the deformation and stress, with residual stress, in a two-layer model for a rabbit carotid arterial wall subject to the physiological loading. For this idealized two-layer model, we introduce different values of residual stress calculated from exact mathematical expression, associated with different values of opening angle, into the finite element model as an initial stress field. The extended finite element method is used to simulate the inflation of both the lumen and tear. We plot the trend of critical pressure, beyond which the tear propagates, on the opening angle. The critical pressure increases almost linearly with the opening angle. In conclusion, the residual stress can protect the arterial wall by elevating the critical pressure for the initial propagation of the dissection.

5.1 Introduction

The stress that exists in a unloaded solid body is called residual stress. Most biological soft tissues include residual stress, which maybe because of the different growth rates at different locations or the coherent structure by composing multiple components. The residual stress in the blood vessels has been observed in many studies [e.g. Cardamone et al., 2009; Chuong and Fung, 1986]. Fung [1991] showed that a radial cut along artery without any loading opens out and releases most of the residual stress (Figure 1.5). The value of the opening angle is often used to quantify the residual strain. Using a constitutive law, the residual stress is calculated from the residual strain. Holzapfel et al. [2000] employed this method to get the residual stress in a two-layer model for a rabbit carotid arterial wall, followed by inflated subject to internal pressure and stretched axially. The comparison of Cauchy stress across the arterial wall at the physiological loading condition [Holzapfel et al., 2000], showed that residual stress reduces variation in the stress distribution, and decreases the peak stress (Figure 1.6). A discussion, on how important to the physiological function of artery the residual stress is, was presented by Fung [1991].

In this chapter, we study what role the residual stress plays in the critical pressure for initial propagation of the dissection. Our models simulate the pressure-driven tear propagation in the two-layer model for a rabbit carotid artery wall, which was originally used to analyse the effect of residual stress on stress distribution across the intact arterial wall [Holzapfel et al., 2000]. An initial tear is introduced at the centre of the media and we employ the XFEM to simulate the inflation of both the lumen and tear until the tear propagates. We introduce different values of residual stress, associated with different values of the opening angle, into the computational models. The residual stress is computed analytically in this study, and then is imported into the FE model as an initial stress field. This is an *easy* method for introducing different values of residual stress into the FE model with the same geometry. For all simulations, we only build one FE model in the commercial FE solver Abaqus, and then import different values of residual stress. However, this technique cannot be used for a model with an anisotropic hyperelastic material in Abaqus 6.13. For comparison with the HGO model in Chapter 6, we use the incompressible neo-Hookean strain energy function as a hypothetical test case in this chapter. Comparing the results of these simulations, we obtain the effect of residual stress on the critical pressure for tear propagation. Finally, we find that the critical pressure increases almost linearly with the opening angle.

This chapter is organized as follows. The key ingredients of the computational model are summarized in Section 5.2. Section 5.3 includes the techniques about how to compute analytical residual stress. Before using this model to investigate the effect of residual stress on the arterial dissection in Section 5.6, we verify this model in Section 5.5. The discussion and limitations of this computational model are presented in Section 5.7.

5.2 Methods

5.2.1 Material

We use an incompressible neo-Hookean material for the two-layer rabbit carotid arterial wall with residual stress, the cross-section of which is shown in Figure 5.1. The incompressible neo-Hookean strain energy function is for the media and adventitia layer

$$W = c_j(I_1 - 3), \quad (5.1)$$

where $I_1 = \text{tr } \mathbf{C}$ is the first invariant of the right Cauchy-Green strain tensor $\mathbf{C} = \mathbf{F}^T \mathbf{F}$. The tensor \mathbf{F} is the deformation gradient, the linear mapping from the stress-free configuration to the deformed configuration at equilibrium. The material parameters c_j , ($j = m, a$), are the shear moduli of the media and adventitia layers. These are determined by requiring that the deformation from the stress-free configuration Ω_0 to the deformed configuration Ω_p subject to the physiological loading (see Table 5.1), agrees with that in the experiment 71 in [Chuong and Fung, 1983], i.e. the absolute value of the difference between the inner radius r_i in the model and the experiment is minimal. Assuming that $c_m = 10 c_a$, as in [Holzapfel et al., 2000], we obtain $c_m = 38.45$ kPa and $c_a = 3.845$ kPa.

5.2.2 Geometry

A fixed geometry, Ω_r in Table 5.1, with various values of residual stresses, associated with different values of the opening angle, is used. This fixed geometry is obtained from the equilibrium of Ω_0 , through the forward analysis when letting $p_i = 0$. This geometry Ω_r is the target configuration in our following calculation when introducing different values of residual stress.

An initial tear, spreading an angle of 90° at the centre of the tube, along an arc at the mid-radius of the media, is then introduced in Ω_r (Figure 5.1).

Table 5.1: The geometries of the two-layer arterial wall in different loading conditions. r_i is the inner radius, d_m is the thickness of media, d_a is the thickness of adventitia, α is the opening angle, p_i is the pressure applied on the inner radial surface and λ_z is the axial stretch.

		geometry			loading		
configuration	notation	r_i [mm]	d_m [mm]	d_a [mm]	α [$^\circ$]	p_i [kPa]	λ_z
stress-free	Ω_0	1.43	0.26	0.13	160	0	1
unloaded	Ω_r	0.7395	0.2595	0.1197	0	0	1
physiological	Ω_p	1.2738	0.1001	0.0532	0	13.33	1.7

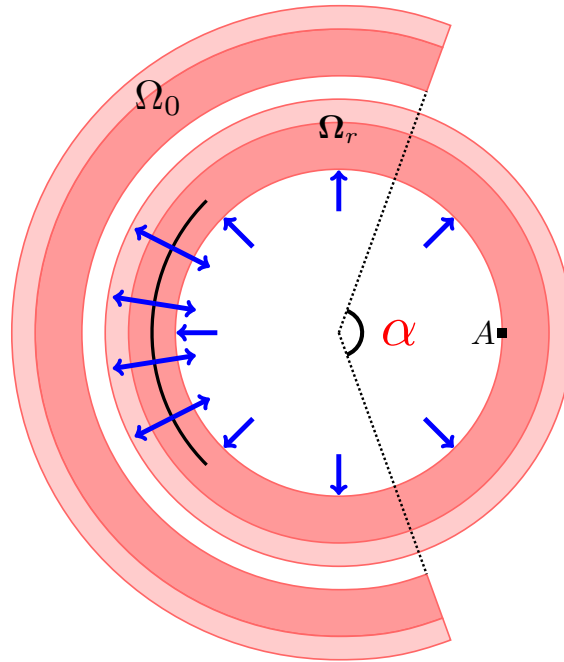


Figure 5.1: An initial tear (black arc) is introduced into the *unloaded configuration* Ω_r with *residual stress*, which is associated with the opening angle α in the *stress-free configuration* Ω_0 . In the simulation, the analytical residual stress is imported to the FE model, the point A is fixed to avoid rigid body motion, and then a pressure (arrows), gradually increasing from zero, is applied on both the inner radial and tear surfaces. The transmural pressure governs the dynamics of the wall. Since the material is incompressible, without loss of generality we assume that the external pressure is zero. If that is not the case, then the internal pressure can be replaced by the transmural pressure.

5.2.3 Damage and failure

Following the theory introduced in Section 4.2.2, we use the XFEM with the linear cohesive traction-separation law (Figure 4.1) to model the propagation of a tear. In the simulation, all elements are enriched by this cohesive law. After calculation of equilibrium in each with a loading incremental, the maximum principal stress at the centroid of each element is used to compares to the T_c : if it is greater than T_c , the tear tends to propagate in that element; so a displacement jump Δu is calculated. When the displacement jump $\Delta u > \Delta u_c$, the tear propagates perpendicular to the principal axis, which is along the direction of the maximum tensile principal stress. The values for parameters in the cohesive law are shown in Table 5.2.

Table 5.2: Cohesive law parameters

	T_c [kPa]	G_c [J/m ²]	Δu_c [mm]
media	76.9	0.001	2.6×10^{-5}
adventitia	7.69	0.0001	2.6×10^{-5}

5.2.4 Boundary conditions

The analytical residual stress is introduced into the finite element model in the initial step via an user subroutine ‘sigini.f’. The details of ‘sigini.f’ are presented in Section 5.4. To avoid the rigid body motion, the point A in Figure 5.1 is fixed. A gradually increasing pressure is applied on both the inner radial and tear surface after the initial step. The critical pressure is identified as that at which the tear starts to propagate.

5.3 Residual stress calculation

Due to the geometrical and constitutive symmetry, the equilibrium equation for the two-layer arterial wall is

$$\frac{d\sigma_{rr}}{dr} = \frac{\sigma_{\theta\theta} - \sigma_{rr}}{r}. \quad (5.2)$$

Thus the radial Cauchy stress σ_{rr} is

$$\sigma_{rr}(\xi) - \sigma_{rr}(r_i) = \int_{r_i}^{\xi} (\sigma_{\theta\theta} - \sigma_{rr}) \frac{dr}{r}, \quad r_i \leq \xi \leq r_o, \quad (5.3)$$

where r_i and r_o are the inner and outer radii of Ω_r .

The inner and outer radial surfaces are traction-free, so that

$$\sigma_{rr}(\xi) = 0, \quad \text{at } \xi = r_i, r_o. \quad (5.4)$$

Substituting (5.4) into the equilibrium equation (5.3) yields

$$\int_{r_i}^{r_o} (\sigma_{\theta\theta} - \sigma_{rr}) \frac{dr}{r} = 0. \quad (5.5)$$

5.3.1 Forward analysis

The forward analysis is to find the unloaded configuration Ω_r from the stress-free configuration Ω_0 , for which

$$R_i \leq R \leq R_o, \quad 0 \leq \Theta \leq (2\pi - \alpha), \quad (5.6)$$

where R_i , R_o , and α denote the inner and outer radii, and the opening angle, respectively.

The unloaded configuration Ω_r is defined by

$$r_i \leq r \leq r_o, \quad 0 \leq \theta \leq 2\pi. \quad (5.7)$$

Incompressibility requires that

$$r = \sqrt{\frac{R^2 - R_i^2}{k} + r_i^2}, \quad \theta = k\Theta, \quad (5.8)$$

where $k = 2\pi/(2\pi - \alpha)$. The principal stretches are,

$$\lambda_r(R) = \frac{\partial r}{\partial R} = \frac{R}{rk}, \quad \lambda_\theta(R) = \frac{r}{R} \frac{\partial \theta}{\partial \Theta} = \frac{kr}{R}, \quad (5.9)$$

and the deformation gradient $\mathbf{F} = \text{diag}[\lambda_r, \lambda_\theta, 1]$. The Cauchy stress is

$$\boldsymbol{\sigma} = -\mathcal{P}\mathbf{I} + 2\mathbf{F} \frac{\partial \Psi}{\partial \mathbf{C}} \mathbf{F}^T = -\mathcal{P}\mathbf{I} + \bar{\boldsymbol{\sigma}}, \quad (5.10)$$

where \mathcal{P} is the Lagrangian multiplier associated with the incompressibility constraint.

From (5.8),

$$r_o(r_i) = \sqrt{\frac{R_o^2 - R_i^2}{k} + r_i^2}. \quad (5.11)$$

Substitute (5.8), (5.10), and (5.11) into (5.5), we obtain a non-linear integral equation,

$$\mathcal{I}(r_i) = \int_{r_i}^{r_o} (\sigma_{\theta\theta} - \sigma_{rr}) \frac{dr}{r} = \int_{r_i}^{r_o} (\bar{\sigma}_{\theta\theta} - \bar{\sigma}_{rr}) \left(\frac{R^2 - R_i^2}{k} + r_i^2 \right)^{-1/2} dr = 0, \quad (5.12)$$

which is solved for r_i using Newton iteration.

5.3.2 Inverse analysis

The inverse analysis determines the stress-free configuration Ω_0 for a given unloaded configuration Ω_r , specifically inner radius R_i in Ω_0 when the inner radius r_i in Ω_r is given.

From (5.8),

$$R = \sqrt{(r^2 - r_i^2)k + R_i^2}. \quad (5.13)$$

This, with together (5.5) and (5.9), can be solved analytically for R_i .

5.3.3 Calculation of the stress

Calculation of the stress is a post-process after obtaining both the stress-free and deformed configurations. Substitution of (5.1) into (5.10) yields

$$\boldsymbol{\sigma} = -\mathcal{P}\mathbf{I} + 2c\mathbf{B}, \quad (5.14)$$

where $\mathbf{B} = \mathbf{F}\mathbf{F}^T$ is the left Cauchy–Green tensor.

Substituting the principal stretches from (5.9) into the (5.10), we have the second term of the Cauchy stress in (5.14).

The Lagrangian multiplier \mathcal{P} is determined from the boundary conditions. From (5.3),

$$\sigma_{rr}(\xi) = p_i + \int_{r_i}^{\xi} (\sigma_{\theta\theta} - \sigma_{rr}) \frac{dr}{r}, \quad r_i \leq \xi \leq r_o, \quad (5.15)$$

where p_i is the internal pressure. Then

$$\mathcal{P}(\xi) = -\sigma_{rr}(\xi) + 2c\lambda_r(\xi)^2, \quad (5.16)$$

substituted into (5.14) yields

$$\sigma_{\theta\theta}(\xi) = -\mathcal{P}(\xi) + 2c\lambda_\theta(\xi)^2. \quad (5.17)$$

The equations (5.15) and (5.17), together with (5.8) and (5.9), are the formulations to compute the residual stress in the cylindrical polar coordinate system.

5.4 Importing residual stress to the FE model: `sigini.f`

The values of the analytical expression for residual stress is imported into the FE model in Abaqus through an user subroutine `sigini.f`. This is done in two steps: 1) obtaining the residual stress components in the cylindrical polar coordinate system at every quadrature

point, and 2) transforming these into the corresponding points in the Cartesian coordinate system.

Isoparametric interpolation is employed in the first step. The analytical stress is computed at $1/(n+1)$ equidistant points across the wall, with spacing $\Delta r = (d_m + d_a)/n$, where d_m and d_a are thickness of the media and adventitia. For a quadrature point $Q : (x, y, z)$ from the FE model, we first calculate its radius

$$s = \sqrt{x^2 + y^2}. \quad (5.18)$$

The location of the point Q is determined by

$$m = s \setminus \Delta r, \quad t = s - m\Delta r, \quad (5.19)$$

where \setminus stands for integer division, $0 \leq t \leq 1$ is a parameter to define the position of Q in the interval $[r_m, r_{m+1}] = [m\Delta r, (m+1)\Delta r]$, and

$$s = (1-t)r_m + tr_{m+1}. \quad (5.20)$$

Following the isoparametric interpolation, we have

$$\boldsymbol{\sigma} = (1-t)\boldsymbol{\sigma}_m + t\boldsymbol{\sigma}_{m+1}, \quad (5.21)$$

where $\boldsymbol{\sigma}_m$ is the value of the analytical residual stress at r_m .

The analytical stress in the cylindrical coordinate system is converted to that in the Cartesian coordinate system in the second step:

$$\begin{bmatrix} \sigma_{xx} & \sigma_{xy} & \sigma_{xz} \\ \sigma_{yx} & \sigma_{yy} & \sigma_{yz} \\ \sigma_{zx} & \sigma_{zy} & \sigma_{zz} \end{bmatrix} = \begin{bmatrix} \cos \theta & -\sin \theta & 0 \\ \sin \theta & \cos \theta & 0 \\ 0 & 0 & 1 \end{bmatrix} \begin{bmatrix} \sigma_{rr} & \sigma_{r\theta} & \sigma_{rz} \\ \sigma_{\theta r} & \sigma_{\theta\theta} & \sigma_{\theta z} \\ \sigma_{zr} & \sigma_{z\theta} & \sigma_{zz} \end{bmatrix} \begin{bmatrix} \cos \theta & \sin \theta & 0 \\ -\sin \theta & \cos \theta & 0 \\ 0 & 0 & 1 \end{bmatrix},$$

where $\cos \theta = x/s$ and $\sin \theta = y/s$.

5.5 Verification

The above computational method, importing the residual stress into the FE model as an initial stress field and using it in subsequent stress analysis, is verified, by comparing the analytical and FE results for the deformation and the Cauchy stress of this two-layer

arterial wall without a tear, inflated subject to an internal pressure $p_i = 13.33$ kPa. The opening angle in the stress-free configuration Ω_0 is 160° .

In the analytical solution, we change the boundary condition in (5.4) to,

$$\sigma_{rr}(r_i) = -p_i, \quad (5.22)$$

and solve the equilibrium equation in (5.3) through the forward analysis.

In the numerical solution, the simulation starts from the unloaded configuration Ω_r . We import the analytical residual stress into the FE model as an initial stress field via ‘sigini.f’, and then the arterial wall is inflated by applying the pressure p_i on the inner radial surface. Finally, we compute numerically the deformed configuration and the Cauchy stress distribution across the wall.

The inner radii of the deformed configuration are $r_i^a = 0.9535$ mm and $r_i^n = 0.9523$ mm in the analytical and numerical solutions, respectively. The relative error is about 0.13%. As shown in the first part of (5.8), the deformation of the arterial wall depends on the value of inner radius r_i . Therefore, we conclude that the deformation of the arterial wall obtained by this numerical method agrees with the analytical solution with a relative error of about 0.13%. In addition, the Cauchy stress across the arterial wall in the numerical solution also agrees with the analytical solution as shown in Figure 5.2. The relative error is less than 0.8%, which is computed by (4.15).

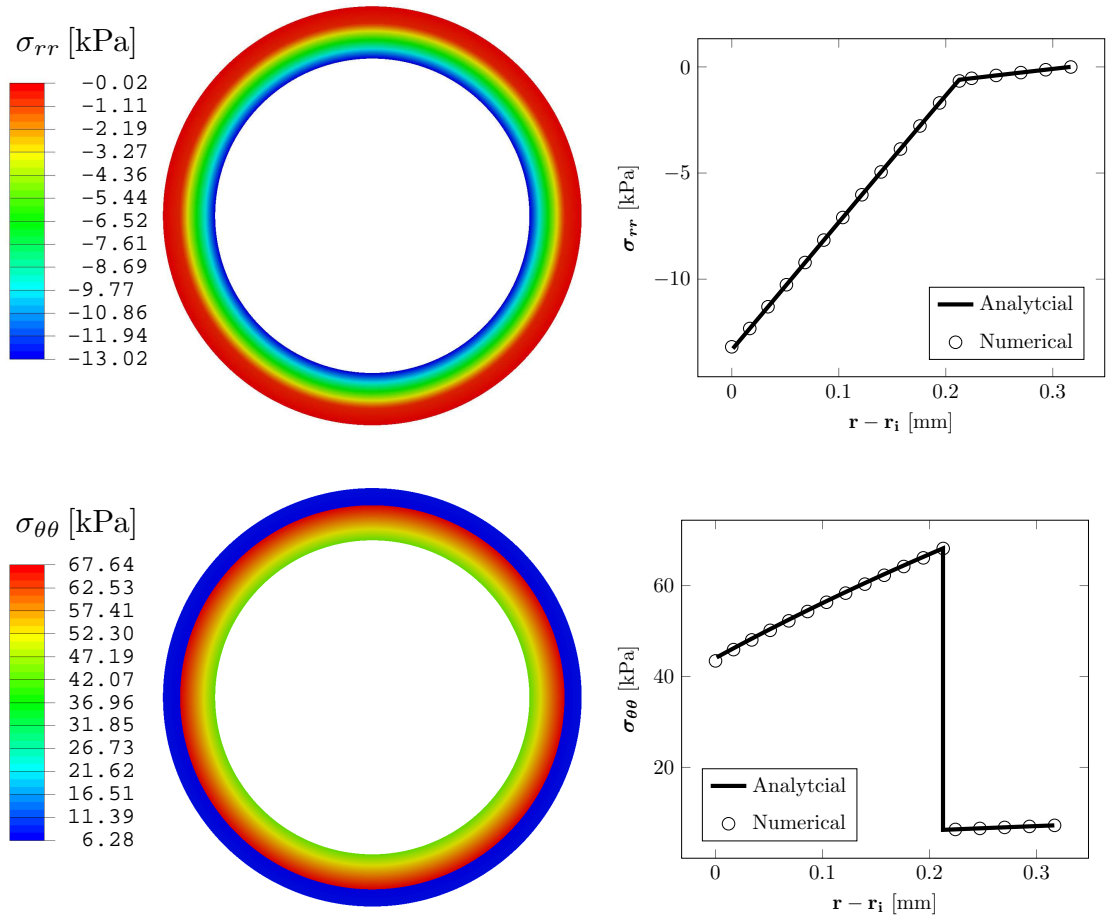


Figure 5.2: Left, the distribution of each Cauchy stress component computed numerically, across the two-layer arterial wall is shown. These numerical results are obtained with an analytical residual stress field for $\alpha=160^\circ$, imported into the FE model by ‘sigini.f’, and subject to $p_i=13.33$ kPa. The computed inner radius of the deformed configuration is $r_i = 0.9523$ mm, which is close to the analytical solution with a relative error of about 0.13%. Right, the comparison of the Cauchy stress across the wall from numerical and analytical solution is shown. The maximum relative error computed by (4.15) in the numerical results is about 0.8%. The tangent-change in σ_{rr} and the discontinuity in $\sigma_{\theta\theta}$ occur at the interface between the media and adventitia. That is because the material properties of the two layers are different.

5.6 Results

For the fixed unloaded configuration Ω_r , we use the inverse analysis in Section 5.3.2 to obtain the stress-free configuration Ω_0 for different values of the opening angle α . The dimensions (inner radius, thickness of the media and adventitia) of these Ω_0 are shown in Table 5.3. The residual stress across the arterial wall in Ω_r associated with each value of α is computed analytically using the formulae in Section 5.3.3. As shown in Figure 5.3, the magnitude of residual stress increases as the opening angle α increases.

Table 5.3: Dimensions of the stress-free configurations Ω_0 for different values of the opening angle α , R_i is the inner radius, D_m and D_a are thickness of the media and adventitia respectively. These stress-free configurations have the same unloaded configuration Ω_r in the equilibrium state, but have different values of residual stress.

α [°]	R_i [mm]	D_m [mm]	D_a [mm]
0	0.7395	0.2593	0.1197
40	0.8472	0.2595	0.1221
80	0.9858	0.2597	0.1246
120	1.1708	0.2599	0.1272
160	1.4300	0.2600	0.1300
200	1.8191	0.2601	0.1329

We import these analytical stresses into the FE model in individual simulation for a particular value of α , and then simulate the inflation of both the lumen and tear subject to the pressure on both inner radial and tear surfaces. The pressure is gradually increasing until the tear propagates. The critical pressure p_c is identified as that at which the tear starts to extend. As discussed in Section 4.4.1, the actual value of p_c depends on material parameters. We focus on the trend of the critical pressure on the opening angle, and thus we scale the critical pressure with the shear modulus of media c_m and plot the *dimensionless critical pressure* $p'_c = p_c/c_m$, where $c_m = 38.45$ kPa, against α .

The maximum principal stress σ_{mp} in the deformed configuration for $\alpha = 40^\circ$ and subject to the critical pressure is shown in Figure 5.4. Because the stress field is singular

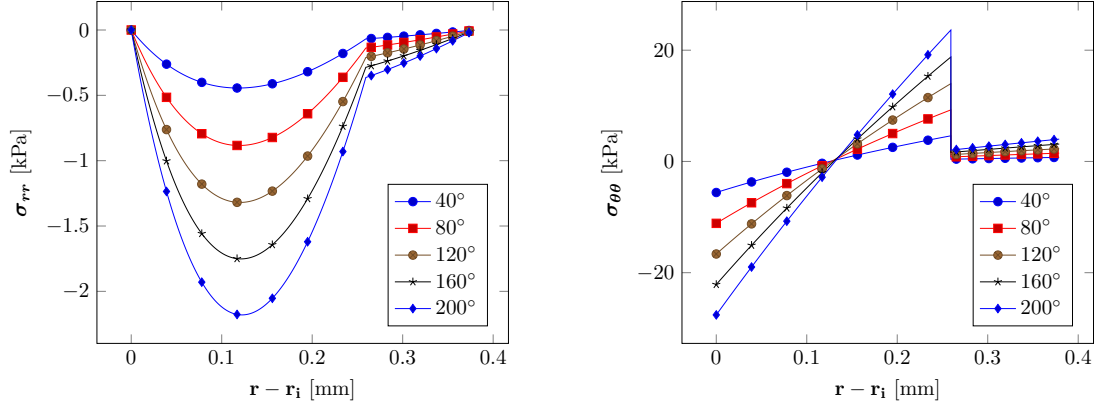


Figure 5.3: The magnitudes of the residual stress components increase with the opening angles. The tangent-change in σ_{rr} and the discontinuity in $\sigma_{\theta\theta}$ occur at the interface between the media and adventitia. That is because the material properties of two layers are different.

around tear tips, the greatest value of σ_{mp} appears at tips. This stress concentration also occurs at the point A , on which we apply a fixing boundary condition to avoid rigid body motion. This boundary condition also results in a bump, which can be avoided using an alternative boundary condition.

The maximum principal stress σ_{mp} in deformed configurations for other values of α is shown in Figure 5.5. These deformed configurations are subject to different values of the critical pressure p_c , which depends on the value of α . In each case, the *inner wall*, i.e. the material section between the tear and lumen, is compressed since $\sigma_{mp} < 0$, and the minimal values of σ_{mp} appear at the two ends of the inner wall along the inner radial surface. The material between the tear and adventitia is stretched the most, and this stretch increases as α increases.

The set-up of these simulations guarantees that the difference in results of these simulations is due to the residual stress, since only is the residual stress different between these simulations. Finally, we plot the trend of critical pressure on the opening angle in Figure 5.6. The critical pressure increases almost linearly with the opening angle.

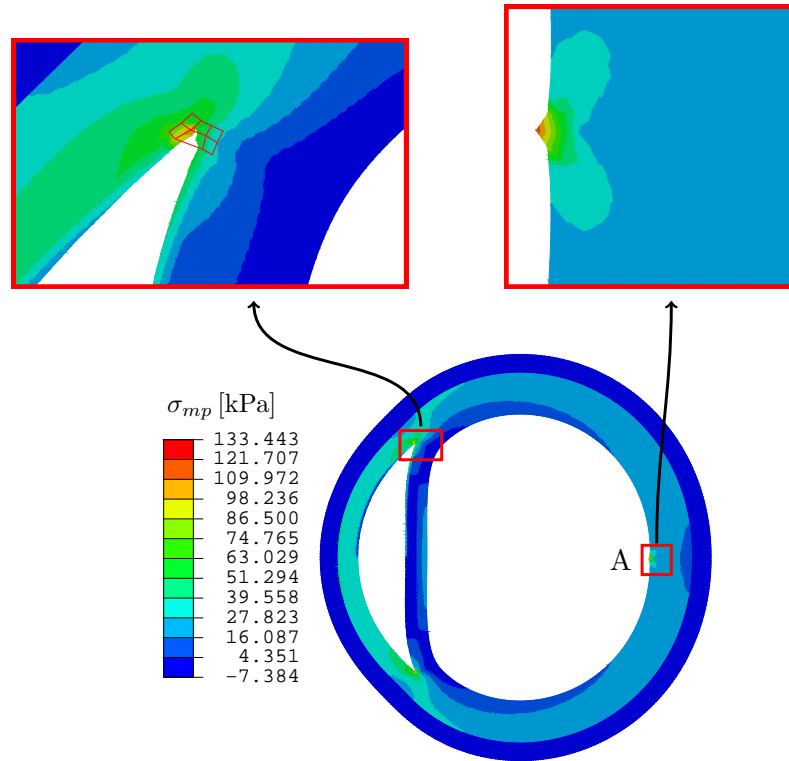


Figure 5.4: The contour of maximum principal stress σ_{mp} in the deformed configuration subject to the critical pressure $p_c = 6.22$ kPa is shown for $\alpha = 40^\circ$. The maximum of σ_{mp} appears at tear tips and point A, at which the fixing boundary condition is applied. The bump and the great value of σ_{mp} at point A are due to the fixing boundary condition. The greatest value of σ_{mp} at tips is because the tip-stress field is singular. To get rid of the singularity of tip-stress field, the stress over the quadrature points of the first ring elements, i.e. the red elements, around the tip is averaged, and replaces the greatest value of σ_{mp} in following plots.

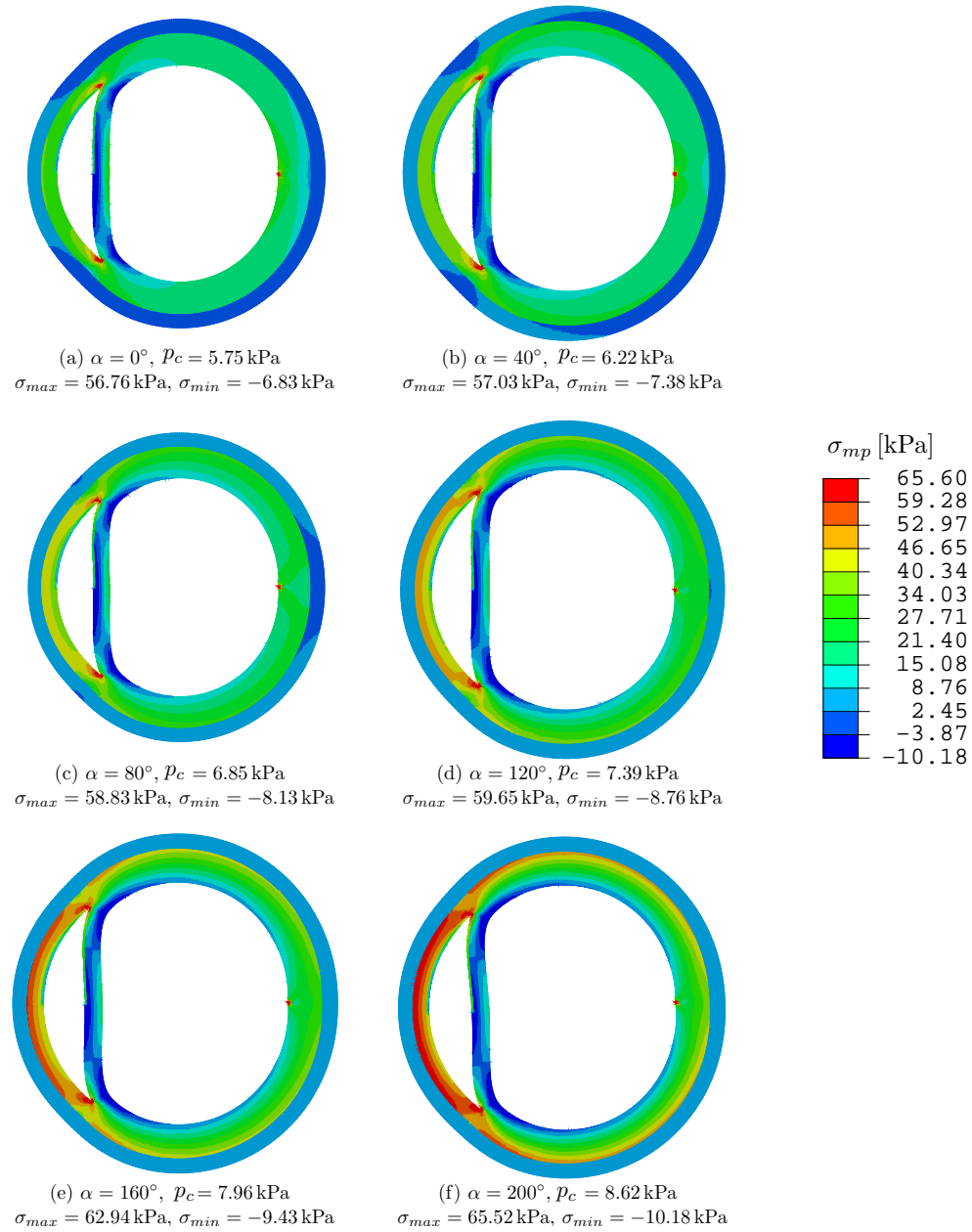


Figure 5.5: The contour of maximum principal stress σ_{mp} in the deformed configuration subject to the critical pressure p_c is shown for different values of the opening angle α . The tip-stress field is averaged over the quadrature points of the first ring elements around tip to obtain σ_{max} .

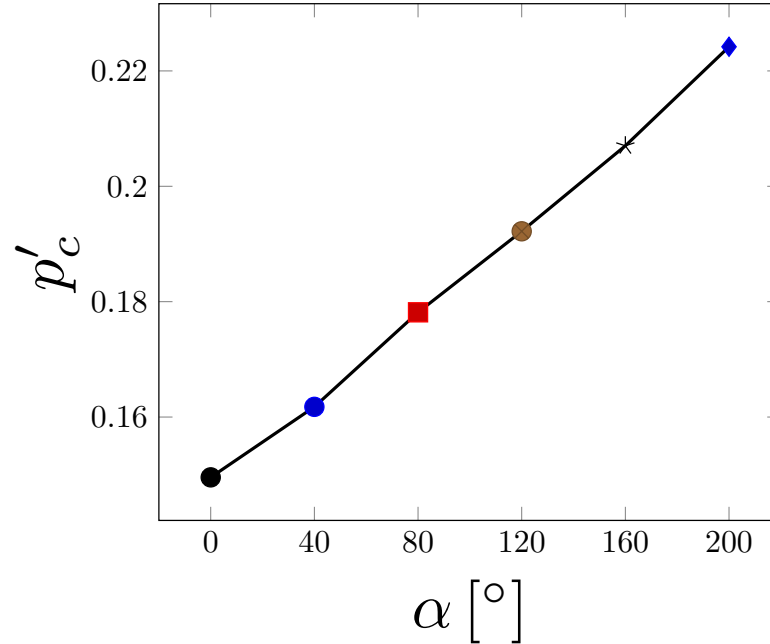


Figure 5.6: The dimensionless critical pressure $p'_c = p_c/c_m$, where $c_m = 38.45$ kPa, is plotted against the opening angle α . This trend shows that the critical pressure increases almost linearly with the opening angle.

5.7 Discussion

5.7.1 The material model

The selection of the isotropic neo-Hookean material model is a limitation of this computational approach. Although the anisotropic HGO constitutive law is better to model the arterial wall, residual stress cannot be introduced into the FE model through this method in Section 5.4. That is because the current version of Abaqus (6.13) does not support including an initial stress field into a FE model with an anisotropic hyperelastic material. In next chapter, we develop another method to cope with this limitation.

5.7.2 Boundary condition

To avoid rigid body motion, we fixed only the point A (Figure 5.1). This boundary condition results in a bump and stress concentration at this point (Figure 5.5). This bump appears only at the two elements, which have the point A as a common node. As we refine the mesh, this bump is reduced. This bump is due to the numerical discretization.

Alternatively, the bump can be avoided by introducing a different boundary condition.

Instead of fixing the point A , we employ a kinematic coupling constraint referring to the centre O on the right half inner radial surface (Figure 5.7). All degrees of freedom at O are fixed. This kinematic coupling constraint fixes all the degrees of freedom of the nodes on this semi circle except the radial component. As a result, the this half circle can only move radially.

In a comparison with the Figure 5.5, the contour of the maximum principal stress σ_{mp} is plotted in the deformed configurations subject to the individual critical pressures in Figure 5.8 for different values of α . The stress along the inner radial surface at the top and bottom are less smooth along the circumferential direction than that in Figure 5.5, which is the effect of the kinematic coupling boundary condition. However, using this boundary condition does avoid the bump due to the fixed point in Figure 5.5. This boundary condition also slightly increases the critical pressure (Figure 5.9) by about 3.7%. That is because the material close to tear tip with this boundary condition is constrained more than with the previous boundary condition.

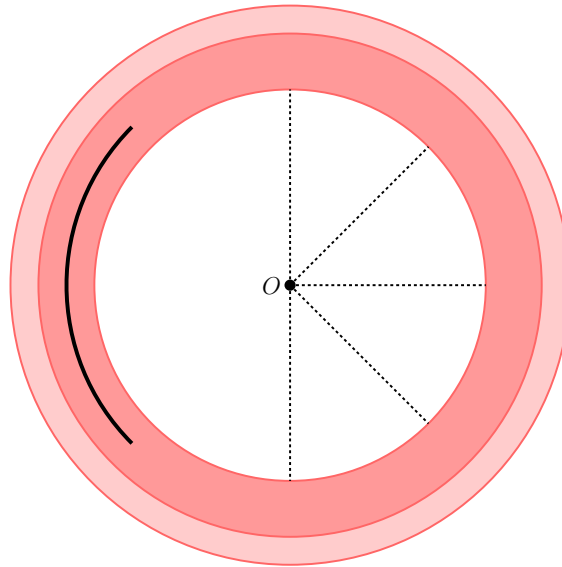


Figure 5.7: The right half inner radial surface is constrained through a kinematic coupling constraint, such that the nodes on this surface can only move radially. The constraint is defined on a polar coordinate system referred to the center O , all degrees of freedom of which are fixed.

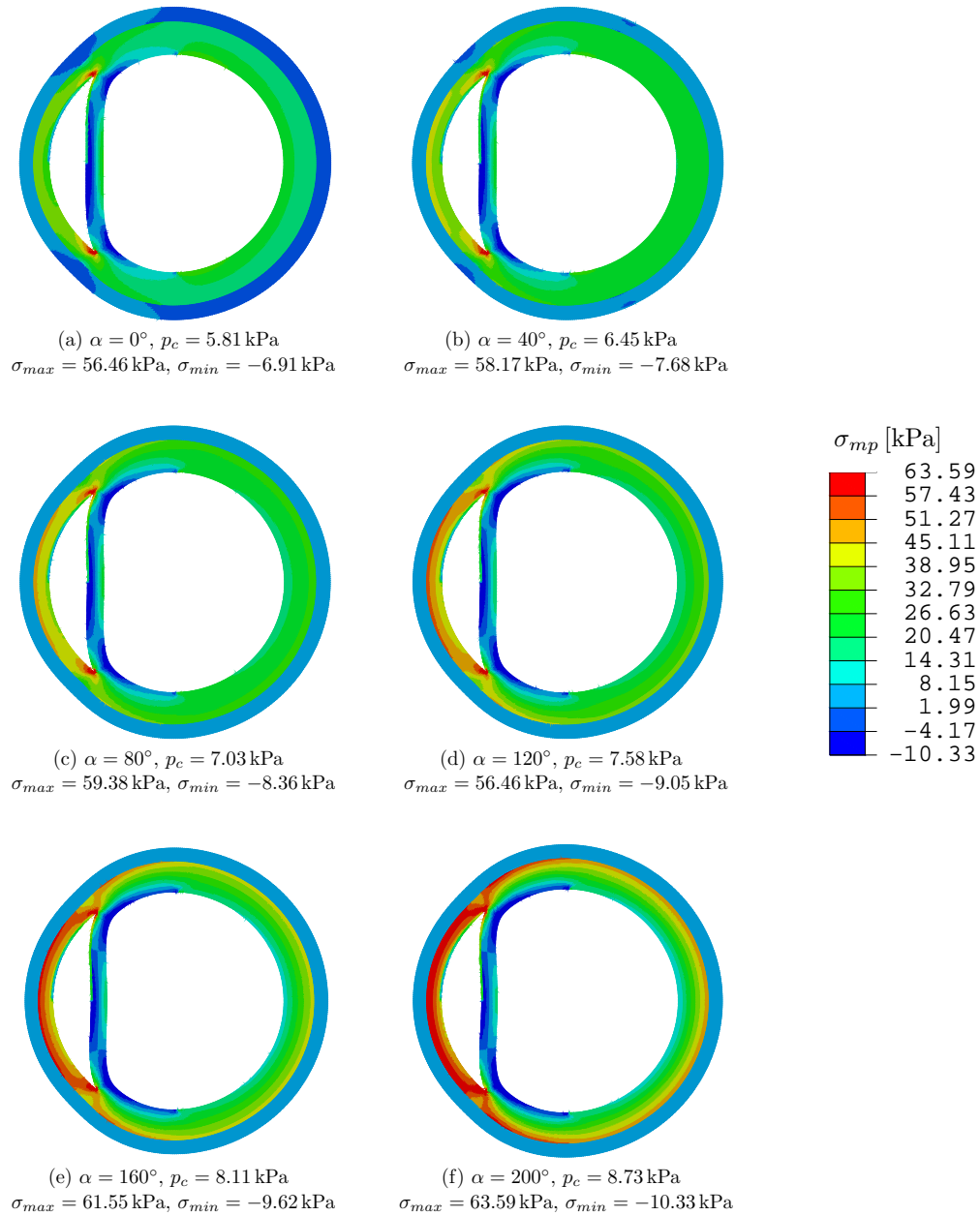


Figure 5.8: The contour of maximum principal stress σ_{mp} in the deformed configuration subject to the critical pressure p_c is shown for different values of the opening angle α . The tip-stress field is averaged over quadrature points of the first ring elements around tip to obtain σ_{max} . Using the kinematic coupling constraint in Figure 5.7 to replace the fixing boundary condition at A in Figure 5.1, avoids the bump and stress concentration at this point as shown in Figure 5.5. The stress patterns are similar to those in Figure 5.5, but there is a jump in σ_{mp} at the top and bottom of the inner radial surface, which is clear in (e) and (f). That is because these two points are the boundary of kinematic coupling constraint as shown in Figure 5.7.

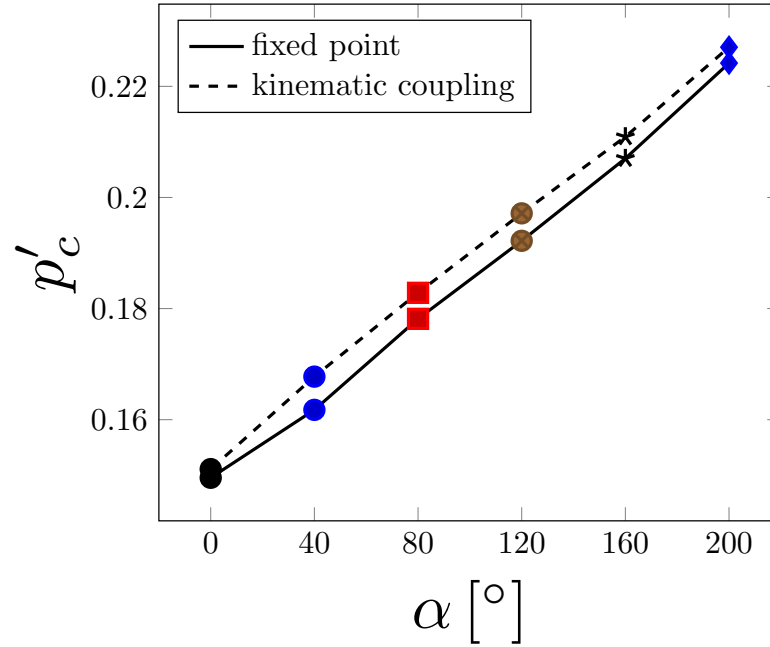


Figure 5.9: The dimensionless critical pressure $p'_c = p_c/c_m$, where $c_m = 38.45$ kPa, is plotted against the opening angle α for the boundary condition of kinematic coupling (dashed) and fixed point (solid). The term ‘fixed point’ refers to Figure 5.1, while ‘kinematic coupling’ refers to Figure 5.7. The relative difference of p'_c for the two boundary conditions is less than 3.7%, showing that the effect of the boundary conditions, used to avoid rigid body motion, on p'_c is small. The maximum relative difference 3.7% is the maximum of the six values of the relative difference for the six values of α indicated by marks.

5.8 Conclusion

We have developed a computational model to study the effect of residual stress on the critical pressure for propagation of the arterial dissection. The residual stress is obtained from the analytical solution and then imported to the finite element model as an initial stress field. The model is verified through analysing the inflation of a two-layer arterial wall without a tear. This computational model is easy to use: simulations for different values of α start from a same geometry Ω_r , and the different values of residual stress are imported by ‘`sigini.f`’. Thus we need only to build one FE model in Abaqus for the studies in this chapter. Using this model with different values of the residual stress, we find that the residual stress elevates the critical pressure for tear propagation, and the critical pressure increases almost linearly with the opening angle. However, this simple computational method cannot be used in a FE model with an anisotropic hyperelastic material, which is a limitation of the current version of Abaqus (6.13). Thus, in next chapter we develop another method, which is to compute the residual stress numerically by closing the stress-free configuration Ω_0 via a sequence of novel boundary conditions, for the HGO material.

Chapter 6

Effect of residual stress in an anisotropic material

In this chapter, we develop a new method to introduce residual stress computed numerically to a FE model for an anisotropic material. This method simulates closing of a stress-free configuration with an opening angle to obtain the unloaded configuration by applying a sequence of boundary conditions, and computes residual stress through the FE analysis. To guarantee the unloaded configuration is the same for different values of the opening angle, we use the inverse analysis of Section 5.3.2 to compute analytically the geometry of the stress-free configuration for a given opening angle. Linux shell and Python scripts are developed to build, edit and run these models *automatically*. This method costs more computational time than the method in Chapter 5. However, it can be used for both isotropic and anisotropic materials. As a verification, we used this method to repeat the simulations with a change in the boundary condition used to avoid rigid body motion in Chapter 5, and obtained very similar stress patterns of the arterial wall and critical pressure for tear propagation. With the HGO material, we find that the critical pressure also increases with the opening angle. In addition, we also investigate the effect of collagen fibres orientation on this trend.

6.1 Introduction

The mechanical response of soft tissues generally has directional preference. The arterial wall, as a typical anisotropic soft tissue has been studied in many papers [e.g. Holzapfel et al., 2000; Holzapfel and Ogden, 2010] and references therein. Notably, in the HGO

SEF [Holzapfel et al., 2000], the arterial wall is assumed to consist of an isotropic matrix reinforced by some stiffer collagen-fibres. The distribution of these collagen fibres leads to the anisotropy of the arterial wall. We employ the HGO model for the mechanical response of arterial wall in this chapter.

The method of importing analytical results for the residual stress into a FE model with an anisotropic hyperelastic material in Chapter 5 is not yet supported by Abaqus. Here, we develop a new method to introduce residual stress into a FE model. The simulation of introducing residual stress in this method is an inverse of the process of demonstrating the residual stress of blood vessels in the experiments of [Fung, 1991]. Those showed that cutting the arterial wall radially along the length of the artery releases most of residual stress, and the stress-free configuration is defined by the opening angle (Figure 1.5). In the simulation, we start from the stress-free configuration, closing which by applying a sequence of novel boundary conditions computes the unloaded configuration in the equilibrium state and introduces the corresponding residual stress. Directly closing the artery results in buckling at the inner radial surface and also the contact between two faces of the tear. Both lead to divergence of the solution or considerable increase in computational cost. In order to deal with this challenge, we apply a pre-pressure on both the inner radial and tear surfaces, such that the lumen and tear are inflated during closing of the opening angle. After successfully closing the artery, the pre-pressure is removed, so that the artery is unloaded and subject to only residual stress.

The different values of residual stress associated with different values of opening angle α are employed in a simulation of inflating lumen and tear until the tear propagates. In order to guarantee the difference between these simulations is only the value of residual stress or opening angle, geometries of the unloaded configurations computed have to be the same for different values of α . We use the inverse analysis of Section 5.3.2 to obtain the geometry of the stress-free configurations for different values of the opening angle, so that the same unloaded configuration is achieved.

This computational approach can be used for both isotropic and anisotropic materials. As a verification, we use it to predict the trend of critical pressure against the opening angle for the neo-Hookean material model, and the result is almost the same as we present in Chapter 5. With the HGO material model, we also find that the critical pressure increases with the opening angle.

6.2 Methods

6.2.1 Material

For either layer, i.e. the media and adventitia, of the arterial wall, we use the incompressible HGO constitutive law [Holzapfel et al., 2000] in the analytical calculation. The strain energy function of the incompressible HGO model is

$$\Psi(\mathbf{C}) = \Psi_m(I_1) + \Psi_f(I_4, I_6) = c(I_1 - 3) + \sum_{n=4,6} \psi(I_n), \quad (6.1)$$

where c is the shear modulus of matrix, I_1 is a deformation measure of the matrix, I_n , $n = 4, 6$ are stretch measure of two families of fibres, and ψ is the strain energy density function for fibres. In the numerical computation, we use an approximation of this incompressible HGO model, i.e. (4.1), which is implemented in Abaqus.

The deformation is quantified by a deformation gradient \mathbf{F} , and the directions of two families of fibres are defined by vectors \mathbf{A}_1 and \mathbf{A}_2 in the reference configuration, and then

$$I_1 = \text{tr } \mathbf{C}, \quad I_n = \mathbf{C} : \mathbf{M}_n, \quad n = 4, 6, \quad (6.2)$$

where $\mathbf{C} = \mathbf{F}^T \mathbf{F}$, $\mathbf{M}_4 = \mathbf{A}_1 \otimes \mathbf{A}_1$, and $\mathbf{M}_6 = \mathbf{A}_2 \otimes \mathbf{A}_2$. As shown in (2.19) and (2.40), the invariants I_4 and I_6 are squares of the stretches in the directions of \mathbf{A}_1 and \mathbf{A}_2 , respectively. Therefore, I_4 and I_6 quantify the deformation of fibres. A common assumption is that the fibres only support tension loading, i.e.

$$\psi(I_n) = \begin{cases} \frac{k_1}{2k_2} (\exp[k_2(I_n - 1)^2] - 1) & \text{when } I_n > 1 \\ 0 & \text{when } I_n \leq 1. \end{cases} \quad (6.3)$$

For the cylindrical tube model, the directions \mathbf{A}_1 and \mathbf{A}_2 are measured by the angle β between the fibre and circumferential directions, i.e. $\mathbf{A}_1 = (0, \cos \beta, \sin \beta)$ and $\mathbf{A}_2 = (0, \cos \beta, -\sin \beta)$, as shown in Figure 6.1.

The associated Cauchy stress for the incompressible HGO model is

$$\boldsymbol{\sigma} = -\mathcal{P}\mathbf{I} + 2c\mathbf{B} + \sum_{n=4,6} 2\psi'(I_n)\mathbf{m}_n, \quad (6.4)$$

where \mathcal{P} is the Lagrange multiplier for the incompressibility constraint, $\mathbf{B} = \mathbf{F}\mathbf{F}^T$, and $\mathbf{m}_n = \mathbf{F}\mathbf{M}_n\mathbf{F}^T$, ($n = 4, 6$). The value of \mathcal{P} is determined by the equilibrium equation and the boundary conditions in any particular problem.

Table 6.1: The values of material parameters in the HGO strain energy function for the two-layer arterial wall model for a carotid artery from a rabbit are obtained from Figure 14 in [Holzapfel et al., 2000]

	c [kPa]	k_1 [kPa]	k_2	β [°]
media	1.5	2.3632	0.8393	29
adventitia	0.15	0.5620	0.7112	62

6.2.2 Geometry

Each simulation starts from a stress-free configuration Ω_0 (Figure 6.1). In order to guarantee the difference among simulations is only the value of the opening angle or residual stress, we use the inverse analysis (Section 5.3.2) to compute analytically the stress-free configuration of the given unloaded configuration Ω_r for each value of the opening angles, $\alpha = 40^\circ, 80^\circ, 120^\circ, 160^\circ$ and 200° , so that the same unloaded configuration Ω_r in Figure 6.1 is obtained in equilibrium status, after closing Ω_0 for different values of α .

The target unloaded configuration Ω_r is that of the two-layer arterial wall in equilibrium, in the absence of pressure ($p_i = 0$) on the inner radial surface of the stress-free configuration with an opening angle $\alpha = 160^\circ$, the geometry of which is obtained from [Holzapfel et al., 2000]. In our simulation, the geometry of this target configuration is obtained by using the boundary conditions associated with this loading condition ($p_i = 0$) through the forward analysis in Section 5.3.1.

The governing equations for analytical solution are the same as those in Sections 5.3.1 and 5.3.2, but with the HGO constitutive law in (6.1).

6.2.3 Boundary conditions

Each simulation starts from a stress-free configuration Ω_0 as in Figure 6.1. Two simulation steps are performed: 1) closing Ω_0 to obtain the unloaded configuration and introduce the residual stress; 2) inflating both the lumen and tear to simulate the arterial dissection subject to a ramping pressure.

The first step includes several boundary conditions in sequence:

- fixing the radius A along the y -axis direction such that it does not move up or down; moving the radius B towards the y -axis such that it reaches the y -axis and does not

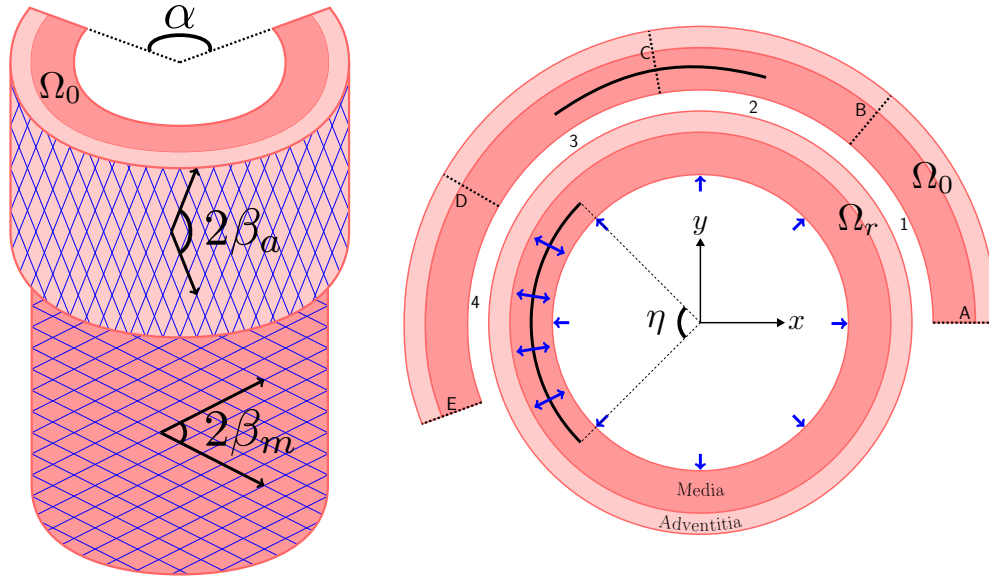


Figure 6.1: We consider cross-section of the arterial wall: the stress-free Ω_0 with an opening angle α and unloaded Ω_r configurations with residual stress, including an initial tear (black arc). This tear subtends $\eta = 90^\circ$ and is at the centre of the media. Each layer is assumed to be a hyperelastic fibre-reinforced material, modelled by the HGO strain energy function. β_m and β_a define the angles between the two families of fibres in the media and adventitia, respectively. The radii A, B, C, D and E are equally spaced and separate the inner surfaces labelled 1,2,3 and 4. In simulations, Ω_0 is closed to obtain Ω_r with residual stress, and then an increasing pressure (arrows) is applied on the inner radial and tear surfaces to simulate the inflation and tear propagation.

move right or left from now on; applying a pre-pressure p_i^0 on both the inner radial surface 1 and tear surface to avoid contact, which would increase the computational cost extremely and cause the divergence of computation.

- moving the radius C towards the x -axis such that it reaches the x -axis and does not move up or down from now on; applying p_i^0 on the inner radial surface 2,
- moving the radius D towards the y -axis such that it reaches the y -axis and does not move right or left from now on; applying p_i^0 on the inner radial surface 3,
- moving the radius E towards the x -axis such that it reaches the x -axis and does not move up or down from now on; applying p_i^0 on the inner radial surface 4,
- applying the $-p_i^0$ on both the inner radial surfaces 1–4 and tear surface to obtain the target unloaded configuration Ω_r .

After the first step, the target unloaded configuration is obtained and the residual stress is included. In the second step, both tear and lumen are inflated subject to the same ramping pressure on both the inner radial surfaces 1–4 and two faces of the tear. The critical pressure is identified as that at which the tear starts to propagate.

6.2.4 Damage and failure

The constitutive law for material damage and failure is the linear cohesive law in the Section 5.2.3. The parameters we used for these simulations with the HGO material model are shown in the Table 6.2.

Table 6.2: Cohesive law parameters for each layer of the two-layer HGO arterial wall

	T_c [kPa]	G_c [J/m ²]	u_c [mm]
media	3	0.001	6.67×10^{-4}
adventitia	0.3	0.0001	6.67×10^{-4}

6.3 Results

As a verification, this method for introducing the residual stress into the FE model, is firstly used in an example for the neo-Hookean material. The critical pressure obtained

by this method is compared to that calculated by the method of Chapter 5, which uses the analytical expression of the residual stress. Then several simulations with the HGO material are performed with different values of the opening angle α . To plot the trend of p'_c against α , we present the effect of residual stress on the critical pressure for tear propagation with the HGO material.

6.3.1 The neo-Hookean material

Inflation of the artery

This simulation is to verify this new method of introducing residual stress computed numerically. Similarly to Section 5.5, inflation of the two-layer arterial wall with the opening angle $\alpha = 160^\circ$ is analysed. The tear is not included in the example of inflation. The internal pressure is $p_i=13.33$ kPa. For verification purposes, we compare the residual stress before inflation and the total Cauchy stress across the arterial wall after inflation, calculated in three ways.

We use three methods to calculate the deformation and stress. They are referred to as *analytical*, *numerical* and *combined*. The *direct numerical method* is introduced in this chapter: the simulation starts from the stress-free configuration Ω_0 , and then the unloaded configuration and following deformation subject to an internal pressure are calculated numerically. The *combined method* is introduced in Chapter 5: the simulation starts from the unloaded configuration Ω_r , and the analytical results for the values of the residual stress are imported into the FE model before any boundary condition is applied. The *analytical method* solves the problem mathematically using the equations in Section 5.3.

The boundary conditions in Figure 6.2 are used to avoid rigid body motion in the combined method. The other techniques are same with those in Chapter 5. These boundary conditions are equivalent to those (Figure 6.1) in the direct numerical method. Using this boundary condition guarantees that the results from the numerical and combined method are comparable.

The comparison of results in Figure 6.3 shows that the residual stress computed numerically similar to the analytical solutions, and the relative error is less than 4.74%, which is computed via (4.15). The residual stresses in the simulation with the combined method are exactly the same as in the analytical solutions. That verifies the implementation of 'sigini.f', which imports the analytical residual stress into the FE model.

The total Cauchy stresses across the arterial wall inflated subject to $p_i = 13.33$ kPa through three methods are also compared in Figure 6.4. Both the numerical and combined methods can compute the stress accurately with very small error: the relative error from the direct numerical method is 0.46%, and the relative error from the combined method 0.49%.

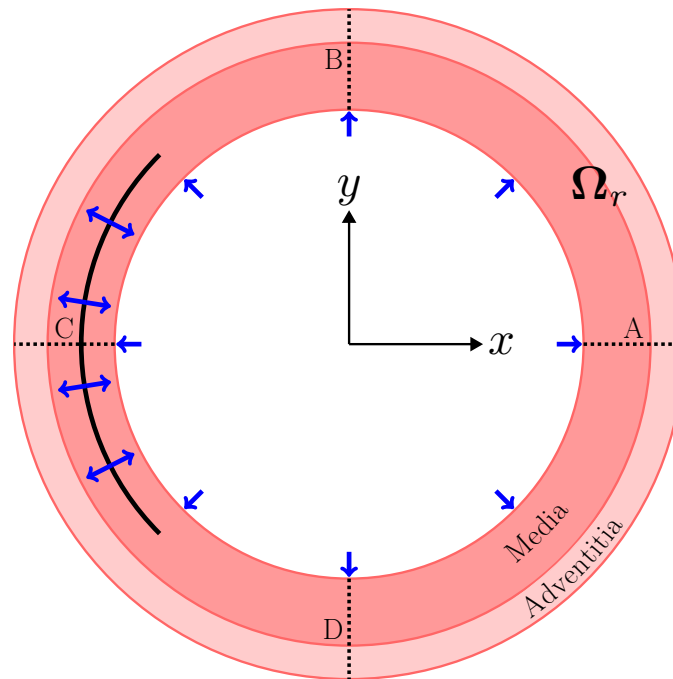


Figure 6.2: The radii A and C are fixed in the y direction, and the radii B and D are fixed in the x direction, to avoid rigid body motion. These boundary conditions are referred to as the *quarter* boundary conditions. The pressure (arrows) is increased on both the inner radial and tear surfaces.

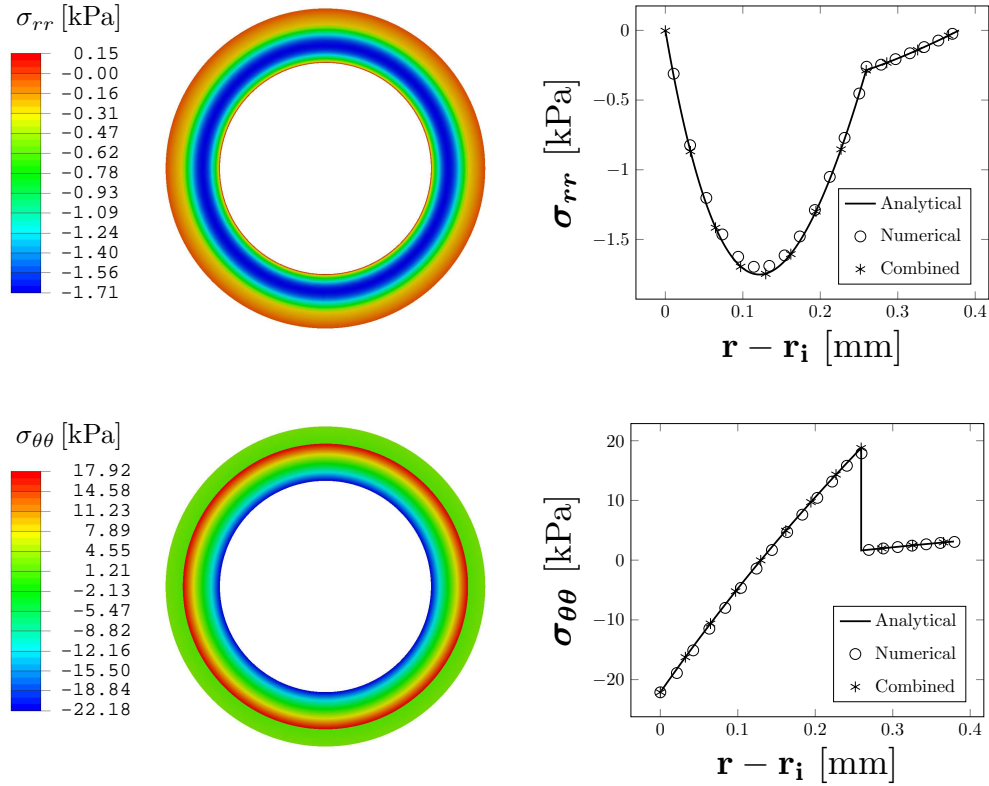


Figure 6.3: Left, the contours of residual stress components computed numerically are shown in the unloaded configuration Ω_r subject to $p_i = 0$ for the stress-free configuration with opening angle $\alpha = 160^\circ$. This computation uses the neo-Hookean material. In this unloaded configuration, the inner radius $r_i = 0.74$ mm, thickness of the media and advenetitia are 0.26 mm and 0.12 mm, respectively. Right, the components of residual stress across the deformed arterial wall are plotted. The residual stress computed by the direct numerical method is similar to the analytical solutions with a relative error of less than 4.74%, and residual stress used in the combined method is the same as the analytical solution. The changes in the tangent of curve σ_{rr} and discontinuity in $\sigma_{\theta\theta}$ occur at the interface between the media and adventitia. That is because the material properties of two layers are different.

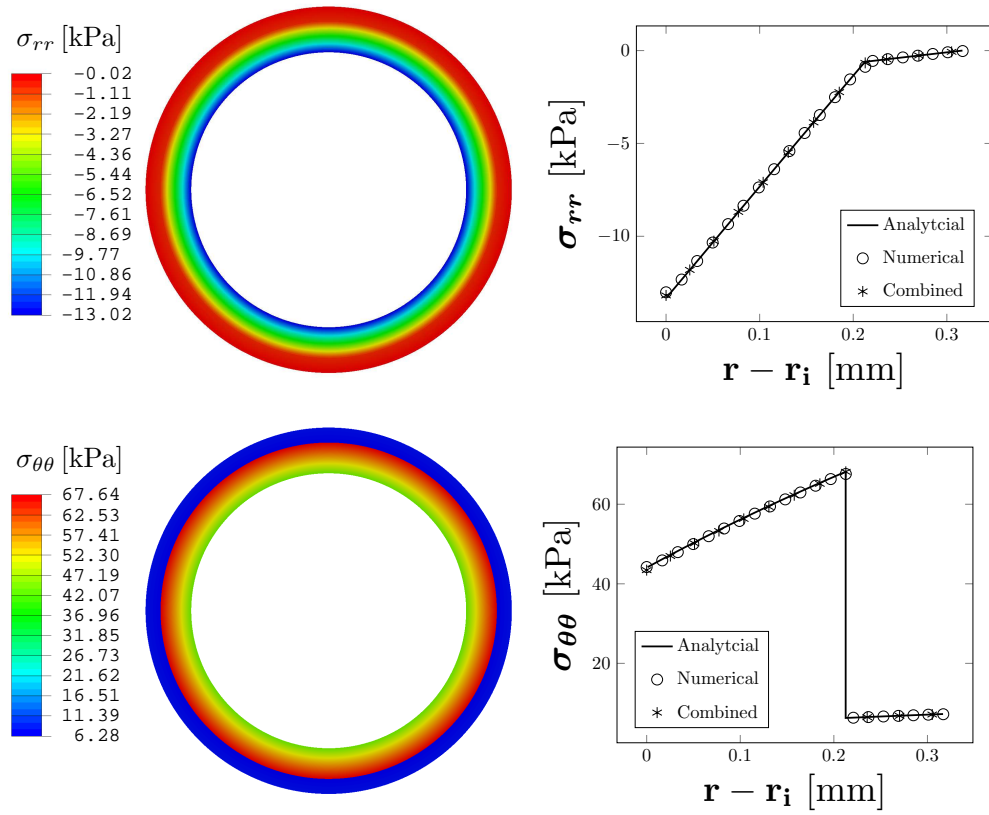


Figure 6.4: Left, the contours of Cauchy stress components calculated numerically are shown in the deformed arterial wall subject to $p_i=13.33$ kPa for the stress-free configuration with opening angle $\alpha = 160^\circ$. This computation uses the neo-Hookean material. In this deformed configuration, the inner radius $r_i = 0.95$ mm, thickness of the media and advenetitia are 0.21 mm and 0.10 mm, respectively. Right, the components of Cauchy stress across the deformed arterial wall are plotted. The stress computed by numerical and combined methods is similar to analytical solutions with relative errors of less than 0.46% and 0.49%, respectively.

Tear propagation

The simulations leading to tear propagation are performed in the two-layer neo-Hookean arterial wall with residual stress using the combined and direct numerical methods. Recall that the combined method in Chapter 5 uses the analytical residual stress, while the direct numerical method in this chapter computes the residual stress numerically in Abaqus, and then simulates the subsequent tear opening. The critical pressures are obtained from each simulation for a particular opening angle. Figure 6.5 confirms our finding, that critical pressure increases almost linearly with the opening angle. The trend in $p'_c(\alpha)$ predicted from two methods is similar with a relative error of less than 2.8%. The good agreement in values of p'_c obtained with these two methods shows that the direct numerical method works as well as the combined method. The direct numerical method can be used in a model with the HGO material, but the combined method cannot.

The stress patterns in the deformed arterial wall subject to the critical pressure for different values of opening angle (Figure 6.6) computed by the direct numerical method are also very similar to those (Figure 6.7) computed by the combined method. As the opening angle increases, the critical pressure increases. Therefore, the greatest value σ_{max} of the maximum principal stress σ_{mp} increases and the least value σ_{min} decreases as the opening angle increases. As shown in Figure 5.4, σ_{max} is obtained by averaging σ_{mp} over the quadrature points of the first ring elements around the tear tip.

The comparison of the critical pressure obtained by the combined method with three different boundary conditions used to avoid rigid body motion is shown in Figure 6.8. The term ‘quarter’ refers to the boundary condition in Figure 6.2, ‘kinematic coupling’ refers to Figure 5.7, and ‘fixed point’ refers to Figure 5.1. The comparison shows that the critical pressures with the quarter BC is similar to others, and the difference in the critical pressures is less when compared to that with the kinematic coupling BC (relative difference of less than 0.6%) than with the fixed point BC (relative difference of less than 3.7%). That is because the stress patterns (Figure 6.7) are more similar to those (Figure 5.8) with the kinematic coupling BC than those (Figure 5.5) with the fixed point BC. This good agreement shows that the effect of these three boundary conditions used to avoid rigid body motion is small on the computation of critical pressure.

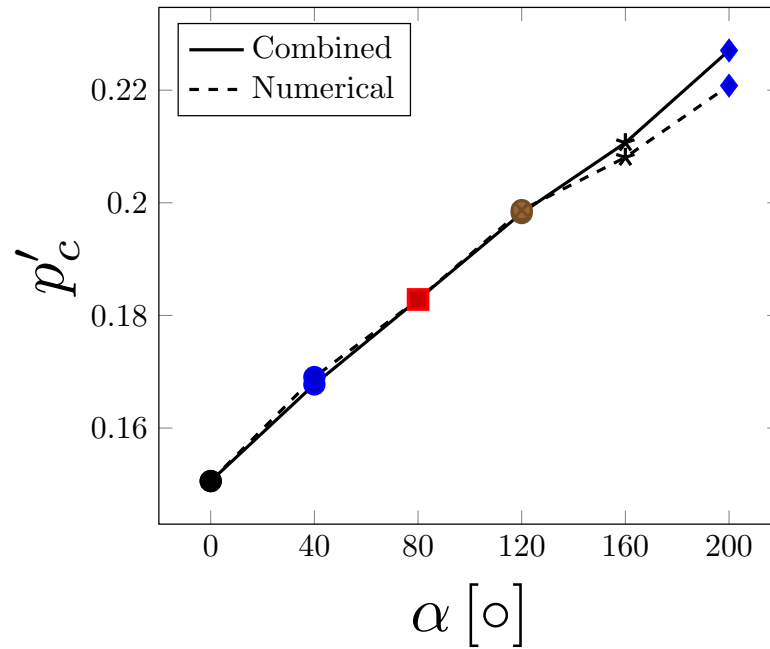


Figure 6.5: The dimensionless critical pressure $p'_c = p_c/c_m$, where $c_m = 38.45$ kPa is the shear modulus of the media, is plotted against the opening angle α . These computations use the neo-Hookean material. The trend in $p'_c(\alpha)$, predicted by the combined and direct numerical methods, are similar with a relative error of less than 2.8%.

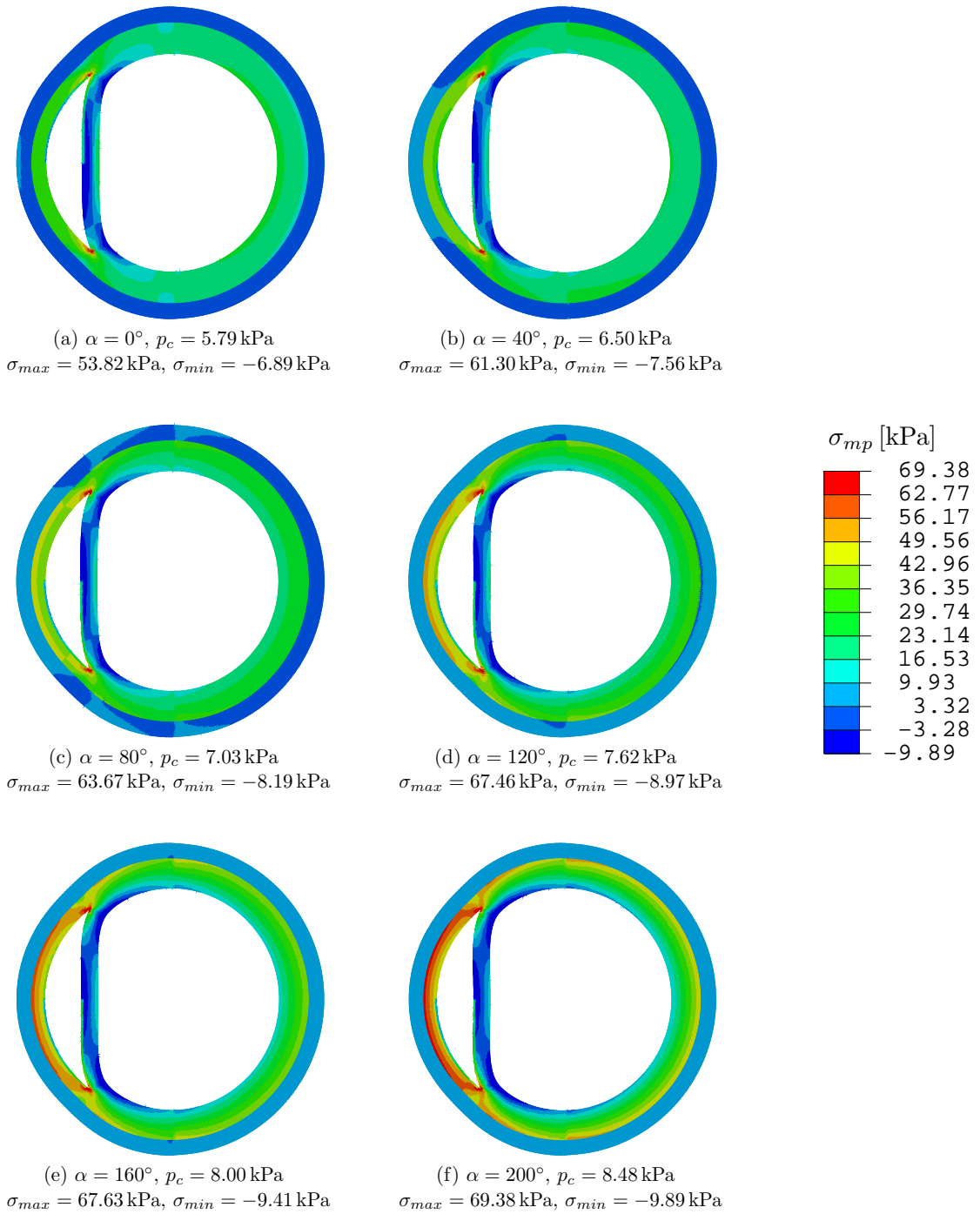


Figure 6.6: The contour of maximum principal stress σ_{mp} in the deformed configurations subject to the critical pressure p_c is shown for different values of the opening angle α . The tip-stress field is averaged over quadrature points of the first ring elements around tip to obtain σ_{max} . In these simulations, the material model is the neo-Hookean, and the residual stress is introduced by the direct numerical method.

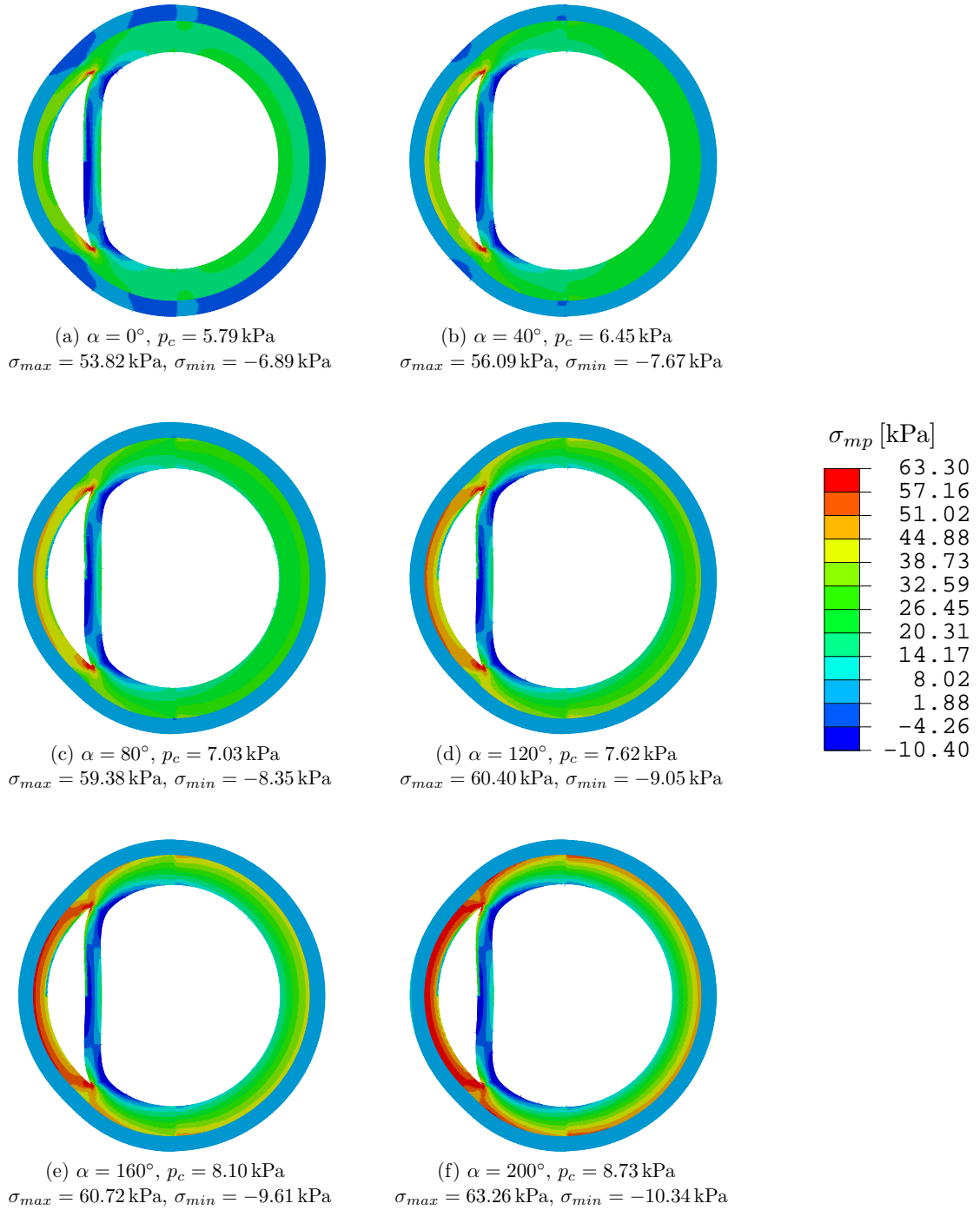


Figure 6.7: The contour of maximum principal stress σ_{mp} in the deformed configuration subject to the critical pressure p_c is shown for different values of the opening angle α . The tip-stress field is averaged over quadrature points of the first ring elements around tip to obtain σ_{max} . In these simulations, the material model is the neo-Hookean, and the residual stress is introduced by the combined method with the quarter boundary condition (Figure 6.2).

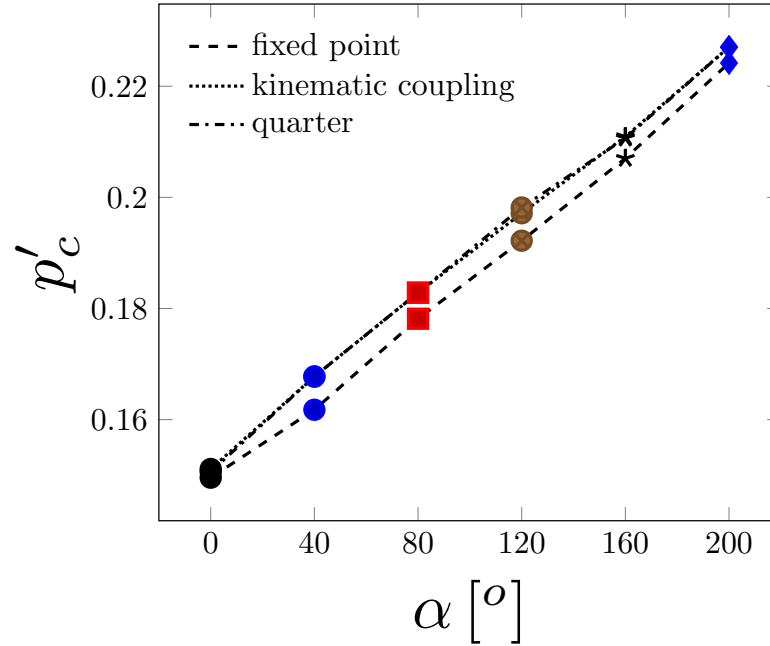


Figure 6.8: The dimensionless critical pressure $p'_c = p_c/c_m$, where $c_m = 38.45$ kPa is shear modulus of the media, is plotted against the opening angle α , with different boundary conditions used to avoid rigid body motion. These simulations use the combined method with the neo-Hookean material. The critical pressures with the quarter BC (Figure 6.2) are almost the same with those with the kinematic coupling BC (Figure 5.7), and the relative difference is less than 0.6%. The critical pressures with the quarter BC are also similar to those with the fixed point BC (Figure 5.1), and the relative difference is less than 3.7%.

6.3.2 HGO material

Inflation of artery

The accuracy of this direct numerical method with the HGO material is checked through the simulation for inflation of the two-layer arterial wall without a tear. Applying boundary conditions in Section 6.2.3 on the arterial wall with the opening angle $\alpha = 160^\circ$, the simulation obtains the unloaded configuration Ω_r in equilibrium and residual stress. The computed inner radius of Ω_r is $r_i^n = 0.738$ mm, which is similar to the analytical solution $r_i^a = 0.739$ mm with a relative error of 0.14%. The computed residual stress σ through the arterial wall in Ω_r agrees with analytical results, as shown in Figure 6.9 with a relative error of less than 5.17%, which is computed by (4.15). After obtaining Ω_r and computing residual stress numerically, the lumen is inflated subject to a pressure $p_i=13.33$ kPa. As shown in Figure 6.10, the computed inner radius of the deformed configuration is $r_i^n = 1.429$ mm, which is similar to the analytical solution $r_i^a = 1.427$ mm with a relative error of 0.14%. As shown in (5.8), the deformation of the arterial wall depends on the inner radius. The computed Cauchy stress across the deformed arterial wall also agrees with the analytical results with a relative error of less than 1.74%. Therefore, the good agreement in inner radius r_i and stress σ verifies this direct numerical method for introducing residual stress with the HGO material.

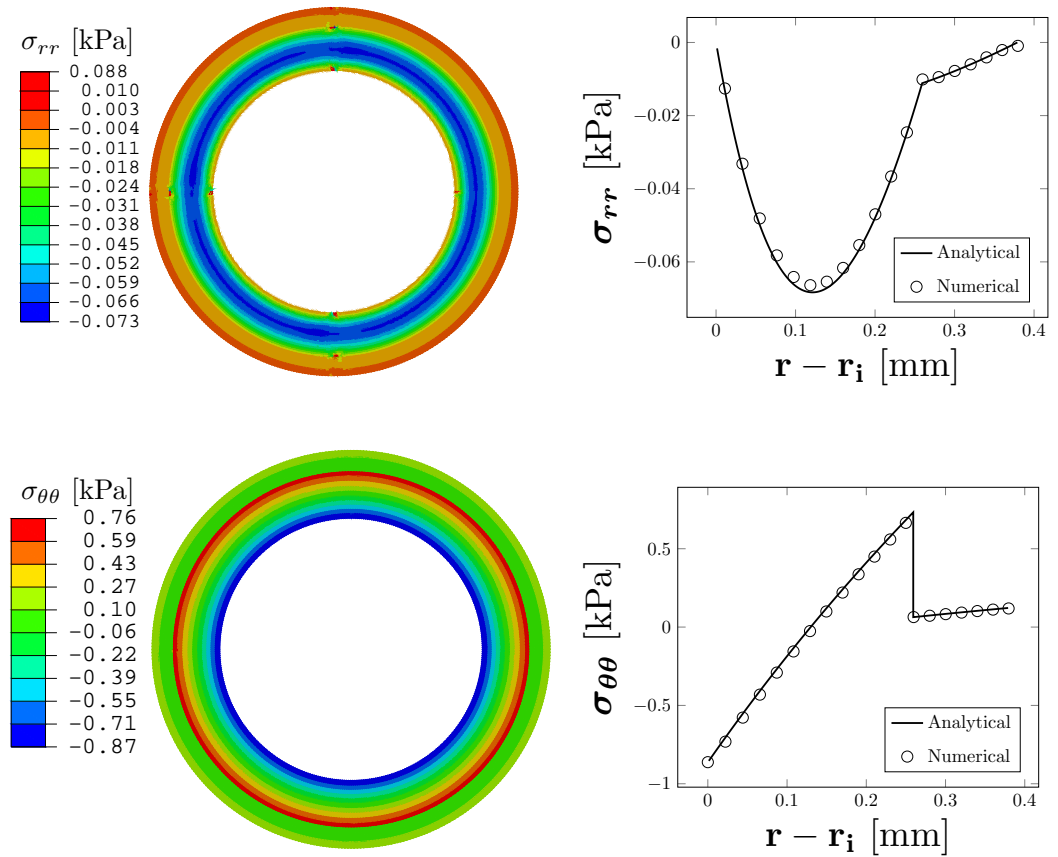


Figure 6.9: Left, the contours of residual stress components computed numerically in the unloaded configuration Ω_r subject to $p_i = 0$ for the stress-free configuration with the opening angle $\alpha = 160^\circ$. The computed inner radius of Ω_r is $r_i = 0.739$ mm, which is close to the analytical solution with a relative error of 0.14%, and thickness of the media and adventitia are 0.259 mm and 0.120 mm, respectively. The material model is the HGO constitutive law. Right, components of residual stress across the arterial wall in Ω_r are plotted against the radial distance $r - r_i$ from the inner radial surface. The change of gradient in σ_{rr} and discontinuity in $\sigma_{\theta\theta}$ occur at the interface between the media and adventitia. That is because the material properties of the media and adventitia are different. The residual stress computed numerically agrees with analytical solution with a relative error of less than 5.17%.

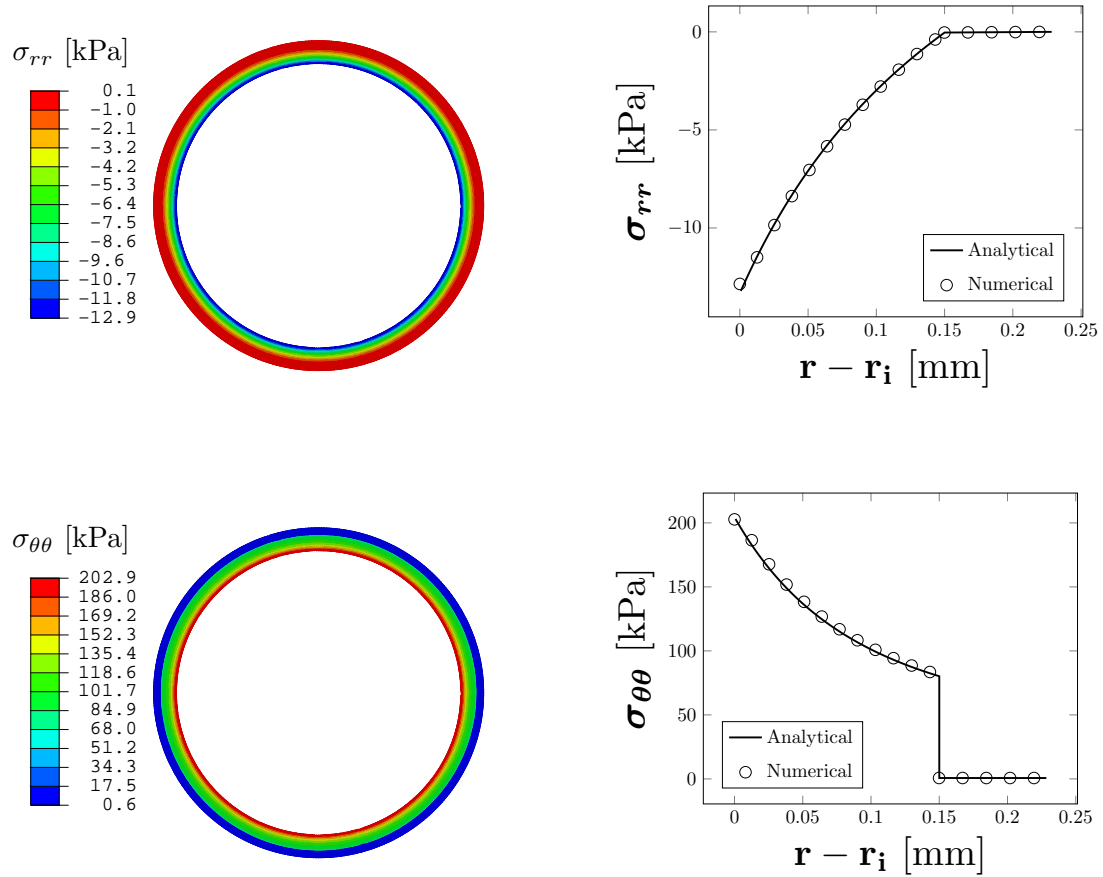


Figure 6.10: Left, the contours of Cauchy stress components computed numerically in the deformed arterial wall subject to $p_i=13.33$ kPa for the stress-free configuration Ω_0 with the opening angle $\alpha = 160^\circ$. In this deformed configuration, the computed inner radius $r_i=1.429$ mm, which is close to the analytical solution with a relative error of 0.14%, and thickness of the media and adventitia are 0.150 mm and 0.078 mm, respectively. The material model is the HGO constitutive law. Right, components of Cauchy stress across the arterial wall in Ω_r are plotted against the radial distance $r - r_i$ from the inner radial surface. The Cauchy stress computed numerically agrees with analytical solution with a relative error of less than 1.74%.

Tear propagation

Obtaining the stress-free configurations associated with different values of the opening angle, for a fixed unloaded configuration, is a crucial step before the FE simulation. Using the inverse analysis in Section 5.3.2, we solve analytically the stress-free configuration associated with a particular value of the opening angle for this HGO arterial wall. These stress-free configurations are used in the simulations. In the meantime, the analytical residual stress is computed. As shown in Figure 6.11, the magnitude of residual stress increases as the opening angle increases.

Each simulation with a particular opening angle starts from the stress-free configuration with an initial tear. Four-node plane-strain hybrid elements are used to construct the mesh for this model as shown in Figure 6.12. A grid independence test was used to select the optimal number of elements for which the computed stresses converge to the analytical solutions (Table 6.3 and Figure 6.13). The intermediate mesh was then chosen in all the simulations.

The two simulation steps with the opening angle $\alpha = 160^\circ$ are shown in Figures 6.14 and 6.15, respectively. During the simulation, the critical pressure was identified as that at which the tear starts to propagate. Finally, we plotted the trend of the critical pressure against the opening angle in Figure 6.16, and find that the critical pressure increases with the opening angle.

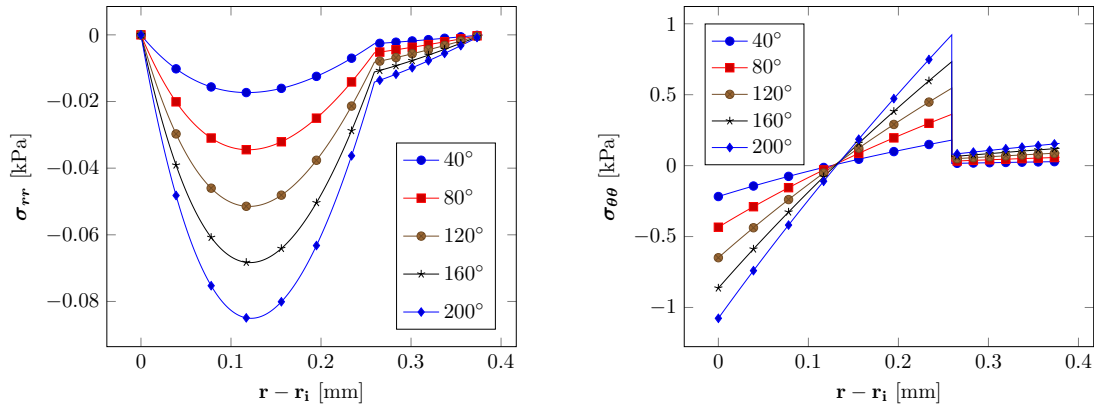


Figure 6.11: The residual stresses for different values of the opening angles are computed analytically. The material model is the HGO constitutive law. The magnitude of residual stress increases with the opening angle.

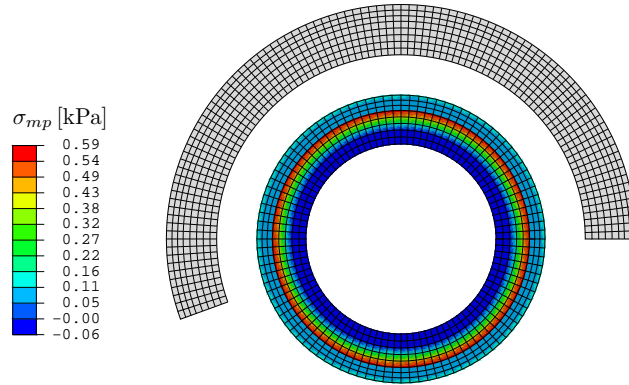


Figure 6.12: The stress-free Ω_0 (grey) and the unloaded Ω_r (coloured) configurations of the HGO arterial wall model with the coarse mesh in Table 6.3, where the colour indicates the maximum principal stress σ_{mp} , and the opening angle in Ω_0 is 160° . The simulation starts from Ω_0 with an inner radius $R_i = 1.43$ mm, and computes the equilibrium state by applying displacement boundary conditions (Figure 6.1) to obtain Ω_r with an inner radius $r_i = 0.74$ mm and residual stress.

Table 6.3: Meshes used for the grid independence tests

Mesh	Nodes	Elements				Relative error in stress computed via (4.15)
		media	adventitia	circumference	total	
coarse	909	5	3	100	800	21.37%
intermediate	3417	11	5	200	3200	5.59%
fine	13233	23	9	400	12800	5.08%

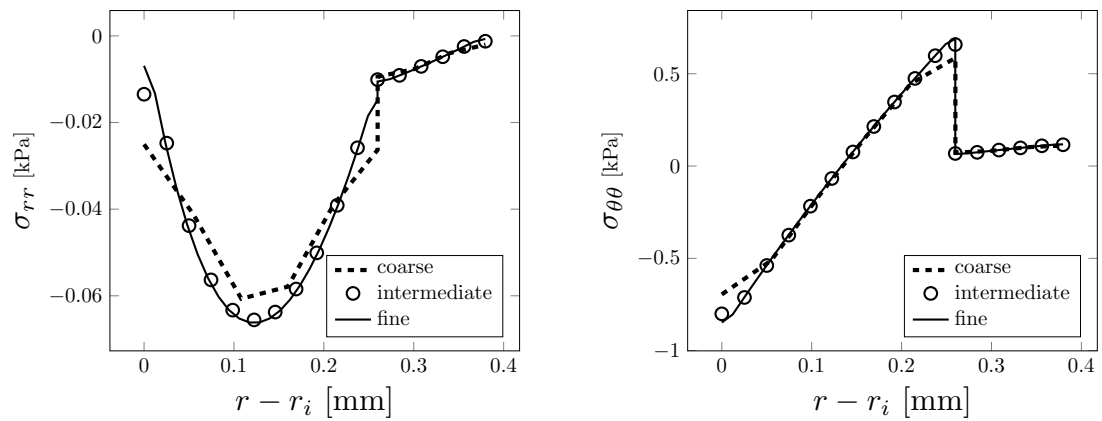


Figure 6.13: Values of the residual stress computed in the unloaded configuration Ω_r when $\alpha = 160^\circ$ for the meshes shown in Table 6.3, showing convergence as the mesh is fined.

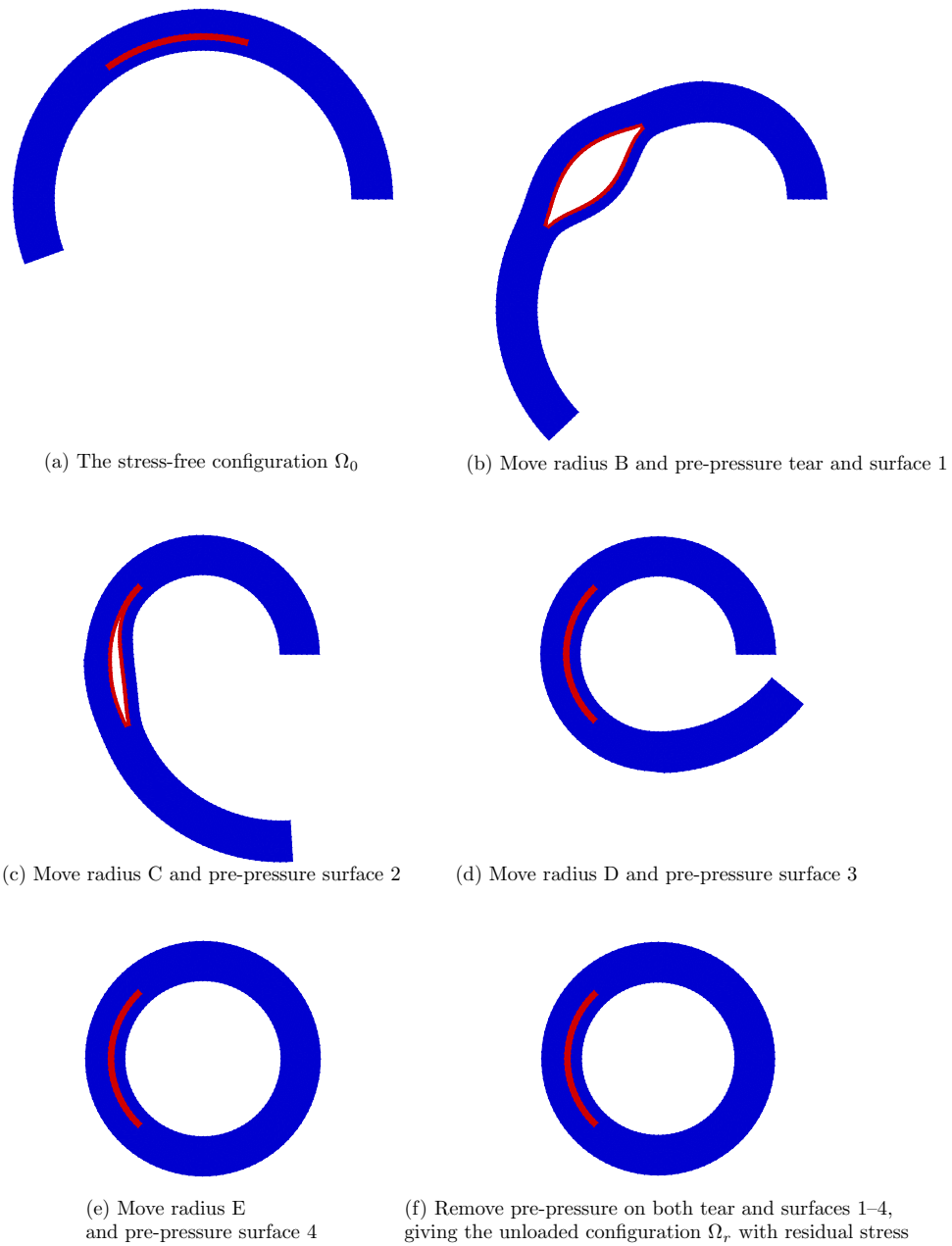


Figure 6.14: The geometries occurring during the closing process from Ω_0 to Ω_r , when $\alpha = 160^\circ$ and $\eta = 90^\circ$. See Figure 6.1 for definitions of the radii and surfaces.

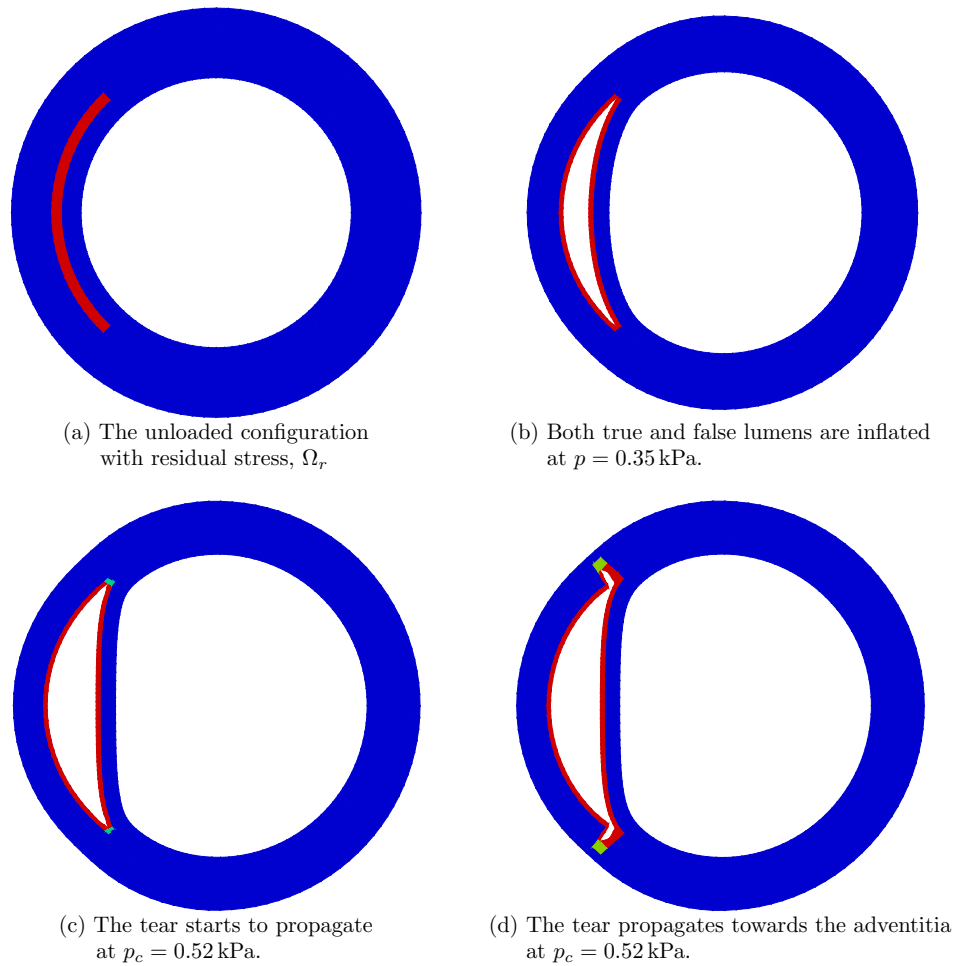


Figure 6.15: Tear propagation in an artery inflated by increased pressure loading at Ω_r when $\alpha = 160^\circ$ and $\eta = 90^\circ$ for (a) $p = 0$ kPa, (b) $p = 0.35$ kPa, (c) $p = p_c = 0.52$ kPa and (d) $p = p_c = 0.52$ kPa. The elements in blue are not damaged; those in red are completely torn. Those in other colours indicate the cohesive zone. The critical pressure is defined as that at which the tear starts to propagate as in (c). Increasing p beyond p_c results in a steady solution for which the tear has propagated radially outwards (d).

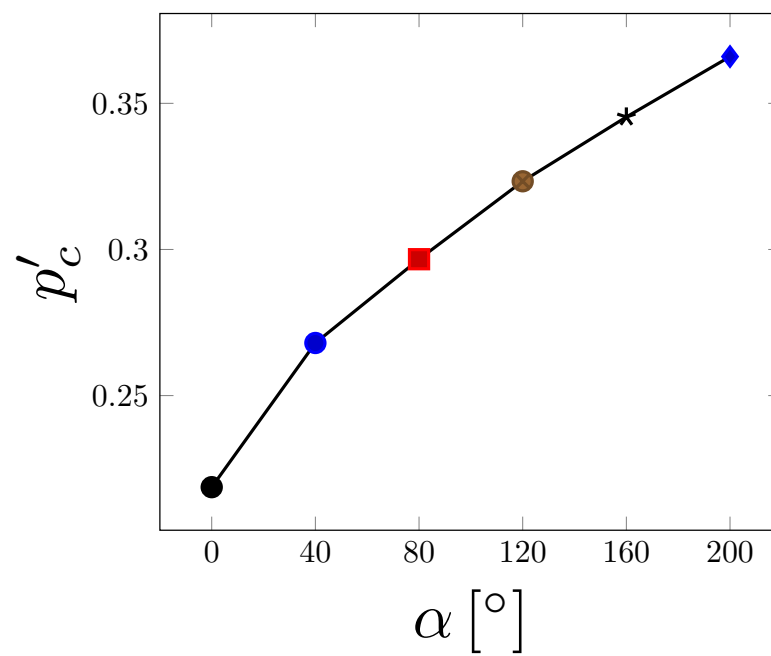


Figure 6.16: The dimensionless critical pressure $p'_c = p_c/c_m$, where $c_m = 1.5$ kPa is the shear modulus of matrix in media as shown in Table 6.1, is plotted against the opening angle α , for the HGO material.

6.3.3 The effect of fibre orientation

Here we vary the fibre orientation in the HGO model. We refer to the simulation in previous section as the physiological or ‘true’ case, since it uses the values of the fibre orientation from [Holzapfel et al., 2000], see Table 6.1. In other simulations, we use the same fibre orientation for the media and the adventitia, so that $\beta_m = \beta_a = \beta$. Simulations are performed with $\beta = 0^\circ, 10^\circ, 15^\circ, 20^\circ, 30^\circ, 60^\circ$ and 90° . In addition, a group of simulations is run without fibres ($k_1 = 0$), referred to as the ‘free’ case.

In order to use the same unloaded configuration Ω_r in each simulation, the stress-free configurations Ω_0 are estimated for each fibre orientation using the inverse analysis of Section 5.3.2. This ensures that the difference between the simulations is only due to the fibre orientations. The normalized thicknesses of the media and adventitia $D'_m = D_m/D_{mr}$ and $D'_a = D_a/D_{ar}$, where D_m and D_a are the thicknesses of media and adventitia in Ω_0 , and D_{mr} and D_{ar} in Ω_r , are plotted against the opening angle α in Figure 6.17 for several fibre distributions. The thickness of media D'_m decreases with the opening angle with smaller values of β (e.g. when $\beta = 0^\circ$ or 10°), but the trend changes as β increases. When $\beta \geq 30^\circ$ it increases monotonically. On the other hand, the thickness of the adventitia D'_a simply increases with the opening angle. For other fibre angles ($\beta = 60^\circ, 90^\circ, \text{free, true}$), the results are identical to that of $\beta = 30^\circ$. This is because fibres beyond this angle are no longer stretched, i.e. $I_4 < 1$ as shown in Figure 6.18, for this deformation $\Omega_0 \rightarrow \Omega_r$.

The critical pressure also changes for different values of β (Figure 6.19). Notice that with the inflation, fibres with $\beta = 30^\circ$ also start to bear load, but fibres at greater angles ($\beta = 60^\circ$ and $\beta = 90^\circ$) still do not take on any load, and hence the critical pressures for these cases remain the same in the ‘free’ case. As expected, the critical pressure when $\beta = 0^\circ$ is the highest since the residual stress is greatest in this case, as shown in Figure 6.20.

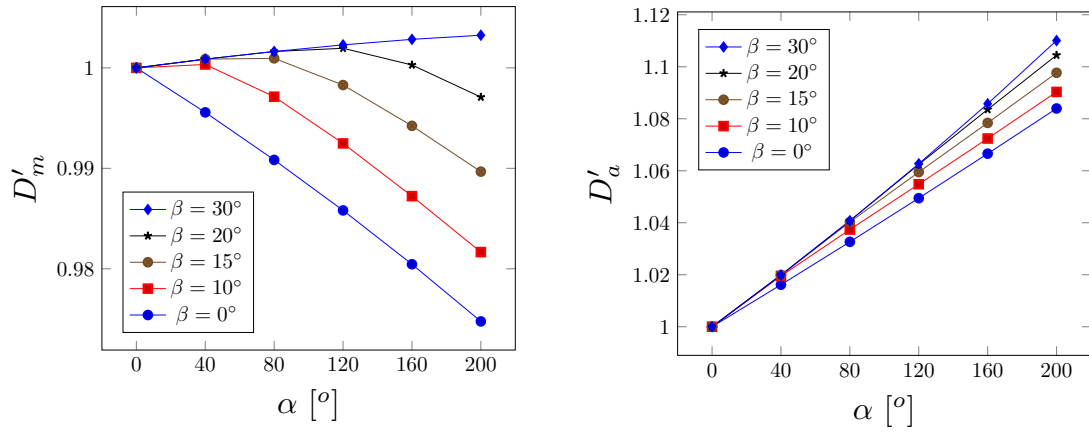


Figure 6.17: Wall thickness D'_m and D'_a for the media and adventitia in Ω_0 normalised with respect to their values in Ω_r , plotted against the opening angle for different fibre angles. For other fibre angles ($\beta = 60^\circ, 90^\circ, \text{free, true}$), the curves overlap that for $\beta = 30^\circ$.

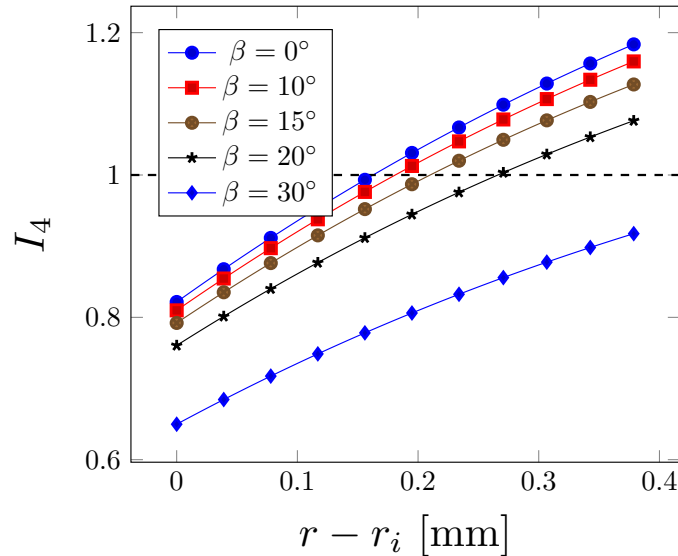


Figure 6.18: Value of the invariant I_4 plotted against the radius in Ω_r for different fibre angles.

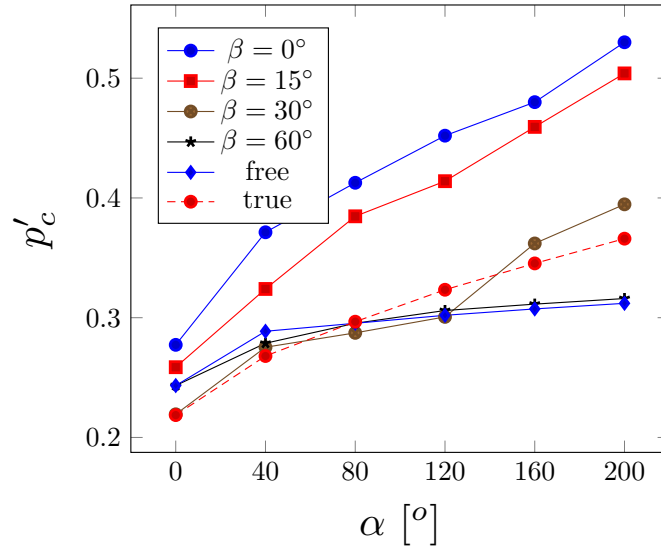


Figure 6.19: The dimensionless critical pressure $p'_c = p_c/c_m$, where $c_m = 1.5$ kPa is the shear modulus of matrix in media as shown in Table 6.1. The results for $\beta = 90^\circ$ (not shown) are identical to $\beta = 60^\circ$, and the ‘free’ case, indicating that the fibres at these angles do not bear a load in these deformations.

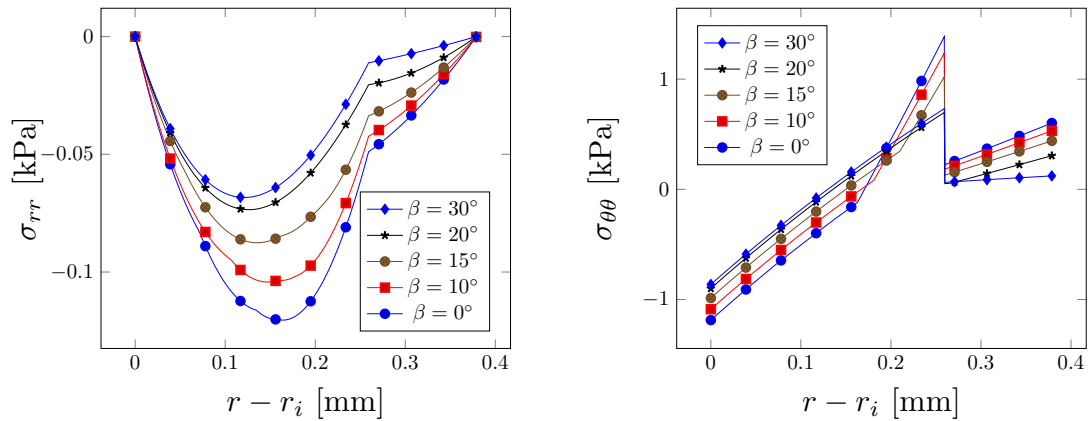


Figure 6.20: Distribution of residual stress components $\sigma_{\theta\theta}$ and σ_{rr} for $\alpha = 160^\circ$ and fibre angles. The values of σ_{rr} and $\sigma_{\theta\theta}$ in the cases $\beta = 60^\circ$, 90° , free, true are the same as for $\beta = 30^\circ$. The change in gradient of $\sigma_{\theta\theta}$ is due to the fibres being stretched, i.e. $I_4 > 1$, see Figure 6.18.

6.4 Conclusion

Directly computing the values of the residual stress in the FE model by closing the opening angle to obtain Ω_r overcomes the limitation that an anisotropic hyperelastic material cannot be used in the combined method of Chapter 5. We performed several simulations with both the neo-Hookean and HGO material.

The stress-free configuration Ω_0 is closed to obtain unloaded configuration Ω_r , using a sequence of boundary conditions. These boundary conditions are crucial in guarantee of computational efficiency and accuracy. Using a pre-pressure on the inner radial face and the two faces of the tear avoids buckling of the arterial wall and contact, reducing the computational cost. Using the quarter boundary condition, see Figure 6.1, guarantees that both ends of Ω_0 have same size and move together in the subsequent simulation for the inflation of the lumen and the tear.

Using this method for the neo-Hookean material shows that the values of the stress and critical pressure are similar to the results from the combined method of Chapter 5. In the simulation of inflation of the artery without a tear, both methods obtain values of the deformation and stress across the wall that are close to the analytical solutions (Figures 6.3 and 6.4). The critical pressures computed by both methods are also very similar; see Figure 6.5, showing that the direct numerical method works as well as the combined method. In addition, the computed critical pressures with different boundary conditions in the combined method are also in good agreement, see Figure 6.8, demonstrating that the quarter boundary condition has only a small effect on the computation of the critical pressure.

For the HGO material, only the direct numerical method can be used. This method is verified by showing that the deformation and stress for inflation of the artery without a tear agree well with the analytical solutions (Figures 6.9 and 6.10). We find that the dimensionless critical pressure p'_c increases with the opening angle α (Figure 6.16). In addition, we investigated the effect of fibre orientation on this trend, also showed that the critical pressure increases when the collagen fibres are in tension, see Figure 6.19.

Chapter 7

FE material model for living fibrous soft tissues

A strain energy function constructed by adding a volumetric term to an incompressible SEF, which is a function of the isochoric deformation gradient, has been used widely to model a nearly incompressible or compressible material. We represent the original incompressible SEF as $\bar{\Psi}$. A SEF based on $\bar{\Psi}$, which incorporates a term that depends on the volumetric deformation is labelled by $\hat{\Psi}$. In the construction of $\hat{\Psi}$, the multiplicative decomposition of deformation gradient $\mathbf{F} = J^{1/3}\bar{\mathbf{F}}$ is used, such that the isochoric deformation gradient $\bar{\mathbf{F}} = J^{-1/3}\mathbf{F}$ is obtained for $\bar{\Psi}$. This method of constructing of $\hat{\Psi}$ from $\bar{\Psi}$ can lead to a loss of anisotropic aspects of the material represented in $\bar{\Psi}$, as shown when applied to the HGO material [Nolan et al., 2014; Vergori et al., 2013]. More generally we find this problem exists for any anisotropic SEF. Here we demonstrate and explain the loss of anisotropy for SEFs constructed in this way, in particular we illustrate using a Fung-type and HGO SEF. We suggest that a possible remedy is that the multiplicative decomposition of \mathbf{F} into volumetric and isochoric parts should not be used in the terms representing anisotropy in $\bar{\Psi}$. A SEF constructed with this remedy from $\bar{\Psi}$ is denoted by $\tilde{\Psi}$. The incompressible HGO SEF $\bar{\Psi}$ includes a term for the isotropic matrix and separate terms for the collagen fibres, and the anisotropy of material is represented by adding these terms related to the fibres. The modified HGO SEF $\tilde{\Psi}$ uses \mathbf{F} instead of $\bar{\mathbf{F}}$ in these terms related to fibres in $\bar{\Psi}$. The anisotropy of material in an incompressible Fung-type SEF $\bar{\Psi}$ is controlled by the values of material parameters, there is no separate terms for the anisotropy of material. Therefore the modified Fung-type SEF $\tilde{\Psi}$ uses \mathbf{F} instead of $\bar{\mathbf{F}}$ in

all terms of $\bar{\Psi}$. Through several analytical examples, we demonstrate that $\tilde{\Psi}$ for both the Fung-type and the HGO SEFs correctly describe the behaviour of material in both the compressible and incompressible region. In some examples, $\tilde{\Psi}$ also provides a faster approximation to incompressibility than $\hat{\Psi}$ by using large values of the bulk modulus. Finally, a user material subroutine is developed in a finite element program FEAP for both $\hat{\Psi}$ and $\tilde{\Psi}$ for the HGO SEF.

In the user material subroutine, we include the living property of soft tissues—growth. We follow the approach of using the decomposition of the deformation gradient $\mathbf{F} = \mathbf{F}_e \mathbf{F}_g$ [e.g. Ambrosi et al., 2011; Rodriguez et al., 1994; Taber, 1995], where \mathbf{F}_e quantifies the elastic deformation and \mathbf{F}_g measures the growth contribution. Currently, the value for the growth tensor \mathbf{F}_g is specified a priori. The subroutine is validated through comparison of stress in simple examples, where the analytical results are the control. A growth law, of using a deformation-dependent value for \mathbf{F}_g , is easily developed in this subroutine. The method on how to implement explicitly and implicitly are discussed.

7.1 Introduction

There are two methods for solving the minimization of a variational problem in the FEM with the constraint of incompressibility. In the Lagrangian Method, a Lagrangian multiplier is introduced as a new variable, whereas the Penalty Method does not need additional variables. For example, when implementing an incompressible SEF $\bar{\Psi}$ using the Penalty Method, a penalty term, which is a function of the volumetric ratio $J = \det \mathbf{F}$, is added to $\bar{\Psi}$, as shown in Table 7.1. As $K \rightarrow \infty$, the SEF $\hat{\Psi}$ approximates the incompressible SEF $\bar{\Psi}$ in theory. $\hat{\Psi}$ also describes the elasticity of compressible material when employing a finite value for K . Therefore, the implementation of an incompressible and compressible SEF is unified within the penalty method as shown in the Table 7.1.

When constructing a SEF, $\hat{\Psi}$, the multiplicative decomposition of deformation gradient

$$\mathbf{F} = J^{1/3} \bar{\mathbf{F}} \quad (7.1)$$

is employed, and the isochoric kinematic tensor $\bar{\mathbf{F}}$ is the argument of $\bar{\Psi}$. This decomposition has been widely used in the many aspects of computational mechanics. This decomposition has significant advantages to deal with difficulty within the finite element approach due to the incompressibility of the plastic flow [Nagtegaal et al., 1974] and rubber-like material [Cescotto and Fonder, 1979; Ogden, 1978]. The decomposition is also

Table 7.1: The constructing SEF $\widehat{\Psi}$, by adding a volumetric term or penalty term Ψ_v onto a incompressible SEF $\bar{\Psi}$, unifies the implementation of a material model for compressible and incompressible finite elasticity, and so simplifies the computation and programming.

	Incompressible	Nearly-incompressible	Compressible
SEF	$\bar{\Psi}(\mathbf{C})$	$\widehat{\Psi}(\mathbf{C}) = \Psi_v(J) + \bar{\Psi}(\bar{\mathbf{C}})$	
		$\Psi_v(J) = KU(J)$ s.t. $U(1) = U'(1) = 0$	
Features	$J^2 = \det \mathbf{C} = 1$	$K \rightarrow \infty$	K
		is penalty parameter	is bulk modulus
Stress	$\boldsymbol{\sigma} = -\mathcal{P}\mathbf{I} + \frac{2}{J}\mathbf{F}\frac{d\bar{\Psi}}{d\mathbf{C}}\mathbf{F}^T$	$\boldsymbol{\sigma} = -\mathcal{P}\mathbf{I} + \frac{2}{J}\mathbf{F}\frac{d\bar{\Psi}}{d\bar{\mathbf{C}}}\frac{d\bar{\mathbf{C}}}{d\mathbf{C}}\mathbf{F}^T$	
	\mathcal{P} is determined by balance equations and BC	$\mathcal{P} = -\frac{d\Psi_v}{dJ}$	

employed when forming a constitutive law [Flory, 1961]. The idea has been used to propose the variational functional of mixed finite element [Simo and Taylor, 1991], where the additional pressure and volume field are introduced for a quasi-incompressible material. Notably, these works consider an isotropic material.

However, extending this idea directly to anisotropic material, naming, constructing a $\widehat{\Psi}$ with $\mathbf{F} = J^{1/3}\overline{\mathbf{F}}$ could lead to problems. Pence [2014] shows that the isotropic SEF within the decomposition automatically satisfies the requirement of stress-free for natural configuration, but an anisotropic SEF with this decomposition fails. Vergori et al. [2013] reported using of the HGO SEF with the decomposition in many finite element solvers leads to a non-physical deformation of a compressible sphere: a transversely isotropic sphere deforms to another sphere under hydrostatic tension, but the physical deformed configuration should be an ellipsoid. Nolan et al. [2014] presented a modified compressible HGO SEF by employing the full anisotropic invariants.

We find that this problem, loss of anisotropy, commonly exists in the FE implementation of any anisotropic material and is independent with the particular formulation of a SEF. In this chapter, we illustrate the problems of constructing compressible SEF $\widehat{\Psi}$ for an general anisotropic material model, through an analysis of the equilibrium of a cube subject to various loadings. In particular, we address the following questions: why does this problem occur? How can we implement a correct SEF for an anisotropic soft tissue?

We find that avoiding the use of (7.1) in the parts associated with anisotropy of a $\overline{\Psi}$, is a possible solution. We propose a physically correct FE SEF, denoted by $\widetilde{\Psi}$, for a fibrous soft tissue.

Both $\widetilde{\Psi}$ and $\widehat{\Psi}$ approximate the corresponding incompressible material SEF $\overline{\Psi}$ when $K \rightarrow \infty$. The effectiveness of them in this approximation is compared. The results show that using $\widetilde{\Psi}$ instead of $\widehat{\Psi}$ improve the computational efficiency and stability.

A user subroutine for the implementation of both $\widetilde{\Psi}$ and $\widehat{\Psi}$ of the incompressible HGO SEF in FEAP is presented. In this user subroutine, we include the volumetric growth property of a living fibrous soft tissue. Currently, the values for the growth tensor are specified a priori. This subroutine is verified through comparison of stress for simple problems. It is easy to update to incorporate a growth law, in which the value for growth tensor depends on mechanical qualities, like stain, stress or stored energy. Both explicit and implicit implementations of such a law in our subroutine are discussed. This subroutine has many applications. For example, the residual stress could be introduced by specifying

the growth tensor as a residual strain. To consider a stress-free two-layer arterial wall, in which we assume the inner layer of the arterial wall grows quicker than outer layer. After some time, at the interface of the inner and outer layers, the undeformed perimeter of the inner layer is greater than the undeformed perimeter of the outer layer due to growth. In order to maintain compatibility (material continuity) at the interface the outer layer is stretched and the inner layer compressed. As a result the two layers will be deformed and reach an equilibrium in which the material is unloaded but which has a non-zero state of stress—the residual stress. The latter approach is consistent with the common assumption that the origin of residual stress in soft tissue is due to the growth and remodelling at a location-dependent rate.

Notably, $\bar{\Psi}$ indicates an incompressible SEF, $\hat{\Psi}$ indicates a constructing FE SEF in the conventional approach and $\tilde{\Psi}$ indicates an FE SEF with our suggestion.

7.2 Problem of a $\hat{\Psi}$

7.2.1 Isotropic SEF

A SEF $\bar{\Psi}$ for an incompressible isotropic hyperelastic material has several equivalent forms. Since a rotation does not result change stored energy, the right Cauchy-Green strain tensor

$$\mathbf{C} = \mathbf{F}^T \mathbf{F}, \quad \det \mathbf{F} = 1$$

is used in a SEF. Alternatively, $\bar{\Psi}$ is defined as a function of Green strain tensor

$$\mathbf{E} = 1/2 (\mathbf{C} - \mathbf{I}).$$

Based on the invariant theory [Spencer, 1971], the SEF $\bar{\Psi}(\mathbf{C})$ has an equivalent form in terms of invariants

$$\bar{\Psi}(\mathbf{C}) = \bar{\Psi}(I_1, I_2), \tag{7.2}$$

where

$$I_1 = \text{tr } \mathbf{C}, \quad I_2 = \frac{1}{2} \left[(\text{tr } \mathbf{C})^2 - \text{tr } \mathbf{C}^2 \right] \tag{7.3}$$

Following [Flory, 1961; Ogden, 1978], the isochoric part of strain measure is obtained from using a multiplicative decomposition of deformation gradient as

$$\mathbf{F} = (J^{1/3} \mathbf{I}) \bar{\mathbf{F}}. \tag{7.4}$$

Then we have the isochoric right Cauchy-Green strain tensor

$$\bar{\mathbf{C}} = \bar{\mathbf{F}}^T \bar{\mathbf{F}} = J^{-2/3} \mathbf{C} \quad (7.5)$$

with $J = \det \mathbf{F}$ and then the isochoric invariants

$$\bar{I}_1 = \text{tr } \bar{\mathbf{C}}, \quad \bar{I}_2 = \frac{1}{2} \left[(\text{tr } \bar{\mathbf{C}})^2 - \text{tr } \bar{\mathbf{C}}^2 \right].$$

To construct a compressible or nearly-incompressible SEF for the implementation of $\bar{\Psi}$, a volumetric term Ψ_v is added, as conventional approach [e.g. Cescotto and Fonder, 1979]. So we have

$$\hat{\Psi} = \Psi_v(J) + \bar{\Psi}(\bar{\mathbf{C}}) \quad (7.6)$$

and

$$\hat{\Psi} = \Psi_v(J) + \bar{\Psi}(\bar{I}_1, \bar{I}_2), \quad (7.7)$$

where

$$J = \det \mathbf{F} \quad (7.8)$$

is the volume ratio after to before deformation, and $\bar{\Psi}$ depends on the isochoric part of strain measure.

To enforce the constraint of incompressibility, we introduce a penalty term Ψ_v

$$\Psi_v(J) = KU(J), \quad (7.9)$$

where the parameter K is called bulk modulus for a compressible material and a penalty parameter for a nearly-incompressible material. There are many models for $U(J)$ that are consistent with the requirement that the SEF is polyconvex and such that $U(1) = U'(1) = 0$ [Hartmann and Neff, 2003]. In the undeformed state, for which $J = 1$, is to be energy- and stress-free then we must have $U(1) = U'(1) = 0$. For our examples, we use

$$U(J) = \frac{1}{2}(J - 1)^2. \quad (7.10)$$

The penalty method [e.g. Bathe, 1996] is such that (7.6) and (7.7) approximate the SEF $\bar{\Psi}$ for perfectly incompressible material when a large value for K is used. In theory, the incompressibility is satisfied when $K \rightarrow \infty$. Therefore, (7.6) and (7.7) with a big value for K are often named by a nearly-incompressible or quasi-incompressible material model.

7.2.2 Anisotropic SEF

Most of soft tissues, like the wall of an artery, the heart and the gallbladder, are nearly incompressible. They are in general reinforced by collagen fibres, which are stiffer than other components including the smooth muscle and elastin fibres, especially in the high stretch regime. Therefore, these soft tissues have significant anisotropy, so the direction-preferred mechanical response should be considered when forming a SEF. For example, the anisotropy is specified through the material parameters in a general Fung-type SEF [Humphrey, 1994], and through using a structure tensor for describing fibres orientation in the Holzapfel–Gasser–Ogden SEF [Holzapfel et al., 2000]. Without loss of generality, we consider the tissue reinforced by one family of fibres, so it has transversely isotropic elasticity.

Fung-type SEF

A general three dimensional incompressible Fung-type SEF, formulated by Humphrey [1994], is

$$\bar{\Psi}(\mathbf{E}) = \frac{a}{2} [\exp(Q) - 1], \text{ s.t. } \det \mathbf{F} = 1, \quad (7.11)$$

where

$$Q = b_1 E_{11}^2 + b_2 E_{22}^2 + b_3 E_{33}^2 + 2b_4 E_{11} E_{22} + 2b_5 E_{22} E_{33} + 2b_6 E_{33} E_{11} + b_7 E_{12}^2 + b_8 E_{23}^2 + b_9 E_{31}^2.$$

The material parameters b_i , $i = 1, \dots, 9$ are the entries of the fourth-order elasticity tensor. For this transversely isotropic material, the elasticity tensor only depends on five constants derived from the symmetry of material.

Analogous to (7.6), the constructing compressible Fung-type SEF is

$$\hat{\Psi} = \Psi_v(J) + \bar{\Psi}(\bar{\mathbf{E}}), \quad (7.12)$$

where $\bar{\mathbf{E}} = 1/2(\bar{\mathbf{C}} - \mathbf{I})$.

Holzapfel-Gasser-Ogden SEF

The HGO SEF [Holzapfel et al., 2000] employs a structure tensor, which defines the orientation of collagen fibres, to specify the anisotropy. Here we consider a transversely isotropic material, which is only reinforced by one family of fibres. Assume the orientation of fibre is defined by a unit vector \mathbf{A}_1 in the reference configuration. When the material is

loaded, a fibre will have the deformation specified by $\mathbf{a}_1 = \mathbf{F}\mathbf{A}_1$. According to [Spencer, 1984], two additional anisotropic invariants are introduced

$$I_4 = \mathbf{A}_1 \cdot \mathbf{C} \cdot \mathbf{A}_1, \quad I_5 = \mathbf{A}_1 \cdot \mathbf{C}^2 \cdot \mathbf{A}_1. \quad (7.13)$$

or

$$I_4 = \mathbf{a}_1 \cdot \mathbf{a}_1, \quad I_5 = \mathbf{a}_1 \cdot \mathbf{C} \cdot \mathbf{a}_1. \quad (7.14)$$

The invariant I_4 is the square of the fibre stretch. However, I_5 is difficult to relate to any physical quantity. For this reason and lack of sufficient experimental data, it is common to neglect the effect of this invariant in a strain energy function. For example, the transversely isotropic HGO SEF is

$$\begin{aligned} \bar{\Psi}(I_1, I_4) &= \bar{\Psi}_m(I_1) + \bar{\Psi}_f(I_4) \\ &= \frac{c}{2}(I_1 - 3) + H(I_4)\psi_f(I_4), \quad \text{s.t. } \det \mathbf{F} = 1, \end{aligned} \quad (7.15)$$

where the switch condition $H(\cdot)$ indicating that fibres can only take on stretch load, is defined as

$$H(x) = \begin{cases} 0 & x \leq 1 \\ 1 & x > 1 \end{cases}$$

and the exponential stretch stiffening stored energy function for fibres is

$$\psi_f(x) = \frac{k_1}{k_2} \{ \exp[k_2(x-1)^2] - 1 \}.$$

Analogous to (7.7), the compressible HGO SEF is

$$\hat{\Psi} = \Psi_v(J) + \bar{\Psi}(\bar{I}_1, \bar{I}_4), \quad (7.16)$$

where $\bar{I}_4 = \mathbf{A}_1 \cdot \bar{\mathbf{C}} \cdot \mathbf{A}_1$.

7.2.3 The problem of $\hat{\Psi}$ and a possible solution

Through an example we demonstrate the problem—loss of anisotropy—during an elastic deformation of an anisotropic material, when using $\hat{\Psi}$. Consider a uniform dilation,

$$\mathbf{F} = \lambda \mathbf{I} \quad (7.17)$$

and then

$$J = \lambda^3, \quad \bar{\mathbf{F}} = \mathbf{I}.$$

Therefore, the $\bar{\mathbf{C}} = \bar{\mathbf{F}}^T \bar{\mathbf{F}} = \mathbf{I}$ leads to

$$\bar{\mathbf{E}} = \mathbf{0}, \quad \bar{I}_1 = 3 \text{ and } \bar{I}_4 = 1. \quad (7.18)$$

The values for these isochoric strain measures are constant for any value of λ , so they are independent on the deformation. That results in $\bar{\Psi} = 0$ in (7.12) for the Fung-type $\hat{\Psi}$ and in (7.16) for HGO $\hat{\Psi}$. As a result

$$\hat{\Psi} = \Psi_v(J) \quad (7.19)$$

becomes isotropic, so the anisotropy of material is *lost*.

In order to avoid this problem above and correctly model the anisotropy of material in a SEF, we propose that the multiplicative decomposition of the deformation gradient \mathbf{F} in (7.1) should not be used in the terms, associated with the anisotropy, of a SEF $\bar{\Psi}$. That is to replace $\bar{\mathbf{F}}$ by \mathbf{F} in these terms.

In the Fung-type SEF, the anisotropy is specified by the material parameters b_i , $i = 1, \dots, 9$. Therefore in these terms including b_i we should not use the decomposition, that is, $Q(\bar{\mathbf{E}})$ in (7.12) should be replaced by $Q(\mathbf{E})$. It is denoted by

$$\tilde{\Psi} = \Psi_v(J) + \bar{\Psi}(\mathbf{E}). \quad (7.20)$$

In the HGO SEF, the anisotropy is introduced through the invariants associated with fibres, so the calculation for these invariants should use \mathbf{F} rather than $\bar{\mathbf{F}}$, that is, \bar{I}_4 in (7.16) should be replaced by I_4 . It is denoted by

$$\tilde{\Psi} = \Psi_v(J) + \bar{\Psi}(\bar{I}_1, I_4). \quad (7.21)$$

In the following sections, we illustrate the suggestion by solving some equilibria and compare the results based on $\hat{\Psi}$ and $\tilde{\Psi}$.

7.3 Comparison of $\hat{\Psi}$ and $\tilde{\Psi}$ through analytical examples

The equilibria of a cube subject to various loadings are solved with $\hat{\Psi}$ and $\tilde{\Psi}$, respectively. The cube is a transversely isotropic material with one family of fibres along \mathbf{e}_1 . The comparison between results illustrates the problems of $\hat{\Psi}$ and the correctness of $\tilde{\Psi}$. In addition, the performance, including speed of approximation and numerical stability, of $\hat{\Psi}$ and $\tilde{\Psi}$ when approximating incompressibility are compared. The values for material parameters in the Table 7.2 and 7.3 are used in the following examples.

Table 7.2: The values for material parameters in a compressible transversely isotropic Fung-type SEF

K [kPa]	a [kPa]	b_1	b_2	b_3	b_4	b_5	b_6
5.0	1.0	5.0	0.3	0.3	0.1	0.1	0.1

Table 7.3: The values for material parameters in a compressible transversely isotropic HGO SEF

K [kPa]	c [kPa]	k_1 [kPa]	k_2
5.0	1.0	1.0	1.0

7.3.1 Stress in uniform dilatation

Subject to an uniform dilation, the deformation of the cube is specified by the deformation gradient in (7.17). Substitute it to the principal Cauchy stress in components

$$\sigma_i = \frac{1}{J} \lambda_i \frac{\partial \Psi}{\partial \lambda_i}, \quad i = 1, 2, 3 \quad (7.22)$$

derived from the SEF Ψ , we obtain the following

Fung-type material $\widehat{\Psi}$ in (7.12),

$$\sigma_1 = \sigma_2 = \sigma_3 = K(J - 1) = K(\lambda^3 - 1) \quad (7.23)$$

but for $\widetilde{\Psi}$ in (7.20),

$$\sigma_i = K(\lambda^3 - 1) + a \frac{1}{\lambda} \exp(Q) q_i, \quad i = 1, 2, 3, \quad (7.24)$$

where

$$\begin{aligned} q_1 &= b_1 E_{11} + b_4 E_{22} + b_6 E_{33} = \frac{1}{2} (b_1 + b_4 + b_6) (\lambda^2 - 1), \\ q_2 &= b_2 E_{22} + b_4 E_{11} + b_5 E_{33} = \frac{1}{2} (b_2 + b_4 + b_5) (\lambda^2 - 1), \\ q_3 &= b_3 E_{33} + b_5 E_{22} + b_6 E_{11} = \frac{1}{2} (b_3 + b_5 + b_6) (\lambda^2 - 1); \end{aligned} \quad (7.25)$$

and

HGO material $\widehat{\Psi}$ in (7.16),

$$\sigma_1 = \sigma_2 = \sigma_3 = K(J - 1) = K(\lambda^3 - 1), \quad (7.26)$$

but for $\widetilde{\Psi}$ in (7.21),

$$\begin{aligned} \sigma_1 &= K(\lambda^3 - 1) + H(I_4)2\frac{1}{\lambda} \frac{d\psi_f}{dI_4}, \\ \sigma_2 &= \sigma_3 = K(\lambda^3 - 1). \end{aligned} \quad (7.27)$$

Notably, the stress expression in (7.27) does not include a term related to \bar{I}_1 . That is because $\bar{I}_1 \equiv 3$ for this uniform dilatation, thus when we compute the derivative, the term related to \bar{I}_1 vanishes. In general, any isochoric invariant is independent with this uniform dilation. The principal stresses plotted against the stretch (for the Fung-type and HGO SEF) are shown in Figure 7.1 and Figure 7.2, respectively. In Figures 7.1(a) and 7.2(a), the three principal stresses derived from $\widehat{\Psi}$ are identical, denoting then the loss of anisotropy. In contrast, the transverse isotropy is recovered when using $\widetilde{\Psi}$ as shown in Figures 7.1(b) and 7.2(b), since $\sigma_1 > \sigma_2 = \sigma_3$.

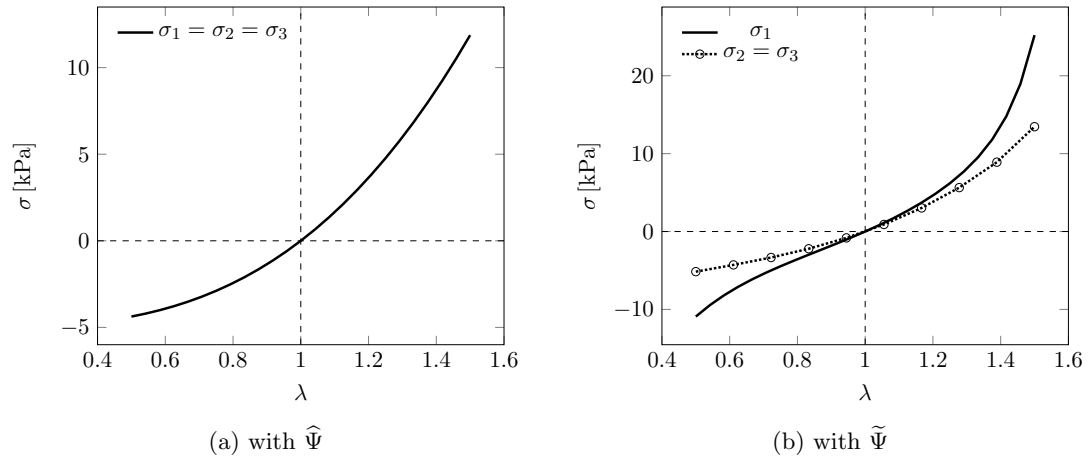


Figure 7.1: The principal stresses against the stretch λ in the uniform dilation of the cube, with a transversely isotropic Fung-type SEF, are plotted. (a) is based on the expression of principal stress in (7.23) derived from $\widehat{\Psi}$, and (b) is based on the expression of principal stress in (7.24) derived from $\widetilde{\Psi}$.

Figure 7.2(b) shows that the stress response derived from the HGO SEF is isotropic when material is compressed ($\lambda < 1$), and anisotropic when stretched ($\lambda > 1$). Figure 7.1(b) shows that the stress response derived from the Fung-type SEF is anisotropic for all values of λ . A common assumption is that collagen fibre does not take on load when

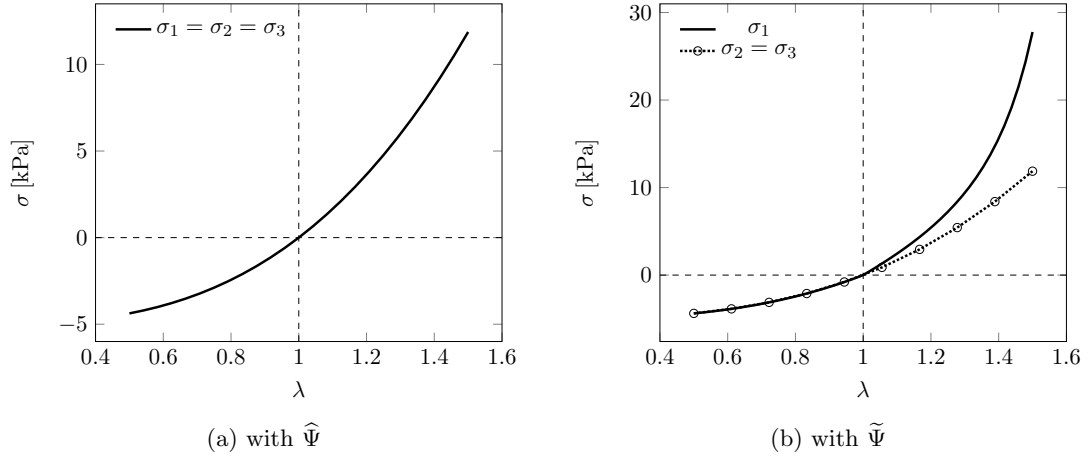


Figure 7.2: The principal stresses against the stretch λ in the uniform dilation of the cube, with a transversely isotropic HGO SEF, are plotted. (a) is based on the expression of principal stress in (7.26) derived from $\hat{\Psi}$, and (b) is based on the expression of principal stress in (7.27) derived from $\tilde{\Psi}$.

compressed. So with a set of values for material parameters, the HGO SEF agrees with the assumption. To be consistent with this assumption in Fung-type SEF, different values for material parameters should be used in the region of compression and tension: a set of values such that mechanical response is isotropic should be used in the region of compression, while the other set of values such that mechanical response is anisotropic should be used in the region of tension.

7.3.2 Deformation subject to a hydrostatic compression or tension

In this section, we calculate the equilibrium configuration of a cube subject to a hydrostatic compression or traction t , for different choices of SEF. When $t > 0$ the loading is hydrostatic tension and when $t < 0$ the loading is hydrostatic compression. We consider the cube to be composed of a transversely isotropic material with one family of fibres oriented in the direction \mathbf{e}_1 . This material symmetry means we expect the principal axes of the Cauchy stress and left Cauchy-Green strain are the same. Therefore the equilibrium deformation of the cube can be determined by solving

$$\frac{1}{J} \lambda_i \frac{\partial \Psi}{\partial \lambda_i} = t, \quad (7.28)$$

for the principal stretches λ_i , $i = 1, 2, 3$.

We substitute the Fung-type SEF in (7.12), (7.20) and the HGO SEF in (7.16), (7.21)

to (7.28). Solve the system of equations to get deformation, presented by λ_i , as shown in Figure 7.3 for Fung-type SEF and Figure 7.4 for HGO SEF. Both of comparisons, (b) to (a) in both Figures 7.3 and 7.4, illustrate that the anisotropy of material is correctly reflected through the proposed SEF $\tilde{\Psi}$ in the regions of both infinitesimal and finite strain.

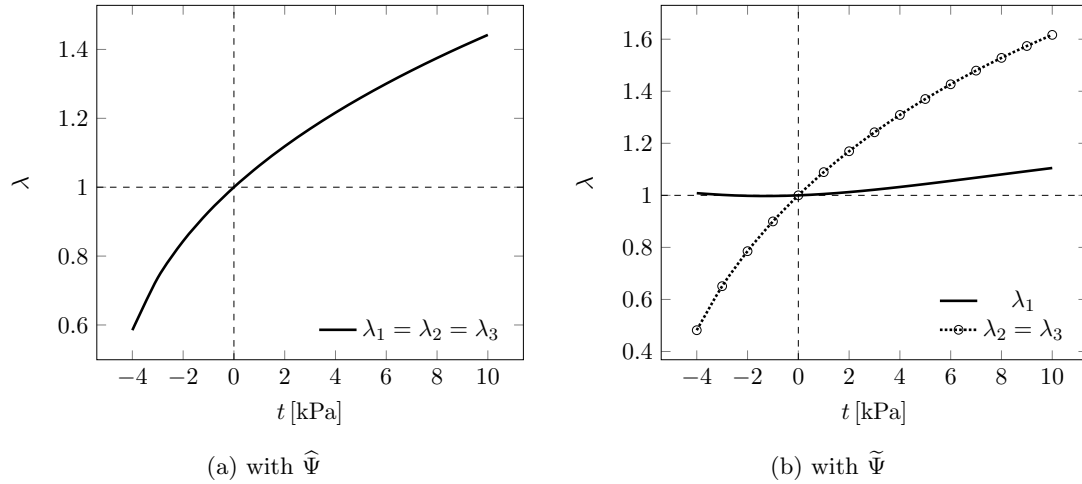


Figure 7.3: The principal stretches λ_i ($i = 1, 2, 3$), computed with the Fung-type SEF for a transversely isotropic cube, against the hydrostatic compression ($t < 0$) or tension ($t > 0$) are plotted.

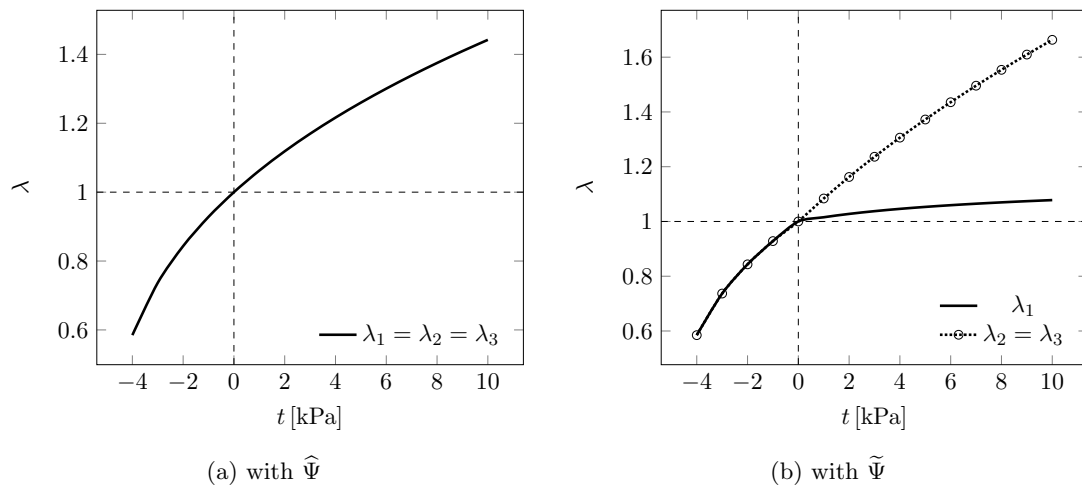


Figure 7.4: The principal stretches λ_i ($i = 1, 2, 3$), computed with the HGO SEF for a transversely isotropic cube, against the hydrostatic compression ($t < 0$) or tension ($t > 0$) are plotted. Notice that the fibre does not support compression loading, so $\lambda_1 = \lambda_2 = \lambda_3$ for $t < 0$.

7.3.3 Performance of approximation to incompressibility

Following the theory of the penalty method, $\widehat{\Psi}$ and $\widetilde{\Psi}$ approximate the incompressible response as $K \rightarrow \infty$. Here we show the process of approximation in some examples with the aim of comparing the difference in using $\widehat{\Psi}$ and $\widetilde{\Psi}$.

Example 1: Hydrostatic tension

In this example, we solve (7.28) with an increasing value for K until the incompressibility is satisfied. From the results with Fung-type SEF in Figure 7.5 and with HGO SEF in Figure 7.6, three points are obtained:

1. both $\widehat{\Psi}$ and $\widetilde{\Psi}$ approximate successfully the incompressible material model $\overline{\Psi}$ as $K \rightarrow \infty$,
2. with $\widehat{\Psi}$, the anisotropy of material is lost in the compressible region since $\lambda_1 = \lambda_2 = \lambda_3$, while the anisotropy is correctly reflected when using $\widetilde{\Psi}$ since $\lambda_1 < \lambda_2 = \lambda_3$,
3. the approximating rates, to incompressibility as $K \rightarrow \infty$, of $\widehat{\Psi}$ and $\widetilde{\Psi}$ are similar. The results show that the constraint of incompressibility is satisfied when $K > 10^3$ kPa.

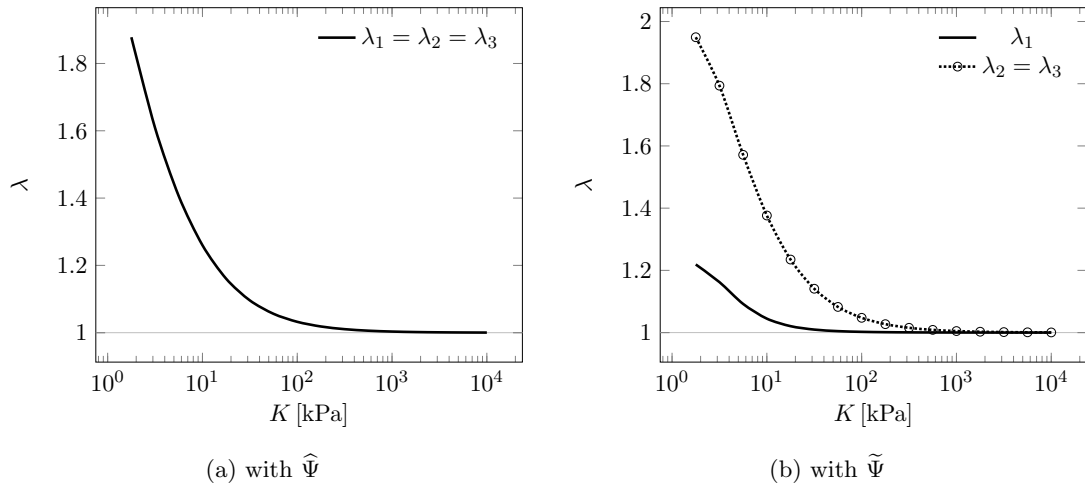


Figure 7.5: The principal stretches λ , computed for a transversely isotropic Fung-type cube subject to a hydrostatic tension $t=10$ kPa, against bulk modulus K are plotted. The values for λ is obtained by solving the equilibrium equations (7.28).

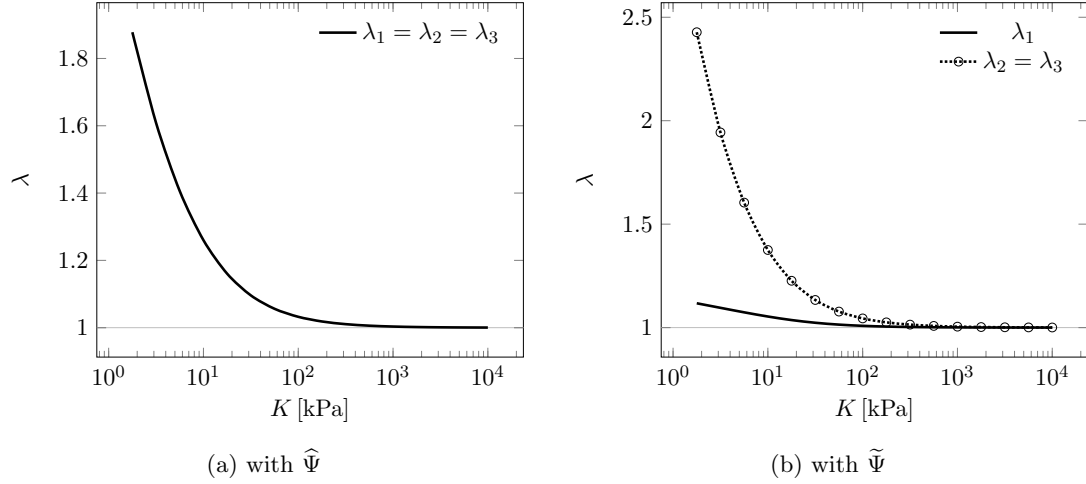


Figure 7.6: The principal stretches λ , computed for a transversely isotropic HGO cube subject to a hydrostatic tension $t=10$ kPa, against bulk modulus K are plotted. The values for λ is obtained by solving the equilibrium equations (7.28).

Example 2: Uniaxial stretch along fibre direction

In this example, we calculate the stress response of a square subject to the uniaxial stretch along the direction of fibres with the plane strain condition. The fibres are orientated along \mathbf{e}_1 . The deformation gradient is

$$\mathbf{F} = \begin{bmatrix} \lambda_1 & 0 & 0 \\ 0 & \lambda_2 & 0 \\ 0 & 0 & 1 \end{bmatrix}. \quad (7.29)$$

Given λ_1 , that is stretch along the fibre direction, solving the equilibrium equation in the absence of body forces

$$\operatorname{div} \boldsymbol{\sigma} = \mathbf{0}, \quad (7.30)$$

gives the λ_2 . When the incompressibility is satisfied, $\lambda_2 = 1/\lambda_1$.

The approximation to incompressibility as $K \rightarrow \infty$ with the Fung-type and HGO SEF is shown in Figure 7.7. In Figure 7.7(a), the incompressibility with $\widehat{\Psi}$ is satisfied when $K > 10^8$ kPa, while with $\widetilde{\Psi}$ when $K > 10^4$ kPa. In Figure 7.7(b), the incompressibility with $\widehat{\Psi}$ is satisfied when $K > 10^7$ kPa, while with $\widetilde{\Psi}$ when $K > 10^2$ kPa. These results show that the approximating rate to the incompressibility with $\widetilde{\Psi}$ is quicker than with $\widehat{\Psi}$. A small value of K , which can let $\widetilde{\Psi}$ behave incompressible, elevates the stability of numerical computation. In the FEM, a big value for K could lead to an ill-conditioned stiffness matrix.

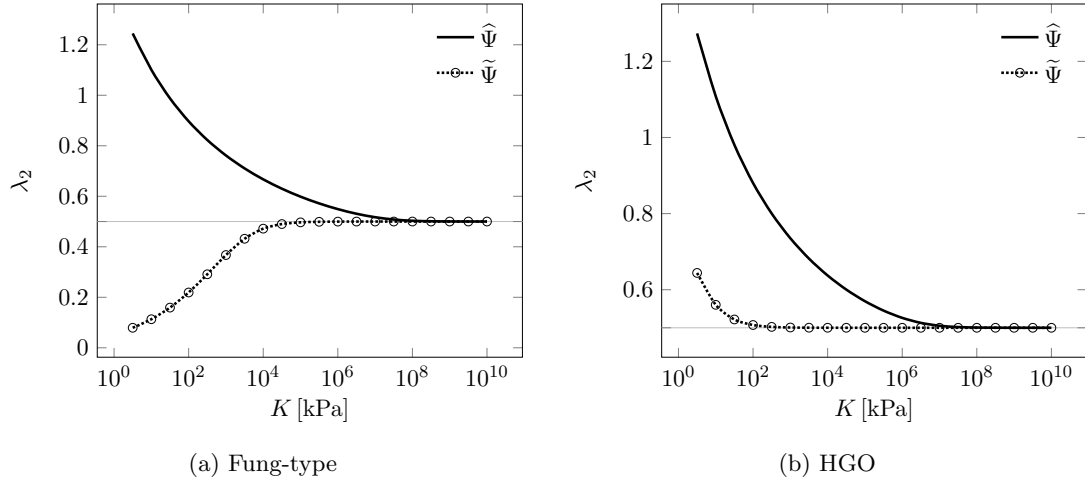


Figure 7.7: Let $\lambda_1 = 2$ in the uniaxial stretch of a square along fibre direction, the transverse stretch λ_2 in equilibrium is calculated and plotted against the bulk modulus K .

7.4 A FE subroutine for the HGO SEF

To use the HGO SEF in a finite element program FEAP, we need to develop a user subroutine. For the incompressible HGO SEF with two families of orientated fibres

$$\bar{\Psi}(\mathbf{F}) = \Psi_m(I_1) + \Psi_f(I_4, I_6), \quad \text{s.t. } \det \mathbf{F} = 1, \quad (7.31)$$

we have two compressible SEFs for its FE implementation: the conventional approach

$$\hat{\Psi}(\mathbf{F}) = \Psi_v(J) + \Psi_m(\bar{I}_1) + \Psi_f(\bar{I}_4, \bar{I}_6), \quad (7.32)$$

and the approach suggested in this chapter

$$\tilde{\Psi}(\mathbf{F}) = \Psi_v(J) + \Psi_m(\bar{I}_1) + \Psi_f(I_4, I_6), \quad (7.33)$$

where Ψ_v is the stored energy due to a pure volumetric deformation, Ψ_m is the stored energy due to isochoric deformation of matrix and Ψ_f is the stored energy due to the stretch of fibres. The necessary derivatives to develop such a subroutine are summarized in this section. In addition, the methods on how to use it and verify it in FEAP are discussed.

7.4.1 Derivatives of Cauchy stress and spatial tangent moduli

A precondition to develop a subroutine for a user-defined material model in FEAP is to have the *Cauchy stress* $\boldsymbol{\sigma}$ and *spatial tangent moduli* \mathbf{c} explicitly in terms of deformation

gradient \mathbf{F} . In a subroutine, \mathbf{F} is an input argument, while $\boldsymbol{\sigma}$ and \mathbf{c} are output arguments. We show how to derive $\boldsymbol{\sigma}$ and \mathbf{c} for (7.32) and (7.33). Since the difference between (7.32) and (7.33) is only the fibre term, so we are using the Ψ to denote both $\widehat{\Psi}$ and $\widetilde{\Psi}$ in following derivatives.

The details of each terms in (7.31) are

$$\begin{aligned}\Psi_m(I_1) &= \frac{c}{2}(I_1 - 3) \\ \Psi_f(I_4, I_6) &= \sum_{n=4,6} H(I_n)\psi_f(I_n).\end{aligned}\tag{7.34}$$

- **Cauchy stress**

Follow the standard formulae in the theory of finite elasticity [e.g. Holzapfel, 2000].

We firstly calculate the second Piola–Kirchhoff stress

$$\mathbf{S} = 2 \frac{\partial \Psi}{\partial \mathbf{C}} = 2 \left(\frac{\partial \Psi_v}{\partial \mathbf{C}} + \frac{\partial \Psi_m}{\partial \mathbf{C}} + \frac{\partial \Psi_f}{\partial \mathbf{C}} \right),\tag{7.35}$$

where

$$\begin{aligned}\frac{\partial \Psi_v}{\partial \mathbf{C}} &= \Psi'_v(J) \frac{\partial J}{\partial \mathbf{C}} = \frac{1}{2} \Psi'_v(J) J \mathbf{C}^{-1} = \frac{K}{2} (J - 1) J \mathbf{C}^{-1}, \\ \frac{\partial \Psi_m}{\partial \mathbf{C}} &= \frac{c}{2} \frac{\partial \bar{I}_1}{\partial \mathbf{C}} = \frac{c}{2} \left(J^{-2/3} \mathbf{I} - \frac{1}{3} \bar{I}_1 \mathbf{C}^{-1} \right), \\ \frac{\partial \Psi_f}{\partial \mathbf{C}} &= \sum_{n=4,6} \psi'_f(\bar{I}_n) \frac{\partial \bar{I}_n}{\partial \mathbf{C}} \quad \text{for } \widehat{\Psi} \\ &= \sum_{n=4,6} k_1 (\bar{I}_n - 1) \exp[k_2 (\bar{I}_n - 1)^2] \left(J^{-2/3} \mathbf{M}^{(n)} - \frac{1}{3} \bar{I}_n \mathbf{C}^{-1} \right), \\ \frac{\partial \Psi_f}{\partial \mathbf{C}} &= \sum_{n=4,6} \psi'_f(I_n) \frac{\partial I_n}{\partial \mathbf{C}} \quad \text{for } \widetilde{\Psi} \\ &= \sum_{n=4,6} k_1 (I_n - 1) \exp[k_2 (I_n - 1)^2] \mathbf{M}^{(n)},\end{aligned}\tag{7.36}$$

where

$$\mathbf{M}^{(4)} = \mathbf{A}_1 \otimes \mathbf{A}_1 \quad \text{and} \quad \mathbf{M}^{(6)} = \mathbf{A}_2 \otimes \mathbf{A}_2.$$

Substitute these into (7.35) to get the explicit expression for the second Piola–Kirchhoff stress, pushing which forward by using

$$\boldsymbol{\sigma} = J^{-1} \mathbf{F} \mathbf{S} \mathbf{F}^T,$$

immediately gives the Cauchy stress for $\widehat{\Psi}$

$$\begin{aligned}\boldsymbol{\sigma} &= K(J - 1) \mathbf{I} + \frac{c}{J} \left(\bar{\mathbf{B}} - \frac{1}{3} \bar{I}_1 \mathbf{I} \right) \\ &\quad + \frac{2}{J} \sum_{n=4,6} k_1 (\bar{I}_n - 1) \exp[k_2 (\bar{I}_n - 1)^2] \left(J^{-2/3} \mathbf{m}^{(n)} - \frac{1}{3} \bar{I}_n \mathbf{I} \right),\end{aligned}\tag{7.37}$$

and for $\tilde{\Psi}$

$$\begin{aligned} \boldsymbol{\sigma} = & K(J-1)\mathbf{I} + \frac{c}{J} \left(\bar{\mathbf{B}} - \frac{1}{3}\bar{I}_1\mathbf{I} \right) \\ & + \frac{2}{J} \sum_{n=4,6} k_1(I_n - 1) \exp[k_2(I_n - 1)^2] \mathbf{m}^{(n)}, \end{aligned} \quad (7.38)$$

where $\bar{\mathbf{B}} = J^{-2/3}\mathbf{F}\mathbf{F}^T$ and

$$\mathbf{m}^{(4)} = \mathbf{a}_1 \otimes \mathbf{a}_1 \quad \text{and} \quad \mathbf{m}^{(6)} = \mathbf{a}_2 \otimes \mathbf{a}_2,$$

where $\mathbf{a}_i = \mathbf{F}\mathbf{A}_i$ ($i = 1, 2$) represents the deformed vector of the unit vector \mathbf{A}_i characterizing the orientation of the i -th family of fibres in the reference configuration.

• Tangent moduli

The material tangent moduli, associated with the increment of the second Piola-Kirchoff stress \mathbf{S} and the Green strain tensor $\mathbf{E} = \frac{1}{2}(\mathbf{C} - \mathbf{I})$, is firstly derived [e.g. Holzapfel, 2000]:

$$\boldsymbol{\mathfrak{c}} = \frac{\partial \mathbf{S}}{\partial \mathbf{E}} = 2 \frac{\partial \mathbf{S}}{\partial \mathbf{C}} = 2 \left(\frac{\partial \mathbf{S}^v}{\partial \mathbf{C}} + \frac{\partial \mathbf{S}^m}{\partial \mathbf{C}} + \frac{\partial \mathbf{S}^f}{\partial \mathbf{C}} \right), \quad (7.39)$$

where $\mathbf{S}^x = 2 \frac{\partial \Psi_x}{\partial \mathbf{C}}$, $x = \{v, m, f\}$. In index notation,

$$\begin{aligned} \frac{\partial S_{IJ}^v}{\partial C_{KL}} &= J C_{IJ}^{-1} \Psi_v''(J) \frac{\partial J}{\partial C_{KL}} + \Psi_v'(J) C_{IJ}^{-1} \frac{\partial J}{\partial C_{KL}} + \Psi_v'(J) J \frac{\partial C_{IJ}^{-1}}{\partial C_{KL}} \\ &= \frac{1}{2} J C_{IJ}^{-1} C_{KL}^{-1} [(J \Psi_v''(J) + \Psi_v'(J))] + J \Psi_v'(J) \frac{\partial C_{IJ}^{-1}}{\partial C_{KL}}, \\ \frac{\partial S_{IJ}^m}{\partial C_{KL}} &= c \left[-\frac{1}{3} \left(\frac{\partial \bar{I}_1}{\partial C_{KL}} C_{IJ}^{-1} + \bar{I}_1 \frac{\partial C_{IJ}^{-1}}{\partial C_{KL}} \right) + \frac{\partial J^{-2/3}}{\partial C_{KL}} \delta_{IJ} \right]. \end{aligned} \quad (7.40)$$

For $\hat{\Psi}$

$$\begin{aligned} \frac{\partial S_{IJ}^f}{\partial C_{KL}} &= \sum_{n=4,6} 4 \left[\psi_f''(\bar{I}_n) \frac{\partial \bar{I}_n}{\partial C_{IJ}} \frac{\partial \bar{I}_n}{\partial C_{KL}} \right. \\ &\quad \left. - \frac{1}{3} \psi_f'(\bar{I}_n) \left(\frac{\partial \bar{I}_n}{\partial C_{KL}} C_{IJ}^{-1} + \bar{I}_n \frac{\partial C_{IJ}^{-1}}{\partial C_{KL}} + J^{-2/3} C_{KL}^{-1} A_{IJ} \right) \right]. \end{aligned} \quad (7.41)$$

We note some useful differentials:

$$\begin{aligned} \frac{\partial C_{IJ}^{-1}}{\partial C_{KL}} &= -\frac{1}{2} (C_{IK}^{-1} C_{JL}^{-1} + C_{IL}^{-1} C_{JK}^{-1}), \\ \frac{\partial \bar{I}_1}{\partial C_{IJ}} &= -\frac{1}{3} \bar{I}_1 C_{IJ}^{-1} + J^{-2/3} \delta_{IJ}, \quad \Psi_v'(J) = K(J-1), \quad \Psi_v''(J) = K, \end{aligned}$$

$$\begin{aligned}\frac{\partial \bar{I}_n}{\partial C_{IJ}} &= -\frac{1}{3}\bar{I}_n C_{IJ}^{-1} + J^{-2/3}A_{IJ}, \quad n = 4, 6, \\ \psi'_f(\bar{I}_n) &= k_1(\bar{I}_n - 1) \exp[k_2(\bar{I}_n - 1)^2], \\ \psi''_f(\bar{I}_n) &= k_1 \exp[k_2(\bar{I}_n - 1)^2][1 + 2k_2(\bar{I}_n - 1)^2].\end{aligned}$$

Substituting (7.40) and (7.41) into (7.39) gives the explicit expression for the material tangent moduli for $\widehat{\Psi}$. Pushing forward it gives the spatial tangent moduli required by a user-provided material model in FEAP. Its components are

$$\begin{aligned}\mathbf{c}_{ijkl} &= \frac{1}{J}F_{iI}F_{jJ}F_{kK}F_{lL}\mathbf{c}_{IJKL} \\ &= \delta_{ij}\delta_{kl} [J\Psi''_v(J) + \Psi'_v(J)] - \Psi'_v(J)(\delta_{ik}\delta_{jl} + \delta_{il}\delta_{jk}) \\ &\quad - \frac{2}{3}\frac{c}{J} \left[-\frac{1}{3}\bar{I}_1\delta_{kl}\delta_{ij} + \delta_{ij}\bar{B}_{kl} + \delta_{kl}\bar{B}_{ij} - \frac{\bar{I}_1}{2}(\delta_{ik}\delta_{jl} + \delta_{il}\delta_{jk}) \right] \\ &\quad + \frac{4}{J} \sum_{n=4,6} \left\{ \psi''_f(\bar{I}_n) \left(-\frac{1}{3}\bar{I}_n\delta_{ij} + J^{-2/3}m^{(n)}_{ij} \right) \left(-\frac{1}{3}\bar{I}_n\delta_{kl} + J^{-2/3}m^{(n)}_{kl} \right) \right. \\ &\quad \left. - \frac{1}{3}\psi'_f(\bar{I}_n) \left[-\frac{1}{3}\bar{I}_n\delta_{ij}\delta_{kl} - \frac{\bar{I}_n}{2}(\delta_{ik}\delta_{jl} + \delta_{il}\delta_{jk}) + J^{-2/3}(m^{(n)}_{ij}\delta_{kl} + \delta_{ij}m^{(n)}_{kl}) \right] \right\}.\end{aligned}\tag{7.42}$$

For $\widetilde{\Psi}$

$$\frac{\partial S^f_{IJ}}{\partial C_{KL}} = \sum_{n=4,6} 4 \left[\psi''_f(I_n) \frac{\partial I_n}{\partial C_{IJ}} \frac{\partial I_n}{\partial C_{KL}} + \psi'_f(I_n) \frac{\partial I_n}{\partial C_{IJ} \partial C_{KL}} \right]\tag{7.43}$$

Similarly, substituting (7.40) and (7.43) into (7.39) gives the explicit expression for the material tangent moduli for $\widetilde{\Psi}$. Pushing forward it gives the spatial tangent moduli required by a user-provided material model in FEAP. Its components are

$$\begin{aligned}\mathbf{c}_{ijkl} &= \frac{1}{J}F_{iI}F_{jJ}F_{kK}F_{lL}\mathbf{c}_{IJKL} \\ &= \delta_{ij}\delta_{kl} [J\Psi''_v(J) + \Psi'_v(J)] - \Psi'_v(J)(\delta_{ik}\delta_{jl} + \delta_{il}\delta_{jk}) \\ &\quad - \frac{2}{3}\frac{c}{J} \left[-\frac{1}{3}\bar{I}_1\delta_{kl}\delta_{ij} + \delta_{ij}\bar{B}_{kl} + \delta_{kl}\bar{B}_{ij} - \frac{\bar{I}_1}{2}(\delta_{ik}\delta_{jl} + \delta_{il}\delta_{jk}) \right] \\ &\quad + \frac{4}{J} \sum_{n=4,6} \psi''_f(I_n)m^{(n)}_{ij}m^{(n)}_{kl}\end{aligned}\tag{7.44}$$

Finally, transforming (7.37, 7.42) and (7.38, 7.44) to the corresponding matrix form gives all of formulas, required for developing the user-subroutine for $\widehat{\Psi}$ and $\widetilde{\Psi}$ of the HGO SEF, respectively.

7.4.2 Verification

Verification of a subroutine for a user-defined material model has been done through comparisons of computation at two levels: in a quadrature point and in applications within the whole FEAP.

In a quadrature point

In the calculation of FEM, $\boldsymbol{\sigma}$ and \mathbf{c} are computed at a quadrature point, from the deformation gradient \mathbf{F} at that point. The user subroutine is called at that time. The verification at this level is to check whether the calculation of $\boldsymbol{\sigma}$ and \mathbf{c} for a given \mathbf{F} is correct. The values of $\boldsymbol{\sigma}(\mathbf{F})$ and $\mathbf{c}(\mathbf{F})$ are compared to those from the Finite Difference Method (FDM).

Analogous to the sequence of derivation of explicit expression of $\boldsymbol{\sigma}(\mathbf{F})$, through the FDM the second Piola-Kirchoff stress is computed first and compared. In component,s

$$S_{IJ} = 2 \frac{\partial \Psi}{\partial C_{IJ}} = 2 \lim_{\delta \rightarrow 0} \frac{\Psi(\mathbf{C} + \delta \mathbf{Y}_{IJ}) - \Psi(\mathbf{C})}{\delta}, \quad (7.45)$$

where \mathbf{Y}_{IJ} is the second-order tensor whose IJ -th component is 1 and all the other components vanish. If the values for $\mathbf{S}(\mathbf{F})$ from the subroutine agree with those from the FDM, the verification can forward so check the material tangent moduli. Through the FDM, the material moduli in component is computed as

$$\mathbf{c}_{IJKL} = 2 \frac{\partial S_{IJ}}{\partial C_{KL}} = 2 \lim_{\delta \rightarrow 0} \frac{S_{IJ}(\mathbf{C} + \delta \mathbf{Y}_{KL}) - S_{IJ}(\mathbf{C})}{\delta}. \quad (7.46)$$

In applications within the whole FEAP

Using FEAP with a subroutine to solve some simple problems, where analytical solutions are available, can check whether the subroutine works well. In this section, we consider two examples. In both examples, the deformation of a cube, the only element in FE model, is analysed. The cube has only one family of fibres along the x -axis direction. The material parameters $c = 3 \text{ kPa}$, $k_1 = 3 \text{ kPa}$, $k_2 = 1$ and a varying value for K . Both $\widehat{\Psi}$ and $\widetilde{\Psi}$ for HGO SEF are employed.

In the first example, the cube is subject to a hydrostatic tension, referring to the deformed configuration. The deformation, quantified by principal stretches λ_i , $i = 1, 2, 3$, are calculated analytically and numerically. The analytical solution is obtained by solving (7.28). The numerical solutions are obtained within FEAP using both subroutines for $\widehat{\Psi}$ and $\widetilde{\Psi}$. The comparison (Figure 7.8) shows the numerical solutions agree with analytical

ones for both compressible (small value for K) and incompressible (big value for K) material. The SEF $\tilde{\Psi}$ correctly describes the transverse isotropy of the compressible material, since $\lambda_1 < \lambda_2 = \lambda_3$ in Figure 7.8(b).

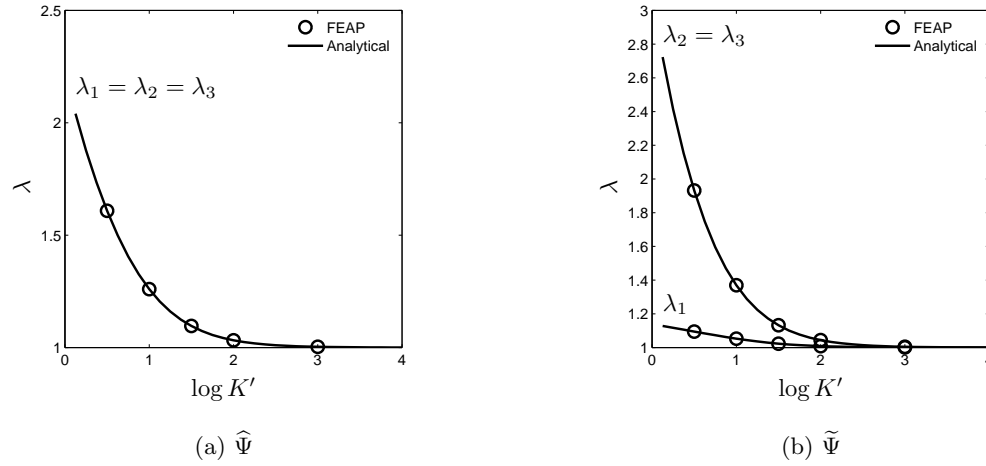


Figure 7.8: The principal stretches λ , of a transversely isotropic cube subject to a uniform traction, is plotted against the logarithm of the dimensionless bulk modulus $K' = K/K_0$, where $K_0 = 1$ kPa. The material is incompressible or nearly-incompressible when $K > 10^3$ kPa.

In the second example, the cube is stretched along the x -axis direction subject to the plane strain condition, such that $\lambda_3=1$. $\lambda_1=2$ is specified, λ_2 is calculated analytically and numerically. The comparison in Figure 7.9 shows numerical solution agrees with analytical one. The material becomes incompressible when $K > 10^3$ kPa in $\tilde{\Psi}$, while $K > 10^8$ kPa in $\hat{\Psi}$. The gradient of curve λ_2 of $\log K'$ in Figure 7.9(b) is higher than that in Figure 7.9(a). That shows the rate of approximating to incompressibility is higher in this example with $\tilde{\Psi}$ than $\hat{\Psi}$.

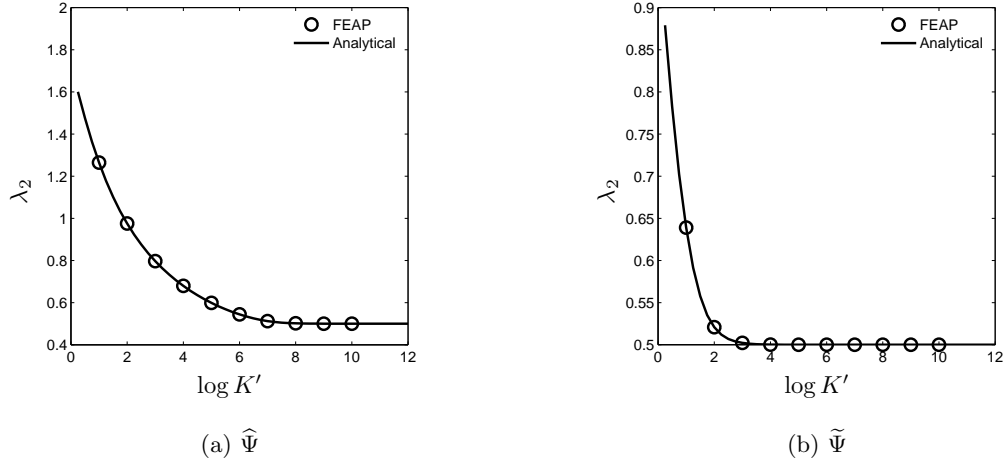


Figure 7.9: The principal stretch λ_2 , of a transversely isotropic cube subject to a uniaxial stretch $\lambda_1=2$, is plotted against the logarithm of dimensionless bulk modulus $K' = K/K_0$, where $K_0 = 1$ kPa. A plane strain condition is considered such that $\lambda_3=1$. The material is incompressible or nearly incompressible when $K > 10^3$ kPa for $\tilde{\Psi}$, but when $K > 10^8$ kPa for $\hat{\Psi}$.

7.5 Add growth property of tissue in the FE subroutine

In a living tissue, the volumetric growth changes the shape of body. The growth generally occurs with an elastic deformation, which also changes the shape of body and result in a stress and stored energy. Therefore, the change of shape in a living tissue is the result of both growth and elastic deformation. A computational approach for this process is that decompose the deformation gradient as

$$\mathbf{F} = \mathbf{F}_e \mathbf{F}_g, \quad (7.47)$$

where \mathbf{F}_e measures the elastic deformation and \mathbf{F}_g measures the change in shape due to growth. A common assumption is that only the \mathbf{F}_e results in a stress and stored energy, so \mathbf{F}_e is the strain measure as an argument in a strain energy function.

In our FE subroutine, we have \mathbf{F} as an input argument. In order to implement a SEF with considering the growth property, we first need to calculate \mathbf{F}_e as

$$\mathbf{F}_e = \mathbf{F} \mathbf{F}_g^{-1}. \quad (7.48)$$

Then the stored energy $\Psi(\mathbf{F}_e)$, Cauchy stress $\boldsymbol{\sigma}(\mathbf{F}_e)$ and spatial tangential moduli $\mathbf{c}(\mathbf{F}_e)$ are obtained from the formulae in Section 7.4.1.

Two examples are used to demonstrate the computation using this FE subroutine and verify this subroutine. In both examples, a uni-axial growth is considered. For example, when the body grows g_1 times in length along \mathbf{e}_1 , we have

$$\mathbf{F}_g = \begin{bmatrix} g_1 & 0 & 0 \\ 0 & 1 & 0 \\ 0 & 0 & 1 \end{bmatrix}. \quad (7.49)$$

In the first example, a simple stretch of a square subject to plane strain condition is considered (Figure 7.10).

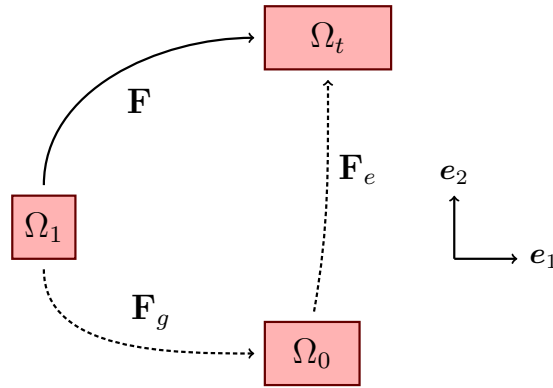


Figure 7.10: The uniaxial stretch of a body ($\Omega_1 \rightarrow \Omega_t$) is demonstrated due to both internal growth and external loading: dash line shows the imaginary theoretical decomposition of \mathbf{F} , while solid line shows the computational process in FEAP.

The square Ω_1 is stretched along the direction of \mathbf{e}_1 , so

$$\mathbf{F} = \begin{bmatrix} \lambda_1 & 0 & 0 \\ 0 & 1 & 0 \\ 0 & 0 & 1 \end{bmatrix}, \quad (7.50)$$

where $1 \leq \lambda_1 \leq 2$.

Thus we calculate the elastic deformation gradient as

$$\mathbf{F}_e = \mathbf{F}\mathbf{F}_g^{-1} = \begin{bmatrix} \lambda_1 g_1^{-1} & 0 & 0 \\ 0 & 1 & 0 \\ 0 & 0 & 1 \end{bmatrix}. \quad (7.51)$$

Here we calculate the Cauchy stress analytically and numerically when the body is in the configuration Ω_t . The analytical stress associated with the incompressible HGO SEF

in (7.15) is

$$\boldsymbol{\sigma} = -\mathcal{P}\mathbf{I} + c\mathbf{B} + 2H(I_4)k_1(I_4 - 1)\exp[k_2(I_4 - 1)^2]\mathbf{m}, \quad (7.52)$$

where $\mathbf{B} = \mathbf{F}_e\mathbf{F}_e^T$, $I_4 = (\mathbf{F}_e\mathbf{e}_1) \cdot (\mathbf{F}_e\mathbf{e}_1)$ and $\mathbf{m} = (\mathbf{F}_e\mathbf{e}_1) \otimes (\mathbf{F}_e\mathbf{e}_1)$ for this deformation from Ω_0 to Ω_t , and \mathcal{P} is determined from the boundary conditions. The boundary conditions associated with the deformation from Ω_0 to Ω_t are: the left boundary is fixed such that there is no displacement in the \mathbf{e}_1 direction, the right boundary has a constant displacement in the \mathbf{e}_1 direction, the bottom is fixed such that there is no displacement in the \mathbf{e}_2 direction, and the top is traction-free. From the top boundary condition, we know $\sigma_{22} = 0$, from which we have

$$\mathcal{P} = c, \quad (7.53)$$

and then the analytical stress is given by

$$\begin{aligned} \sigma_{11} &= -\mathcal{P} + cx^2 + 2H(x^2)k_1x^2(x^2 - 1)\exp[k_2(x^2 - 1)^2] \\ &= (x^2 - 1)\{c + 2H(x^2)k_1x^2\exp[k_2(x^2 - 1)^2]\}, \end{aligned} \quad (7.54)$$

where $x = \lambda_1 g_1^{-1}$.

The deformation from Ω_1 , with initial stress associated with \mathbf{F}_g , to Ω_t is simulated in FEAP with our FE subroutine, and the Cauchy stress is computed numerically. In the computation, the value of \mathbf{F}_g is specified a priori, and the deformation consistent with \mathbf{F} is achieved through a displacement loading on the right end of Ω_1 such that we have $1 \leq \lambda_1 \leq 2$. Other boundary conditions include the left boundary is fixed such that there is no displacement in the \mathbf{e}_1 direction, the bottom is fixed such that there is no displacement in the \mathbf{e}_2 direction, and the top is traction-free.

In Figure 7.11, we plot the Cauchy stress computed analytically and numerically when the body is in the configuration Ω_t , using material parameters $c = 3.0$ kPa, $k_1 = 2.3632$ kPa, $k_2 = 0.8393$, and penalty parameter $K = 10^5$ kPa in the FE computations. The figure shows very good agreement.

In the second example, a simple shear of the square subject to plane strain condition is considered (Figure 7.12) with

$$\mathbf{F} = \begin{bmatrix} 1 & F_{12} & 0 \\ 0 & 1 & 0 \\ 0 & 0 & 1 \end{bmatrix}, \quad (7.55)$$

where $0 \leq F_{12} \leq 0.5$.

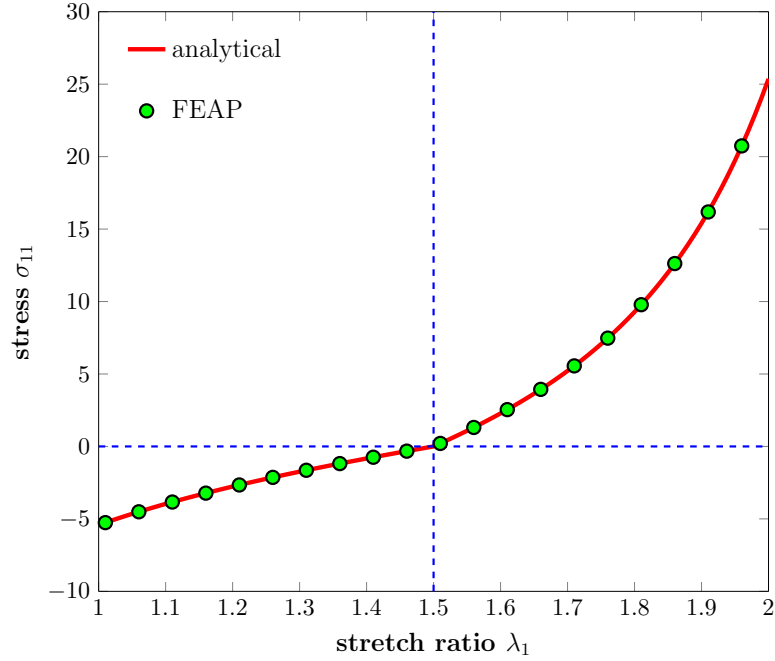


Figure 7.11: Cauchy stress σ_{11} is plotted against the stretch ratio λ_1 in the example of uni-axial stretch. $g_1=1.5$ is used in this example.

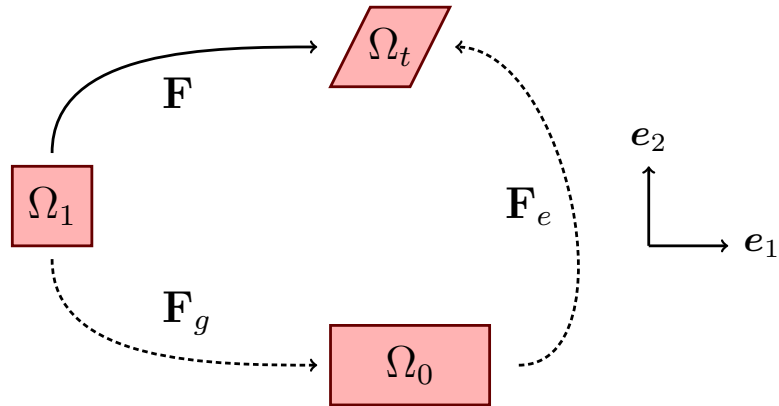


Figure 7.12: The simple shear of a body ($\Omega_1 \rightarrow \Omega_t$) is demonstrated due to both internal growth and external loading: dash line shows the imaginary theoretical decomposition, while solid line shows the computational process in FEAP.

We calculate the elastic deformation gradient as

$$\mathbf{F}_e = \mathbf{F}\mathbf{F}_g^{-1} = \begin{bmatrix} g_1^{-1} & F_{12} & 0 \\ 0 & 1 & 0 \\ 0 & 0 & 1 \end{bmatrix}. \quad (7.56)$$

In this example, we consider a compressible material since the volume changes from Ω_0 to Ω_t . To achieve this, we use a small value for K , say $K = 100$ kPa in our example. Substitution of (7.56) into (7.38) yields the analytical stress

$$\begin{aligned}\sigma_{11} &= K(g_1^{-1} - 1) + \frac{2c}{3}g_1^{5/3}(g_1^{-2} + F_{12}^2 - 1) + 4k_1g_1^{-1}(g_1^{-2} - 1)\exp[k_2(g_1^{-2} - 1)^2], \\ \sigma_{22} &= K(g_1^{-1} - 1) + \frac{c}{3}g_1^{5/3}(1 - g_1^{-2} - F_{12}^2), \\ \sigma_{12} &= cg_1^{5/3}F_{12}^2.\end{aligned}$$

The deformation from Ω_1 , with initial stress associated with \mathbf{F}_g , to Ω_t is achieved by specifying a displacement loading on surfaces of Ω_1 in FEAP, such that we have the simple shear deformation and the stress is computed numerically. The boundary conditions on Ω_1 are: the bottom and top are fixed such that there is no displacement in the \mathbf{e}_2 direction, and the left and right boundaries have constant displacement $u = F_{12}X_2 - X_1$ in the \mathbf{e}_1 direction, where X_1 and X_2 are the coordinate of a point in the left and right boundaries of Ω_1 .

The Cauchy stress computed analytically and numerically when the body is in the configuration Ω_t are plotted in Figure 7.13 and the good agreement between them is shown.

This subroutine with growth property has many applications. The residual stress can be introduced when \mathbf{F}_g^{-1} is a measure of residual strain and a corresponding constitutive law for residual strain to residual stress is specified. Imagine that Ω_1 in Figure 7.10 has a very rigid skin and the growth, specified by \mathbf{F}_g , has already occurred in the skin. In this condition, Ω_1 includes the residual stress due to the growth. If the skin is removed, Ω_1 will relax to Ω_0 . Therefore, \mathbf{F}_g^{-1} is a measure of residual strain in this case.

The growth may be activated by over-stress, over-stretch or over-energy-stored. Associating, a growth law

$$\mathbf{F}_g = \mathbf{F}_g(x) \tag{7.57}$$

is needed. Let $x=\boldsymbol{\sigma}$ define a stress-driven, $x=\mathbf{C}$ define a strain-driven and $x=\Psi$ define a energy-driven growth law. Our FE subroutine can be updated to cope with these mechanics-driven growth law. An implicit implementation of this law is a fully-coupled approach. The mechanical quality ($\boldsymbol{\sigma}$, \mathbf{C} or Ψ) in the growth law depends on \mathbf{F}_e , so the isolation of \mathbf{F}_e through

$$\mathbf{F}_e = \mathbf{F}\mathbf{F}_g^{-1}(\mathbf{F}_e) \tag{7.58}$$

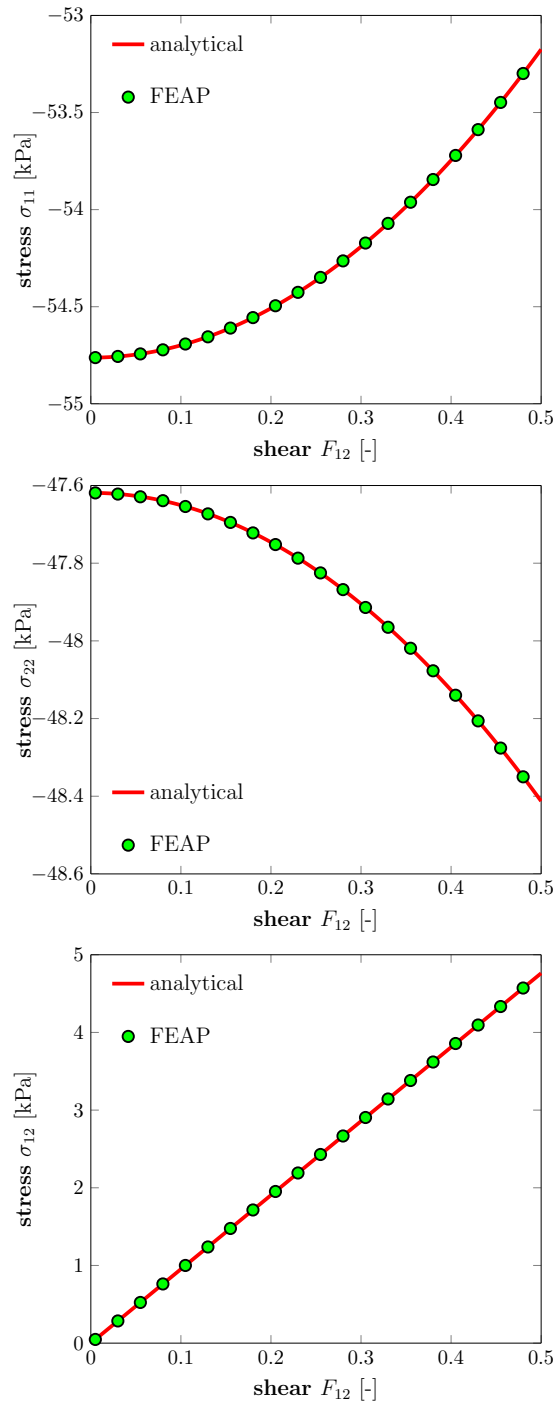


Figure 7.13: Components of Cauchy stress are plotted against the shear F_{12} in the example of simple shear. $g_1=2$ is used in this example.

is difficult. On the other hand, an explicit implementation is easy. Since the nonlinear deformation is solved as a sequence of linearised problems or proportional steps. The calculation of \mathbf{F}_g in n -th step uses the mechanical qualities from the equilibrium at $n - 1$ -th step. Analogous to the simple examples above, the n -th step only solves the equations for elastic deformation.

7.6 Conclusion

We have shown that a strain energy function $\widehat{\Psi}$, constructed for a nearly-incompressible or compressible material from an incompressible material model $\overline{\Psi}$ following the conventional approach of using $\overline{\Psi}$ in a FE program, may lead to loss of anisotropy. To avoid this problem, we propose a possible solution: do not use of the decomposition of \mathbf{F} in parts of $\overline{\Psi}$ associated with anisotropy. The suggestion is demonstrated through application in a Fung-type and HGO SEF, so we have a new compressible SEF $\widetilde{\Psi}$. The FE subroutines for both $\widehat{\Psi}$ and $\widetilde{\Psi}$ of HGO SEF are developed. In this subroutine, the growth of living soft tissue is also considered. The subroutines have been verified and can be used in the FE computation for living fibrous soft tissues.

Chapter 8

Conclusions

This thesis has focussed on the development of computational models to understand mechanical issues in arterial dissections. The computational models use FE-based methods: standard FEM with tears that coincide with the interfaces between elements; XFEM with tears expressed via enrichment functions that appear in the specification of the discretisation. We have developed several computational techniques and reported the effects of a number of mechanical parameters on the criteria for tear propagation.

The computational techniques developed in this thesis include how to: calculate the energy release rate of a fibre-reinforced soft tissue subject to internal pressure, introduce the residual stress into a FE model, calculate the stress-free configuration through inverse analysis and develop a material model for living fibrous soft tissue in a FE program. These techniques are verified through comparison with theoretical analysis of simple cases. The numerically calculated deformation and stress of a two-layer arterial wall with residual stress inflated by internal pressure agree with analytical results. A comparison between analytical and numerical calculations of the stress for a soft tissue that includes growth shows good agreement.

Using the techniques above we have reported the critical pressure and direction of propagation at the onset of propagation of a tear in soft tissue. We have investigated the effect of several geometric, material and loading parameters on the propagation as follows:

- In the models of pressure-driven tear propagation in longitudinal strips (Chapter 3), we found the energy release rate increases with the axial length of tear, so the critical pressure decreases with the length. In contrast, the surrounding tissues will decrease the energy release rate and result in arrest when the surrounding tissues are

stiff enough. Therefore, the decrease in stiffness of surrounding tissues will increase the risk of dissection propagation.

- Through the simulations of peeling-driven tear propagation in strips and discs (Chapter 4), we found the tear is likely to propagate along the material axis with the maximum stiffness, which is determined by the orientation of fibres. Therefore, fibre plays an important role in the direction of propagation.
- The study on the effect of circumferential length and radial depth of tear (Chapter 4), shows that a shallow and long tear tends to buckle inner wall and collapse lumen, while a deep tear more likely to propagate. For a short tear, the critical pressure increases with the depth, while decreases with the depth for a long tear. Some shapes of the deformed arterial wall, predicted by our simulation, are similar to CT scans of arterial dissections in the clinic.
- The residual stress can prevent tear propagation (Chapter 5 and 6). Our simulations show the critical pressure for tear propagation increases with the opening angle or residual stress. This results might explain why the ageing is an important factor in diagnosis of an AD, since residual stress varies significantly with age.

In Chapter 7 we demonstrated that the implementation of a material model in a finite element program for an anisotropic material can lead to loss of the anisotropy unless care is taken in the implementation. The issue arises when using an incompressible material in a compressible calculation with a volumetric term whose parameter K is adjusted so that the constraint of incompressibility is approximately satisfied. This issue has been shown by Nolan et al. [2014]; Vergori et al. [2013] for the HGO SEF. In this thesis, we extended this finding to show that this issue exists for any anisotropic SEF, including HGO and Fung-type SEF. However, the problem disappears for incompressible material, in other words, as the controlling parameter $K \rightarrow \infty$. To deal with the issue in the compressible region, we found a way to avoid the loss of anisotropy, i.e. avoiding using of the volumetric and deviatoric decomposition in terms related to the anisotropy. In addition, a detailed derivative for implementation of a strain energy function in a FE program was shown, and the HGO SEF was implemented in an open-source FE program FEAP. Using this program, we also demonstrated our findings from analytical solutions above in the numerical computations.

The findings of this thesis might help to explain the governing mechanical factors for many phenomena in dissection of the arterial wall.

8.1 Limitations and future directions

Biomechanical modelling of the dissection of the arterial wall and the evolution of the dissection is challenging, what we face is a coupled fluid-solid interaction problem, complicated by large deformations, a complex geometry and boundary conditions and uncertainty regarding many material parameters. For instance, the mechanical properties of the multi-layer and multi-component arterial wall are very complex, the loading on the arterial dissection and the surrounding tissues is difficult to measure and geometry of arterial wall is not easily determined. To explore the behaviour of a dissection we have had to make a number of modelling assumptions. In this thesis, we have assumed that the arterial wall is a hyperelastic, fibrous soft tissue [Holzapfel et al., 2000]. We have employed static pressure loading on both the lumen and the tear and used idealised geometries to examine the effects of residual stress. These simplifications may be relaxed in a number of ways to bring us closer to modelling the behaviour of an actual tear in an actual human artery.

In Chapter 3, we proposed a computational framework to compute the energy release rate associated with a tear extension. The advantage of this approach is that we do not need to know the singularity of the tip-stress field a priori, which is generally unknown for the nonlinear elastic material. However, we have to specify additionally the direction of tear extension. For illustration of this computational framework, we used a two-dimensional trip with a tear in the centre, subjected to pressure loading on the tear faces. The symmetry of the geometry suggests that the tear will extend along the centre-line, as used in our examples. However, for other geometries without the symmetry we must choose a physical principle that selects the direction of propagation. One such choice is that the tear proceeds in a direction that maximises the energy release rate. In order to simulate this we would have to compute the energy release rate as a function of extension direction. There are theoretical aspects to this approach that would be interesting to explore, e.g. the equivalent of the J-integral for nonlinear materials and the derivation from physics and thermodynamics of a selection criterion for direction.

Using the simplified model in Chapter 3, we demonstrated that connective tissues with larger elastic modulus can resist tear opening, decrease the energy release rate and lead

to arrest tear extension. In the arterial dissection, the effect of connective tissues is more complex. There are two inherited connective tissue disorder (Marfan and Ehlers-Danlos syndromes) highly related to dissections [Braverman, 2010; Milewicz et al., 2005]. The dissection does not tend to occur in the Marfan syndrome until the aortic root diameter reaches about 5 cm, while in the vascular Ehlers-Danlos syndrome the dissection commonly occurs at normal vascular dimensions. The vascular wall is very different in these conditions, with thickening, increased collagen and decreased elastin in the Marfan syndrome, but decreased collagen and normal elastin in the vascular Ehlers-Danlos syndrome. Thus, it is worth to model this effect of collagen and elastin on the risk of dissection and build the connection with both types of connective tissues diseases. However, to perform this modelling, we have to develop new material models, because the HGO strain energy function we used is a homogenised constitutive law. In addition, our current model with the HGO strain energy function can not model the percentage change of both collagen and elastin. An alternative to be considered in future is the strain energy function based on the constrained mixed theory, e.g. (1.1), which allows one to control the percentage of the each component in computation models and to investigate the effect of change in percentages of both elastin and collagen on energy release rate.

In Chapter 4, we employed the extended finite element method with a cohesive traction-separation law for the tear. In comparison with the approach of Chapter 3, this method automatically calculates the path of the tear as it extends, based on the deformation and the cohesive law. In Chapter 4, we focus on the effects of tear length and depth on critical pressure p_c for arterial dissection propagation and shapes of the deformed arterial wall. The value of p_c for a particular arterial dissection depends on the material parameters, the geometry of the artery and the geometry of the tear. For example, the maximum cohesive stress T_c plays an important role. However, the value of T_c is not easy to be estimated for a given tissue. Ferrara and Pandolfi [2010] used $T_c \approx 8.6 c$ when modelling the peeling apart of strips using standard FEM with cohesive surfaces. We found that simulations in Abaqus did not converge unless $T_c \leq 2c_m$, where c_m is the shear modulus of the matrix in the media. This ratio of $T_c/c_m = 2$ is lower than that achieved in the literature [Ferrara and Pandolfi, 2010], and results in the value of p_c being small. This limitation does not affect our present study, the aim of which is to identify the trends in the variation of the critical pressure with tear length and depth, and thus we also scaled p_c from the simulation by c_m to form a dimensionless critical pressure p'_c .

In Chapters 5 and 6, we focused on the effect of the residual stress on the critical pressure. The two challenges in this study are 1) how to include residual stress into a finite element model, and 2) how to guarantee simulations start from a same stress-residual configuration, i.e. the difference between simulations is only residual stress. In Chapter 5, we imported the analytical residual stress through a subroutine `sigini.f` as an initial stress field, but this can not work for a model with an anisotropic hyperelastic material in Abaqus 6.13. Therefore, in Chapter 6 we developed a computational protocol that involves a sequence of novel boundary conditions to close an opening angle, starting from the stress-free configuration. The numerical approach has the following two requirements: after closing, the two ends should have same dimensions and this joint end can move during the subsequent inflation. For the simplified geometry in Chapter 6, these two requirements are automatically satisfied through our boundary conditions. However, these boundary conditions have to be updated for a general geometry or an alternative approach may be considered for including the residual stress in a finite element model.

In Chapter 7, we demonstrated a special care should be taken in the implementation of a strain energy function for an anisotropic material in a finite element solver, and also incorporated a growth tensor \mathbf{F}_g in our formulations. With this approach, we can analyse the elastic deformation of a body Ω_1 with existing stress, e.g. initial stress consistent with boundary conditions or residual stress. This growth tensor transforms Ω_1 to the stress-free configuration Ω_0 . We have implemented the HGO strain energy function with this special care and growth tensor in FEAP, and verified this subroutine through some examples of simple geometries and loading scenarios, for which the analytical solutions are available. In future, we will use this approach to include the residual stress, as demonstrated in Figure 8.1, in the models of arterial dissection. The constraint of this method is that we need to specify \mathbf{F}_g a priori. For our simplified geometries, we can obtain the \mathbf{F}_g analytically. For a general geometry, \mathbf{F}_g may be obtained by tracking the deformation from Ω_1 to Ω_0 using markers.

Our work in Chapter 7 is a preliminary step towards including the growth and remodelling of the arterial wall in our models. Currently, we assumed the tear will extend in the extreme loading condition like hypertension, which is true for ex-vivo tissues. However, the living tissues can adapt the change of loading environment through its biological function. For example, Qi et al. [2015] showed how the collagen fibres redistribute through the arterial wall subject to the internal pressure. To model a living soft tissue, both the tear

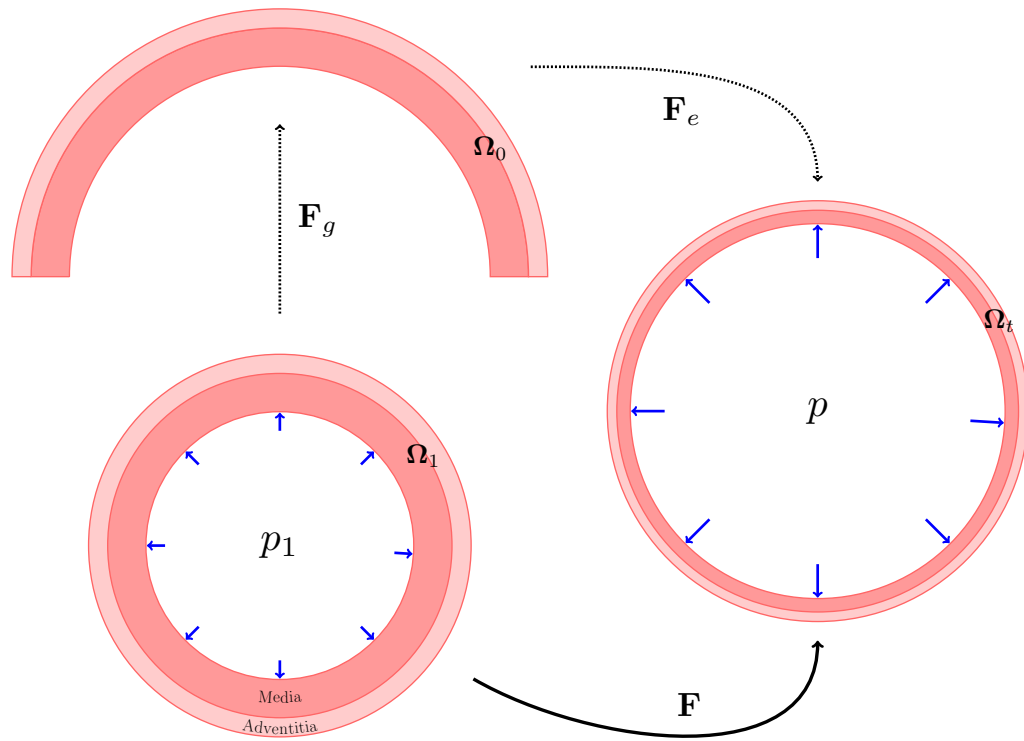


Figure 8.1: With an implementation of strain energy function $\Psi(\mathbf{F}\mathbf{F}_g^{-1})$ with a given \mathbf{F}_g in a FE solver, the deformation from Ω_0 to Ω_t can be simulated using Ω_1 as the initial configuration in a computational model. That is, the computational simulation starts from Ω_1 , but the computation is for the deformation from Ω_0 to Ω_t . Let $p_1 = 0$, Ω_1 is the zero-loading configuration with residual stress. The residual stress is determined by the residual strain in the deformation from Ω_0 to Ω_1 and a constitutive law. This is an alternative approach to include the residual stress into a finite element model.

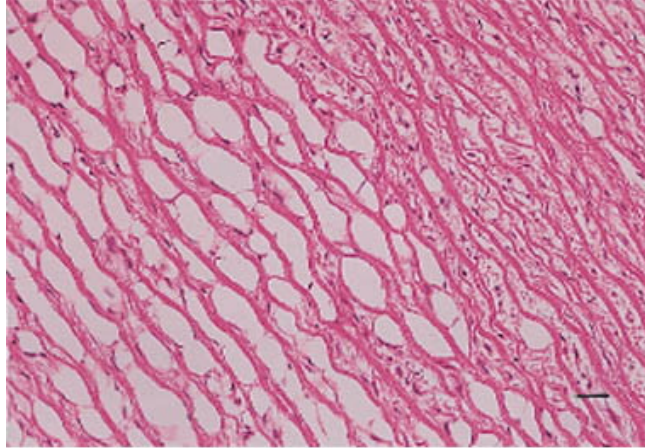


Figure 8.2: Experiments performed by MacLean et al. [1999]: square tissue samples were cut from a porcine thoracic aortas and were elongated 3.5 times in the radial direction with a tensile testing machine. This figure shows that the elastin layers was separated and the muscle cell nuclei (dark purple) was reorientated. Scale bar is $30\ \mu\text{m}$.

extension and growth and remodelling occur as a result of loading environment change.

All of the failure criteria we used are based on the assumption that the arterial wall is a homogeneous continuum. However, due to the complex structure of the arterial wall a new failure criterion might be developed, which is likely to be multiscale—modelling different components being damaged at different length-scales. Some experiments to support this hypothesis were performed by MacLean et al. [1999], in which a histological analysis of porcine thoracic aorta subject to a radial stretch was performed. This analysis showed that the damage of aortic wall involves separation of the elastin layers, change in orientation of smooth muscle cells and torn elastin fibres, as shown in Figure 8.2.

Another thing to be considered in the failure criterion may be the failure mode, because the driving force for dissection propagation in reality is different with that in many experiments [e.g. MacLean et al., 1999; Sommer et al., 2008]. In [MacLean et al., 1999], the damage of arterial wall was caused by a tension. In [Sommer et al., 2008], the propagation of dissection was also caused by a tension when peeling strips of arterial wall. However, in reality the dissection occurs in the radially compressed arterial wall subject to the luminal blood pressure, and is highly related to the hypertension [Braverman, 2010]. Subject to the pressure, the elastin layers should be compressed rather than stretched radially. We think the radial separation in a dissection may be due to filling of the dissection by dynamic blood flow. Therefore, a failure criterion including these two aspects (multiscale damage

of the arterial wall and pressurized fluid-driven tear propagation) must be developed.

Finally, it has been observed that a fluid-structure interaction model of arterial dissection [Alimohammadi et al., 2015] is necessary to support clinicians. We used a static pressure as the driving force for the extension of an arterial dissection. Pressure-penetration technique—the new generated tear surface will be subject to pressure loading during tear extension, was used to simulate the fluid pressure, this is a simple modelling strategy for fluid-solid interaction. Loading from the dynamic blood flow should be considered as the driving force for the tear extension.

References

- Abaqus (2014). *ABAQUS Documentation*. Dassault Systèmes.
- Alastrué, V., Rodríguez, J., Calvo, B., and Doblare, M. (2007). Structural damage models for fibrous biological soft tissues. *International Journal of Solids and Structures*, 44(18):5894–5911.
- Alimohammadi, M., Sherwood, J.M., Karimpour, M., Agu, O., Balabani, S., and Díaz-Zuccarini, V. (2015). Aortic dissection simulation models for clinical support: fluid-structure interaction vs. rigid wall models. *Biomedical Engineering Online*, 14(1):14–34.
- Allegri, G. and Scarpa, F. L. (2014). On the asymptotic crack-tip stress fields in nonlocal orthotropic elasticity. *International Journal of Solids and Structures*, 51(2):504–515.
- Alshoaibi, A. M., Hadi, M., and Ariffin, A. (2007). An adaptive finite element procedure for crack propagation analysis. *Journal of Zhejiang University SCIENCE A*, 8(2):228–236.
- Ambrosi, D., Ateshian, G., Arruda, E., Cowin, S., Dumais, J., Goriely, A., Holzapfel, G. A., Humphrey, J., Kemkemer, R., Kuhl, E., et al. (2011). Perspectives on biological growth and remodeling. *Journal of the Mechanics and Physics of Solids*, 59(4):863–883.
- Babu, A. R., Byju, A. G., and Gundiah, N. (2015). Biomechanical properties of human ascending thoracic aortic dissections. *Journal of Biomechanical Engineering*, 137(8):081013.
- Babusška, I. and Rheinboldt, W. C. (1978). Error estimates for adaptive finite element computations. *SIAM Journal on Numerical Analysis*, 15(4):736–754.
- Badel, P., Avril, S., Sutton, M. A., and Lessner, S. M. (2014). Numerical simulation of arterial dissection during balloon angioplasty of atherosclerotic coronary arteries. *Journal of Biomechanics*, 47(4):878–889.

- Balzani, D., Brinkhues, S., and Holzapfel, G. A. (2012). Constitutive framework for the modeling of damage in collagenous soft tissues with application to arterial walls. *Computer Methods in Applied Mechanics and Engineering*, 213:139–151.
- Bathe, K. (1996). *Finite Element Procedures*. Prentice Hall.
- Belytschko, T. and Black, T. (1999). Elastic crack growth in finite elements with minimal remeshing. *International Journal for Numerical Methods in Engineering*, 45(5):601–620.
- Belytschko, T., Gracie, R., and Ventura, G. (2009). A review of extended/generalized finite element methods for material modeling. *Modelling and Simulation in Materials Science and Engineering*, 17(4):043001.
- Bhattacharjee, T., Barlingay, M., Tasneem, H., Roan, E., and Vemaganti, K. (2013). Cohesive zone modeling of mode I tearing in thin soft materials. *Journal of the Mechanical Behavior of Biomedical Materials*, 28(0):37–46.
- Bogousslavsky, J., Despland, P. A., and Regli, F. (1987). Spontaneous carotid dissection with acute stroke. *Archives of neurology*, 44(2):137–140.
- Braverman, A. C. (2010). Acute aortic dissection clinician update. *Circulation*, 122(2):184–188.
- Campos-Herrera, C. R., Scaff, M., Yamamoto, F. I., and Conforto, A. B. (2008). Spontaneous cervical artery dissection: an update on clinical and diagnostic aspects. *Arquivos de Neuro-Psiquiatria*, 66(4):922–927.
- Canham, P. B., Finlay, H. M., Dixon, J. G., Boughner, D. R., and Chen, A. (1989). Measurements from light and polarised light microscopy of human coronary arteries fixed at distending pressure. *Cardiovascular Research*, 23(11):973–982.
- Cardamone, L., Valentin, A., Eberth, J., and Humphrey, J. (2009). Origin of axial pre-stretch and residual stress in arteries. *Biomechanics and Modeling in Mechanobiology*, 8(6):431–446.
- Cescotto, S. and Fonder, G. (1979). A finite element approach for large strains of nearly incompressible rubber-like materials. *International Journal of Solids and Structures*, 15(8):589–605.

- Chuong, C. and Fung, Y. (1983). Three-dimensional stress distribution in arteries. *Journal of Biomechanical Engineering*, 105(3):268–274.
- Chuong, C. and Fung, Y. (1986). Residual stress in arteries. In *Frontiers in Biomechanics*, pages 117–129. Springer.
- Courant, R. (1943). Variational methods for the solution of problems of equilibrium and vibrations. *Bulletin of the American Mathematical Society*, 49(1):1–23.
- Davies, R. R., Goldstein, L. J., Coady, M. A., Tittle, S. L., Rizzo, J. A., Kopf, G. S., and Elefteriades, J. A. (2002). Yearly rupture or dissection rates for thoracic aortic aneurysms: simple prediction based on size. *The Annals of Thoracic Surgery*, 73(1):17–28.
- de Figueiredo Borges, L., Jaldin, R. G., Dias, R. R., Stolf, N. A. G., Michel, J. B., and Gutierrez, P. S. (2008). Collagen is reduced and disrupted in human aneurysms and dissections of ascending aorta. *Human Pathology*, 39(3):437–443.
- Delfino, A., Stergiopoulos, N., Moore, J., and Meister, J. J. (1997). Residual strain effects on the stress field in a thick wall finite element model of the human carotid bifurcation. *Journal of Biomechanics*, 30(8):777–786.
- Dobrin, P. B., Schwarcz, T. H., and Mrkvicka, R. (1990). Longitudinal retractive force in pressurized dog and human arteries. *Journal of Surgical Research*, 48(2):116–120.
- Dolbow, J. and Belytschko, T. (1999). A finite element method for crack growth without remeshing. *International Journal for Numerical Methods in Engineering*, 46:131–150.
- Elices, M., Guinea, G., Gomez, J., and Planas, J. (2002). The cohesive zone model: advantages, limitations and challenges. *Engineering Fracture Mechanics*, 69(2):137–163.
- Ferrara, A. and Pandolfi, A. (2010). A numerical study of arterial media dissection processes. *International Journal of Fracture*, 166(1-2):21–33.
- Flory, P. (1961). Thermodynamic relations for high elastic materials. *Transactions of the Faraday Society*, 57:829–838.
- Foundation., M. H. I. (2013). Mortality for acute aortic dissection near one percent per hour during initial onset. *ScienceDaily*.

- Fung, Y. (1991). What are the residual stresses doing in our blood vessels? *Annals of Biomedical Engineering*, 19(3):237–249.
- Gasser, T. C. and Holzapfel, G. A. (2006). Modeling the propagation of arterial dissection. *European Journal of Mechanics-A/Solids*, 25(4):617–633.
- Gasser, T. C., Ogden, R. W., and Holzapfel, G. A. (2006). Hyperelastic modelling of arterial layers with distributed collagen fibre orientations. *Journal of the Royal Society Interface*, 3(6):15–35.
- Griffith, A. A. (1921). The phenomena of rupture and flow in solids. *Philosophical Transactions of the Royal Society of London. Series A, containing papers of a mathematical or physical character*, 221:163–198.
- Gurtin, M. E. (1982). *An introduction to continuum mechanics*. Academic Press.
- Hagan, P. G., Nienaber, C. A., Isselbacher, E. M., Bruckman, D., Karavite, D. J., Rusan, P. L., Evangelista, A., Fattori, R., Suzuki, T., Oh, J. K., et al. (2000). The International Registry of Acute aortic Dissection (IRAD): new insights into an old disease. *Journal of the American Medical Association*, 283(7):897–903.
- Hartmann, S. and Neff, P. (2003). Polyconvexity of generalized polynomial-type hyperelastic strain energy functions for near-incompressibility. *International Journal of Solids and Structures*, 40(11):2767 – 2791.
- Henshell, R. and Shaw, K. (1975). Crack tip finite elements are unnecessary. *International Journal for Numerical Methods in Engineering*, 9(3):495–507.
- Holzapfel, G. A. (2000). *Nonlinear solid mechanics*. Wiley Chichester.
- Holzapfel, G. A. (2006). Determination of material models for arterial walls from uniaxial extension tests and histological structure. *Journal of Theoretical Biology*, 238(2):290–302.
- Holzapfel, G. A., Gasser, T. C., and Ogden, R. W. (2000). A new constitutive framework for arterial wall mechanics and a comparative study of material models. *Journal of Elasticity and the Physical Science of Solids*, 61(1-3):1–48.

- Holzapfel, G. A. and Ogden, R. W. (2010). Constitutive modelling of arteries. *Proceedings of the Royal Society of London A: Mathematical, Physical and Engineering Sciences*, 466(2118):1551–1597.
- Holzapfel, G. A. and Ogden, R. W. (2015). On the tension–compression switch in soft fibrous solids. *European Journal of Mechanics-A/Solids*, 49:561–569.
- Humphrey, J. and Rajagopal, K. (2002). A constrained mixture model for growth and remodeling of soft tissues. *Mathematical Models and Methods in Applied Sciences*, 12(3):407–430.
- Humphrey, J. D. (1994). Mechanics of the arterial wall: review and directions. *Critical Reviews in Biomedical Engineering*, 23(1-2):1–162.
- Ionescu, I., Guilkey, J. E., Berzins, M., Kirby, R. M., and Weiss, J. A. (2006). Simulation of soft tissue failure using the material point method. *Journal of Biomechanical Engineering*, 128(6):917–924.
- Irwin, G. and Wells, A. (1965). A continuum-mechanics view of crack propagation. *Metallurgical Reviews*, 10(1):223–270.
- Khan, I. A. and Nair, C. K. (2002). Clinical, diagnostic, and management perspectives of aortic dissection. *Chest Journal*, 122(1):311–328.
- Knees, D. and Mielke, A. (2008). Energy release rate for cracks in finite-strain elasticity. *Mathematical Methods in the Applied Sciences*, 31(5):501–528.
- Krishnan, V. R., Hui, C. Y., and Long, R. (2008). Finite strain crack tip fields in soft incompressible elastic solids. *Langmuir*, 24(24):14245–14253.
- Li, B. (2013). *Mathematical modelling of aortic dissection*. PhD thesis, University of Glasgow.
- MacLean, N. F., Dudek, N. L., and Roach, M. R. (1999). The role of radial elastic properties in the development of aortic dissections. *Journal of vascular surgery*, 29(4):703–710.
- Makarawate, P. and Chaosuwannakit, N. (2013). Prevalence and significance of incidental extracardiac findings of a cardiac ct angiography. *Srinagarind Medical Journal*, 28(1):47–55.

- Milewicz, D. M., Dietz, H. C., and Miller, D. C. (2005). Treatment of aortic disease in patients with marfan syndrome. *Circulation*, 111(11):e150–e157.
- Mohammadi, S. (2008). *Extended finite element method: for fracture analysis of structures*. John Wiley & Sons.
- Nagtegaal, J. C., Parks, D. M., and Rice, J. (1974). On numerically accurate finite element solutions in the fully plastic range. *Computer Methods in Applied Mechanics and Engineering*, 4(2):153–177.
- Nolan, D., Gower, A., Destrade, M., Ogden, R., and McGarry, J. (2014). A robust anisotropic hyperelastic formulation for the modelling of soft tissue. *Journal of the Mechanical Behavior of Biomedical Materials*, 39:48–60.
- Ogden, R. (1972). Large deformation isotropic elasticity-on the correlation of theory and experiment for incompressible rubberlike solids. *Proceedings of the Royal Society of London A: Mathematical, Physical and Engineering Sciences*, 326:565–584.
- Ogden, R. (1978). Nearly isochoric elastic deformations: application to rubberlike solids. *Journal of the Mechanics and Physics of Solids*, 26(1):37–57.
- Ogden, R. W. (1997). *Non-linear elastic deformations*. Courier Corporation.
- Ortiz, M. and Pandolfi, A. (1999). Finite-deformation irreversible cohesive elements for three-dimensional crack-propagation analysis. *International Journal for Numerical Methods in Engineering*, 44(9):1267–1282.
- Pape, L., Tsai, T., Isselbacher, E., Oh, J., O’gara, P., Evangelista, A., Fattori, R., Meinhardt, G., Trimarchi, S., Bossone, E., et al. (2007). Aortic diameter $>$ or $=$ 5.5 cm is not a good predictor of type A aortic dissection: observations from the International Registry of acute Aortic Dissection (IRAD). *Circulation*, 116(10):1120–1127.
- Peano, A., Szabo, B., and Mehta, A. (1978). Self-adaptive finite elements in fracture mechanics. *Computer Methods in Applied Mechanics and Engineering*, 16(1):69–80.
- Pence, T. (2014). Distortion of anisotropic hyperelastic solids under pure pressure loading: Compressibility, incompressibility and near-incompressibility. *Journal of Elasticity*, 114(2):251–273.

- Phongthanapanich, S. and Dechaumphai, P. (2004). Adaptive delaunay triangulation with object-oriented programming for crack propagation analysis. *Finite Elements in Analysis and Design*, 40(13):1753–1771.
- Qi, N., Gao, H., Ogden, R.W., Hill, N.A., Holzapfel, G.A., Han, H.C. and Luo, X.Y. (2015). Investigation of the optimal collagen fibre orientation in human iliac arteries. *Journal of the Mechanical Behavior of Biomedical Materials*, 52:108–119.
- Rahulkumar, P., Jagota, A., Bennison, S., and Saigal, S. (2000). Cohesive element modeling of viscoelastic fracture: application to peel testing of polymers. *International Journal of Solids and Structures*, 37(13):1873–1897.
- Rajagopal, K., Bridges, C., and Rajagopal, K.R.(2007). Towards an understanding of the mechanics underlying aortic dissection. *Biomechanics and Modeling in Mechanobiology*, 6(5):345–359.
- Roach, M. R. and Burton, A. C. (1957). The reason for the shape of the distensibility curves of arteries. *Canadian Journal of Biochemistry and Physiology*, 35(8):681–690.
- Rodriguez, E. K., Hoger, A., and McCulloch, A. D. (1994). Stress-dependent finite growth in soft elastic tissues. *Journal of Biomechanics*, 27(4):455–467.
- Shah, S. B., Witzenburg, C., Hadi, M. F., Wagner, H. P., Goodrich, J. M., Alford, P. W., and Barocas, V. H. (2014). Prefailure and failure mechanics of the porcine ascending thoracic aorta: experiments and a multiscale model. *Journal of Biomechanical Engineering*, 136(2):21–28.
- Showalter, W., Esekogwu, V., Newton, K. I., and Henderson, S. O. (1997). Vertebral artery dissection. *Academic Emergency Medicine*, 4(10):991–995.
- Simo, J. C. and Taylor, R. L. (1991). Quasi-incompressible finite elasticity in principal stretches. continuum basis and numerical algorithms. *Computer Methods in Applied Mechanics and Engineering*, 85(3):273–310.
- Sommer, G., Gasser, T. C., Regitnig, P., Auer, M., and Holzapfel, G. A. (2008). Dissection properties of the human aortic media: an experimental study. *Journal of Biomechanical Engineering*, 130(2):021007.
- Spencer, A. (1971). Theory of invariants. *Continuum physics*, 1(Part III):239–352.

- Spencer, A. (1984). Constitutive theory for strongly anisotropic solids. In *Continuum theory of the mechanics of fibre-reinforced composites*, pages 1–32. Springer.
- Stephenson, R. A. (1982). The equilibrium field near the tip of a crack for finite plane strain of incompressible elastic materials. *Journal of Elasticity*, 12(1):65–99.
- Sun, Z., Al Moudi, M., and Cao, Y. (2014). CT angiography in the diagnosis of cardiovascular disease: a transformation in cardiovascular ct practice. *Quantitative Imaging in Medicine and Surgery*, 4(5):376–396.
- Taber, L. A. (1995). Biomechanics of growth, remodeling, and morphogenesis. *Applied Mechanics Reviews*, 48(8):487–545.
- Tada, H., Paris, P. C., Irwin, G. R., and Tada, H. (2000). *The stress analysis of cracks handbook*. ASME Press New York.
- Tam, A. S., Sapp, M. C., and Roach, M. R. (1998). The effect of tear depth on the propagation of aortic dissections in isolated porcine thoracic aorta. *Journal of biomechanics*, 31(7):673–676.
- Taylor, R. L. (2011a). *FEAP - - A Finite Element Analysis Program: Version 8.3 Programmer manual*. University of California at Berkeley.
- Taylor, R. L. (2011b). *FEAP - - A Finite Element Analysis Program: Version 8.3 User manual*. University of California at Berkeley.
- Tsai, T., Trimarchi, S., and Nienaber, C. (2009). Acute aortic dissection: Perspectives from the International Registry of acute Aortic Dissection (IRAD). *European Journal of Vascular and Endovascular Surgery*, 37(2):149–159.
- Tsai, T. T., Schlicht, M. S., Khanafer, K., Bull, J. L., Valassis, D. T., Williams, D. M., Berguer, R., and Eagle, K. A. (2008). Tear size and location impacts false lumen pressure in an ex vivo model of chronic type B aortic dissection. *Journal of Vascular Surgery*, 47(4):844–851.
- Vergori, L., Destrade, M., McGarry, P., and Ogden, R. (2013). On anisotropic elasticity and questions concerning its finite element implementation. *Computational Mechanics*, 52(5):1185–1197.

- Volokh, K. Y. (2004). Comparison between cohesive zone models. *Communications in Numerical Methods in Engineering*, 20(11):845–856.
- Waffenschmidt, T., Polindara, C., and Menzel, A. (2015). A gradient-enhanced continuum damage model for residually stressed fibre-reinforced materials at finite strains. In *Biomedical Technology*, pages 19–40. Springer.
- Wang, Y., Johnson, J., Spinale, F., Sutton, M., and Lessner, S. (2014). Quantitative measurement of dissection resistance in intimal and medial layers of human coronary arteries. *Experimental Mechanics*, 54(4):677–683.
- Wang, L., Roper, S. M., Luo, X. L., and Hill, N. A. (2015). Modelling of tear propagation and arrest in fibre-reinforced soft tissue subject to internal pressure. *Journal of Engineering Mathematics*, 15(1):249–265.
- Weiss, J. A., Maker, B. N., and Govindjee, S. (1996). Finite element implementation of incompressible, transversely isotropic hyperelasticity. *Computer Methods in Applied Mechanics and Engineering*, 135(1):107–128.
- Willis, J. (1967). A comparison of the fracture criteria of griffith and barenblatt. *Journal of the Mechanics and Physics of Solids*, 15(3):151–162.
- Wulandana, R. and Robertson, A. (2005). An inelastic multi-mechanism constitutive equation for cerebral arterial tissue. *Biomechanics and Modeling in Mechanobiology*, 4(4):235–248.
- Zehnder, A. T. (2007). *Fracture mechanics. Lecture notes in applied and computational mechanics*, volume 62. Springer.
- Zienkiewicz, O. C. and Taylor, R. L. (2005). *The finite element method for solid and structural mechanics*. Butterworth-heinemann.